

QUANTUM MODELLING OF ORGANIC MATERIALS
FOR ELECTRONICS, THERMOELECTRIC, AND
PHOTOLUMINESCENT APPLICATIONS

MOHAMAD SYAFIE BIN MAHMOOD

FACULTY OF ENGINEERING
UNIVERSITY OF MALAYA
KUALA LUMPUR

2018

**QUANTUM MODELLING OF ORGANIC MATERIALS
FOR ELECTRONICS, THERMOELECTRIC, AND
PHOTOLUMINESCENT APPLICATIONS**

MOHAMAD SYAFIE BIN MAHMOOD

**THESIS SUBMITTED IN FULFILMENT OF THE
REQUIREMENTS FOR THE DEGREE OF DOCTOR OF
PHILOSOPHY**

**FACULTY OF ENGINEERING
UNIVERSITY OF MALAYA
KUALA LUMPUR**

2018

UNIVERSITY OF MALAYA
ORIGINAL LITERARY WORK DECLARATION

Name of Candidate: MOHAMAD SYAFIE BIN MAHMOOD

Matric No: KHA140032

Name of Degree: DOCTOR OF PHILOSOPHY

Title of Thesis (“this Work”): QUANTUM MODELLING OF ORGANIC MATERIALS FOR ELECTRONICS, THERMOELECTRIC, AND PHOTOLUMINESCENT APPLICATIONS

Field of Study: Renewable Energy

I do solemnly and sincerely declare that:

- (1) I am the sole author/writer of this Work;
- (2) This Work is original;
- (3) Any use of any work in which copyright exists was done by way of fair dealing and for permitted purposes and any excerpt or extract from, or reference to or reproduction of any copyright work has been disclosed expressly and sufficiently and the title of the Work and its authorship have been acknowledged in this Work;
- (4) I do not have any actual knowledge nor do I ought reasonably to know that the making of this work constitutes an infringement of any copyright work;
- (5) I hereby assign all and every rights in the copyright to this Work to the University of Malaya (“UM”), who henceforth shall be owner of the copyright in this Work and that any reproduction or use in any form or by any means whatsoever is prohibited without the written consent of UM having been first had and obtained;
- (6) I am fully aware that if in the course of making this Work I have infringed any copyright whether intentionally or otherwise, I may be subject to legal action or any other action as may be determined by UM.

Candidate’s Signature

Date:

Subscribed and solemnly declared before,

Witness’s Signature

Date:

Name:

Designation:

QUANTUM MODELLING OF ORGANIC MATERIALS FOR ELECTRONICS, THERMOELECTRIC, AND PHOTOLUMINESCENT APPLICATIONS

ABSTRACT

Organic semiconductors are dominating a niche segment of applications in electronic devices, as an alternative to inorganic semiconductors. They are becoming mainstream in electronic devices such as organic light emitting diode (OLED) and nanowires due to their promising advantages such as low cost, ease of synthesis and high throughput fabrication methods. In this thesis, 3 families of organic materials; discotic liquid crystal (DLC), protic ionic liquid (PIL), and chalcone are chosen for their potential applications in electronics, thermoelectric, and fluorescence respectively. Therefore, this work is separated into 3 corresponding major sections as follows; (1) correlation between molecule structure and electronic properties of the 2,3,6,7,10,11-hexahydroxytriphenylene (HAT6) DLC molecule using first principle Density Functional Theory (DFT), (2) quantum thermodynamic calculations of entropy for amine based PILs, and (3) photoluminescent efficiency evaluation of 4-dimethylamino-2'-hydroxychalcone (DHC) based on molecular conformation. In (1), the columnar stacking of HAT6 molecules allows π - π orbital overlap at the molecular core which allows electronic charge transfer along the column. The electronic transfer is affected by conformation of DLC molecules in columnar phases, namely core-core facial separation (D), angular twist (θ), and lateral slide (L). The correlation between molecular structure and electronic properties are evaluated in terms of its formation energy, band gap (BG), and density of state (DOS). The preservation of π - π interaction by maintaining the integrity of its columnar structural characteristics is key to maintaining the DLC's charge transfer efficacy. In (2), quantum thermodynamic simulation of a series of amine based PILs (ethylammonium triflate (EaTf), diethylammonium triflate (DicaTf), triethylammonium triflate (TriaTf), and 2-methylpyridinium triflate (2mpTf)) was

carried out to calculate the entropy of the system. Analysis in terms of vibrational and conformational contribution to entropy was then extended to evaluate the role of PIL in a thermoelectric solution. In this section, the focus is on the vibration of proton attachment, which has the biggest influence on their thermodynamic properties. Then, a hypothetical thermodynamic cycle is built around the states where the thermodynamic-conformation mechanism was discussed. Thus, the relationship between molecule properties to the thermoelectric properties such as Seebeck coefficient was elucidated. In (3), the photoluminescence capability of the DHC from the chalcone family was evaluated using first principle DFT calculation. The conformation of the DHC in the ground and excited states were evaluated in crystalline state and in solutions. The conservation of planarity in the ground to excited state are expected to provide large photoluminescence yield. In solution, it is shown that the minimum energy in the excited state are achieved by a twist in the conformation, this provided a non-radiative pathway which quenches photoluminescence. In the crystalline state, the calculations show that the planarity is conserved going from the ground to excited state which encourage a high quantum yield of photoluminescence. These simulations are strongly supported by femtosecond spectroscopy results and provide a promising pathway for the use of chalcone in optoelectronic/bioimaging applications. Thus, this thesis provides a pathway for molecular design using first principle DFT calculations, to provide an optimisation strategy of better organic electronic materials for applications in electronics, thermoelectric, and optoelectronic.

Keywords: first principle DFT, molecular conformation, discotic liquid crystals, protic ionic liquid, chalcone

PEMODELAN MOLEKUL BAHAN ORGANIK UNTUK APLIKASI ELEKTRONIK, TERMOELEKTRIK, DAN PENDARKILAU

ABSTRAK

Semikonduktor organik mendominasi sebahagian daripada segmen yang diaplikasi dalam peranti elektronik sebagai alternatif kepada semikonduktor inorganik. Ia semakin menjadi kelaziman di dalam peranti elektronik seperti diod pemancar cahaya organik (OLED), dan wayar nano kerana kelebihan seperti kos yang rendah, kesenangan sintesis dan kaedah fabrikasi trupert yang tinggi. Di dalam tesis ini, 3 jenis bahan organik, iaitu cecair kristal diskotik (DLC), cecair ionik protik (PIL), dan *chalcone* telah dipilih kerana berpotensi aplikasi dalam elektronik, termoelektrik dan pendarkilau. Oleh itu, kerja ini terbahagi kepada 3 bahagian utama seperti berikut; (1) hubungkait antara struktur molekul dan sifat elektronik molekul DLC 2,3,6,7,10,11-heksaheksilositriphenilina (HAT6) menggunakan teori fungsi ketumpatan (DFT) prinsip pertama, (2) pengiraan entropi termodinamik quantum untuk PIL berasaskan amina, dan (3) penilaian kecekapan pendarkilau 4-dimetilamina-2'-hidoksichalcon (DHC) berdasarkan konformasi molekul. Dalam (1), susunan turus molekul HAT6 menyebabkan pertindihan orbital π - π di teras molekul yang mana membenarkan pergerakan caj elektron di sepanjang lajur. Pergerakan elektron dipengaruhi oleh konformasi molekul DLC dalam fasa turus, iaitu pisahan muka teras-teras (D), sudut pulas (θ), dan gelangar lateral (L). Hubungkait antara struktur molekul dan sifat elektronik dinilai dalam bentuk tenaga pembentukan, sela jalur (BG), and ketumpatan keadaan (DOS). Pengekalan interaksi π - π dengan memelihara keutuhan ciri-ciri struktur turus kolumnar adalah kunci untuk mengekalkan kecekapan pergerakan caj dalam DLC. Dalam (2), simulasi termodinamik kuantum ke atas suatu siri PIL berasaskan amina (etilammonium triflat (EaTf), dietilammonium triflat (DieaTf), trietilammonium triflat (TrieaTf), dan 2-metilpiridinium triflat (2mpTf)) telah dijalankan untuk mengira entropi sistem. Analisis dalam bentuk sumbangan getaran dan konformasi

kepada entropi kemudian dilanjutkan untuk menilai peranan PIL didalam larutan termoelektrik. Dalam bahagian ini, fokus utama adalah kepada pautan proton, yang mana mempunyai pengaruh terbesar kepada sifat termodinamik. Seterusnya, kitaran hipotesis dibina mengelilingi keadaan di mana mekanisme termodinamik-konformasi telah dibincangkan. Oleh itu, hubungan antara sifat molekul kepada sifat termoelektrik seperti pekali Seebeck telah dihuraikan. Dalam (3), keupayaan pendarkilau fotoluminesens DHC dari keluarga *chalcone* telah dinilai menggunakan pengiraan DFT prinsip pertama. Konformasi DHC di keadaan asas dan teruja dinilai dalam keadaan berhablur dan di dalam larutan. Pengekalan kesatahan dari keadaan asas kepada keadaan teruja dijangka akan menghasilkan pendarkilauan yang tinggi. Di dalam larutan, telah ditunjukkan bahawa tenaga minimum semasa keadaan teruja dicapai dengan piuh dalam konformasi. Ini memberi laluan tidak bersinar yang memadamkan pendarkilau. Dalam keadaan berhablur, pengiraan menunjukkan kesatahan dikekalkan dari keadaan asas ke teruja yang mana menggalakkan hasil kuantum pendarkilauan yang tinggi. Simulasi-simulasi ini adalah disokong kuat oleh keputusan spektroskopi femto saat dan ini membuka laluan untuk kegunaan *chalcone* dalam aplikasi optoelektronik/pengimejan bio. Oleh itu, tesis ini memberi laluan untuk reka bentuk molekul menggunakan pengiraan DFT prinsip pertama, untuk memberi strategi pengoptimuman bahan elektronik yang lebih baik untuk aplikasi organik elektronik, termoelektrik dan optoelektronik.

Kata kunci: DFT prinsip pertama, konformasi molekul, cecair kristal diskotik, cecair ionik protik, *chalcone*

ACKNOWLEDGEMENTS

Alhamdulillah.

The completion of this thesis could not have been possible without the participation and assistance of so many people whose name may not be enumerated. Their contributions are sincerely appreciated and gratefully acknowledged. However, I would like to express my deep appreciation and indebtedness particularly to the followings:

Foremost gratitude to all my supervisors, Dr. Suhana, Dr. Asrina, Dr. Mohammad Noh for their endless support, kind and understanding spirit during my study.

To all relatives and my friends, especially my wife Normashita Maira, my kids, Muqri Sofiyullah, Maryam Sofieyya and Marina Syahiyya, and parents for their support throughout this journey.

Special thanks to UiTM and KPT, for financial support through Tenaga Pengajar Muda Programme.

Above all, to the Great Almighty, the author of knowledge and wisdom, for his countless love.

Thank you.

TABLE OF CONTENTS

ABSTRACT	iii
ABSTRAK	v
ACKNOWLEDGEMENTS	vii
TABLE OF CONTENTS	viii
LIST OF FIGURES	xiii
LIST OF TABLES	xx
LIST OF SYMBOLS	xxi
LIST OF ABBREVIATIONS	xxii
CHAPTER 1: INTRODUCTION	1
1.1. Problem statement	5
1.2. Objectives	5
1.3. Scope of works	6
1.4. Thesis outline	6
CHAPTER 2: COMPUTATIONAL CHEMISTRY	9
2.1. Molecular modelling	9
2.1.1. Born-Oppenheimer Approximation	10
2.1.2. Molecular mechanics (MM)	11
2.1.3. First-principle calculations	12
2.1.3.1. The Hartree-Fock approximation	13
2.1.3.2. The Hartree-Fock Self-Consistent Field Method	14
2.1.4. Semi empirical calculations	14
2.1.5. Density functional calculations	15
2.1.5.1. Kohn-Sham approach	16
2.1.5.2. Local Density Approximation	17
2.1.5.3. Generalised Gradient Approximation	17

2.1.5.4.	Meta-GGA.....	18
2.1.5.5.	Hybrid Approximation	18
2.1.6.	Functionals overview	19
2.2.	Selection of computational methods	20
2.2.1.	Computational requirements of DLC system	21
2.2.2.	Computational requirements of Protic Ionic Liquid (PIL) systems	21
2.2.3.	Computational requirements of Chalcone system.....	22
2.3.	Refinement of the selected methods	23
2.4.	Limitations of this work	24
CHAPTER 3: CORRELATION OF COLUMNAR STRUCTURAL PARAMETERS AND ELECTRONIC CHARGE TRANSFER FOR THE HAT6 LIQUID CRYSTAL COLUMNAR PHASE		25
3.1.	Discotic liquid crystals as organic electronic material.....	25
3.2.	Charge transfer in DLCs	29
3.2.1.	Charge mobility in DLCs	30
3.2.2.	Improving charge transfer in DLCs.....	31
3.2.3.	Applications of DLCs.....	32
3.2.4.	Molecular modelling of DLCs	35
3.2.5.	Modelling of DLC structure	37
3.2.5.1.	Molecular Dynamics Investigations on DLC structure.....	38
3.2.5.2.	The Potential Energy Surfaces (PES) approach	40
3.2.6.	Modelling of DLC dynamics.....	41
3.2.6.1.	Core and tail dynamics	41
3.2.6.2.	Lattice dynamics	43
3.2.7.	Modelling of DLC charge transfer	44
3.2.7.1.	Thermally Activated Charge Hopping	45

3.2.7.2.	Charge Hopping Parameters.....	46
3.2.7.3.	Computational Methods.....	46
3.2.7.4.	Examples of charge transfer modelling.....	48
3.2.8.	Modelling of Electronic Orbitals.....	52
3.3.	Study of correlation of the electronic structure for HAT6 columnar phase.....	54
3.3.1.	Methodology	55
3.3.1.1.	Simulation settings	57
3.3.2.	Results and Discussion.....	59
3.3.2.1.	Highest Occupied Molecular Orbital (HOMO) and Lowest Unoccupied Molecular Orbital (LUMO)	59
3.3.2.2.	Structural stability and band gap (BG).....	61
3.3.2.3.	Density of states (DOS).....	64
3.3.2.4.	Population analysis.....	70
3.3.2.5.	Electronic density mapping.....	77
3.4.	Summary	79
CHAPTER 4: PROTIC IONIC LIQUID THERMODYNAMIC SIMULATION IN PERSPECTIVE OF THERMOELECTRIC APPLICATIONS		81
4.1.	Introduction of Ionic Liquids	81
4.2.	Types of Ionic Liquids	82
4.2.1.	Aprotic Ionic Liquids	83
4.2.2.	Protic Ionic Liquids	83
4.2.3.	Zwitterion	84
4.3.	Physicochemical Properties of Ionic Liquids.....	85
4.4.	Application of Ionic Liquids	86
4.4.1.	Ionic Liquids in Batteries	86
4.4.2.	Ionic Liquids in Fuel Cells	87

4.4.3.	Ionic Liquids in Solar Cells.....	88
4.4.4.	Ionic Liquids in Thermoelectric Generator	90
4.5.	Thermodynamic study of Ionic Liquids	92
4.6.	Thermodynamics of Protic Ionic Liquids	94
4.6.1.	Defining entropy from free energy.....	95
4.6.2.	Defining entropy component using harmonic oscillator	97
4.7.	Relationship between thermodynamics and thermoelectricity	102
4.7.1.	Onsager-Callen Model	103
4.7.1.1.	Irreversible Thermodynamics	103
4.8.	Study on thermodynamic-thermoelectric correlation of PILs.....	105
4.8.1.	Methodology	106
4.8.1.1.	Simulation flow	108
4.8.1.2.	Simulation settings	110
4.8.2.	Results and discussion.....	112
4.8.2.1.	Conformation effect to IR spectra.....	112
4.8.2.2.	Entropy difference of 2 conformations	114
4.8.2.3.	Temperature effect on N-H bond length	117
4.8.2.4.	Thermodynamic cycle under a temperature gradient.....	118
4.9.	Summary	122
CHAPTER 5: CORRELATION OF FLUORESCENCE-CHALCONE CONFORMATION AND RELATIONSHIP TO PROTON AND CHARGE TRANSFER MECHANISM		124
5.1.	Introduction to excited state intramolecular proton transfer	124
5.2.	Chalcones	126
5.2.1.	Applications of chalcone in opto-electronics	127
5.2.2.	Photoexcitation mechanism in Chalcone.....	128

5.3.	4-dimethylamino-2'-hydroxychalcone (DHC).....	129
5.4.	Study of correlation of fluorescence-conformation of Chalcone and its relationship to ESIPT and ICT effect.....	131
5.4.1.	Methodology	132
5.4.1.1.	Simulation settings	135
5.4.2.	Results and discussion.....	136
5.4.2.1.	Solvent effect on structural stability in the ground and excited states	136
5.4.2.2.	Crystalline conformation in ground and excited state.....	140
5.4.2.3.	Analysis of bond length-proton transfer.....	142
5.4.2.4.	Absorption and emission energy analysis	144
5.5.	Summary	147
	CHAPTER 6: CONCLUSION.....	149
6.1.	Structural effect of DLC.....	149
6.2.	Thermodynamic study of PIL	150
6.3.	Excitation-structure effect in Chalcone.....	150
	REFERENCES.....	153
	LIST OF PUBLICATION AND PAPERS PRESENTED	174

LIST OF FIGURES

- Figure 1.1.** Molecular structure of polyaniline (above), and polyacetylene (below).
Conjugating double bond gives rise to conductive properties. 3
- Figure 2.1.** Figure (a), (b), (c), and (d) show the electron cloud are fixed to H atom despite
H to H distance changes. Figure (e) shows how many interactions have to be
solved for an H₂ system without Born-Oppenheimer approximation compared to
(d) with only one interaction. 10
- Figure 2.2.** The Hartree-Fock approximation model. Electron-electron interaction of
different energy level are considered. 13
- Figure 2.3.** Representative of molecular structure of DLC, PIL and Chalcone used in this
works. Abbreviations are detailed in each corresponding chapter. 20
- Figure 3.1.** A schematic of one dimensional charge conduction through the columnar axis
of a stack of DLCs. 29
- Figure 3.2.** Structure of HATNA and its alkyl substituents which provide long range
molecular order for good charge mobility (Liu, Usui, & Hanna, 2014). 30
- Figure 3.3.** Example of fan shaped dendrons studied by Miyajima et al. Reprinted with
from Miyajima et al. (2012). Copyright 2007 Science. 34
- Figure 3.4.** (A, B) Illustrations of a minimum-energy orientation with the aromatic rings
nearly superimposed. (C) and (D) were minimized from a 45° phase difference
between disks. Reprinted from Mulder et al. (2003). Copyright 2003 American
Chemical Society. 41
- Figure 3.5.** Elastic structure factor at 336, 348, and 358 K (overlapping solid lines at the
top) showing Bragg peaks due to liquid crystalline ordering. The dashed lines
(in the middle) without Bragg peaks at 368 and 378 K, and the dotted line
(bottom) is for 433 K. Rigidity of column are shown at 336, 348, and 358 K
because the peaks overlapping which indicate the structure is rigid in that

temperature range. Reprinted from Mulder et al. (2003). Copyright 2003 American Chemical Society.	42
Figure 3.6. Calculated CTIs (J) and their dependence on the twist angle θ obtained using the fragment approach (full circles) and the dimer approach (open circles). The co-facial separation and the lateral slide between two stacked HAT6 molecules are kept fixed at $D= 3.5 \text{ \AA}$ and $L= 0 \text{ \AA}$, respectively. Reprinted from Zbiri et al. (2009). Copyright 2009 Springer.	48
Figure 3.7. Calculated CTIs (J) and their dependence on the co-facial separation D obtained using the fragment approach (full circles) and the dimer approach (open circles). The twist angle and the lateral slide between the two stacked HAT6 molecules are kept at $\theta= 30^\circ$ and $L= 0 \text{ \AA}$, respectively. Reprinted from Zbiri et al. (2009). Copyright 2009 Springer.	49
Figure 3.8. Calculated CTIs (J) and their dependence on the lateral slide (offset) L between the two stacked HAT6 molecules. The twist angle θ and the co-facial separation D are kept fixed at their equilibrium values, 30° and 3.5 \AA , respectively. Reprinted from Zbiri et al. (2009). Copyright 2009 Springer.	50
Figure 3.9. Frontier orbitals calculated at the B3LYP/6-31G** level for molecule (a) (left) and (b) (right). Reprinted from Barlow et al. (2007). Copyright 2007 Wiley-VCH.	53
Figure 3.10. Molecular structure of DLC HAT6.	56
Figure 3.11. An all-atom model of two stacked HAT6 dimer molecules parameter investigated in this work. Variables to the stack structure are introduced in the form of (a) core-core facial separation, D , and twist angle, θ , (b) and lateral slide, L	57
Figure 3.12. Simulation flow of structural effect study of HAT6.	58

Figure 3.13. (a)HAT6 single point energy calculation setting. (b)Core electron treatment and basis set settings. (c)SCF options settings.....	59
Figure 3.14. (a) HOMO and (b) LUMO of HAT6 single molecule. (c) HOMO of and (b) LUMO of HAT6 in 5 layer stacking where HOMO and LUMO are concentrated at the triphenylene core and dispersed throughout layers.....	60
Figure 3.15. Total energy, BG in the function of core-core distance, D. θ and L are fixed at 0° and 0 \AA respectively.	61
Figure 3.16. Total energy, BG in the function of molecular twist angle, θ . D and L are fixed at 3.6 \AA and 0 \AA respectively.....	62
Figure 3.17. Total energy, BG in the function of molecular lateral slide, L. D and θ are fixed at 3.6 \AA and 0° respectively.....	63
Figure 3.18. DOS of HAT6 by varying distance, D. (a) Total DOS, (b) S orbital PDOS, (c) P orbital PDOS, (d) D orbital PDOS.....	65
Figure 3.19. DOS of HAT6 by varying twist, θ . (a) Total DOS, (b) S orbital PDOS, (c) P orbital PDOS, (d) D orbital PDOS.	67
Figure 3.20. DOS of HAT6 by varying lateral slide distance, L. (a) Total DOS, (b) S orbital PDOS, (c) P orbital PDOS, (d) D orbital PDOS.	68
Figure 3.21. LDOS zoomed in at Fermi level. [From left] (a) LDOS of D= 3.0, 3.6, and 4.2 \AA . (b) LDOS of $\theta= 20^\circ, 30^\circ,$ and 60° . (c) LDOS of L= 0.50, 1.25, and 2.00 \AA . D, θ , and L are fixed at $3.6 \text{ \AA}, 0^\circ,$ and 0 \AA respectively unless specified. (d) Numbering of atom.	70
Figure 3.22. Charge population of triphenylene atoms with varied distance, D at fixed $\theta= 0^\circ, L= 0 \text{ \AA}$. (a) Plot for triphenylene core. (b) Plot for tail. (c) Atom numbering.	72

Figure 3.23. Charge population of triphenylene carbon atoms with varied twist, θ at $D=3.60 \text{ \AA}$, $L=0 \text{ \AA}$. (a) Plot for triphenylene core. (b) Plot for tail. (c) Atom numbering.	74
Figure 3.24. Charge population of triphenylene carbon atoms with varied lateral slide distance, L at $D=3.60 \text{ \AA}$, $\theta=0^\circ$. (a) Plot for triphenylene core. (b) Plot for tail. (c) Atom numbering.	76
Figure 3.25. Representation of electronic density mapping of HAT6 at core section where slice is taken at midpoint of co-facial distance. Maximum (red) mapping is set at $0.1 \text{ electron/\AA}^3$ and minimum (blue) is 0 e/\AA^3 . The parameter is fixed at $D=3.6 \text{ \AA}$, $\theta=0^\circ$, and $L=0 \text{ \AA}$ unless specified otherwise. Line drawings are guide for the eye. (a) $D=3.2 \text{ \AA}$, (b) $D=3.6 \text{ \AA}$, (c) $D=4.6 \text{ \AA}$, (d) $\theta=30^\circ$, (e) $\theta=60^\circ$, (f) $L=1.5 \text{ \AA}$, (g) $L=3.0 \text{ \AA}$	77
Figure 4.1. Examples of common cation and anion pairs used in the formation of ILs, and general progression of changes in IL properties with anion type.	82
Figure 4.2. General types of IL and its applications.	83
Figure 4.3. Simple schematic of fuel cells with PIL electrolyte. Insertion of H_2 gas turned into H^+ at anode, then transferred to cathode by charge carrier PIL, in which react with O_2 gas at cathode producing electrical current and end product H_2O	88
Figure 4.4. Simple schematic of DSSC. Dye absorb incoming light to an excited state, which then releases electron into semiconductor through reduction by charge carrier. The oxidised charge carrier recombined with electron at counter electrode to complete the circuit.	89
Figure 4.5. Simple schematic of TEC cells. Example $[\text{Fe}(\text{CN})_6]^{-3/-4}$ redox couple is oxidised at hot electrode injecting electron into electrode, then the $[\text{Fe}(\text{CN})_6]^{-3}$ is reduced at cold electrode through electron recombination.	90
Figure 4.6. Types of molecular vibrations.	95

Figure 4.7. Diatomic simple harmonic oscillator model.....	97
Figure 4.8. Depiction of diatomic potential energy of harmonic oscillator.	97
Figure 4.9. Diatomic rigid rotator model.	100
Figure 4.10. Diatomic translation model of the centre of mass.	100
Figure 4.11. Schematic of simple thermoelectric device depicting an electromotive force (emf) generated by a temperature gradient where $\Delta T = T_H - T_C$, where $T_H > T_C$, T_n is ambient temperature. Material A is thermoelectric material, while B is a conductor material (wire). When direction of emf is generated as above, A is a p-type thermoelectric material, and if it is in opposite direction then A is an n-type.	102
Figure 4.12. Work flowchart of amine based PIL in thermodynamic study for TE. ...	110
Figure 4.13. (a) PILs annealing setting. (b) Dynamics parameters used for annealing process. (c) Forcefield settings for annealing.	111
Figure 4.14. PIL GO settings. (a) Selection of GO task. (b) Core electron treatment and basis set settings. (c) SCF options settings.	112
Figure 4.15. IR spectra of for PIL (a) 1 , (b) 2 , (c) 3 , and (d) 4 . Peaks of highest intensity are due to vibration of N-H atom in anion (Tf).	113
Figure 4.16. Schematic to show correlation S_{vib} to number of proton attachment to N atom. Larger number of proton increases ΔS_{rot} in entropy where the anion is more likely to rotate.	116
Figure 4.17. Comparison of bond length distribution of N-H of protonated (a) Ea (b) Diea (c) Tria (d) 2mp at $T = 300$ K and 400 K.	118
Figure 4.18. The hypothetical thermodynamic cycle of (a) 1 , (b) 2 , (c) 3 and (d) 4 depicted on entropy curve in arbitrary temperature range. (Inset) Calculated entropy in the function of temperature for respective PILs. Two curves are contributed by 2 stable states in different conformation.	119

Figure 4.19. Calculated Seebeck coefficient across temperature of all PIL studied....	120
Figure 4.20. Work output and theoretical maximum efficiency at ΔT ($= T_H - T_C$) when $T_C = 298$ K for (a) 1 , (b) 2 , (c) 3 , and (d) 4	121
Figure 5.1. Depiction of a DHC undergoes ESIPT (from enol form to keto form) after a photoexcitation.....	124
Figure 5.2. J and H aggregation crystalline packing of DHC.	125
Figure 5.3. Reversible four-level photocycle.	126
Figure 5.4. (2 <i>E</i>)-1,3-Diphenylprop-2-en-1-one. Molecular structure of parent chalcone. With O atom at ketone group is often acting as acceptor site, while donor sites may come from aromatic structures or their addition groups such as -NH ₃ and -OH.....	127
Figure 5.5. Molecule structure of chalcone in simulation, 4-dimethylamino-2'-hydroxychalcone (DHC). UIPAC name (E)-3-[4-(dimethylamino)phenyl]-1-(2-hydroxyphenyl)prop-2-en-1-one.....	130
Figure 5.6. Steady-state absorption (solid lines) and fluorescence (dashed lines) spectra of DHC dissolved in methanol (black) and in crystalline form (red). $\lambda_{ex} = 450$ nm.	131
Figure 5.7. Torsion axis location of (a) hydroxylphenyl, (b) p-(dimethylamino)phenyl, and (c) dimethylamino group.....	134
Figure 5.8. Simulation flow of DHC ESIPT study.	134
Figure 5.9. (a)Chalcone GO calculation setting. (b)Core electron treatment and basis set settings. (c) SCF options settings. (d)Solvent effect settings.....	136
Figure 5.10. PES in the function of torsion of DHC in (a) ground state and (b) excited state. (inset) Torsion axis location of hydroxylphenyl group.	137
Figure 5.11. PES in the function of torsion of DHC in (a) ground state and (b) excited state. (inset) Torsion axis location of p-(dimethylamino)phenyl group.	138

Figure 5.12. PES in the function of torsion of DHC in (a) ground state and (b) excited state. (inset) Torsion axis location of dimethylamino group.	139
Figure 5.13. DHC packing conformation in crystal phase of (a) edge-face packing and (b) face-face packing.....	141
Figure 5.14. Position of O_{enol} , O_{keto} and involved H atoms and corresponding $O_{\text{enol-H}}$ and $O_{\text{keto-H}}$ bond lengths.	142

University of Malaya

LIST OF TABLES

Table 2.1. Summary of DFT approximation and exchange-correlation (XC) functional characteristics.....	19
Table 3.1. Common classes of DLC molecule core structure and its chain substituents.	27
Table 4.1. Molecular structure of PIL cation and anion in study.	107
Table 4.2. Energy contribution of PILs in comparison from State I to II in term of kinetic energy difference, $\Delta E_{kinetic}$, electrostatic energy difference, ΔE_{es} , and difference of total formation energy, ΔE_{total} . Energy unit (kJ/mol).	114
Table 4.3. Comparison of 2 conformation separated by entropy contribution, vibrational entropy, S_{vib} , rotational entropy, S_{rot} , and translational entropy, S_{tra} . (J/mol.K) at 298 K.	115
Table 4.4. Summary of maximum work output, W_{out} , optimum temperature difference, ΔT_{opt} , and Seebeck coefficient, Se , for each PIL.	121
Table 4.5. Comparison of Seebeck coefficient, Se (mV/K) of pure PILs (unless stated) between this work calculated value and literatures.....	122
Table 5.1. Relative formation energy, E_{form} of DHC crystal edge-face and face-face packing with respect to ground state edge-face packing.	142
Table 5.2. Bond lengths and corresponding torsion angles of O_{enol-H} and O_{keto-H} in ground and excited state for solvent condition and crystalline phase. Torsion of hydroxylphenyl, p-(dimethylamino)phenyl and dimethylamino are labelled 1 , 2 , and 3 respectively. Shorter bond lengths values are bolded.	143
Table 5.3. Absorption energy, E_{ab} and emission energy, E_{em} of hydroxylphenyl (1), p-(dimethylamino)phenyl (2) and dimethylamino (3) stable bond torsion in excited state.	145

LIST OF SYMBOLS

Symbol	Property [Units]
k_B	Boltzmann constant
I	Current [A]
h_e	Effective heat transfer coefficient [$\text{W}/\text{m}^2 \cdot \text{K}$]
η	Efficiency
E	Energy [J]
F	Amplitude of the electric field [V/m]
ΔS	Entropy difference [J/K]
\hat{H}	Hamiltonian operator
h	Planck constant
r	Position vector
T_{ref}	Reference temperature [K or $^{\circ}\text{C}$]
S_e	Seebeck coefficient [$\mu\text{V}/\text{K}$]
T_H	Temperature at hot [K]
T_C	Temperature at cold [K]
ΔT	Temperature difference [K]
κ	Thermal conductivity [$\text{W}/\text{m} \cdot \text{K}$]
Z	Thermoelectric figure of merit
t	Time [s]
S_{vib}	Vibrational entropy [J/mol·K]
S_{rot}	Rotational entropy [J/mol·K]
S_{tra}	Translational entropy [J/mol·K]
V	Voltage [V]
Ψ	Wave function of quantum system

LIST OF ABBREVIATIONS

Abbreviation	Expanded name
AIL	Aprotic ionic liquid
ALDA	Adiabatic local density approximation
BG	Band gap
DFT	Density functional theory
D-A	Donor-Acceptor
DLC	Discotic liquid crystal
DOS	Density of States
emf	Electromotive force
ESIPT	Excited state intramolecular proton transfer
GO	Geometry optimization
HF	Hartree-Fock
HOMO	Highest occupied molecular orbital
ICT	Intramolecular charge transfer
IL	Ionic liquid
IR	Infrared
KS	Kohn-Sham
LC	Liquid crystal
LUMO	Lowest unoccupied molecular orbital
MM	Molecular Mechanics
MS 2016	Materials Studio 2016
NIR	Near-infrared
NMR	Nuclear magnetic resonance
OFET	Organic field effect transistor
OLED	Organic light emitting diode
PES	Potential energy surface
PIL	Protic ionic liquid
SE	Semi-empirical
SCF	Self-consistent field
TDDFT	Time dependent density functional theory

LIST OF ABBREVIATIONS (continued)

Abbreviation	Expanded name
TEC	Thermoelectrochemical
TICT	Twisted intramolecular charge transfer
TOF	Time of flight
UV	Ultra violet
XRD	X-ray diffraction

University of Malaya

CHAPTER 1: INTRODUCTION

The advancement of the silicon in electronic field has brought heralded as one of the important innovation to modern society. The applications of silicon are vast, which include transistors, integrated circuits, light emitting diodes, display, lighting, solar cells, photo sensors, electro optical devices, and optoelectronic sensors. Most of today's electronic devices are made from an element that once was mere sand, which has been turned into a semiconductor. Silicon is the most common semiconductor, others such as germanium, and gallium are doped with phosphorus, or boron which creates functioning information switches. In around early to mid-1800, Thomas Seebeck, and Michael Faraday were amongst the first who observed electronic characteristics in semiconductors where the resistivity dropped when heated, which it is contrary to metallic materials. From then, a developed unified theory of solid state physics has been developed to explain the charge transport phenomena which we know today.

In the past decades, researches and development on semiconductors have probably reached saturation, in which the advancement of semiconductor based electronics reaching a plateau in terms of computing power. This is based on the ubiquitously known Moore's law, that was introduced in 1965, when Gordon Moore, who was then working as director of research and development of Fairchild Semiconductor predicted that the density of device components in an integrated circuit will double at a rate approximately in every two years. Moore's Law has been proven in several decades, but in current development, the component density in an integrated circuit basis lagged behind the initial prediction. This matter poses a problem to conventional semiconductor technologies, which governs almost all of the electronic devices we use today. In particular, the current record for semiconductor fabrication is sub-10 nm metal wire with sub-1 nm precision (Pi, Lin, & Xia, 2016) and transistor structure is a single silicon atom (Fuechsle et al., 2012).

In a recent prediction, the processing power of standard computers is likely to reach its maximum in the next 10 to 25 years. In addition, even at maximum power, traditional computers will not be able to handle a particular class of problems in parallel computing that involve combining variables to come up with many possible answers, and looking for the best solution, it is still true even for a supercomputer based on traditional architecture. This is where newer architecture such as chaos computing and quantum processors looks promising, but the technologies still would not be available commercially for a few next decades. To overcome this problem, researches around the world are searching, developing, and optimizing new materials, that is more suitable for more robust and complex chip design. The field of nanotechnology has also been conceived and developed, partly due to popularisation of its concept by Richard Feynman: "There is plenty of room at the bottom," which encourages the exploitation of nanoscale materials and devices for technology.

One of very popular solution is the use of organic materials as the successor to conventional silicon based electronics. Carbon and silicon belong to the same group element 14 which can be applied to existing electronic silicon based electronic knowledge seamlessly. The research and development of organic/polymeric electronic materials and devices have grown rapidly. Compared to the inorganic counterpart, these new organic materials have exhibited several advantages such as improved speed, reduced power consumption, and improved processability which leads to flexible devices and low cost mass production potential.

Historically, the dawn of organic electronics started with the discovery of electrically conducting organic structure. Inorganic materials such as copper, aluminium, and many alloys are traditionally and currently still dominant used as conductive materials. The first reported conductive organic material was polyaniline (Figure 1.1), by Henry Letheby in 1862. Then the work was continued with discovery of highly conductive (1 S/m)

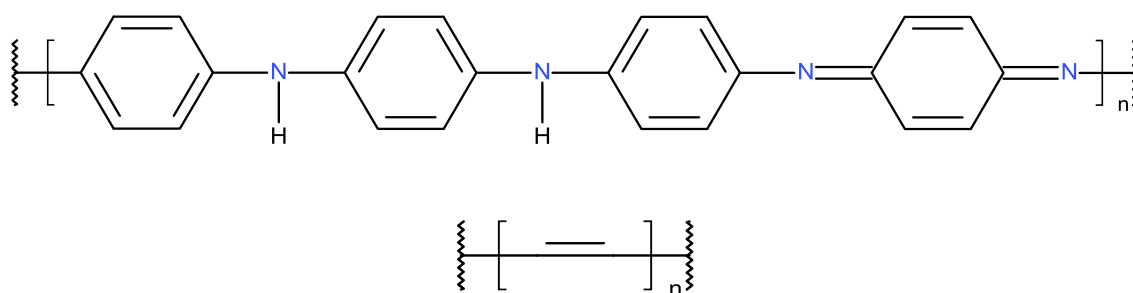


Figure 1.1. Molecular structure of polyaniline (above), and polyacetylene (below). Conjugating double bond gives rise to conductive properties.

tetraiodopyrrole in 1963 (McNeill et al., 1963). Later, research on oxidization of polyacetylene (Figure 1.1) with halogen leads to produce conducting materials from either insulating or semiconducting materials which won Alan J. Heeger, Alan G. MacDiarmid, and Hideki Shirakawa in 2000 the Nobel Prize in Chemistry (Chiang et al., 1977).

Since the discovery of conductive polymers, research and development of organic electronic experienced a boom in R&D interest, which include to new categories of organic materials and structure such as discotic liquid crystals (DLC), protic ionic liquids (PIL) and chalcones which will be explored in this thesis.

DLCs, PILs and chalcones are among of few materials that are less studied in electronic application but have very interesting characteristics. In any electronic material, as stated above, the charge transfer characteristics is the most important property as it governs the information transfer rate, and thus determines the applicability of the material. In addition to that, DLCs have self-healing properties that is promising feature in organic electronic where they are prone to UV exposure damage and mechanical shock. Meanwhile, a PIL is a molten salt that exists in liquid form in room temperature, which is a very promising material in thermoelectric, fuel cell, and pyroelectric application since they have very high temperature tolerance and non-volatile. Chalcones is another interesting material that has donor and acceptor atom in a molecule. The application of

chalcone is already widespread in biology and they also show a promising characteristic in opto-electronic applications.

In materials science, organic electronics are extensively used in the manipulation of atoms and molecular structures, where its electronic properties can be highly tuned as a function of its structural parameters. This is in line to Feynman's vision in nanotechnology, where atoms are individually manipulated into useful applications, and atomic scale electronic circuits can be designed and built, literally atom by atom. This is achievable by understanding the atom's electronic properties for example the electronic band gap (BG), conductivity, excitability, and oscillation when arranged in a certain way. Thus, investigation of molecular structure-electronic correlation of organic molecules poses an importance towards advancing electronic fields by providing a fundamental basis for rational design of the molecules for electronics applications.

However, although it is possible to arrange individual atom into desired structure, it is very difficult and costly because it requires ultimate precision control where the physical properties of a system will vary greatly even at the order scale of one unit of Angstrom is changed. Furthermore, to repeat the process to find an optimised structure would consume time and money. Therefore, investigation of physical properties is done using quantum modelling to provide prediction of the physical behaviour changes at optimum cost.

Quantum modelling is a powerful tool to investigate the physical properties of a material at molecular level. It focuses on the application of quantum mechanics in physical models as well as experiments of a chemical system. There are many types of quantum modelling where among the first are based on simpler classical mechanics, and also those are based on Hartree-Fock theory and density functional theory (DFT). The quantum modelling using mechanical theory are cheaper in terms of computational cost and is more capable to handle calculations for bulk materials. On the other hand, both Hartree-Fock and DFT solve the time dependent Schrödinger equation for many body

systems i.e. electrons or molecules problem as described in Born-Oppenheimer approximation method. They are also more capable tool to study the physical and chemical properties at atomic or molecular level. Therefore, quantum modelling is a perfect tool to investigate the correlation of structural- electronic properties of materials that could not be achieved by experimental means.

1.1. Problem statement

In finding the next class of cutting edge materials for the development of future devices, an understanding of the electronic characteristics mechanism at molecular level is needed to exploit the true potential of material performance. DLCs, PILs and chalcones are very promising materials in electronic applications but its true potential is still underutilised due to lack of understanding in molecular electronic properties mechanism in particular.

In the field of electronic materials, typically a lot of effort in terms of time, manpower, and cost have been expended, especially through an experimental trial and error method to find the best materials for a given application. On the other hand, there is a wealth of theoretical studies on molecular and quantum models to understand the physical characteristics of these materials. However, rarely do these domain meet in a practical manner, as molecular models are not always represented realistically for experimental systems. This work seeks to provide a structural-electronic/physical correlation between the molecular structure and its corresponding physical characteristics.

1.2. Objectives

The main objective of this study is to study the structural-electronic/physical properties relationship of the following classes of materials. This exercise is expected to provide a logical link in the approach of utilising molecular design to produce optimal materials for particular application. The following materials and their corresponding applications are chosen:

1. To elucidate the electronic structure of columnar phase of the discotic liquid crystal (DLC) 2,3,6,7,10,11-hexahydroxytriphenylene (HAT6). DLCs can be constructed into a 1 dimensional nanowires using its charge transfer characteristic and many applications in future organic electronic devices.
2. To explain the relationship between thermoelectric properties and molecular thermodynamics of amine based PILs using quantum thermodynamic. This relationship is expected to improve thermoelectric potential of PILs in future thermoelectrochemical cell (TEC) design.
3. To elucidate the mechanism of excited state intermolecular proton transfer (ESIPT) in solutions and crystalline 4-dimethylamino-2'-hydroxychalcone (DHC), by identifying the optimal structural characterisation for increase fluorescence. High quantum yield of NIR fluorescence for chalcones are expected to be used as biomarkers as well as organic display device.

1.3. Scope of works

This work will cover purely on DFT simulation of structural effect on the electronic structure of HAT6 in columnar phase, thermodynamics mechanism on PILs thermoelectric capability, and structural effect on DHC fluorescence. Only results of simulations are discussed. It does not cover synthesis of the materials and any experimental measurements.

1.4. Thesis outline

This thesis reports on the quantum modelling of organic materials for electronics, thermoelectric and photoluminescence application using density functional theory approach which discuss the structural effect to physical properties of the material for specific applications. It is structured to consist of 6 chapters of which explained below.

In chapter 1, the background of organic materials and its applications are narrated. Then, it introduces the characteristics and applications of DLC, PILs, and chalcone that

these are main materials studied in this thesis. After that it leads to merit of using quantum modelling as main tool for molecular design. Here the difficulties to study materials are elaborated in problem statement, and from there the objectives are built. The scope of works also covered in this chapter.

The second chapter discusses about computational chemistry where it detailed on molecular modelling. It introduces the fundamental ideas in molecular modelling and then compare the classical and quantum modelling in term of their mechanism, characteristics and capabilities. The main features of quantum modelling are elaborated extensively to differentiate techniques involved between first-principle calculation method such as in solving Schrödinger equation and DFT, empirical and a hybrid. Then it briefly explores several functionals in DFT and suitability to simulate DLC, PILs, and chalcone systems. Limitation of the simulations are then discussed here.

Chapter 3 discusses the first part of the study, correlation of columnar structural parameters and electronic charge transfer of DLC HAT6. It introduces DLCs as an organic electronic material featuring DLCs' properties and their applications. Then, it reviews molecular modelling of DLCs with examples of works done by other researchers. Next, the works done on structural effect of HAT6 column towards its electronic structure are elaborated. At the end of this chapter, findings from this exercise are summarised.

Thermodynamic study of PILs is discussed in chapter 4. First part of this chapter introduces ILs and its types which eventually covers the properties of ILs and their applications. Then, relationship between thermodynamics and thermoelectrics are elucidated. Works on thermodynamic mechanism of PILs towards thermoelectric potential are elaborated here. The findings are summarised at the end of the chapter.

In chapter 5, correlations between fluorescence and chalcone conformation are discussed. First, it introduces the main mechanism of fluorescence of DHC, the ESIPT. Then, it talks about chalcones, their applications and photoexcitation mechanism. The

main simulation works of DHC are elaborated, and the results from simulation discussed subsequently. Findings of this work is discussed.

In the last chapter, chapter 6, the main findings from the 3 works which was elaborated in chapter 3 to 5 is concluded. The importance of the findings is highlighted.

University of Malaya

CHAPTER 2: COMPUTATIONAL CHEMISTRY

2.1. Molecular modelling

Molecular modelling is a powerful technique to investigate the chemical questions through computer calculations (Jensen, 2007; Lewars, 2016). This technique provides information to a set of commonly required properties in chemical questions which are;

1. Molecular geometry: Shape of molecules, including bond length, angles and packing.
2. Energies: This include the conformation energy and transition state energy. Calculating the energies will give the information of favoured isomer at an equilibrium, as well as chemical reaction rate.
3. Electronic structure: Calculations on electronic distribution that identify nucleophilic sites and electrophilic sites, and predict attack site of a reagent which is helpful in estimating chemical reactivity.
4. IR, UV and NMR spectra: Calculation of these spectra give an estimate of what to look for to an unknown molecule, and also provide molecular vibration information.
5. Physical properties: Combination of questions above may help answering molecule behaviour in bulk material. For example, the strength and melting point of a polymer depend on intermolecular interaction of force between the molecules which is related to molecular geometry, energy and electronic structure. This is very useful in designing new materials in material science.

In order to obtain those information, a simple chemical system is treated as particles with elastic bond, which correspond to atom and its binding bond. Solving the interaction between the particles will provide information as mentioned above. Accurate results can be analytically easily obtained with one or two particles system; however more than three particles require very large number of mathematical operations. This is called the many-

body problem. Solving the many-body problem has spawned a new field in chemistry called computational chemistry.

2.1.1. Born-Oppenheimer Approximation

When solving the many body problem in computational chemistry, a potential energy surface (PES) is plotted to find energy minimum as will be described in subsequent sections. PES is a plot of the total energy of nuclei and electrons as a function of geometric coordinates of the nuclei. Normally to solve many body problems in computational chemistry would require defining both nuclei and electrons coordinates, however using Born-Oppenheimer approximation will simplify the solution of the many body problem (Born & Oppenheimer, 1927). Born and Oppenheimer (1927) showed that the nuclei in a molecule are stationary with respect to the electrons. In this approximation, the many body problem can be simplified into easier equations, where Schrödinger equation will only have to be solved in terms of the electronic contribution and then add internuclear repulsion energy to obtain a PES instead of defining both nuclei and electrons using the Schrödinger equations. It is done by allowing consideration to be made only on nuclei coordinates since they are much slower than electrons, thus the electrons are identified with distribution clouds surrounding nuclei. This is depicted in Figure 2.1. Through this approximation, van der Waals surface surrounding nuclei give up to 98% accuracy of the distribution of electronic position.

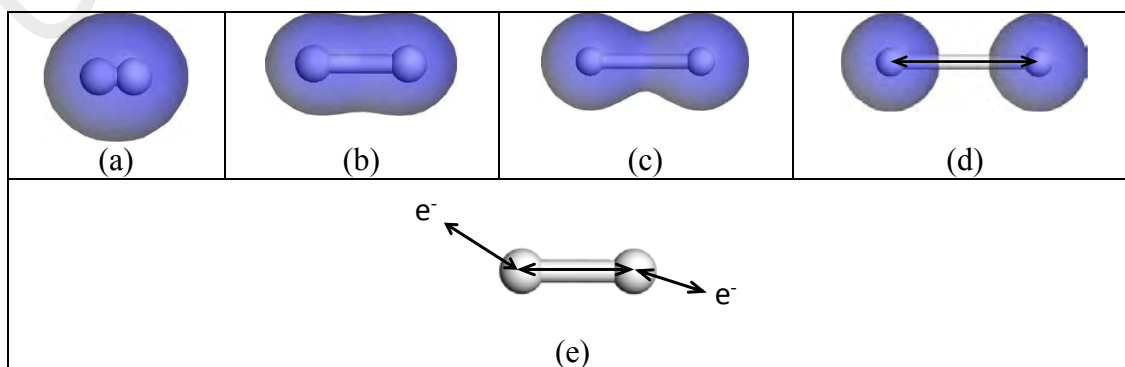


Figure 2.1. Figure (a), (b), (c), and (d) show the electron cloud are fixed to H atom despite H to H distance changes. Figure (e) shows how many interactions have to be solved for an H₂ system without Born-Oppenheimer approximation compared to (d) with only one interaction.

A large fraction of computational power is used to solve the perturbation in many-body problem. Computational chemistry is used to provide approximate solution, which is then refined to a desired degree of accuracy. Mainly there are 5 types of methods used to solve many-body problem in chemistry which is explained in subsections below.

2.1.2. Molecular mechanics (MM)

Molecular mechanics (MM) is based on Newtonian mechanics to solve the molecular system. The energy of the system is calculated using force field. Functional form of MM includes potential energy due to interaction of atoms that is bound through covalent bonds and noncovalent forces. The general form of the total force field energy is contributed as below.

$$E_{total} = E_{covalent} + E_{noncovalent} \quad (2.1)$$

where, covalent and noncovalent terms are formed from other force field energy components as the following,

$$\begin{aligned} E_{covalent} &= E_{bond} + E_{torsional} + E_{dihedral} \\ E_{noncovalent} &= E_{electrostatic} + E_{van\ der\ Waals} \end{aligned} \quad (2.2)$$

The bond and torsional terms are often calculated as quadratic and sinusoidal energy functions or more accurately described by Morse potential functions, whilst dihedral energy is dependent to the molecular geometry. In noncovalent energy, the van der Waals force is calculated using Lennard-Jones potential and the electrostatic is calculated using Coulomb potential. Since there are different types of atoms, force fields are defined in a set of parameters for each type of atom. The atomic mass, van der Waals radius, partial charge, bond length, bond angles, dihedral angles and effective spring constant are among parameters that are defined in force fields. This also includes distinct parameter set of values on atoms in functional groups, for example oxygen atoms in hydroxyl and carbonyl groups.

Due to the simple nature of MM calculations, MM is a fast tool to optimize very large molecular system containing thousands of atoms, and also uses low computational power. Most of the time, it will give low accuracy geometries but it can be used as initial input for more demanding calculations as will be discussed in next sections.

However, the speed of MM is not always at expense of accuracy which sometimes it can rival the experimental values in terms of data reliability under well parameterised conditions. The main weakness of MM is lack of electronic contribution in calculations. Electronic structure calculations in MM is mainly by analogy in its parameter, where the reliability of result is questionable when it encounters unexpected electronic factors. The other weakness of MM is that, solvent and nearby ions effects are ignored which become dominant in systems containing polar molecules and that reverts back to the electronic structure problem mentioned earlier. This is vital in biomolecular simulations where the solvents will change the geometries of molecules. Additionally, due to the fact that MM is heavily dependent to parameterisation, the parameters may differ when comparing between one MM program to another.

2.1.3. First-principle calculations

To obtain a more accurate result, the first-principle of quantum mechanics (QM) calculations are based on the solution of the Schrödinger equation. The equation describes the physical characteristics at quantum level, and most importantly on electronic behaviour. First-principle calculations solves Schrödinger equation to give the molecular energy and wavefunction, which is then calculated for electronic distribution around the molecule. The term ‘first-principle’ implies to the only input into the calculation are physical constants. Equation (2.3) and (2.4) below are general time dependent and time independent Schrödinger equations respectively.

$$i\hbar \frac{\partial}{\partial t} \Psi(\mathbf{r}, t) = \hat{H}\Psi(\mathbf{r}, t) \quad (2.3)$$

$$\hat{H}\Psi = E\Psi \quad (2.4)$$

Where i is the imaginary unit, \hbar is reduced Planck constant, Ψ is the wave function of quantum system, r is position vector, t is time, \hat{H} is Hamiltonian operator, and E is energy of state Ψ .

However, the Schrödinger equation is impossible to be solved exactly for any molecule with more than one electron. Although the Born-Oppenheimer approximation may reduce solution burden on computational power as discussed above, it is not suitable for quantum system as it assumes that the nucleus is infinitely heavier than the electrons. Further approximation on solving the electronic Schrödinger equation can be performed using the Hartree-Fock (HF) calculation.

2.1.3.1. The Hartree-Fock approximation

The Hartree-Fock (HF) approximation treats many-body problem into a pseudo one particle system by taking the average electron-electron interaction i.e. electron repulsion into account, which offers more refined calculations. This method treats all nuclear and electronic degrees of freedom in a quantum framework when quantum effects such as tunnelling become significant. Amongst the advantages of Hartree-Fock over Born-Oppenheimer is the ability to include both tunnelling and vibrational effects. In addition, it is able to selectively treat some nuclei as classical, allowing simplification of large systems. The HF approximation model is depicted in Figure 2.2.

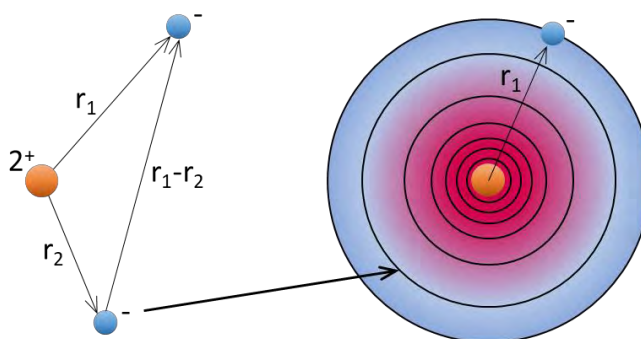


Figure 2.2. The Hartree-Fock approximation model. Electron-electron interaction of different energy level are considered.

2.1.3.2. The Hartree-Fock Self-Consistent Field Method

The Hartree-Fock self-consistent field (SCF) method is one of the most prominent computational method currently. HF SCF and its descendants are used in many first principle calculations. The SCF method developed by Hartree includes the electronic interaction term in the energetic calculations because of analytically solving the Schrödinger equation for systems with more than one electron is not possible (Hartree, 1928). Numerically, the SCF method approximates the N number of electronic wavefunction with a product of N one-electron wavefunctions which is called Hartree product.

As mentioned, the first principle calculation is based on a fundamental physical equation i.e. Schrödinger equation without arbitrarily parameterisation like MM or empirically adjustments of the SE (section 2.1.4). Therefore, it provides the most reliable approach for solving chemical problems at molecular level. Using first principle method enables calculation to be performed on any kind of molecular species which includes transitions states and non-stationary systems, compared to empirical dependent method which may restrict to only on parameterised systems. Even though this method is the most reliable and robust, it is the most computationally demanding method. However, the advancement of computational technology has made this method to be commonly used on systems with hundreds of electrons.

2.1.4. Semi empirical calculations

Semi-empirical (SE) method is simplification of first principle method where it uses empirical value such as obtained from experiments over equations. It uses the same SCF procedure but without evaluation of wavefunction at the first principle level. Compared to the first principle, the integrals in the SCF procedure are approximated to experimental quantities, and neglected trivial terms.

SE calculations are very fast compared to SCF or DFT method (discussed in section 2.1.5), but less accurate where the empirical value may not be valid under different conditions since most of the parameters are obtained from the most stable molecular structures. The geometries obtained from SE calculations are often adequate to be used in many applications. However, reaction and activation energies obtained from SE are unreliable. Unless it is comparable to experimental results or first principle calculations, SE can be assumed to be unreliable outside empirical parameter. Especially when dealing with novel molecules or atoms that is outside of training sets, where the references can be obtained from the first principle or high-level DFT calculation.

2.1.5. Density functional calculations

Density functional theory (DFT) is not based on the wavefunction as opposed to two earlier methods, but DFT is based on the electron probability density function. The properties in DFT is the probability of finding an electron in a function of volume, where it considers electronic charge is smeared out in electronic cloud surrounding nucleus. The variation of probability in the cloud corresponds to the varying density of the electrons in the volume element. The electron density function is the basis of the whole methods of studying atoms and molecules, where this density is measurable through such as X-ray diffraction and electron diffraction in contrast to wavefunction method.

DFT is close to the Born interpretation of one-electron wavefunction ψ for electronic probability density at any point X . Probability of finding an electron around the point X over infinitesimal volume $dx dy dz$ is

$$\rho = |\psi|^2 dx dy dz. \quad (2.5)$$

For multielectron condition, the relationship between wavefunction ψ and probability ρ is more complicated, where ψ is related to summation over all spin states of all electrons in one-electron spatial wavefunctions ψ_i , that is can be approximated to as:

$$\rho = \sum_{i=1}^n n_i |\psi_i|^2 \quad (2.6)$$

The n is number of the occupied molecular orbitals in ψ_i and for a closed-shell molecule each $n_i = 2$, where total electron is $2n$.

2.1.5.1. Kohn-Sham approach

Current DFT calculations in computational chemistry are based on the Kohn-Sham (KS) approach (Hohenberg & Kohn, 1964). The KS approach is to introduce orbitals in the free electron gas calculations. This is an important measurement where the initial DFT method did not use wavefunction to define orbitals. This method is analogous to the HF method discussed before which is to find solutions for the wavefunction, in DFT density function. The main difference between HF and KS is HF uses $4N$ variables (three spatial and one spin coordinates for each electron) while KS is a function of spatial density coordinates (which uses three-dimensional axis x, y, z to define density coordinates) times the number of orbitals involved to become $3N$. This reduces the computational load in DFT calculations.

However, the KS theory calculates kinetic energy using non-interacting electrons. To overcome this shortcoming, the exchange-correlation term is introduced. In a real system, electrons interact which therefore the remaining kinetic energy is described in exchange-correlation terms. The general term of DFT energy in KS is described as below.

$$E_{DFT}[\rho] = T_S[\rho] + E_{ne}[\rho] + J[\rho] + E_{xc}[\rho] \quad (2.7)$$

Where $T_S[\rho]$ is kinetic energy (notation S means it is derived from Slater determinant, expression to describe electrons that satisfies anti-symmetry requirements of Pauli principle), $E_{ne}[\rho]$ is nuclear-electron attraction energy, $J[\rho]$ is Coulomb potential energy, and $E_{xc}[\rho]$ is exchange-correlation energy.

From equation (2.7), the term $E_{xc}[\rho]$ is defined as below in term of kinetic and potential energies as below:

$$E_{xc}[\rho] = (T[\rho] - T_S[\rho]) + (E_{ee}[\rho] - J[\rho]) \quad (2.8)$$

where the energy terms in the first and second parenthesis denotes kinetic and potential energies respectively. The $T[\rho]$ is exact kinetic energy, and $E_{ee}[\rho]$ is electron-electron repulsion energy. The $E_{xc}[\rho]$ term describes the interacting electrons energy in the orbitals.

The functional used to describe equation (2.7) and (2.8) are based on the approximation level. In next subsections, several types of approximation schemes are introduced.

2.1.5.2. Local Density Approximation

Local Density Approximation (LDA) approximates local density as uniform electron gas and it is purely dynamical correlation system. Accurate correlation energy is found by quantum Monte Carlo methods (Nekovee, Foulkes, & Needs, 2003). For molecular systems, LDA approximation is not suitable where it underestimates exchange energy and overestimates correlation energy. Consequently, LDA overestimates bond strength in molecules.

2.1.5.3. Generalised Gradient Approximation

Generalised Gradient Approximation (GGA) method is an improvement to LDA method, where it considers a non-uniform electron gas. GGA is the most popular and the most extensively studied approximation model. In terms of accuracy, it is comparable to first principle methods.

There are a number of exchange-correlation functional of GGA, among popular ones are BLYP (B88 (A. D. Becke, 1988) + LYP (C. Lee, Yang, & Parr, 1988)), PW91 (Perdew & Wang, 1992), and PBE (Perdew, Burke, & Ernzerhof, 1996).

BLYP (combination of B88 and LYP functional) is one of early functionals that is able to produce comparable result to HF. The B88 corrects the asymptotic behaviour in energy density and LYP counterpart was derived from data fitting of He atom. However, the

BLYP does not include parallel spin correlation when all the spin are aligned which proved to be problematic when dealing with excited states.

PBE exchange-correlation functional are improvement over PW91 which uses same model. This functional proposed to remove invalid oscillation in expansion to first order and ensuring exchange and correlation terms integrate to required values. PBE functional is widely applicable and good functional, for example when the system is a combination of organic and metallic system, the PBE gives both system a good approximation compared to other more specific functional. Later PBE is modified to improve on periodic system to RPBE (Hammer, Hansen, & Nørskov, 1999) and PBEsol (Perdew et al., 2008). However, both RPBE and PBEsol is however is not suitable for non-solid systems, furthermore RPBE is not able to fulfil hole condition for exchange energy.

2.1.5.4. Meta-GGA

Extension to GGA methods is to allow exchange-correlation functional to depend on higher order derivatives of electron density for improvement. Alternatively, extension through a functional which is dependent on the orbital kinetic energy density. TPSS (Tao et al., 2003) and revTPSS (Perdew et al., 2009) are examples of meta-GGA exchange-correlation functionals.

2.1.5.5. Hybrid Approximation

Hybrid approximation is a mix of DFT and HF methods, where the exchange energy is exactly given by HF theory which it is precisely calculated through wavefunction solution compared to a single Slater determinant of KS orbitals. One of the most popular hybrid functional is B3LYP (Axel D. Becke, 1993; Stephens et al., 1994) where it uses Becke 3 parameter functional and LYP functional. The result is a highly accurate functional. Another example is TPSSh (Staroverov et al., 2003).

However, the drawback of hybrid functional is higher computational cost as it uses HF wavefunction solution to obtain exchange energy thus consumes more time. In addition, B3LYP also inherited bad correlation energy in metallic system from LYP.

2.1.6. Functionals overview

In this section, advantages and disadvantages of approximation methods and their exchange-correlation functional is summarised. DFT is considered as first principle quantum chemistry tools in which it uses first principle of electronic density function to describe the chemical systems. DFT results especially GGA and above are comparable to HF methods in terms of reliability to experimental data at less computational cost.

Table 2.1. Summary of DFT approximation and exchange-correlation (XC) functional characteristics.

Approximations /XC Functional	Empirical	Remarks
LDA	No	Valid with slowly varying densities. Long range interactions are ignored.
GGA		Improvement over LDA. Long range interactions such as van der Waals are poor.
BLYP	Yes	Underestimate H bond energies but good estimation in liquid water. Not suitable for metallic system
PW91	No	Give good results in solid phase.
PBE	No	Universal (moderately good for composite system e.g. organic + metal system). Typically overestimates H bond energies.
RPBE	No	Improvement of PBE in periodic systems i.e. solid.
PBEsol	No	Improvement of PBE in solids, also better results for linear molecules.
Meta-GGA		Improved over GGA in term of surface energies and better weak interactions.
TPSS	No	Improvement of PBE for surface energy and corrects overestimation of H bond energies.
revTPSS	No	Improvement of TPSS using PBEsol as basis, have same characteristic to PBEsol.
Hybrid		Corrects self-interaction error, gives better BGs and reaction barrier. Computationally more expensive than GGA thus not suitable for periodic systems.
B3LYP	Yes	Very successful functional in many systems and purposes but poor for metallic systems
TPSSH	No	Improvement over TPSS using HF exchange energy

Therefore, it is logical to use DFT over costly HF methods. It is however, many choices of functional with each has unique characteristics depends on the molecular systems in study.

Table 2.1 summarises the main characteristics of each functional. In addition of which exchange-correlation functionals uses empirical parameters (but much smaller than SE methods) are also listed. Using empirical data is not a severe problem, however it shows the principal model of the functional is adequately correct in order to understand the mechanism of chemistry system itself.

2.2. Selection of computational methods

The works in this thesis mainly consist of organic materials with focus to electronic structure studies i.e. density of states (DOS), band gap (BG), electronic density, and H bonds. In addition, dynamics calculations are used to study the thermodynamics mechanism of molecule vibrations. Three types of molecular systems are studied that are, Discotic Liquid Crystal (DLC) (discussed in Chapter 3), Protic Ionic Liquid (PIL) (discussed in Chapter 4), and Chalcone (discussed in Chapter 5). Each of molecular structures of each materials are depicted in Figure 2.3.

In this section, the computational requirements to study each system are listed and the most suitable computational method are chosen.

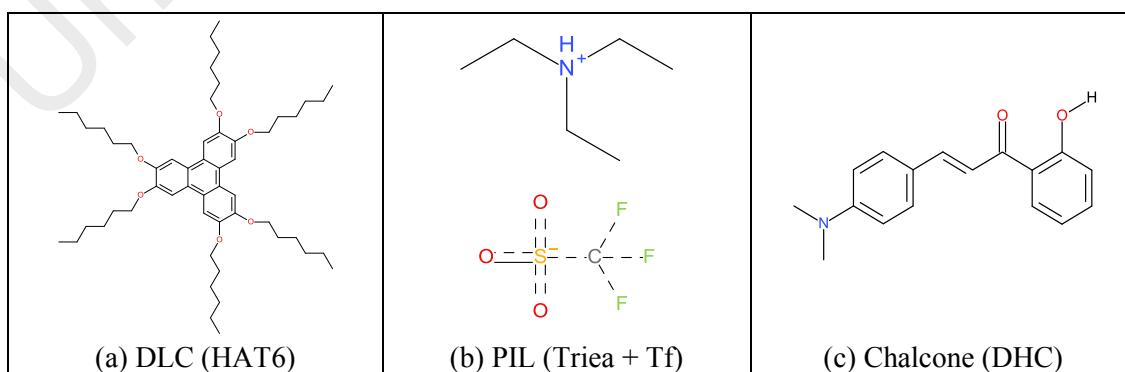


Figure 2.3. Representative of molecular structure of DLC, PIL and Chalcone used in this works. Abbreviations are detailed in each corresponding chapter.

2.2.1. Computational requirements of DLC system

In DLC study, 2,3,6,7,10,11-hexahydroxytriphenylene (HAT6) molecules are used to study the electronic properties of stacked DLC. Stacked HAT6 in columnar phase is able to allow current conduction through π - π orbital overlap at their core as shown in Figure 3.1.

The HAT6 is an organic molecule, only containing of C, H and O atoms with double bonds at the aromatic structure at the HAT6 discotic core. Basically, all the computational chemistry methods can treat very well organic molecules. However, the most challenging part is to simulate the molecules stacks part which requires proper repetition of molecules in the column axis. This requires computational method that can treat periodic system as well. In the periodic system, the HAT6 column will be approximated by stacking infinitely HAT6 molecules, thus requires a less demanding computational approach. In this sense, a computationally expensive method such as the HF methods is not considered.

The study of HAT6 will be focusing on the electronic properties such as orbitals, electronic DOSs, electronic densities, and BGs. Of this reason, the method must be able to calculate at electronic energy levels, which make the MM methods out of scope as it ignores electronic structure calculations. Here the only methods to be approximated used are SE and DFT.

2.2.2. Computational requirements of Protic Ionic Liquid (PIL) systems

The segment of the PIL studies requires thermodynamic analysis of PIL molecules, in order to assess the entropy of the PIL system as a function of temperature. this study will link quantum mechanical parameters of the PIL (such as entropy) to a bulk materials property, i.e. Seebeck coefficient of the PIL. This link will be useful in designing suitable PIL which can be used in thermoelectric applications.

The chosen PIL systems is an amine based organic molecule consisting of N, C, and H atoms which are combinations of ethylammonium (Ea), diethylammonium (Diea),

triethylammonium (Tria) and 2-methylpyridine (2mp) at cation side and O, C, S and F atoms which form trifluoromethanesulphonate (Tf) at anion side. All of the PILs are in liquid phase. Nonetheless, most of the computational methods are able to handle liquid phase simulation at least in approximated gas phase condition.

This study will be focusing on the thermodynamic properties of the PILs molecule, namely entropy which is a combination of vibrational, rotational and translational entropy. This evaluation requires vibrational analysis. In addition, the ionicity of PILs originates from the proton transfer from anion to cation via the H bond (long range interaction) cannot be disregarded. Vibrational analysis is a very demanding analysis as it calculates at least $3N - 6$ (N is number of atoms) degrees of freedom as discussed in section 4.6 and it also involves short and long interactions on each atoms. Thus, again a less demanding computational method and additionally able to simulate short and long range interactions is preferred. The HF method is good for short and long range calculations is but it requires a lot of computer resources. Therefore, computational methods that can be utilised are MM, SE and possibly DFT with right functional.

2.2.3. Computational requirements of Chalcone system

The segment of study involving chalcones investigates the correlation of the conformation of the chalcone molecules in the crystalline state and in solution, in order to identify its feasibility as a fluorescent material. The chalcone studied in this work is 4-dimethylamino-2'-hydroxychalcone (DHC) consisting of C, H, N and O atoms. In solution, the computation is not much different than liquid condition of PILs with addition of long range effect by solvent dielectric polar. In crystalline phase, DHC in a periodic system is considered.

The objective is to study the relationship between structural conformation energy of DHC and its fluorescent mechanism. The conformation of DHC involves the torsion of around the chalcone-phenol bond which has an important role for DHC fluorescence due

to excited state intermolecular proton transfer reaction to form keto or enol tautomer. The torsion itself involves the electronic and bond order changes, which make the electronic and orbital considerations important.

Consideration to computational method must fulfil requirements as mentioned above. Calculation in crystalline phase involves the repetition of molecular conformation, which therefore a less consumption of computer resource that be able to handle periodic system is needed. Study of DHC fluorescence involves electronic calculations, which therefore, the MM methods are not suitable and only SE and DFT methods can be considered.

2.3. Refinement of the selected methods

From the requirements as mentioned above, the main computational problem is the heavy computation loads that come from the nature of periodic system in DLC and Chalcone systems, and vibrational analysis in PILs thermodynamic study.

In terms of computational performance, DFT is not as fast as MM or SE, yet it may give better result than HF provided that given the right functional setup. DFT is also suitable for electronic calculations as it based on function of electron density. The additional orbital calculations included in KS theory would give more accurate description of the orbital properties of DLC and Chalcone.

In DFT, level of functional to yield good results is at GGA level and above. It is noted that LDA uses uniform electron gas which is unrealistic for non-solid calculations. Hybrid and meta-GGA level functionals are probably would give better results, especially B3LYP. Although B3LYP is vastly used and recommended functional, in terms of computational cost, it is insubstantially faster than full HF due to extensive adoption of HF for its exchange energy calculations. The TPSS family functionals are good for Chalcone as it yields comparable results to B3LYP (Espinoza-Hicks et al., 2013) and also for ionic liquid systems (Grimme, Hujó, & Kirchner, 2012). However, due to its relatively new functionals, it is yet extensively studied for many DLC systems (Hachmann et al.,

2011). Due to these facts, B3LYP and TPSS are not considered in the current DFT calculations.

Among those BLYP, PW91 and PBE functionals, PBE is the most popular and extensively studied functional due to the facts that it is suitable for many applications. For HAT6 DLC, PBE results are relatively comparable experimentally (X. M. Zhao et al., 2016). In addition, PBE functional also give a better result in simulating ionic liquids compared to B3LYP (Zahn & Kirchner, 2008). Chalcone derivatives are already studied using PBE computational and acceptably agree to experimental values (Chaudhry et al., 2017; Shkir et al., 2015).

Despite the above, there needs to be a compromise with regard to H bonding in PILs and Chalcone systems as PBE functional is less accurate to simulate long range interaction. However, as elaborated above, where the results are within acceptable range, this work uses DFT on GGA level with PBE exchange-correlation functional as standard in each calculation.

2.4. Limitations of this work

An important limitation of DFT simulation is poor treatment of non-covalent long range interaction. Therefore, over a large scale and bulk systems the effect may not as prominent as claimed, as it will be influenced by many external factors that is not considered in this work.

In terms of weaknesses the functional, GGA-PBE functional selected in this work generally gives good approximation to many systems as discussed above. In any way it will not give excellent results as may need functional optimisation which is out of this thesis aim and scope. The best way to interpret the results is considering the data trends.

**CHAPTER 3: CORRELATION OF COLUMNAR STRUCTURAL
PARAMETERS AND ELECTRONIC CHARGE TRANSFER FOR THE HAT6
LIQUID CRYSTAL COLUMNAR PHASE**

3.1. Discotic liquid crystals as organic electronic material

Discotic liquid crystals (DLC) are attractive candidates for molecular electronics devices, given their low cost, ease of processability and potential for self-assembly. DLCs are defined by their overall disc-shaped molecular structure, which comprises of a rigid planar central core surrounded by 6-8 aliphatic side chains which serve to stabilise the liquid crystalline phase (Laschat et al., 2007; Wohrle et al., 2016).

The binding between molecules is in most cases mainly due to van der Waals forces (N. Boden et al., 1999). The presence of these tails help to stabilise the structure of columnar liquid crystalline phase, and can be categorised according to their two dimensional packing structures, such as columnar hexagonal (D_h) and columnar rectangular (D_{rd}) (Muller & Mullen, 2007; Sergeyev, Pisula, & Geerts, 2007). There are also tilted columns where the cores of the disks are tilted with respect to the column axis, better known as oblique columnar (Col_{ob}) phases (Asahina & Sorai, 2003; Hagele et al., 2009). These packing structures are a function of the columnar symmetry and also intracolumnar van der Waals forces. X-ray studies suggest that within these columns, a long range intracolumnar helical order exists as studied by Fontes, Heiney, and de Jeu (1988), and Malthete et al. (1982). This helical order is proposed to be a competition between an attraction of the cores and the steric repulsion of the alkyl side chains.

One-dimensional self-assembly within the columns is enabled by steric packing and π - π interactions between the rigid cores. A column's order is a function of temperature, whereas they are bound within core-core interaction where the columnar arrangement is preferred. Furthermore, a high entropy and disorder of flexible aliphatic chains on the periphery of the central rigid core prevents the formation of a 3D crystal and is crucial to

the formation of liquid crystalline phase (Wohrle et al., 2016). For example, 2,3,6,7,10,11-hexapentyloxytriphenylene (HAT5) can spontaneously form well aligned, micrometer long, yet only tens of nanometers thick, nanowires on solid surfaces (Park et al., 2015). A shorter side chain is also found to be more beneficial for columnar stability (Arikainen et al., 1995). Solvents also influence the arrangement and order by acting on spontaneous self-organization of discotic LCs (Kastler et al., 2005; Park et al., 2015; Tong et al., 2010).

Due to the liquid crystalline nature of these columns, they do not exhibit true 1-D order and are instead defined as 1D-fluids where there is a degree of liquid-like dynamic disorder within the mesophase (Neville Boden et al., 1998; Wohrle et al., 2016). Hence, the ‘columnar’ configuration which is thought to be useful for charge transfer, is not perfect. It is a stochastic average in terms of its positional and orientational order. However, instead of viewing the fluid-like behaviour of DLCs as a liability, this liquid-like property of DLCs allows self-healing of defects and charge traps within the columns, which are able to average out over a temporal scale (N. Boden et al., 1995).

Common classes of DLCs are listed in Table 3.1, such as triphenylenes, porphyrins, perylenes, thiophenes and hexa-peri-benzocoronenes. Amongst the classes of DLCs, triphenylenes were amongst the first synthesised. In particular, hexaazatriphenylene derivatives (HAT) have formed the building blocks for many DLC systems in a range of molecular electronic applications, given their ability to accept electrons, and have a rigid, planar core which encourages π - π stacking. Porphyrins, on the other hand, with their fused six-member rings provided even larger π - π overlap. To my knowledge, metal-porphyrin complexes were first invented by Bruce et al. (Milgrom et al., 1997), whilst other coordination complexes include phthalocyanines and n-aryl Schiff bases (Abdullah, Hashim, et al., 2015; Abdullah, M. Noor, et al., 2015; Segura et al., 2015). Later metallomesogens have shown spin crossover behaviour, which are useful for potential

applications in dye-sensitized solar cells (DSSC) and memory devices (Abdullah, Arifin, et al., 2016; Abdullah, Azil, et al., 2015; Abdullah, Halid, et al., 2016). Hexa-peri-benzocoronenes were synthesised by Fechtenkötter et al. (1999) and exhibited highly ordered columnar structures. Thiophenes came into the picture in 2002, when S. H. Eichhorn et al. (2002) developed di, tri, and tetra-catenary liquid crystals carrying thiophene cores.

Table 3.1. Common classes of DLC molecule core structure and its chain substituents.

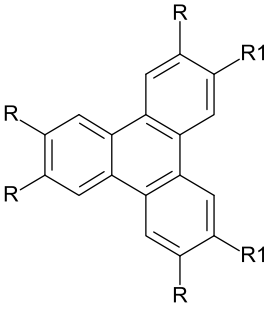
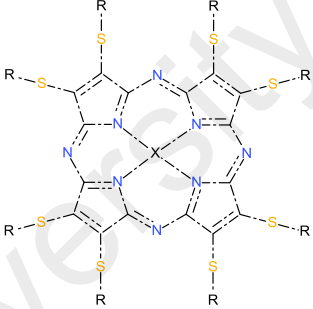
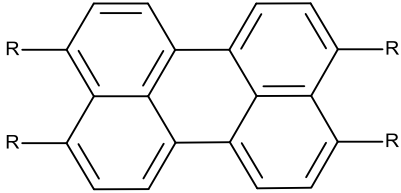
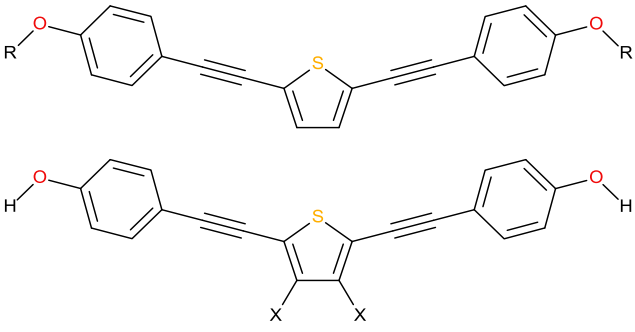
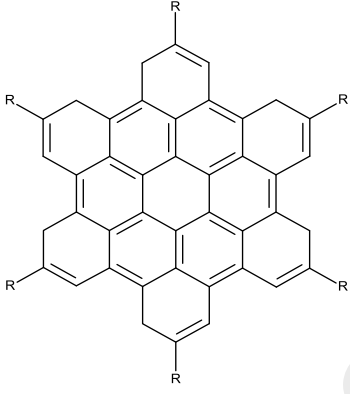
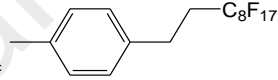
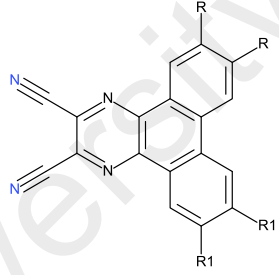
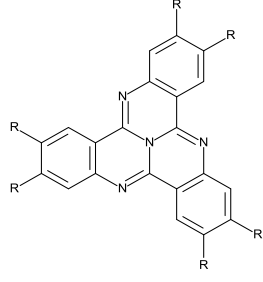
Core	Examples of Substituents
 <p data-bbox="568 1070 715 1104">Triphenylene</p>	<p data-bbox="1002 757 1422 815">R= R1= O(CH₂)₅CH₃ (HAT5) (Park et al., 2015),</p> <p data-bbox="995 833 1428 925">R= R1= O(CH₂)₆CH₃ (HAT6) (Haverkate et al., 2011; Warman & Van De Craats, 2003),</p> <p data-bbox="1010 943 1414 1001">R= R1= S(CH₂)₆CH₃ (G. Vaughan et al., 1992). (Kumar, 2004, 2006)</p> <p data-bbox="1050 1019 1374 1077">R= O-n-hexyl, R₁= S-n-hexyl (Camidge et al., 2015).</p>
 <p data-bbox="587 1460 699 1494">Porphyrin</p>	<p data-bbox="1091 1254 1326 1288">X= Cu, R= (CH₂)₃N₃,</p> <p data-bbox="999 1301 1422 1359">X= Cu, R= (CH₂)₃C≡CH. (Kayal et al., 2013)</p>
 <p data-bbox="592 1753 691 1787">Perylene</p>	<p data-bbox="1129 1610 1289 1644">R= COOC₂H₅,</p> <p data-bbox="1010 1657 1414 1691">R= COOC₃H₇. (Benning et al., 2000)</p>

Table 3.1. Continued.

Core	Examples of Substituents
 <p style="text-align: center;">Thiophene</p>	<p>R= Tetrahydropyran, X= H, Br, CN. (S Holger Eichhorn et al., 2002)</p>
 <p style="text-align: center;">Hexa-peri-hexabenzocoronene</p>	<p>R= C₈F₁₇ (Alameddine et al., 2005),  R= (Alameddine et al., 2005), R= C₁₂H₂₅ (Craats et al., 1999).</p>
 <p style="text-align: center;">Azatriphenylene</p>	<p>R= R1= C₁₀H₂₁ (Mohr, Wegner, & Ohta, 1995), R= C₁₀H₂₁ R1= C₆H₁₃ (Foster et al., 2006).</p>
 <p style="text-align: center;">Tricycloquinoxaline</p>	<p>R= C₃H₇, R= C₅H₁₁. (Kumar, Wachtel, & Keinan, 1993)</p>

3.2. Charge transfer in DLCs

1-D charge transfer is enabled along these columns, and these columnar liquid crystals have been described as molecular wires. In terms of electronic charge transfer, DLCs are seen to be advantageous over amorphous conjugated polymers as their 1-D order allows overlap of the HOMO to a larger extent. The spatial overlap of π^* orbitals of adjacent aromatic rings in the DLC core is expected to lead to quasi one-dimensional conductivity (Adam et al., 1994) (illustrated in Figure 3.1), as there is sufficient proximity between the cores, approximately 3.5 Å for hexakis(n-alkoxy)triphenylene (HATn) (N. Boden et al., 1995). Hexa-peri-hexabenzocoronenes derivatives are able to produce high electronic charge carrier mobility up to $1.1 \text{ cm}^2 \text{ V}^{-1} \text{ s}^{-1}$, which is comparable to amorphous silicon, and charge mobility for 2,3,6,7,10,11-hexahexyloxytriphenylene (HAT6) is $2 \times 10^{-3} \text{ cm}^2 \text{ V}^{-1} \text{ s}^{-1}$ (Lucas A. Haverkate et al., 2012; Warman & Van De Craats, 2003). The exchange of charge carriers between neighbouring columns is strongly hindered due to the insulating alkyl chains. DLCs are characterised by anisotropic charge transfer along and perpendicular to the columns, where charge mobility along the columns have been found to be around 1000 times higher than that across the columns. The relatively high mobilities along the stacking direction of the columns in the liquid crystalline phase have

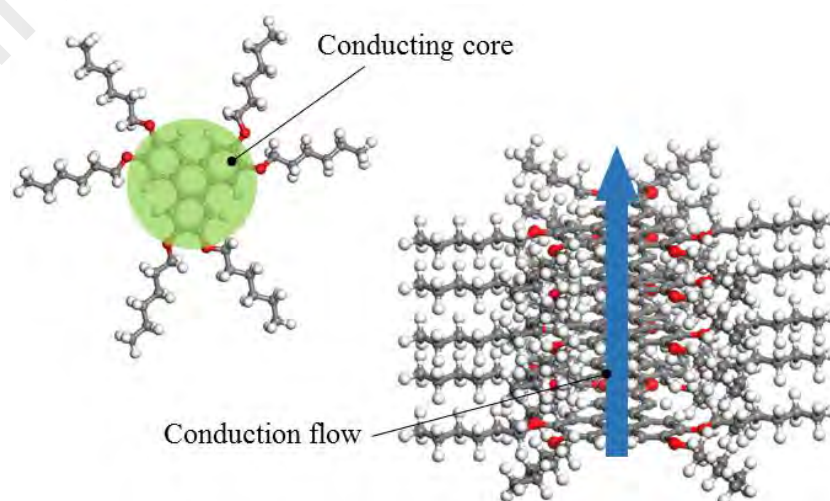


Figure 3.1. A schematic of one dimensional charge conduction through the columnar axis of a stack of DLCs.

been explained by liquid-like self-healing of structural defects on a time scale faster than hopping of charge carriers (Ochse et al., 1999).

3.2.1. Charge mobility in DLCs

Charge mobility is a macroscopic characteristic of DLCs which is related to the fundamental charge transfer on DLCs. There have been many investigations on the experimental and theoretical aspects on mobility in DLCs, given its premise for molecular electronics applications. A comprehensive list of charge mobilities for DLCs, measured through different experimental methods has been compiled by Wohrle et al. (2016). For example, the HAT derivative, 2,3,8,9,14,15-hexakisdecylsulfanyl and 2,3,8,9,14,15-dodecylsulfanyl of -5,6,11,12,17,18-hexaazatrinaphthylene have shown a mobility of $0.9 \text{ cm}^2 \text{ V}^{-1} \text{ s}^{-1}$ using the pulse-radiolysis time-resolved microwave (PR-TRMC) (Segura et al., 2015). These compounds are relatively small, and mobility is a function of side chain length. On the other hand, for molecules such hexabenzocoronenes mobilities in the LC phase are independent of the side chains. Synthesis of a series of self-organizing n-type hexaazatrinaphthylenes (Liu et al., 2014) such as that illustrated in Figure 3.2, with various bay-located side have the ability to form long-range molecular columns with well-defined growth directions. One particular variant of perpendicular to substrate columnar configuration exhibited mobilities of up to $10^3 \text{ cm}^2 \text{ V}^{-1} \text{ s}^{-1}$ using the Time of Flight (TOF) method. This provides some clues on the chemical structure required for fast mobility: in

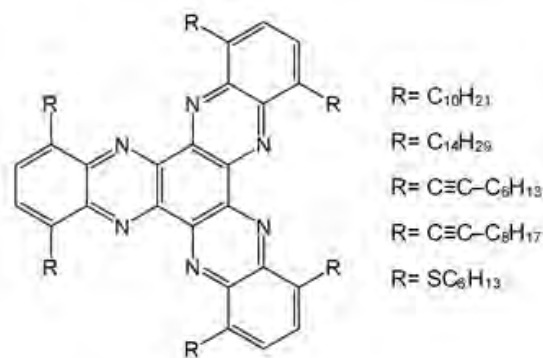


Figure 3.2. Structure of HATNA and its alkyl substituents which provide long range molecular order for good charge mobility (Liu, Usui, & Hanna, 2014).

this case the electron deficiency of the HAT core, coupled with long range columnar order. The charge transfer mechanism is elaborated in Section 3.2.4 and above.

3.2.2. Improving charge transfer in DLCs

In undoped DLCs, the bandgap is rather large, due to van der Waals forces being the main binding force, and hence the direct electronic wave function overlap between two adjacent molecules is very weak. For example, in HAT_n system, a HOMO–LUMO gap is ~4 eV or more. Doping will further improve the charge transfer characteristics of DLCs. When a charge is injected into a DLC system, the extra charge in the LUMO band is weakly bound and hence its wave function is more extended in space. Thus, the overlap of the electron cloud is increased, which provides a potential for the electron to transfer to the next molecule. Consequently, a bias field that promotes tunnelling resonance transfer to the neighbouring molecule is induced (Neville Boden et al., 1999).

DLCs are generally good electron acceptors. The low oxidation potential of HAT6 facilitates formation of radical cations when electron acceptors are introduced, they will become good conductors. G. B. Vaughan et al. (1992) doped 2,3,6,7,10,11-hexakis(phenyl)thiophene with iodine, which increased the conductivity by several orders of magnitude. N Boden, Bushby, and Clements (1994) used HAT5 with AlCl₃, which transformed the insulating HAT5 into a p-doped semiconductor, in which the conduction along the columns was three orders of magnitude greater than in the perpendicular direction (Laschat et al., 2007). Doping with gold nanoparticles or quantum dots has also been shown to improve charge mobility without disturbing its mesomorphic structure/organisation (Kumar, 2013, 2014). Binary DLC mixtures such as two triphenylene derivatives, HAT6 and 2,3,6,7,10,11-Hexakis(4-nonylphenyl)triphenylene in a 1:1 stoichiometry has been shown to increase the structural robustness of the discotic mixture and better order. This has been proposed to be due to the favourable enthalpy of intercalation between the stacks of the two different DLCs. The

charge mobility in the hexagonal columnar mesophase has also been shown to benefit from this binary mixing, where up to 3 orders of magnitude higher mobility than a single HAT6 composition has been shown.

Charge injection is also induced through contact with a metal surface in actual devices. This results in either a stronger or weaker coupling (depending on the orientation of the molecule at the substrate) between the π electrons in the core of the DLC and the s-electrons on the metal surface (N. Boden et al., 1999).

3.2.3. Applications of DLCs

Given their charge transfer characteristics mentioned above, DLCs find applications in electronics such as light emitting diodes, photovoltaic devices and organic field effect transistors (Kaafarani, 2011; Kumar, 2014). Organic light emitting diodes (OLED), for example, have been fabricated by Bock et al. through devices comprising of aluminium/perylene (as electron transporter)/ triphenylene (as hole transporter)/ITO (Seguy et al., 2001). However, the liquid crystalline properties were not exploited for these room temperature devices, and currently device lifetime is a particular issue. On the other hand, Organic Photovoltaics (OPVs) containing DLCs are thought to have the advantages of being stable and robust, with the particular characteristics of liquid crystals providing self-assembly and self-healing abilities. In theory, DLCs have the following advantages for application in OPVs: large diffusion length, large charge carrier mobility, and large solar absorption windows. They can be highly tuned to match the energy levels of dopants and electrodes, and their solution processability allow large area fabrication. A blend of electron-acceptor perylene tetracarboxdiimide (EPPTC) and electron-donor HBC achieved a photovoltaic response with an external quantum efficiency up to 29.5% at 460 nm and an open circuit voltage of 0.70 V (Schmidtke et al., 2006).

In sensing applications, exposed DLC films have been shown to undergo electronic coupling or charge transfer reactions upon exposure to gases which induce

conformational change. This can be measured in terms of the conductivity or polarisation response, and may be useful to detect weakly interacting nonpolar gases such as benzene, pentane, hexane, and heptane gases (Neville Boden et al., 1999). Furthermore, self-organised molecular dynamics prefer to keep charged and uncharged impurities near the free surface of the liquid crystal. Directionality of alignment is of essence in such electronic devices which exploit one dimensional charge transfer along the columns: unidirectional planar alignment is ideal for Organic Field-Effect Transistors (OFET) (Pisula et al., 2005) while the homeotropic alignment is ideal for OPV or OLED applications (Gearba et al., 2007).

Other less known applications for DLCs include Organic Magnetoresistance (OMAR) devices, Organic Thermoelectric (OTE) devices, current rectifiers and memory devices.

OMAR refers to the change in electrical resistivity for sandwiched structures of nonmagnetic and organic materials, when subjected to a magnetic field. HAT-CN derivatives have been shown to exhibit this effect. Such devices hold potential formagnetoresistive devices without ferromagnetic materials. Reichert, Saragi, and Salbeck (2012) reported the first magnetoresistive field effect transistors sensitive to ultrasmall magnetic fields (0.5mT). They employed a charge transport layer comprising of a mixture of HAT-CN (as electron acceptor) and 2,20,7,70 -tetrakis-(N,N-di-p-methylphenylamino)-9,90 -spirobifluorene (spiro-TTB) (as electron donor).

Thermoelectricity, on the other hand, is a solid state conversion of a temperature gradient to electric potential. It is currently being intensively explored for its potential in waste heat energy harvesting applications. Organic Thermoelectric materials are fast closing the gap with inorganic materials (Sun & Dalton, 2016). Some preliminary work has been done on DLCs for thermoelectricity (Chandrasekhar & Balagurusamy, 2002; Said et al., 2015), but the tunability of the DLC's density of states (DOS) is expected to have a direct impact on the OTE's Seebeck coefficient, i.e. its ability to generate electrical

potential per degree Kelvin of temperature difference ($\Delta V/\Delta T$) which is a point of further investigation (Bubnova & Crispin, 2012).

In terms of memory devices, the first structurally stable Ferroelectric DLC was synthesised by Miyajima et al. in 2012, with fan-shaped dendrons which have a supramolecular conical arrangement as shown in Figure 3.3 (Miyajima et al., 2012; Takezoe & Araoka, 2013). If the switching speeds can be improved, they are promising for high density memory applications, where each individual column may serve as an electrically addressable memory. On the other hand, current rectification has been demonstrated by Tsuji and Yoshizawa (2012) in stacked structures of Donor (Hydroquinone)–Acceptor (Quinone) Cyclophane materials. Their investigations included calculations of electron transport in these materials based on Density Functional Theory (DFT) (Stokbro, Taylor, & Brandbyge, 2003). They have observed nearly symmetrical current–voltage (I–V) characteristics resulting in limited rectification.

The above examples illustrate the different ways that the DLCs can be utilised in applications: applications such as OPVs and OLEDs exploit the quasi-one dimensional charge transfer characteristics and rely on the fact that higher charge mobility DLCs potentially make better performing devices. Others, such as OMAR rely on exploitation

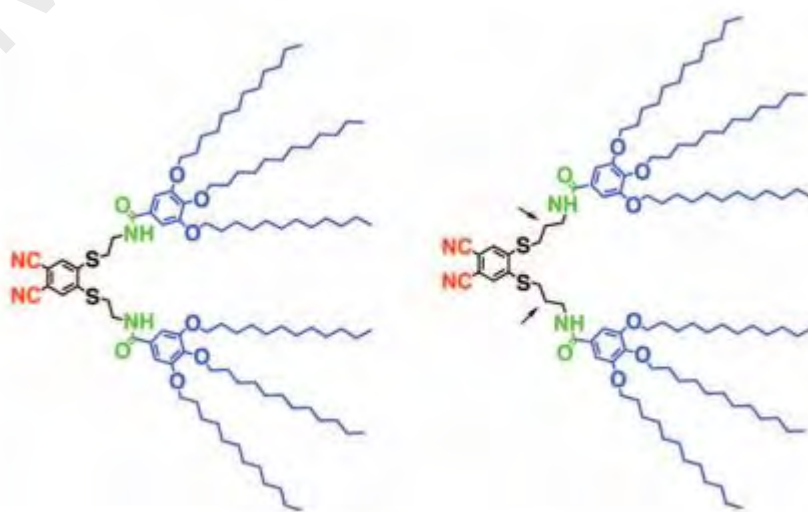


Figure 3.3. Example of fan shaped dendrons studied by Miyajima et al. Reprinted with from Miyajima et al. (2012). Copyright 2007 Science.

of its magnetic properties, whilst OTEs rely on the information of the electronic DOS. Thus, in terms of development of DLCs for applications, some challenges remain. Unlike inorganic devices, the spectral sensitivity of organic materials is limited. One of the major limitations is their narrow absorption window. The diffusion length of excitons to the donor–acceptor interface is much shorter than the optical absorption length. Direct electronic wave function overlap from one molecule into the positive core of a neighbouring molecule in the ground state is typically weak. The liquid crystalline nature of DLCs, whilst promising in terms of self-assembly, also contain spatial and temporal perturbation which act as barriers to charge transfer. Variations in terms of core-core spacing, twist and lateral slide may disturb the charge transfer process. In the next sections, understanding of DLC structure, dynamics and electronic properties will be provided from a Molecular Modelling perspective.

3.2.4. Molecular modelling of DLCs

Molecular modelling is defined to encompass all theoretical and computational approaches to emulate the behaviour of molecules. For the purpose of this paper, the different types of molecular modelling approaches which have been useful in DLC research will be summarised in this section. Molecular mechanics (MM), for example, uses Newtonian mechanics to describe atoms as point charges with an associated mass. The interactions between the atoms are then described by van der Waals forces and electrostatic interactions. The van der Waals forces are quantified using the Lennard-Jones potentials, whilst electrostatic interactions are quantified using Coulomb's law. These terms are collected to describe the system's internal energy (U) through a potential function. Minimisation of energy to deduce a system's equilibrium position is obtained through techniques such as steepest descent; this approach is elaborated further within the context of the Potential Energy Surface in Section 2.2.

The behaviour of such a system as a function of time is known as Molecular Dynamics (MD). The trajectories of atoms or molecules are solved using Newton's laws of motion, which are then solved using numerical methods. Typically results from MD simulations are correlated with experiments which measure molecular dynamics, such as nuclear magnetic resonance (NMR) spectroscopy.

Complementary to the MD approach, Monte Carlo (MC) molecular modelling is an approach heavily relied upon in the charge transfer studies outlined in Section 2.4.2. The fundamental difference between this and MD approaches is that the MC approach relies on equilibrium statistical mechanics. States are generated based on Boltzmann probabilities through a Markov chain procedure.

In contrast to the Newtonian based approaches described above, the electronic structure of the molecule is solved through the quantum mechanical (QM) approach. A molecule's chemical properties can then be extracted through understanding of its electronic structure. The first step is to solve the Schrödinger equation with the electronic molecular Hamiltonian. Since an exact solution of the Schrödinger equation can only be obtained for hydrogen atoms, solutions to other systems may be obtained through an approximation. For example, in the Molecular Orbital (MO) approach, the electrons are not assigned to individual bonds, but as under the influence of the molecule's nuclei. Thus, the molecular orbitals of these electrons are defined by the spatial and energetic properties of these electrons. The positions of these orbitals are approximated by the Density Functional Theory (DFT) or Hartree-Fock (HF) models to solve the Schrödinger equation. In particular, the DFT is favoured for its relative speed of computation and accuracy. It describes the electron population in terms of electronic density instead of wavefunctions using the Kohn-Sham method. In this approach, the density functional is split into (i) the Kohn-Sham kinetic energy, (ii) an exchange potential, (iii) exchange energies and (iv) correlation energies.

3.2.5. Modelling of DLC structure

Simulation of liquid crystal systems using Molecular Modelling approaches has been instrumental in understanding and predicting liquid crystal behaviour, either through MM, MC or QM approaches, or a combination thereof. There has been an established body of work, especially related to calamitic (rod-like) liquid crystals. In the case of DLCs, molecular modelling techniques are not as established. For example, QM allows quantification of LC order, identification of LC packing, and prediction of charge carrier mobility (Vincent Lemaire et al., 2004). MC simulation based on idealised models of discs portraying the Gay-Berne potential has been used to study phase formation in DLCs (Care & Cleaver, 2005). MM potentials have been used to establish the phase diagrams of DLCs mixtures (Caprion, Bellier-Castella, & Ryckaert, 2003). An early MD work on understanding of the molecular properties and order of DLCs was put forward by Ono and Kondo, through their studies of the disc-like hexakis(pentyloxy)triphenylene (HAT5) molecule (Ono & Kondo, 1992). The early models did not pay fine attention to the exact structural packing or chemical structure. This was improved upon by refining the model according to the understanding of the liquid crystalline structure afforded by XRD analysis; furthermore hybrid classical/quantum mechanical calculations have been applied to cases such as rigid columnar structures subjected to an explicitly described energetic disorder (Zbiri et al., 2009). Investigations on DLC molecular structure and its correlation with FTIR has also been explored (Abdullah, Mohd Said, et al., 2015).

Mulder et al. (2003) developed an all-atom molecule for four atoms within a discotic column, to investigate the dynamics of HAT6, in the columnar and isotropic liquid phases. On the other hand, charge transport parameters of semiconducting LCs; for example, charge mobility of triphenylene molecules have been determined from band structure calculations (Y. C. Cheng et al., 2003; Palenberg et al., 2000). Later DFT approaches have been used to study charge transfer in triphenylene derivatives. In

particular, Bredas et al. have performed theoretical studies on charge transfer integrals and reorganisation energies of DLCs as a function of molecular structure and order (Vincent Lemaire et al., 2004).

3.2.5.1. Molecular Dynamics Investigations on DLC structure

G. Cinacchi, R. Colle, and A. Tani (2004) have conducted atomistic MD studies of discotic HAT5 (Hexakis(pentyloxy)triphenylene) molecules was carried out to study its (i) molecular conformation, (ii) structural order and (iii) translational dynamics. They used AMBER and OPLS force fields to provide the parameters for the empirical model potential. The potential energy was described by bonded interactions (E_b) comprising of a sum of bond-bending interactions described by its harmonic potential and torsional energies; and nonbonded energies (E_{nb}) which is dependent on two interacting atoms described by Coulomb and Lennard-Jones terms. This work suggested a structure of the alkyl chains with respect to the triphenylene core, formed an intermediate state between the diablo-like configuration, with the chains in the triphenylene plane; and the octopus-like configuration, with the chains alternating out of the triphenylene plane, which was suggested by ^{13}C and ^2H NMR, respectively.

A system containing 80 HAT5 molecules was then simulated to enter the liquid crystalline phase. Their evaluation of positional and orientational correlation suggested that: i) the initial hexagonal positional order is retained throughout the simulation; ii) the parallel correlation function gives a spacing between molecules of 3.55 Å which is very close to the experimental value for intramolecular distances of 3.6 Å for adjacent cofacial molecules; and iii) molecules within a column have a helicoidal arrangement, with a twist angle of 36 degrees from between adjacent molecules, which again compare very well with experimental data. In brief, the outcome of the bulk structural properties of the simulated system agrees well with the D_{h0} phase of a real HAT5 system.

A picture of the translational dynamics was also provided by this work, through mean square displacement (MSD) analysis of the molecular centre of mass. The system demonstrated liquid crystal behaviour through the following observations: The solid-like behaviour observed perpendicular to the columnar axis, agreed substantially with NMR experiments that yield a diffusion coefficient, D_{\perp} , of the order $10^{-14} \text{ m}^2 \text{ s}^{-1}$. Along the columnar axis, the MSD indicates significant diffusion which they concluded to be liquid-like sliding motion between the columns.

Summarily, this work successfully simulates a representation of the liquid crystal order within a discotic system, which allows us an insight into the molecular conformation, positional and orientational order, and liquid-like flow within the columnar structure. This provides an insight into the structural characteristics of DLCs, upon which understanding of dynamics and charge transfer can be built up.

From a different perspective, Haverkate et al. (2011) have investigated the probabilistic distribution of DLC's structural parameters within a bulk DLC material: core-core separation (D), in-plane twist angle (θ), and lateral slide between the polyaromatic cores. They used MD simulations to predict structure and dynamics of discotic liquid crystals using Force-field methods. The force field was described by the London dispersion energy using Lennard-Jones function, using COMPASS in Materials Studio suite, which is able to include cross terms in energy expression to account for bond and torsional distortions.

This work used a 72-all-atom supercell (12x6 matrix), with 3.65 Å between molecules in a column, and 21.04 Å intercolumn spacing which agrees well with most other works (Giorgio Cinacchi, Renato Colle, & Alessandro Tani, 2004) and the results were compared to powder NMR diffraction. The simulated average equilibrium twist angle was between 36 and 38 degrees, which correlated well with experiments. Positional order was correlated, and it was found that the lateral deviation with respect to column axis was

2.5 Å or higher, which indicated significant barrier to the smooth charge transfer along the columnar axis. They also noted that a competition between the van der Waals interactions of the cores, vs the steric repulsion of the tails resulted larger distribution of core-core distances. For example, 35% were larger than 3.7 Å and 20% were larger than 4 Å, compared to the well-established 3.6 Å intermolecular spacing. Spacing of more than 4 Å are considered as structural traps on the picosecond time scale, and again provide a barrier to charge transfer. The effect of these variations in the values of the structural parameters have a direct impact on the charge transfer characteristics of the DLCs, as illustrated further in Section 3.2.7.4.

3.2.5.2. The Potential Energy Surfaces (PES) approach

Equilibrium states in liquid crystal position and orientation can be identified through the global energy minima of potential energy surface (PES) plots. For example, Chakrabarti group, has used the PES approach to understand the relationship between orientational and translational order in the calamitic mesophases (Chakrabarti & Bagchi, 2006; Chakrabarti & Wales, 2008).

In the case of DLCs, PES was employed by Zbiri et al. (2009) through a DFT study on two stacked HAT6 molecules to determine the most stable configuration. The PES of two stacked molecules was described in terms of its co-facial separation (D), twist angle (θ), and lateral slide (L), and its potential energy surface calculations were carried out using Gaussian software. The exchange-correlation (XC) meta-hybrid functional PBE1KCIS was employed. This functional includes a defined amount of the exact Hartree–Fock exchange combined with a high-level kinetic energy density. Through the PES approach they estimated a distinct energy minimum for the equilibrium structure at $D= 3.5 \text{ \AA}$ and $\theta= 30^\circ$ when $L= 0 \text{ \AA}$, which agrees well with other work (Senthilkumar et al., 2003).

3.2.6. Modelling of DLC dynamics

3.2.6.1. Core and tail dynamics

A work by Mulder et al. (2003) combined quasielastic neutron scattering (QENS) measurements with molecular dynamics simulations on the discotic molecule hexakis(*n*-hexyloxy)triphenylene (HAT6) in order to investigate the core and tail dynamics of the molecule. This work focused on the dynamics of HAT6's polyaromatic cores, which play a key role in the charge transfer of DLCs. A model of a single HAT6 molecule was constructed, comprising of a stack of four triphenylene cores each with the six side chains of $O(CH_2)_5CH_3$. The minimum energy conformations are shown in Figure 3.4. The use of a single short column eliminated the consideration of intercolumn interaction, which was on a longer time scale. The COMPASS force field was used to optimise the molecular structure. Analysis was only carried out on one of the centre cores, with its associated chains, for comparison with the QENS spectra, as this is seen to be mainly responsible for the charge transfer mechanism. The MD simulation parameters were adjusted to fit to

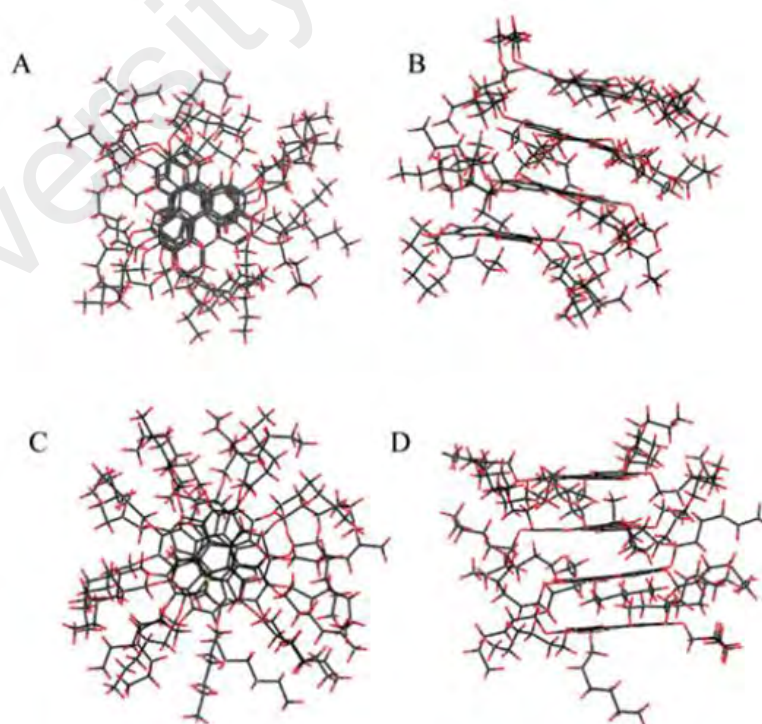


Figure 3.4. (A, B) Illustrations of a minimum-energy orientation with the aromatic rings nearly superimposed. (C) and (D) were minimized from a 45° phase difference between disks. Reprinted from Mulder et al. (2003). Copyright 2003 American Chemical Society.

the EISF data from QENS, where it was found that a core-core spacing between 3.5 and 3.7 Å provided the best fit in terms of the time scale compared to the experimental time scale. The intermolecular charge transfer was on similar time scales of the dynamics which is dominated by van der Waals interactions. In addition, the EISF data (as shown in Figure 3.5) implied not only are the dynamics of core and tails on different time scales, but the whole molecule is moving in different dimensions on different time scales.

Furthermore, the EISF data above 360 K (i.e. in the isotropic states) shown in Figure 3.5, indicated the same spectral components which are present in the columnar phase, despite evidence that phase transition had occurred. Thus, this interestingly suggests that although the material has entered the isotropic phase, the positional correlations still exist on a time scale longer than that measured by QENS. Structurally speaking i) the core-core and tail-tail van der Waals interactions drive the self-assembly of the columns, and ii) coupling between the tail and core motion are instrumental to the alignment of the cores, and hence rigidity of the columns.

Comparison between MD simulations and QENS experiments was also carried out by Haverkate et al. (2011), to measure the temporal and spatial dynamics in the liquid

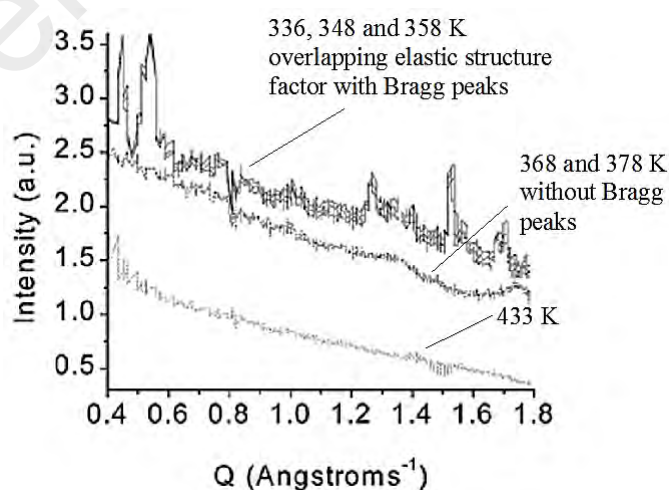


Figure 3.5. Elastic structure factor at 336, 348, and 358 K (overlapping solid lines at the top) showing Bragg peaks due to liquid crystalline ordering. The dashed lines (in the middle) without Bragg peaks at 368 and 378 K, and the dotted line (bottom) is for 433 K. Rigidity of column are shown at 336, 348, and 358 K because the peaks overlapping which indicate the structure is rigid in that temperature range. Reprinted from Mulder et al. (2003). Copyright 2003 American Chemical Society.

crystalline phase. They modelled an all-atom force field system on hexagonal periodic supercell comprising of 72 HAT6D molecules, which was compared with neutron powder diffraction patterns and QENS data. They showed that on the picosecond the tilt of the core was shown to be too fast to be followed by the tail. The tilt of the core shows an amplitude of 1.5° whilst the overall tilt of the molecule remains unchanged. In comparison, the translational motion of the core and tail are correlated, with comparable amplitudes of 0.1 \AA and 0.15 \AA . The directions of translation are perpendicular and parallel to the column axis, respectively. On a 7 ps time scale, the rotational motion of the tail begins to follow that of the core. Correlation between the tail and core on the parallel motion is weaker. They concluded that in-plane motion contributed most to the 0.2 ps QENS spectrum, whilst on the 7 ps scale, both tilt and twist of the molecule contributed to the spectra.

3.2.6.2. Lattice dynamics

In DLC systems, charge trapping arises due to the presence of impurities, mostly from reactions with the metal electrode. In DLCs, structural defects are able to heal over time. Typically, the time to heal, τ_d is in the range of 10^{-5} to 10^{-6} s, whilst τ_t , the transit time of a hole or electron across a distance d is $\sim 10^{-3}$ s (Neville Boden et al., 1998). The main scattering events involving the transit of charge carriers in a discotic column is the oscillation of the molecule parallel and perpendicular to the director (Wegewijs et al., 2002).

For the DLC system in question, it is important to decide whether the system is defined as fully static or whether there exists a significant dynamic contribution. Olivier et al. (2009), through their MC modelling, have incorporated a factor of lattice dynamics into system of liquid crystalline phthalocyanine stacks. They noted that even at high driving fields, there exist situations where there is negligible charge transfer, or charge transfer against the direction of the applied electric field. This is thought to occur when the charge

transfer is momentarily blocked by a segment of the column which acts as a defect, which will self-anneal over time, as discussed earlier. In order to understand the effect of these dynamic structural defects, lattice dynamics was incorporated into the Monte Carlo model for two different cases: (i) a frozen lattice motion and (ii) inclusion of fast thermal motions.

In the case where the lattice motion was frozen, the lifetime of the defect was considered to be infinite. Consequently, low mobility values for holes were obtained, i.e. 3.12×10^{-3} and $2.92 \times 10^{-3} \text{ cm}^2 \text{ V}^{-1} \text{ s}^{-1}$ in the rectangular and hexagonal mesophases, respectively. These values actually corresponded quite well to TOF measurements of similar PC molecules. On the other hand, a simulation incorporating fast thermal fluctuations averaged for each dimer over 650 snapshots over a period of 65 ns. This model yielded a hole mobility about 2 orders of magnitude larger and corresponds to the experimentally measured PR-TRMC technique (μ) 0.08-0.37 $\text{cm}^2 \text{ V}^{-1} \text{ s}^{-1}$. The difference between the two models imply that there exist many dynamic structural defects along the columns.

Taking into consideration the molecular and lattice dynamics described above, a representation of how the MD of the DLC columnar system contributes to the charge transfer is starting to build up. Next, further considerations related to the electronic behaviour and charge transfer specific to the DLC phase will be discussed.

3.2.7. Modelling of DLC charge transfer

Charge transport in DLCs are either through banded conduction or charge hopping, depending on the nature of the polaron formed. Excess charge accumulation distorts the surrounding medium and gives rise to a polaron. If electron motion that is sufficiently faster than the timescale of molecular vibrations, the lattice does not have time to relax to the distorted geometry whilst the excess charge remains on the lattice. In this case, the large polaron is dragged along with the charge, causing an increase in effective mass and

narrowing of bandwidth, i.e. the band structure is perturbed. This band transport model has been discussed at length by Lever et al. (Lever, Kelsall, & Bushby, 2005). On the other hand, for slower electron motion, the lattice is able to relax to the distorted geometry and this causes charge localisation (trapping) in the lattice. In this case, charge transfer is through phonon-assisted hopping. The phonon hopping description suits many scenarios for DLCs and will be the focus of discussion in the following sections.

On a final note, there a quantum tunnelling mode has also been proposed for binary mixtures of DLCs, in order to explain intercolumnar charge transport of binary DLC mixtures. Given that binary mixtures have been mentioned to stabilise the overall bulk DLC system through intercalation, a quantum tunnelling model has been proposed to explain the enhancement of charge mobility of such systems (which can be 3 orders of magnitude higher than single DLCs. Wegewijs et al. (2002) have evaluated the tunneling viability of binary mixtures based on three triphenylene derivatives and compared them against charge mobility measured using TOF and PR-TRMC techniques. They concluded that the high integrity columnar structure afforded by binary mixtures, together with long-range alloy band structure contribute to the increased mobility of the binary mixtures.

3.2.7.1. Thermally Activated Charge Hopping

Charge hopping rates strongly depend on the chemical composition and local molecular ordering of the liquid crystal director, whilst the global charge carrier pathway is defined by the presence of defects and overall morphology. Bäessler (1993) has written a comprehensive review of the charge transport in DLCs modelled through MC simulations. Charge transport is due to a hopping mechanism, where charges jump from molecule to molecule at a rate determined by its governing parameters.

A theoretical description which relates the charge hopping in a columnar stack of DLCs, to the mobility is described by Vincent Lemaire et al. (2004) which will be discussed in this section. They assumed charge hopping to be localised and jumps from

disc to disc in the stack. The charge hopping frequency is approximated to the first degree by semiclassical Marcus theory:

$$k_{et} = \left(\frac{4\pi^2}{h} \right) t^2 (4\pi\lambda k_B T)^{-0.5} \exp\left(-\frac{\lambda}{4k_B T}\right) \quad (3.1)$$

where λ is reorganisation energy, t is intermolecular transfer integral, T is absolute temperature, k_B is Boltzmann constant, and h is Planck constant.

3.2.7.2. Charge Hopping Parameters.

In this model, the system goes through a transition state where the two molecules involved in charge transfer assume identical geometrical conformations in order for charge transfer to occur.

The two main parameters which govern charge hopping are as follows:

1. Reorganisation energy (λ), which is the sum of the inner reorganization energy of the molecule (λ_i) and the reorganization energy of the surrounding medium (λ_s) (Olivier et al., 2009). λ_i represents the energetic relaxation involved with the conformational change of the molecule and radical ion when going from the neutral to ionised state. The alkyl chains are generally substituted by hydrogen atoms since they have little impact on the charge hopping parameters. λ_s describes the change in electronic polarization of the surrounding molecules and their possible reorientations. It is generally found that the packing density of the discs are have a larger contribution to this parameter compared to the molecular structure.
2. Intermolecular transfer integral (t) quantifies the electronic coupling between the molecules.

3.2.7.3. Computational Methods.

The reorganization energies were modelled at the density functional theory (DFT) level using the UB3LYP functional and a 6-31G(d,p) basis set (Hatsusaka et al., 2001; Norton & Brédas, 2008). The charge transfer integral, J , in its basic form, is calculated

by the dimer model, which assumes zero spatial overlap between two adjacent molecules, and allows an approximation of the charge transfer between the molecules given this condition. The charge transfer integral for hole transport in such a situation is then calculated from the energetic splitting of the two highest-occupied molecular orbitals (HOMO and HOMO-1) in a system. These splittings are calculated using the semiempirical intermediate neglect of differential overlap (INDO) Hamiltonian (Coropceanu et al., 2007) based on the geometry optimised conjugated cores at the DFT/B3LYP level.

However, in a columnar system, the dimer model is inaccurate, and a different approach is needed to model the large spatial overlap of the stacked discs. A preferred way of doing so is using the fragmented approach through the Amsterdam DFT (ADFT) calculations and the quantitative molecular orbital (MO) model. Symmetry-adapted orbitals of a stack of discotic molecules are employed in ADFT. The charge transfer integrals and site energies are directly obtained from the off-diagonal and diagonal matrix elements of the Kohn-Sham Hamiltonian, respectively. A correction is then added to account for the large molecular overlap of the molecules in a stack.

These DFT calculations have been carried out at the generalized gradient approximation (GGA) level using the newly developed asymptotically corrected exchange and correlation functional SAOP (statistical average of orbital potentials) and an atomic basis set of Slater-type orbitals (STOs) of triple- ζ quality including two sets of polarization functions on each atom (TZ2P basis set in ADF) (Dimitrakopoulos & Mascaro, 2001; Troisi & Orlandi, 2006).

The mobility μ of the charge carriers within the stack can then be written as:

$$\mu = \frac{v}{F} = \frac{\Delta x}{F\Delta t} \quad (3.2)$$

with v the net drift velocity of the charge carriers and F the amplitude of the electric field inducing the charge drift. In an ideal columnar stack, Δx can be assumed to be core-core distance, D ; and Δt as the hopping time.

3.2.7.4. Examples of charge transfer modelling

The above approach has been verified by V. Lemaire et al. (2004) against the mobility values of a range of DLCs based on triphenylene, hexaazatriphenylene, hexaazatrinaphthylene, and hexabenzocoronene derivatives, measured using the pulse radiolysis time-resolved microwave conductivity (PR-TRMC) technique.

Similarly, Zbiri et al. (2009) has evaluated the charge transfer integrals in terms of separation (D), twist angle (θ) and lateral slide (L) using the Amsterdam Density Functional (ADF). The generalized gradient approximation (GGA) was adopted, where the exchange contribution to GGA was approximated by the Becke gradient correction (Becke88) and the correlation part by the Perdew–Wang correction (PW91c).

Following on their work on identifying equilibrium DLC structure parameters through the use of PES as described in section 3.2.5.2, the spatial overlap integrals (S) and charge transfer integrals (J) were then evaluated as function of D and θ , as shown in Figure 3.6 and Figure 3.7. Both the dimer and fragmented approaches were used, and the outcomes compared. Evaluation of J as a function of θ differs significantly between the fragmented

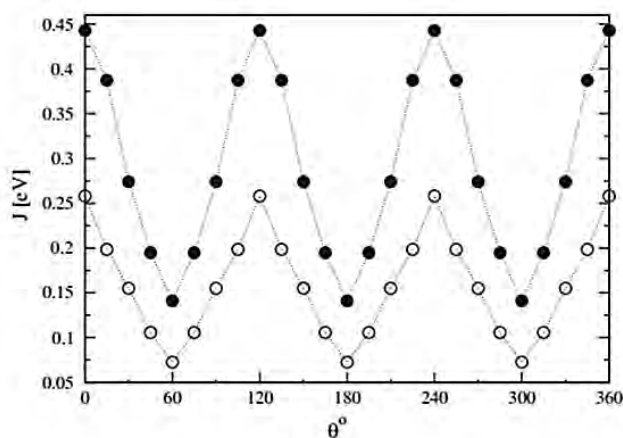


Figure 3.6. Calculated CTIs (J) and their dependence on the twist angle θ obtained using the fragment approach (full circles) and the dimer approach (open circles). The co-facial separation and the lateral slide between two stacked HAT6 molecules are kept fixed at $D= 3.5 \text{ \AA}$ and $L= 0 \text{ \AA}$, respectively. Reprinted from Zbiri et al. (2009). Copyright 2009 Springer.

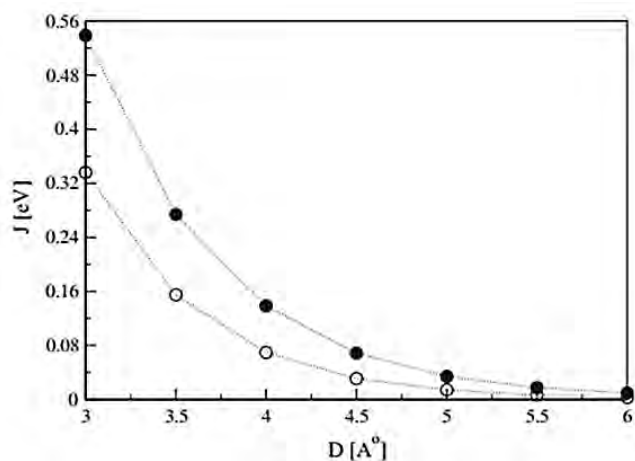


Figure 3.7. Calculated CTIs (J) and their dependence on the co-facial separation D obtained using the fragment approach (full circles) and the dimer approach (open circles). The twist angle and the lateral slide between the two stacked HAT6 molecules are kept at $\theta = 30^\circ$ and $L = 0 \text{ \AA}$, respectively. Reprinted from Zbiri et al. (2009). Copyright 2009 Springer.

approach and the dimer approach. There is significant difference between the calculations from the fragmented and dimer approach, due to neglect of spatial overlap in the dimer approach. The maximum and minimum values of J from the fragmented approach are 0.55 and 0.02 eV, whilst from the dimer approach they are 0.34 and 0.0 eV, respectively.

For variation of D , the value of J decreases exponentially with increased separation, D , until it reaches the monomeric zero overlap limit. In this work, amongst the three parameters, D is seen as the limiting factor to charge transfer. In addition, the effects of L , lateral slide on symmetry breaking and spatial overlap can significantly perturb the charge transfer process.

When D and θ are fixed at their equilibrium values of 3.5 Å and 30° respectively, and a lateral slide is induced in the model, it is observed that the changes in J are reflected by their local maximal and minima, as shown in Figure 3.8. This can be viewed in terms of the constructive/destructive characteristics of the overlap as the molecule slides laterally. This is further supported by the spatial overlap representation in, where zero overlap will result in zero charge transfer.

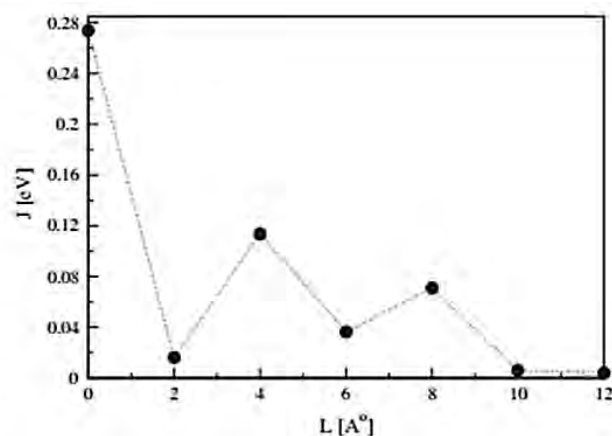


Figure 3.8. Calculated CTIs (J) and their dependence on the lateral slide (offset) L between the two stacked HAT6 molecules. The twist angle θ and the co-facial separation D are kept fixed at their equilibrium values, 30° and 3.5 \AA , respectively. Reprinted from Zbiri et al. (2009). Copyright 2009 Springer.

Charge transfer in phthalocyanines was studied by Olivier et al. (2009), through evaluation of the in-plane and out of plane tilt angles, β and τ , respectively. They concluded the following points:

1. Tilt angle, β between two adjacent stacked molecules. The charge transfer integral was shown to increase as function of β , due to the increased proximity of the molecules upon tilting, regardless of the distance created by the further ends of the molecules.
2. In plane rotation angle, θ , shows a broad peak in the CTI between 60° and 120° , with a peak at 90° . This corresponds to an eclipsed conformation preferred by adjacent PC molecules in order to maximise the van der Waals interactions between the saturated chains. A marked difference was observed between the rectangular and hexagonal phases. A rotation in the rectangular phase was accompanied by a lateral slide of the molecules; resulting in a lower overall charge transfer integral compared to the hexagonal phase. In comparison, the hexagonal phase gives a rather isotropic 2D map and nonzero probability for the cofacial configuration. This implies that the rectangular phase is more constrained compared to the hexagonal phase.

Senthilkumar et al. (2003) investigated the charge transfer integrals for unsubstituted and methoxy- or methylthio-substituted triphenylene derivatives, similar to the approach outlined above by V. Lemaire et al. (2004) and Zbiri et al. (2009). They found that the charge transfer integrals were highly dependent on the twist angle, θ , with a maximum of almost for $\theta=0^\circ$ and a minimum of 0.1 eV $\theta=60^\circ$. The charge transfer integrals decreased with the distance between the stacked molecules. The charge transfer integrals calculated for methylthio-substituted triphenylene from this work is approximately double that reported by Cornil et al. (2002). This is reasonable as Cornil et al. (2002) used the dimer model to calculate their CTI. They also suggested unsubstituted triphenylene are most affected by lateral slide, compared to substituted triphenylene, for which the effects are quite minimal. Their calculations also indicated that charge transfer integrals and site energy fluctuations for methoxy- and methylthio-substituted triphenylenes were not significantly different. This is in agreement with the similar charge carrier mobility of 0.002 and 0.008 $\text{cm}^2 \text{V}^{-1}$, measured by PR-TRMC measurements on the D_h phase of hexyloxy- and hexylthio-substituted triphenylenes, respectively. In contrast, the low mobility values measured by TOF measurements on alkoxy-substituted triphenylenes seem to match the results for large lateral slide and small charge transfer integral, which results in a low mobility of the magnitude of 0.001 $\text{cm}^2 \text{V}^{-1}$.

Bag et al. (2015) used atomistic MD studies to evaluate the positional and orientation characteristics, hexa-peri-hexabenzocoronene (HBC) core with six pendant oligothiophene unit (Bag et al., 2015). They also evaluated the charge transfer characteristics of this molecule based on the equilibrium structure, where the twist angle (θ) was 25° , but also that two adjacent HBC molecules in a stack are tilted by 5° with respect to each other. The HBC cores are also tilted at an average of 43° with respect to the column axis.

The HBC cores of the molecules formed a very well ordered columnar structure and consequently, mobility along the column was high. Once the charge transfer integral was calculated, kinetic Monte Carlo (MC) method was used to simulate charge carrier dynamics and calculate mobility, which was calculated to $0.23 \text{ cm}^2 \text{ V}^{-1} \text{ S}^{-1}$ in this phase.

3.2.8. Modelling of Electronic Orbitals

So far, most of the discussion has been on the investigation of charge transfer models in DLCs, as it has a direct impact on charge mobility, and hence device application potential. Whilst valuable insight into the structure, dynamics and charge transfer mechanism have been achieved by merging simulation works with experimental results, there remains some space for exploration. The information on the electronic DOS, especially of π electron levels in DLCs are also of significant importance, especially in cases of charge injection from electrodes, and applications such as current rectification and thermoelectricity.

Previously, Barlow et al. (2007) have used DFT to calculate the frontier orbitals and reorganization energies of the HAT derivatives which they synthesized. This is an interesting example where the investigation of molecular structure, ionization potential and electron affinities. Figure 3.9 shows the frontier orbitals for two of the structures shown, and their calculations of the conformational changes due to oxidation and reduction of these molecules then led to their analysis on reorganisation energy. For these derivatives, they suggested that the rather exothermic electron affinities, the ability for π -stacking of the orbitals and low intramolecular organisation energies suggested by the DFT calculations indicated the potential of these materials as for electron transport.

Interestingly, these calculations also indicated that the valence level orbital (HOMO) is spread over the oxygen atoms which bridge the core and alkyl chains. Thus, for certain conformational configurations of the columnar phase, oxygen atom position influences the C-C and C-O tail bond order. This also implies that the overlap of the HOMO over

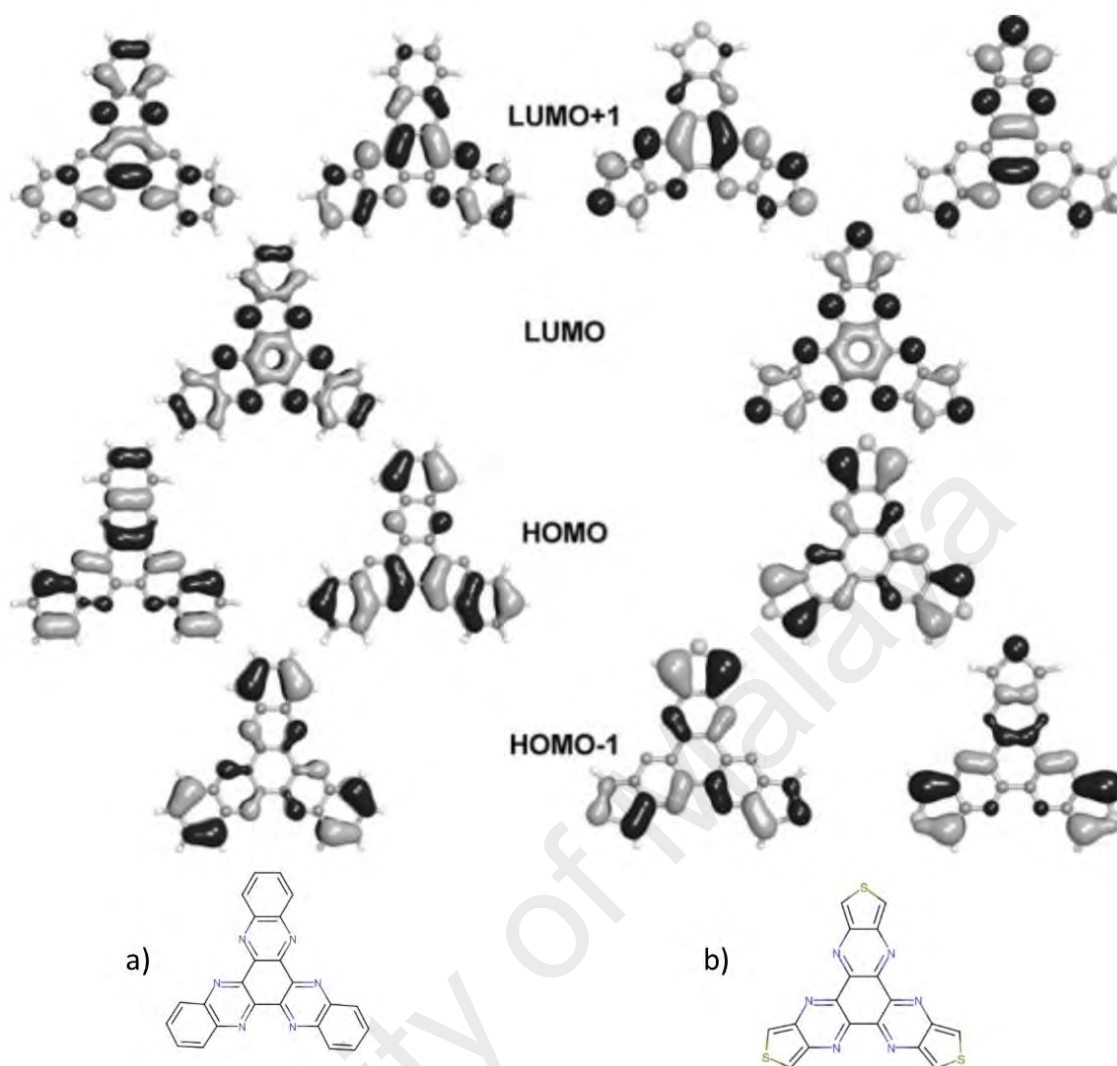


Figure 3.9. Frontier orbitals calculated at the B3LYP/6-31G** level for molecule (a) (left) and (b) (right). Reprinted from Barlow et al. (2007). Copyright 2007 Wiley-VCH.

the bridging oxygen atoms confers an electronic role to the tails, in addition to stabilising the columnar phase.

Efforts to obtain an insight into the electronic configuration of DLCs through a combination of experimental and modelling works have been explored by Crispin et al. (2004). In this work, experimental data from angle-resolved ultraviolet photoelectron spectroscopy (ARUPS) has allowed insight into the electronic structure. The photoemission process due to the ultraviolet photoelectron is much faster than the nuclear geometry relaxation, and hence allows a direct probe into the electronic states of the molecule. Quantum-chemical calculations on the isolated molecule, and in stacks of 2-6 molecules are then correlated with the experimental data to understand the π -electron

delocalisation. The theoretical UPS spectra of the isolated molecule and of stacks containing from two to six molecules have been simulated, based on the intermediate neglect of differential overlap (INDO) semi empirical Hartree-Fock method developed by Zerner et al. (1980). These calculations implied the creation of new electron orbitals in the forbidden energy gap of the isolated conjugated core. This has been fully confirmed by the ARUPS experiments, and implies the formation of a quasi-band structure which extends over several molecules in the column.

3.3. Study of correlation of the electronic structure for HAT6 columnar phase

As elucidated above, a DLC HAT_n is a popular DLC which is a molecular system that requires between five and seven carbons in the alkyl tail to form the columnar phase. One derivative from HAT_n system, the 2,3,6,7,10,11-hexahexyloxytriphenylene (HAT6) is a DLC with triphenylene as the discotic core and 6 hexyloxy ligand tail. It is among other HAT_n systems that is commonly used as sample model to investigate the charge transfer and charge carrier mobility due to changes of structural conformation and disorder of columnar axis (Haverkate et al., 2014; Haverkate et al., 2011; McKenzie et al., 2010; Zbiri et al., 2009).

The HAT6 is a popular DLC model due to its simple structure, and it has an optimum tail length that gives broad mesophase range. As mentioned sections above, electronic structure of HAT6 and many DLCs are heavily dependent to the conformation of their columnar phase. It is because stacking in the columnar phase will affect the π - π orbital overlap that is formed during this phase. Thus, effectively changing the electronic structure in the column and eventually in HAT6 molecule. The van der Waals, hydrogen bonds, and various intermolecular interactions between the cores, and the stabilization provided by the aliphatic chains results in a columnar stacking conformation of the DLCs within the liquid crystal temperature range (Brunsveld et al., 2001), typically forming ordered

columnar hexagonal (Col_h) or columnar rectangular (Col_r) phases. The packing configuration are function of column symmetry and intracolumnar van der Waals forces.

The changes of π - π overlap is measured from 3 stacking parameters that is, core-core separation, twist with respect to the columnar axis, and lateral slide. The electronic structure is evaluated through the electronic calculation from the DFT in terms of HOMO-LUMO, band gap (BG), electronic DOS, charge population and electronic density. Determination of HOMO-LUMO provide the position of valence orbital and next unoccupied orbitals thus giving direction of electronic charge transfers. The BG calculation is compared to the stability of the HAT6 column to know the best conformation for electronic transport. Then, all other electronic parameters that is DOS, charge population and electronic density provides in elucidating the electronic structure and the best conformation for electronic applications.

The π - π conjugation between the cores allows 1-D charge transfer along the columnar axis, which ultimately lead to DLCs to act as a potential nanowire in molecular electronic devices as well as tuneable electronic material. This makes DLC a promising material for applications in organic electronics such as organic field-effect transistor, light emitting diodes, gas sensors, thermoelectrics and photovoltaic cells (Said et al., 2016).

The objective of this work is to investigate the electronic structure of columnar phase of HAT6, which the information obtained from this work is expected to be useful for future rational molecule design of DLCs, such as for optimal charge transfer and applications towards organic electronic devices.

3.3.1. Methodology

In this study, the geometrical configurations and energetic stabilities of the DLC molecule, HAT6 were investigated using first principle calculation density functional theory (DFT) using spin polarised DMol³ of Materials Studio 2016 (MS 2016) package (B. Delley, 1990, 2000).

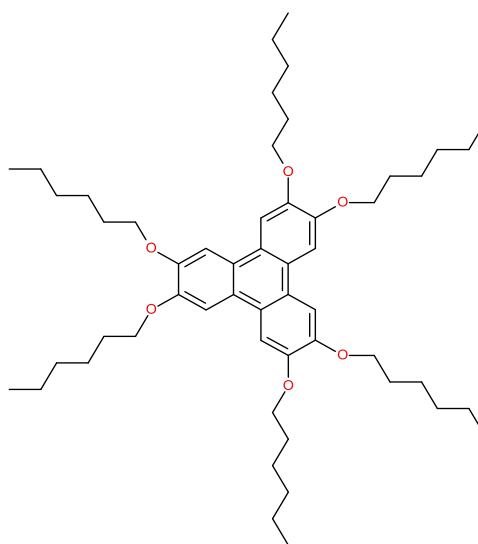


Figure 3.10. Molecular structure of DLC HAT6.

The HAT6 molecule (2,3,6,7,10,11-hexahexyloxytriphenylene (shown in Figure 3.10, 144 atoms) was constructed using benzene as basic building block for the core and the tails were constructed using hexyloxy ($R = OC_6H_{13}$). The initial geometrical structure was assigned to a planar D_{3h} symmetry, and the only out-of-plane atoms are the hydrogens of the tails. Optimization of the geometrical structure of a single HAT6 was carried out by first principle of density functional theory (DFT) calculations performed using the Generalised Gradient Approximation (GGA) with Perdew–Burke–Ernzerhof (PBE) exchange–correlation functional (Perdew et al., 1996).

A periodic cell containing 2 geometrically optimised stacked HAT6 dimer molecules was used to simulate the stacking columnar HAT6. Columnar structure molecular packaging parameter studied are stacking distance, alignment twist, and lateral slide. The columnar structure is represented by core co-facial separation distance, D , twist, θ , and lateral slide distance, L as shown in . The normal axis of the column was defined as the centre of the triphenylene core. The core-core distance, D was varied from an initial distance of 2.8 Å to a final distance 5.0 Å in increment of 0.2 Å. Similarly, the twist parameter, θ , was initiated at 0° and incremented in steps of 10° until it completes a full 360° rotation. For lateral slide, L , was calculated from 0 Å, to the final value was 6.75 Å.

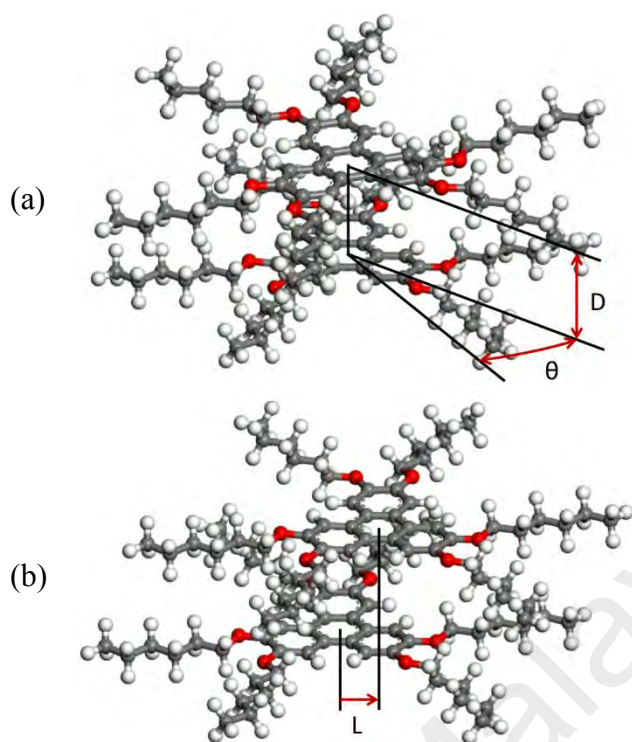


Figure 3.11. An all-atom model of two stacked HAT6 dimer molecules parameter investigated in this work. Variables to the stack structure are introduced in the form of (a) core-core facial separation, D , and twist angle, θ , (b) and lateral slide, L .

In the simulations of the three parameters, the physical properties calculated formation energy, electronic DOS, BG and charge population. The formation energy calculates the stability of the structure which determines the more stable formations. The DOS gives of the electronic structure of the structure which decides the BG of the structure and the possibility of electronic excitation thus allowing electronic transfer in the HAT6 column, furthermore the local DOS and partial DOS will give detailed information of which orbital play the role. Calculation of the charge population determines the electronic localisation in the HAT6. Combination of DOS, BG and charge population provide information to determine the mechanism of charge transfer in HAT6. Figure 3.12 shows the overall simulation flow for this exercise.

3.3.1.1. Simulation settings

The investigation of geometrical and energetic stabilities of HAT6 were investigated using the density functional spin polarized calculations and Perdew–Burke–Ernzerhof (PBE) exchange–correlation functional (B. Delley, 1990, 2000; Perdew et al., 1996), in

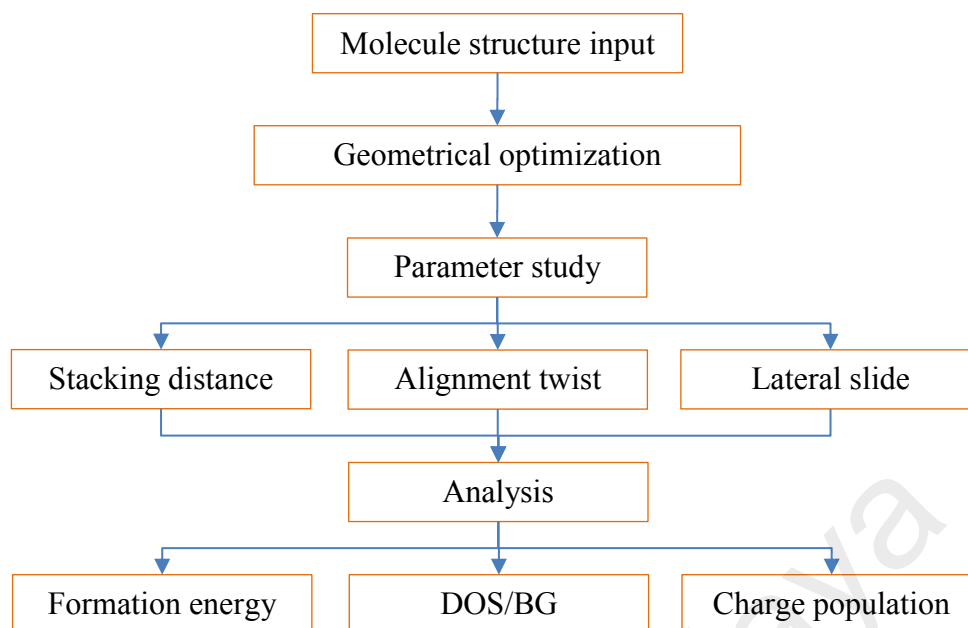


Figure 3.12. Simulation flow of structural effect study of HAT6.

which the functional provide great accuracy in wide range of system especially with well-established atoms (O, C, and H) (Toulouse, Colonna, & Savin, 2005). The Kohn–Sham equation was expanded in a double numeric quality basis set (DNP) (B Delley, 2006) with polarization functions which should provide accurate approximation until d orbital. The DFT semi-core pseudo-potentials (B. Delley, 2002) were used for the treatment of the electrons. The self-consistent-field (SCF) procedures were performed in order to achieve good convergence of geometrical and electronic structures using a convergence criterion of 10^{-6} a.u. The energy, maximum force and maximum displacement convergence were set as 10^{-5} Ha, $0.002 \text{ Ha } \text{\AA}^{-1}$ and 0.005 \AA respectively.

In all cases, the charge population employed was the Hirshfeld population analysis (Hirshfeld, 1977). Since electronic interaction only occurs at very close distance, charge transfer in dimer is enough to represent charge transferability as demonstrated earlier by Zbiri group (Zbiri et al., 2010; Zbiri et al., 2009). The settings of these calculation parameters in MS 2016 are depicted in Figure 3.13.

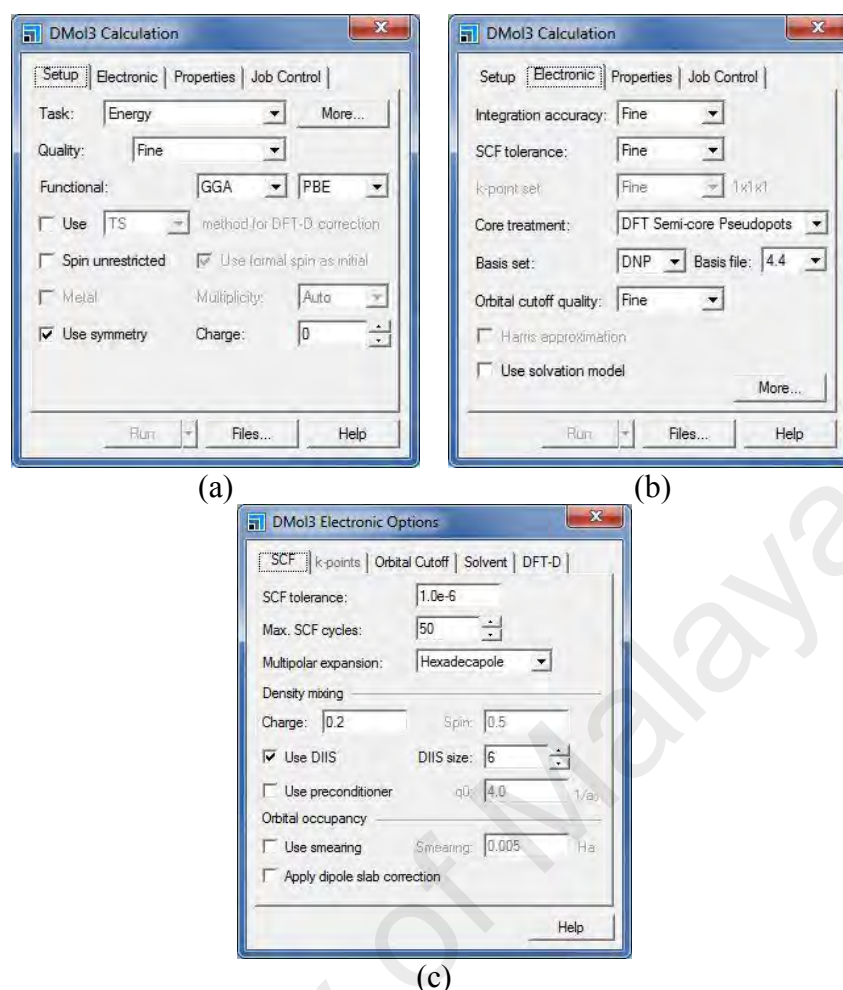


Figure 3.13. (a)HAT6 single point energy calculation setting. (b)Core electron treatment and basis set settings. (c)SCF options settings.

3.3.2. Results and Discussion

3.3.2.1. Highest Occupied Molecular Orbital (HOMO) and Lowest Unoccupied Molecular Orbital (LUMO)

A single molecule first principle DFT calculations shows that HAT6 has energy of HOMO to be -4.238 eV and LUMO -1.135 eV, which effectively creates a BG of 3.103 eV which is comparable to other literature (Zbiri et al., 2010; Zbiri et al., 2009). In Figure 3.14 (a) and (b), HOMO and LUMO extend to the oxygen bond which bridge the carbon atoms at the core to the hexaloxo end chains. Thus, the orbital is able to contribute to electronic delocalization from the core to the tails, thus creating corresponding bond order

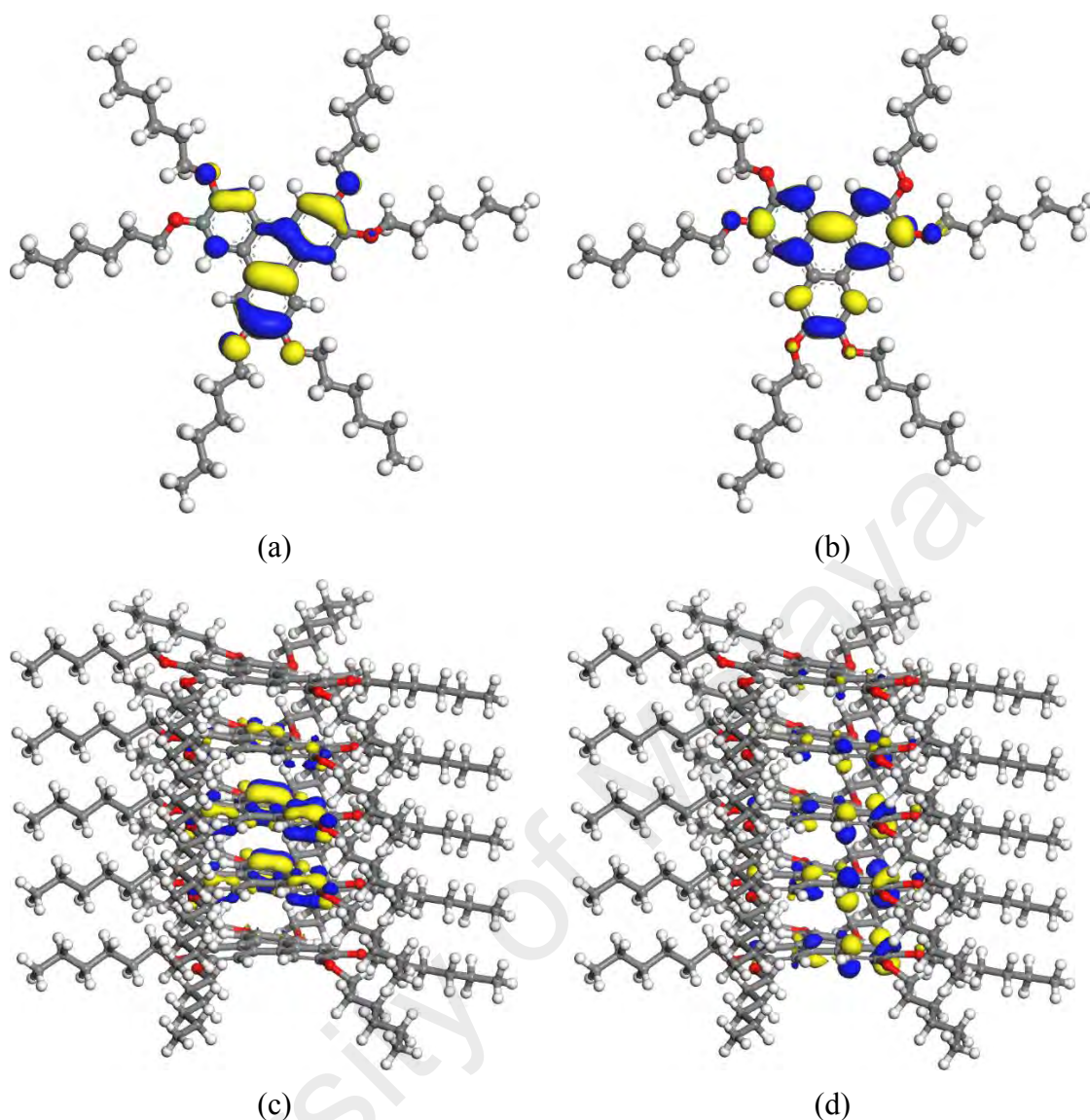


Figure 3.14. (a) HOMO and (b) LUMO of HAT6 single molecule. (c) HOMO of and (b) LUMO of HAT6 in 5 layer stacking where HOMO and LUMO are concentrated at the triphenylene core and dispersed throughout layers.

of $C_{\text{core}}\text{-O}$ and O-C_{tail} . Hence, it is suggested that the ligand plays a dual role in both mechanically stabilizing the DLC columnar structure, and conferring electronic functionality over the core to the tails (Zbiri et al., 2009).

Excitation from HOMO to LUMO yields the largest contribution, where $\sim 80\%$ of BG covered that originates from the largest oscillator strength, which is sufficient to simplify calculation in applications (Zbiri et al., 2010).

A non-periodic simulation of a 5 layers HAT6 stacked on top of each other shows that the HOMO and LUMO are concentrated at the triphenylene core of the DLC as shown in

Figure 3.14 (c) and (d). The calculated HOMO and LUMO spread out through layers are representative of valence and conduction orbital electrons which indicate the possibility of electronic jumping at π - π overlap at the triphenylene core which confirms the 1-D conduction model of DLCs along the axis of the columns.

3.3.2.2. Structural stability and band gap (BG)

In the calculations, stability of molecular conformation increases as the distance grows larger. This model shows that the conformation energy becomes constant beyond 4.0 Å. A number of past experimental was quoted that the separation of core-core to stabilise around 3.4~3.65 Å (L. A. Haverkate et al., 2012; Mulder et al., 2003; Zbiri et al., 2009). A steep energy slope at a shorter distance implies electronic repulsion between the triphenylene cores. At this distance, the π orbital overlap is higher which causes the BG to reduce. The interaction of π - π orbital overlap is important to the electronic transfer mechanism as they may propagate through the overlap, this will be elaborated further in section 3.2.7.

In general, the BG calculated is inversely proportional to stability as shown in Figure 3.15 (a). The BG is calculated to be in a range from near 0 eV to 2.45 eV, at distance of 2.8 to 5.0 Å respectively. At distances below 3.0 Å, the HAT6 is calculated to possess very little to no BG which mean in this molecular conformation at such distance, electrons from core can be excited with very little energy, as represented by a narrow BG is

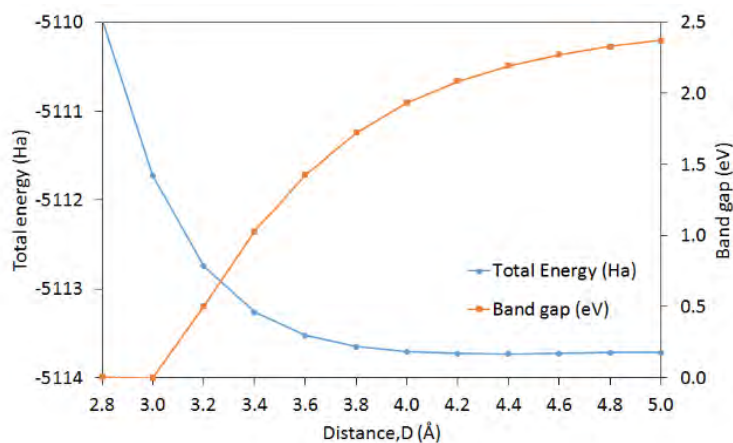


Figure 3.15. Total energy, BG in the function of core-core distance, D. θ and L are fixed at 0° and 0 Å respectively.

achieved at extremely near distance. The increase in BG as distance increase also be correlated to the CTI investigated by Zbiri et al. (2009). Their investigation of CTI as a function of D indicates that the CTI drastically decreases as a function of D, and this corresponds to observation of increasing BG as D increases.

Calculations under a variation of twist, θ , in HAT6 conformation shows the D_{3h} symmetry characteristics where a wave pattern is periodically repeated in every 120° as shown in Figure 3.16 (a). In the calculations, the most stable twist conformation is calculated to be 25° , whilst in other literature, experiments have indicated that twist have tendencies to stabilise from 34° to 38° for HAT6 (Haverkate et al., 2011) and around 36° for a comparable molecule, HAT5 (G. Cinacchi et al., 2004). However, the simulated value is quite close to other simulated HAT6 systems. For example, Haverkate et al. studied the conformation effects using models to depict the different twist angles ($\theta = 25^\circ$ and 60° , named TWIST25 and TWIST60 respectively), and the core-core distance and lateral slide (Haverkate et al., 2011). They concluded that the TWIST25 model is more ordered and mimicked the Col_h order expected in HAT6 molecule. The reason for this is that the columnar structure becomes stable when it has slight twist angle is due to the repulsion of superimposing tails, and also stabilises as it finds free space after a slight twist from core to core.

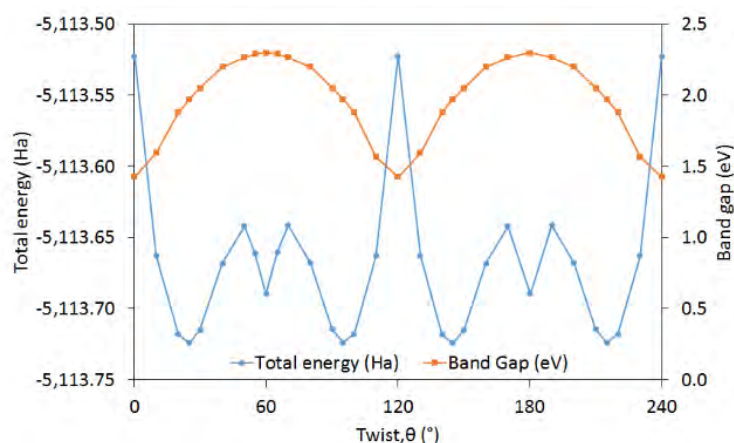


Figure 3.16. Total energy, BG in the function of molecular twist angle, θ . D and L are fixed at 3.6 \AA and 0 \AA respectively.

The BG also has 120° repeating pattern which shows the BG is also directly affected by changes of π overlap at the triphenylene core, since HOMO and LUMO are concentrated at the core. In the twist parameter, the BG changes from lowest 1.43 eV when it has no twist to 2.27 eV at 60° twist, which is the middle point of the D_{3h} symmetry. This implies that the BG relies on the whole π overlap of triphenylene core. As HAT6 is twisted, the outer benzene rings will become detached to superimposing counterparts and reduce overall overlapping of the π orbitals. In comparison to CTI calculations, BG result is opposite to the CTI where maximum BG is achieved when $\theta = 60^\circ$ when the CTI is at a minimum and vice versa as shown in Figure 3.7. Both BG and CTI shows 120° repeating cycle which strongly confirms that the charge transfer is affected by twist.

In varying lateral slide distance, there are two major minima in the conformation of the energy plot as in Figure 3.17. A global minimum is found at 3.8 Å, and one of local minimum is found at 1.5 Å. In comparison, the lateral slide was reported to distribute from 0.4 to 3.5 Å (L. A. Haverkate et al., 2012; Haverkate et al., 2011). The local minimum is contributed by the relaxation of columnar axis of atomic and electronic repulsion, followed by a local maximum that is due to adjacent atom π - π overlapping attraction forces, and also core-core and tail-tail van der Waals interactions stabilise the columnar phases. The global minimum at 3.8 Å is perhaps due to the relaxation of HAT6

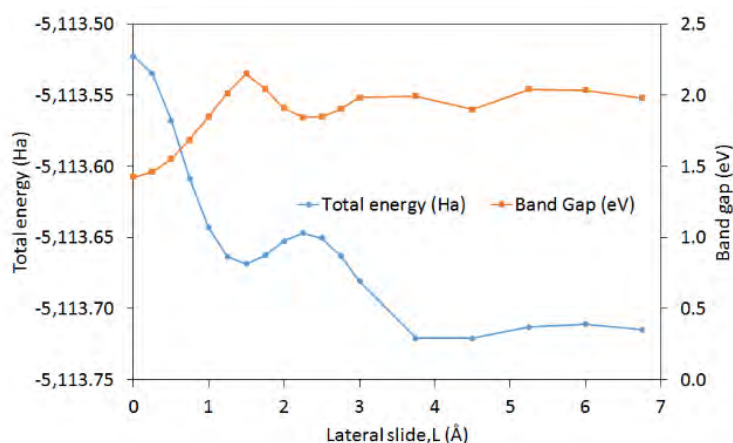


Figure 3.17. Total energy, BG in the function of molecular lateral slide, L. D and θ are fixed at 3.6 Å and 0° respectively.

molecule when it breaks away from columnar phases, until it finally achieves a relaxed state when the adjacent molecule is sufficiently far away.

The minimum BG at 1.43 eV is found when there is no lateral slide, then it increases to 2.15 eV at a lateral slide distance of 1.5 Å. At even larger distances, the BG remains around 2.0 eV. From 0 to 1.5 Å, the BG rises indicate the π overlap reduction when HAT6 molecule slides away from columnar axis. The inverse relation of BG to CTI holds true when $L < 2.0$ Å comparatively shown in Figure 3.17 and Figure 3.8, where BG increases to maximum around 1.5 Å, compared to CTI where it decreases to a local minimum at 2.0 Å. When $L > 2.0$ Å the relationship breaks down probably due to difference of the traced trajectory path. Therefore, it is convincing to say that local minimum and local maximum at 1.5 and 2.25 Å respectively are due to core-core relaxation and π overlap interaction, and after that distance, the energetic consideration are mainly due to tail interactions.

This finding is compared to the simulation work by Haverkate et al. (2011), who concluded that a significant fraction of molecules show a probabilistic distribution of lateral slide with respect to columnar axis is 2.5 Å. In addition, in a 2,4,7-trinitro-9-fluorenone (TNF) doped charge transfer complex HAT6 system the lateral slide is caused by tilted mesogens relative to column axis is $L = \sim 3.5$ Å (L. A. Haverkate et al., 2012).

3.3.2.3. Density of states (DOS)

The DOS defines the number of available states per energy. The number of electrons at each energy is obtained by multiplying the number of states available with the probability that a state is occupied by an electron. DOS is used to visualise the analysis of electronic structure by analysing the width of the valence band, energy gap in insulators, and intensity.

In DOS analysis, local DOS (LDOS) and partial DOS (PDOS) are useful tools to qualitatively analyse the electronic structure. The local DOS (LDOS) is DOS of a

selection of atom or atoms which contribute in the system electronic states to various parts of energy spectrum. In PDOS, this can be analysed further of the DOS of each orbital by resolving the contribution according to the angular momentum of the states with addition to virtual orbitals which depends on the basis set used. It can identify whether the peaks of DOS are of s, p, or d orbital character through PDOS. Combination of DOS, LDOS, and PDOS analysis give a qualitative depiction of the nature of electron hybridization in the system.

(a) DOS and PDOS vs. distance, D

From the DOS of HAT6, DOS spectrum is affected largely by varying the co-facial distance. Figure 3.18 shows the evolution of DOS spectrum when subjected to different core-core facial distance, D, in which differences can be seen to the DOS near the Fermi level (defined when energy is at 0 eV) that is directly related to BG. From the total DOS spectrum in Figure 3.18 (a), the availability of electronic states near the Fermi levels at small D can be deduced, valence orbital states move to higher energy enlarging the BG

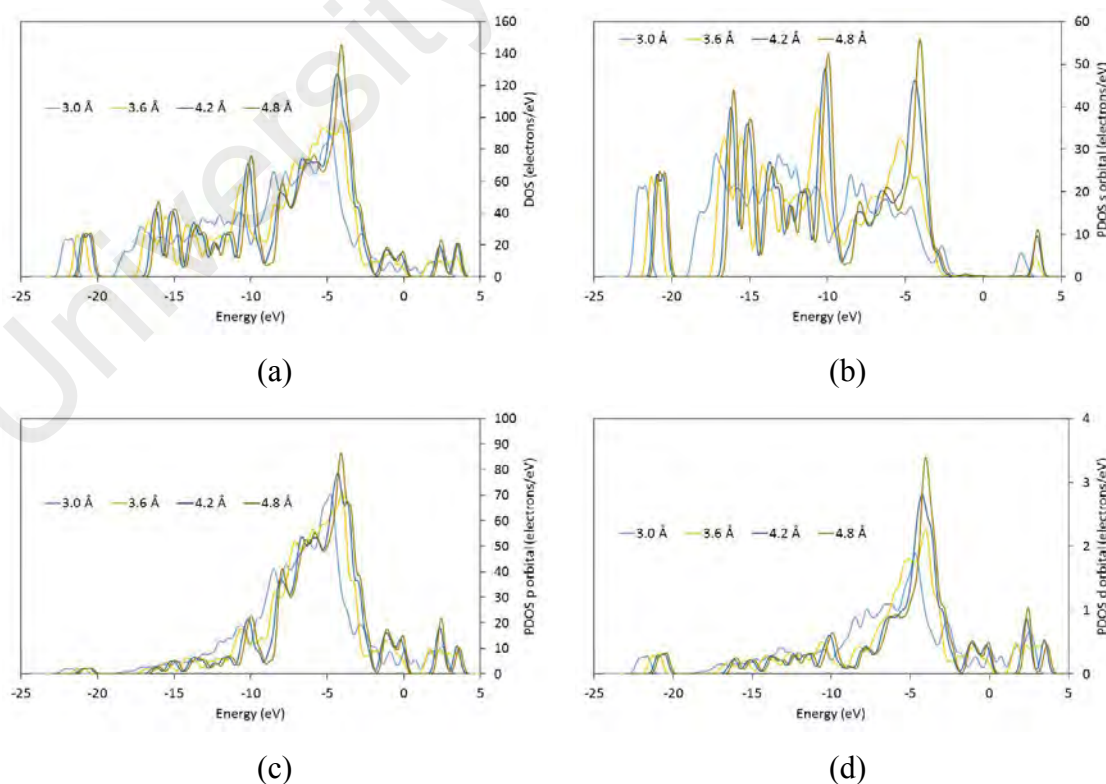


Figure 3.18. DOS of HAT6 by varying distance, D. (a) Total DOS, (b) S orbital PDOS, (c) P orbital PDOS, (d) D orbital PDOS.

at larger distance, D .

Calculation of a PDOS was also calculated to further analyse the electronic states as shown in Figure 3.18 (b), (c), and (d) which correspond to s orbital, p orbital and d orbital PDOS respectively. From the PDOS it is clearly showing that s orbital states are available in deeper energy, especially from -3 eV and below, whilst the p and d orbitals states mainly contribute to the Fermi level electronic occupation. These orbitals originated from the combination C, O and H atoms which make up the HAT6 molecule which explain the electronic occupation mostly occurs at s and p orbital, and d orbital emerged from virtual orbital in calculation. Comparing to the HOMO LUMO positions, the electrical conduction is allowed at core-core overlap where it was assumed that HOMO is the valence orbital whilst LUMO is the conduction orbital. The intensity in s orbital gradually increases as D increases which suggest localization at larger D occurs at s orbital compared to p and d orbital, as they have less changes of intensity. It is also of note that the intensity of the p orbital PDOS is higher, which implies that the probability of electron excitation coming from the p orbital is much higher than the d orbital and supports the π - π conduction.

A small BG encourages electron excitation to conduction band. This supports the first hypothesis that small co facial distance is preferred for conducting electrons.

(b) DOS, PDOS vs. twist, θ .

Variation of the θ , on the twist parameter, DOS is shown to be less responsive to changes in θ . This also correlates to minor changes in BG value when HAT6 molecules are twisted. From total DOS in Figure 3.19 (a) a shoulder of DOS in conduction orbital when θ is 0° and 10° is observed as they have narrower BG than other twist angle of 1.43 and 1.60 eV respectively.

For the twisted state, PDOS analysis indicate that the s orbital does not contribute to valence nor conduction band, whilst p and d orbitals dominate states near the Fermi level.

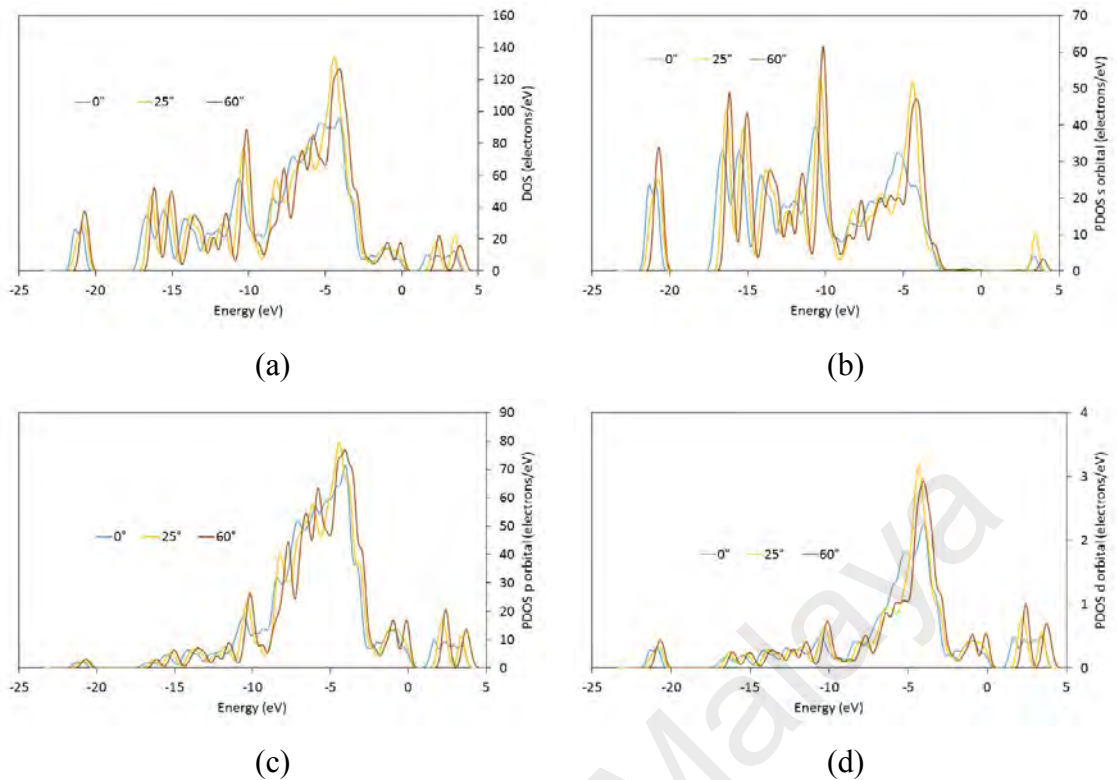


Figure 3.19. DOS of HAT6 by varying twist, θ . (a) Total DOS, (b) S orbital PDOS, (c) P orbital PDOS, (d) D orbital PDOS.

Here it is seen that a narrow BG is achieved by a shift of the conduction band to lower energy states. In a larger twist angle, it is also observed that the DOS peak becomes narrower and sharper near the Fermi level, as also observed in p and d PDOS, which reaches a maximum at 60° . Increase of intensity is due to localization of electrons as there are more states can be filled in that particular energy level. In addition, since the BG is less affected by twist, increase of electronic occupation near Fermi level make twist is more favourable in change transfer as higher electrons probabilistically occupies the valence band.

(c) DOS, PDOS vs. lateral slide, L

Similar to twist, the influence of lateral slide on the changes on the BG is also small. The difference of the maximum and minimum BG is 0.5 eV across the range of interest, and it is reflected in the DOS spectrum. In Figure 3.20, it is observed that there are no available states near the Fermi level as the BG remains wide through all L parameter.

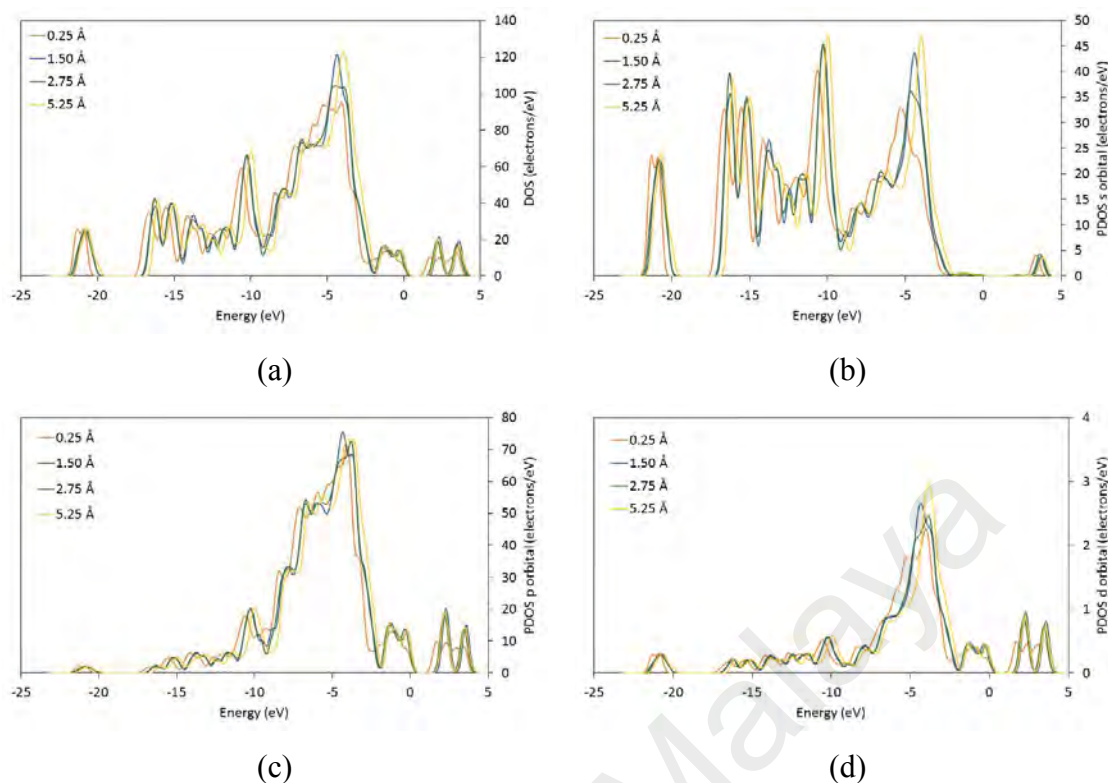


Figure 3.20. DOS of HAT6 by varying lateral slide distance, L . (a) Total DOS, (b) S orbital PDOS, (c) P orbital PDOS, (d) D orbital PDOS.

Electronic localization is observed at extremely large lateral distances, and are particularly noticeable when $L > 3.0 \text{ \AA}$, as sharp peaks develop near Fermi level. This can be seen in the total DOS spectrum as well as in p and d orbital PDOS spectra as shown in Figure 3.20 (a), (c) and (d) respectively.

It is interesting to relate these findings, that for lateral slide $> 3.0 \text{ \AA}$, that the charge transfer along the column becomes significantly hindered with respect to the simulation results on conformational studies of HAT6 column by Haverkate et al. They concluded that a significant fraction of the molecule showed a lateral slide 2.5 \AA , which will effectively disrupt the charge conduction along the column. Thus, to retain the electronic transfer capabilities, the lateral slide should be kept at least below 3.0 \AA .

Thus, whilst the determining factor for charge transfer is the core-core co-facial distance, D , with induced twist also contributing to higher occupation of the Fermi level, it appears that the capability of charge transfer in a realistic DLC column is ultimately limited by its lateral slide. Thus for better charge transfer, column rigidity is an imperative

characteristic which needs to be engineered into the molecular structure, through strategies such as cross linking of tails (Imrie & Henderson, 2007; Pisula et al., 2005; Segura et al., 2015), and also doping (Haverkate et al., 2014; L. A. Haverkate et al., 2012).

(d) Local DOS at Fermi Level

Further analysis on DOS using LDOS of atom C^1 , C^{13} , and C_{t1}^1 near Fermi level shown in Figure 3.21 (d), which represents the numbering of atoms in the core and a hexyloxy ligand. C^1 is representative of a C atom of outer ring in triphenylene core, while C^{13} is in the inner ring, and C_{t1}^1 is a C atom of a hexyloxy ligand nearest to the core after O. The study of LDOS in this section will be focused on quantifying the DOS for a carbon atom representative of the inner ring and outer ring core, against another carbon atom representative of the tail, as a function of the structural parameters (D , θ , and L).

In Figure 3.21 (a), at $D=3.0 \text{ \AA}$, the occupied electronic states are near the Fermi level. This allows electrons to transfer freely from the valence to the conduction band thus mimicking metallic behaviour. As D grows larger the BG becomes apparent and wider because of the separation of adjacent core reduces the π - π orbital overlap.

DOS peaks at the Fermi level are contributed by C^1 and C^{13} where it is supported by HOMO LUMO calculations, on the BG where it is concentrated at the core. In all conformation parameters, the intensity of C^1 is stronger than C^{13} whenever a BG is present. This suggests that, the probability of electronic occupancy is higher at outer ring C atoms compared to the inner ring C atom, thus confirming that there is a higher degree of delocalization at the core. This is also influenced by a strong electronegativity of O which located near the outer C.

The C_{t1}^1 DOS peak near Fermi level is not available in all conformations. The lack of states near the Fermi level means less probability of electronic excitation or relaxation in the tails, thus preventing electronic transfer at the tails.

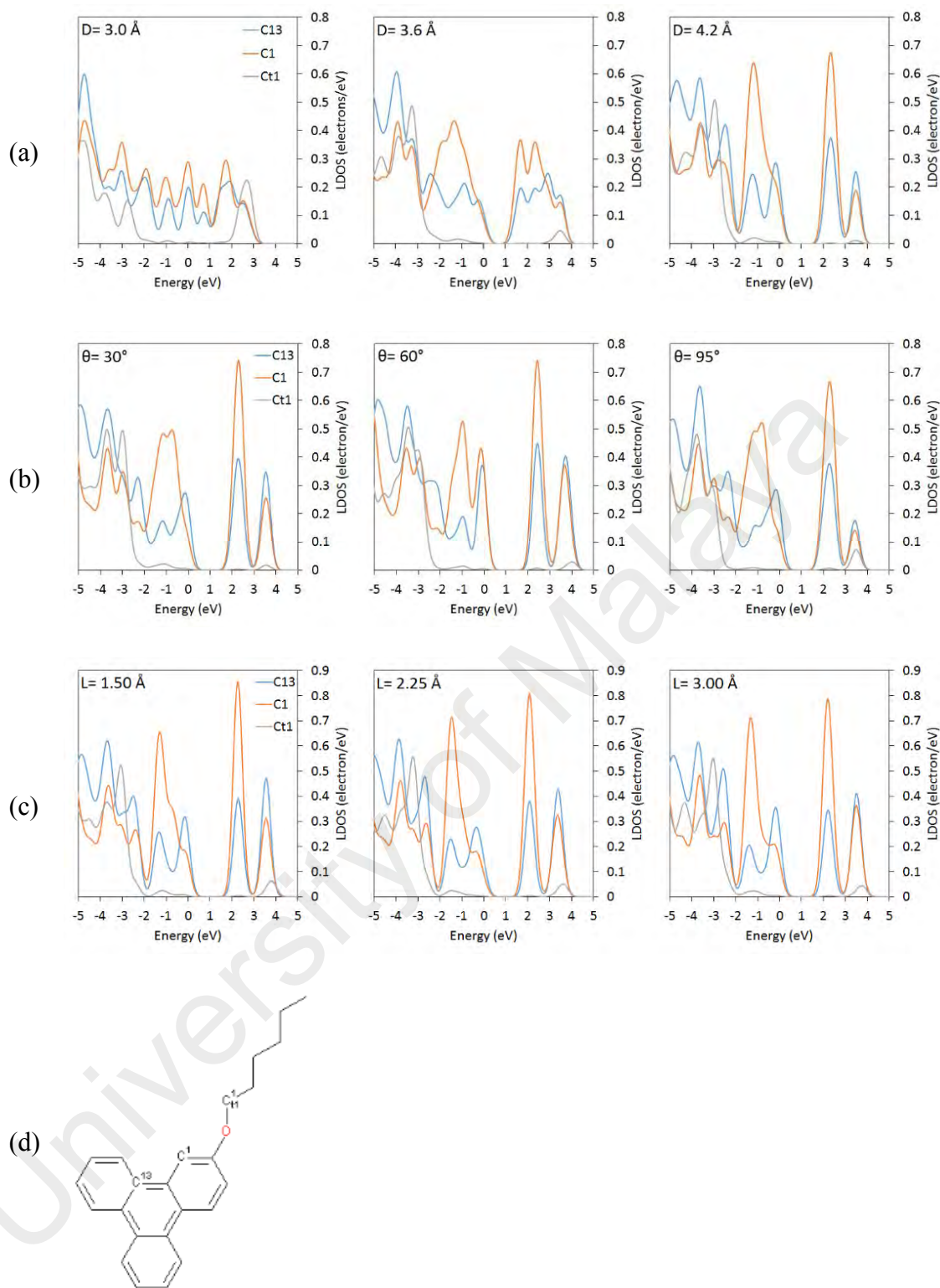


Figure 3.21. LDOS zoomed in at Fermi level. [From left] (a) LDOS of $D= 3.0, 3.6,$ and 4.2 \AA . (b) LDOS of $\theta= 20^\circ, 30^\circ,$ and 60° . (c) LDOS of $L= 0.50, 1.25,$ and 2.00 \AA . $D, \theta,$ and L are fixed at $3.6 \text{ \AA}, 0^\circ,$ and 0 \AA respectively unless specified. (d) Numbering of atom.

3.3.2.4. Population analysis

To further understand the electronic structure in columnar HAT6, Hirshfeld population analysis was performed to estimate atomic partial charge (Hirshfeld, 1977). The

population analysis is used for quantitative descriptions of charge distributions in molecules or solids as it is convenient to divide a system into well-defined sub-molecular fragments. The population analysis correlates to electronic density to an atom, where it is useful to predict which effect dominates, based on chemical understanding.

The Hirshfeld population analysis scheme has tendency to produce non-negative atoms when in the vicinity of strong electronegative atoms such as O in HAT6 compared to other schemes such as Mulliken (Saha, Roy, & Ayers, 2009). This is the reason why atoms C², C_{tl}¹ and other parts of HAT6 atoms possess a non-negative value which realistically represent changes to electron density in the frontier orbital as contributed in the Fukui function value.

(a) Charge population of varying core-core distance, D

Figure 3.22 (a) and (b) show the population of HAT6 under influence of core-core co-facial distance, D. The charge plot in Figure 3.22 (a) can be divided into 3 parts;

1. C atoms which are in the inner ring core (C¹³, C¹⁴ ... C¹⁸), which possess close to zero net charge, i.e. indicating a high degree of delocalization of the π electron in the core. The delocalised electrons are distributed intermolecularly through σ and π bond, and also intramolecularly through π overlap to the adjacent molecule.
2. C atoms in the core which are adjacent to O atom (C², C³, C⁶, C⁷, C¹⁰, C¹¹). These atoms were observed to possess an overall positive charge due to the electronegative nature of the O atom, which draw the π electrons towards itself.
3. The C atoms between the C atoms in (1) and (2), (C¹, C⁴, C⁵, C⁸, C⁹, C¹²). These were observed to be negatively charged and almost equivalent in magnitude to the C atom in (2) above. This is expected to be due to the fact that these C atoms try to balance the positive charges induced in the atoms of group (2).

When subjected to different core separation distances, D, all core C atoms are more negatively charge due to electronic localization where the BG widens as discussed

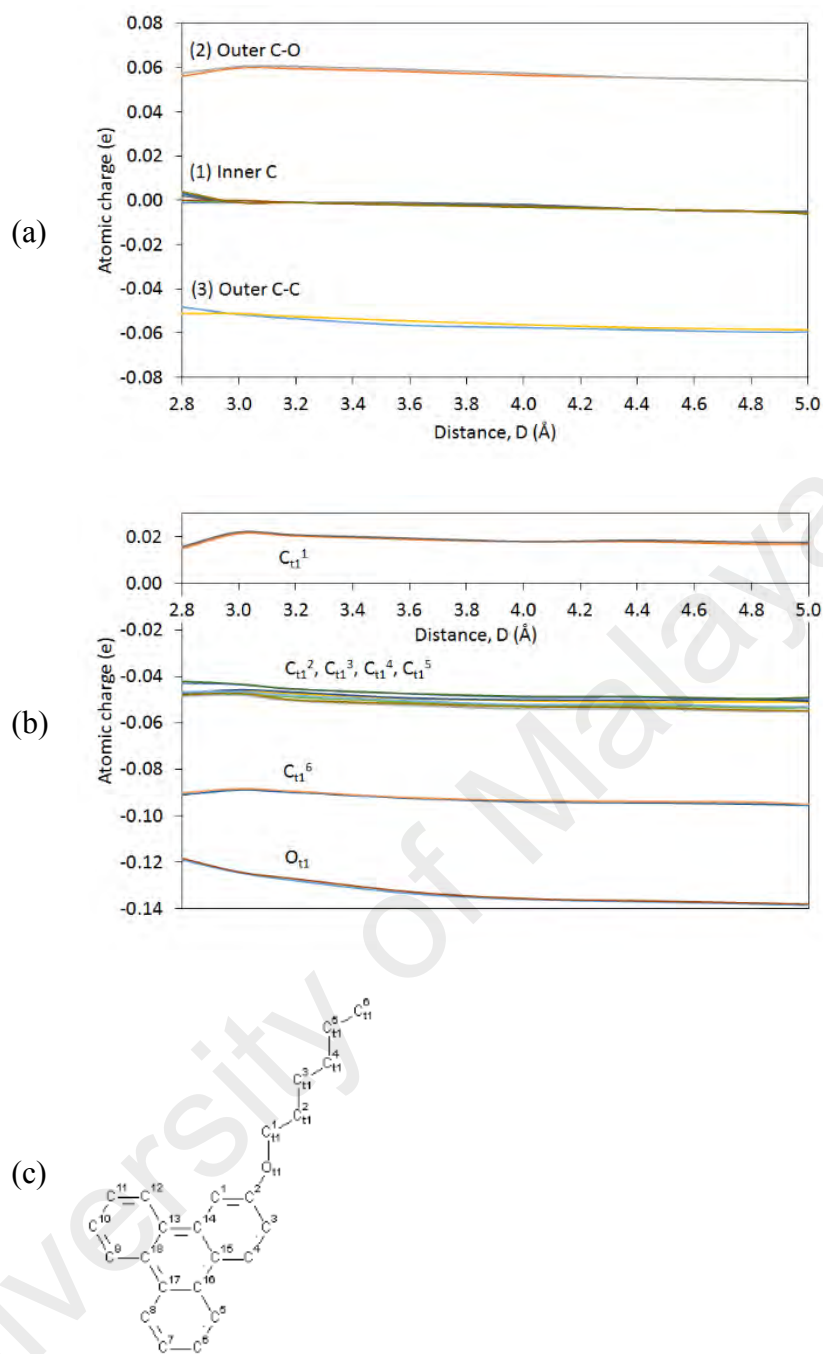


Figure 3.22. Charge population of triphenylene atoms with varied distance, D at fixed $\theta = 0^\circ$, $L = 0 \text{ \AA}$. (a) Plot for triphenylene core. (b) Plot for tail. (c) Atom numbering.

previously for the DOS plot. This prevents electronic transfer to the adjacent molecule. The electronic localization at the outer ring of the core helps to stabilise the columnar phases in HAT6.

Figure 3.22 (b) shows the population of atoms at the hexyloxy tail under variation of the D parameter. All atoms are negatively charged except C_{t1}^1 which is bonded to an O atom.

The O atom also has the highest absolute magnitude of charge in HAT6 where its electronegative nature attracts electrons from adjacent atoms in the core (e.g. C2, C3) and tail section (C_{t1}^1). As D increases, all atoms become more negatively charged except C_{t1}^1 which become more positively charged as O attracts more electrons from C_{t1}^1 . It was also observed that the electron-withdrawing behaviour of O predominantly attract electrons from the core compared to the tail, for example, the magnitude of electron population for C3 is almost three times higher than C_{t1}^1 .

(b) Charge population of varying twist, θ

In variation of the twist parameter, θ , the charge population is shown in Figure 3.23 (a) for core atoms. Taking the 0° degree angle as reference, as the twist angle θ becomes larger, the charge population traces an almost sinusoidal pattern until 120° which completes the D_{3h} symmetry. Again, the results of the electronic population can be grouped into three regions;

1. C atoms of the inner ring in the central core ($C^{13}, C^{14} \dots C^{18}$). Electronic delocalisation occurs at 0° , upon twisting they experience a maximum localisation of their electrons at 30° , then reduces to delocalisation again at 60° . This pattern repeats itself until 120° , but this time with delocalisation of its holes (nett charge is positive).
2. The core C atoms adjacent to the O atom ($C^2, C^3, C^6, C^7, C^{10}, C^{11}$) undergo a more distinct delocalisation pattern compared to the core C atom in (1). These atoms such as C^2 and C^3 possess an overall positive charge due to its proximity to the electronegative O atom as discussed in the case for the core-core distance previously described. It is also interesting to note that the minima for delocalisation of C^2 and C^3 is asymmetric due to the off-centre position of these atoms with respect to the central axis of twist at the centre of the core. It is expected that the nett of twisting results in an overall chiral column, despite the fact that the HAT6 molecule itself is achiral.

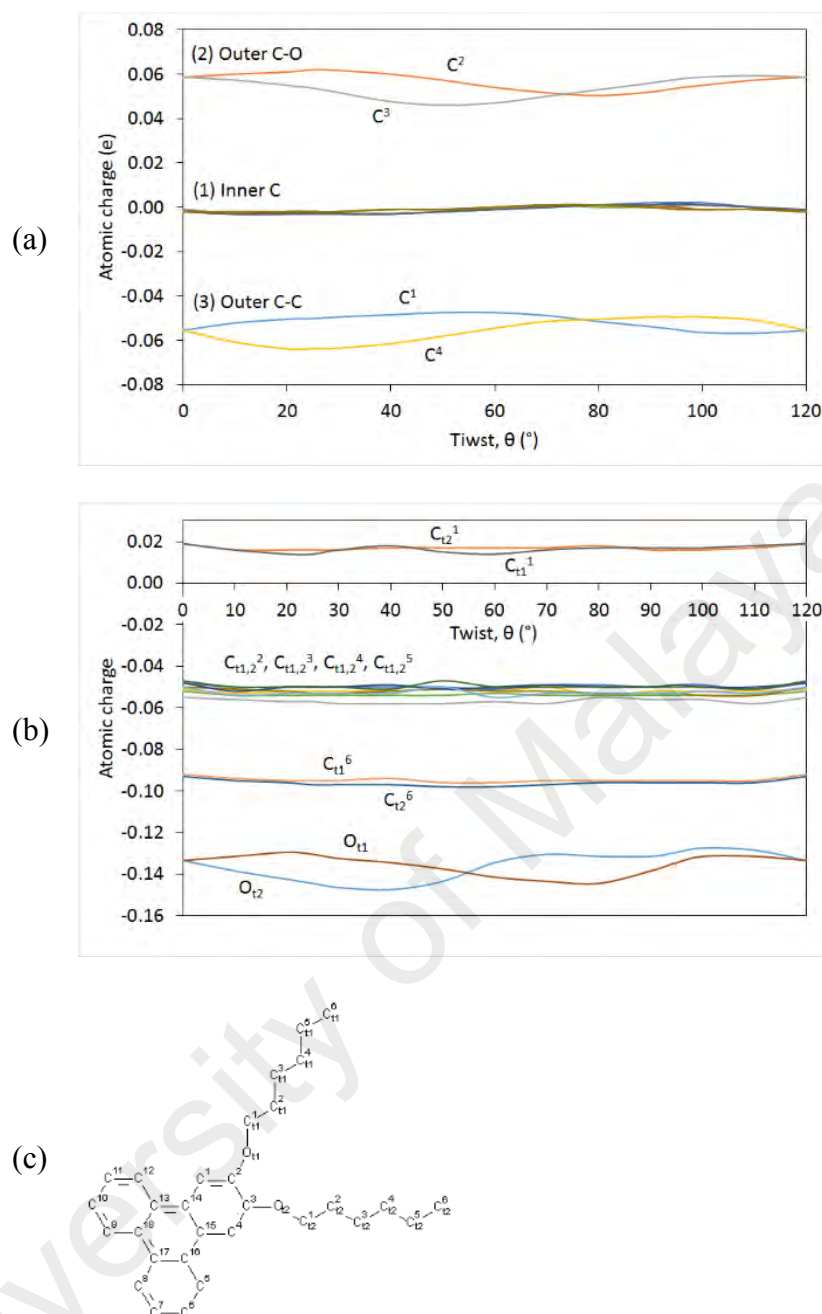


Figure 3.23. Charge population of triphenylene carbon atoms with varied twist, θ at $D= 3.60 \text{ \AA}$, $L= 0 \text{ \AA}$. (a) Plot for triphenylene core. (b) Plot for tail. (c) Atom numbering.

- The group of C atoms between (1) and (2) are approximately equal in magnitude and negative in order to balance the charge distribution in (2).

It is also interesting to observe the electron withdrawing nature of the O atoms (e.g. O₁, O₂) in relation to its adjacent C atom on the inner ring and outer ligand as in Figure 3.23 (b). There is a strong fluctuation of the core C atoms delocalisation as described in (2), and this is even more even more distinct when compared against the charge fluctuation of C_{t1}¹, which remain reasonably constant. Thus, it is concluded that the effect

of electron donating from core to the O atom is more dominant upon twisting, compared to core-core co-facial distance.

Figure 3.23 (b) shows the charge population at tails under twist. The figure traces charge population of two hexyloxy tails, namely ligand 1 and its next tail, ligand 2 as seen in (c). Here, almost sinusoidal charge of two O atoms in adjacent ligand in (b) is observed, where they trace charge fluctuation with difference phase, then reflected to group (2) and (3) as discussed above. Overall C atoms charge fluctuation is minor in tails, since there are no π orbital overlap exist in the tail section.

(c) Charge population of varying lateral slide distance, L

In Figure 3.24 (a) and (b) charge population against lateral slide L are shown. There is no systematic correlation between charge population changes trend against L. This is due to a large number of overlapping factors, such as electronegativity of neighbouring atom, type of nearby orbital, and breaking of the columnar phase. Following above flow, the triphenylene C core atoms is categorised into three group;

1. The inner ring C atoms (C^{13} , C^{14} ... C^{18}) possess charge fluctuation near zero as L progresses. There are several factors which influence the charge fluctuation, however on one note that charge population of C^{14} is greatly influenced by bypassing other HAT6 molecule O atom starting from 2.75 Å and retain its charge positive as seen in Figure 3.24 (a).
2. The outer ring C atoms adjacent to the O atom (C^2 , C^3 , C^6 , C^7 , C^{10} , C^{11}) begin with the same degree of charge delocalisation at $L=0$ Å, but as L increases, the charge diverges indicating electronic localisation and delocalisation occurs at the same time at different C atoms.
3. Similarly, the C atoms between (1) and (2) followed trends in (2) where the charge is same initially and diverged as L progresses.

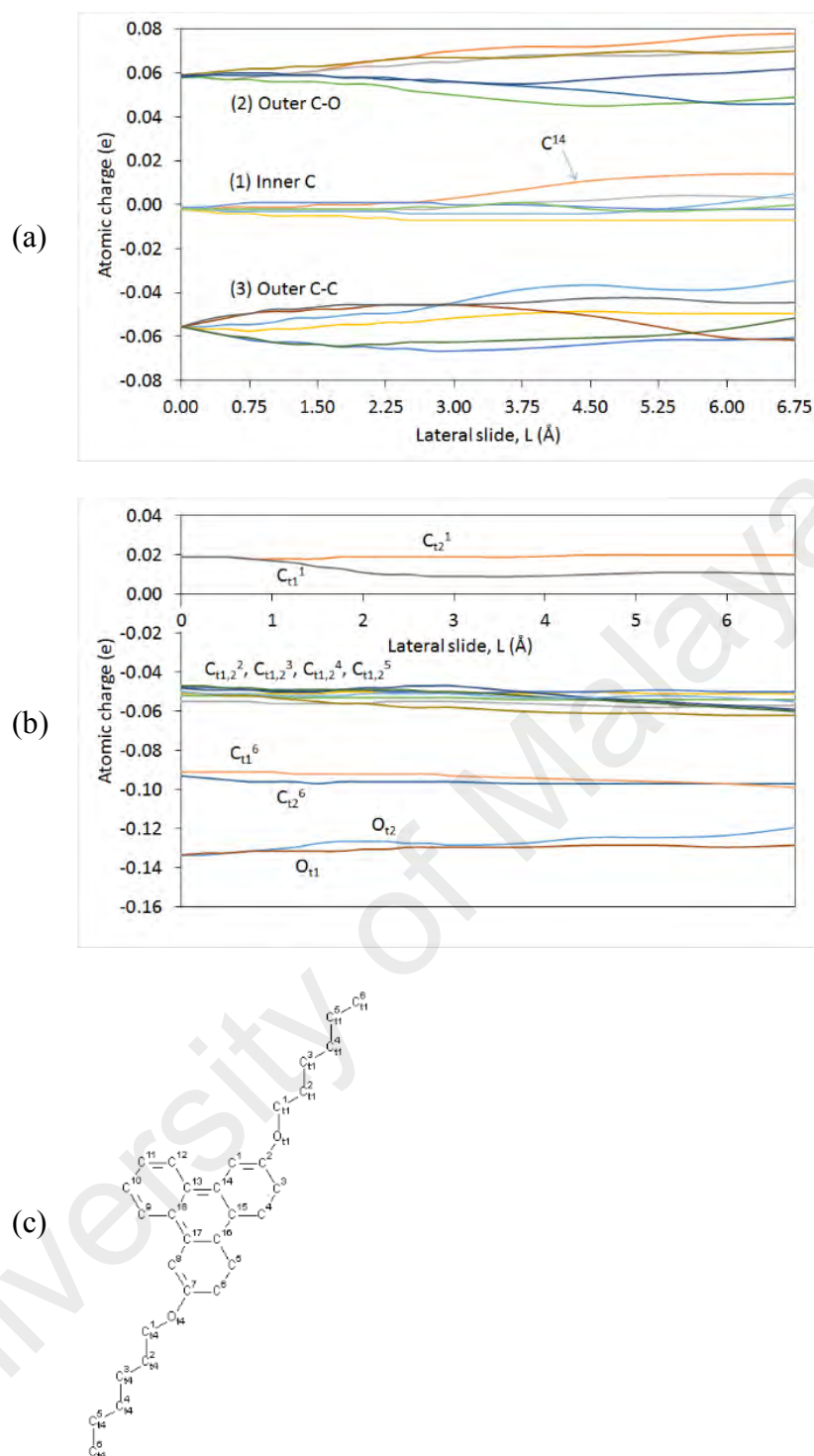


Figure 3.24. Charge population of triphenylene carbon atoms with varied lateral slide distance, L at $D = 3.60 \text{ \AA}$, $\theta = 0^\circ$. (a) Plot for triphenylene core. (b) Plot for tail. (c) Atom numbering.

Figure 3.24 (b) depicts two different tail regions. The C atoms at the ligand end like C_{t1}^6 and C_{t2}^6 are more negative as L progresses, they break the columnar phase and become electronically localised. Both tracked O atoms reduce their charges against L, this is caused by the electronic localization on many atoms has caused reduction of

electron withdrawal of nearby atoms. Comparing Figure 3.24 (a) and (b), charge changes at the core section is less correlated to that of tail section.

3.3.2.5. Electronic density mapping

In the previous section, charge population was calculated using the Hirshfeld scheme which is responsive to electronic small changes in the frontier orbitals. Electronic density mapping can visualise the occupation in this orbital.

To support electronic charge study, the plotted electronic density morphology is as shown in Figure 3.25. Quantitatively from the morphology, denser electronic structure near the core is observed because of the excess electrons from the double bonds. In Figure 3.25 (a), (b), (c) reduction of electronic density as the core-core distance, D , is increased, indicating that less electronic occupation at those distances.

However, in Figure 3.25 (d) and (e), which depict the density mapping as a function of twist at $\theta = 30^\circ$ and 60° respectively, the core electronic density remains constant which indicate insignificant changes during parameter change. This correlates to BG and charge population which is not as strongly coupled to twist, θ , compared to the core-core distances, D .

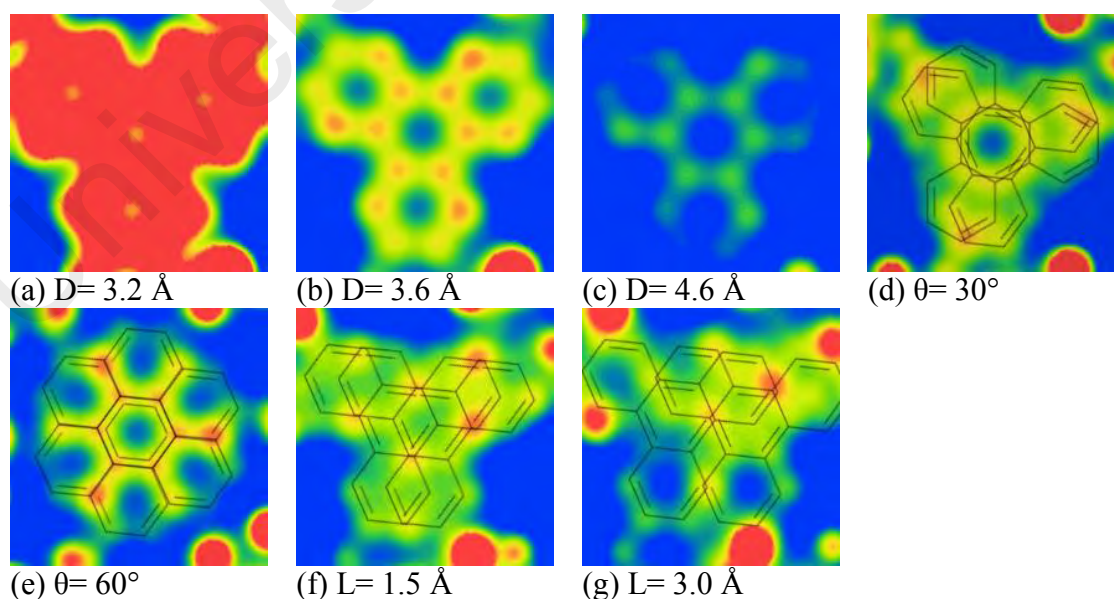


Figure 3.25. Representation of electronic density mapping of HAT6 at core section where slice is taken at midpoint of co-facial distance. Maximum (red) mapping is set at $0.1 \text{ e}/\text{\AA}^3$ and minimum (blue) is $0 \text{ e}/\text{\AA}^3$. The parameter is fixed at $D=3.6 \text{ \AA}$, $\theta=0^\circ$, and $L=0 \text{ \AA}$ unless specified otherwise. Line drawings are guide for the eye. (a) $D=3.2 \text{ \AA}$, (b) $D=3.6 \text{ \AA}$, (c) $D=4.6 \text{ \AA}$, (d) $\theta=30^\circ$, (e) $\theta=60^\circ$, (f) $L=1.5 \text{ \AA}$, (g) $L=3.0 \text{ \AA}$.

Lateral slide electronic density mapping is shown in Figure 3.25 (f) and (g) for $L= 1.5$ and 3.0 \AA respectively. In these mapping, a partial reduction of electronic density is observed. Partial reduction is caused by the reduction of π orbital overlap at core, thus eliminating the π - π bridge and forbid electronic occupations at that state.

This is consistent with population finding where a significant change is observed in D variation in comparison to other parameters.

From the findings above, the electronic properties of columnar HAT6 are studied as a function of three parameters (core-core distance, twist and lateral slide). The electronic population against core-core distance has linear changes as the distance increased, whilst it is periodically changes as twist angle increased. In lateral slide, the changes is not systematic due to interference of neighbouring molecules. The electronic conduction of HAT6 is influenced by the electronic band structure and occupation. The BG calculated from band structure determine how easy of electrons to jump into conduction bands, and electronic occupation at each atom influence the probability of electrons into the conduction band.

In the function of core-core distance, the BG is increased as the distance increased, whilst the population decreased as the distance increased. Thus, the maximum conduction is when the distance is minimum.

In twist, the changes of BG is small. The electronic occupation is increased as twist angle increased until 60° . However the conduction in variation of twist is not only influenced by BG and occupation but with addition of how much of π - π overlap. This can be seen in the electronic mapping where high occupation is at 0° and 60° , while low occupation when the overlap is not aligned. Thus, higher conduction is found at 0° and 60° .

It is very hard to trace the relationship of electronic properties and lateral slide due to interference of adjacent molecules. The trace is only up to 1.5 \AA of slide; where the BG

increased as the slide increased, and no significant changes to the Fermi level occupation. Therefore, the maximum conduction is when there is no slide.

3.4. Summary

A theoretical approach based on first principle calculations provides useful information for rational design of future any discotic molecules with promising high charge carrier mobilities. Such a modelling approach is useful since it is difficult to directly assess the molecular conformation parameters that governs charge transport directly from a molecular structure.

From this work, the following key understanding of the correlation between structure and electronic properties of the DLC molecule was obtained:

1. The stacking parameter of HAT6 which allow maximum electronic transfer are close co-facial distance, no twist, and no lateral slide as these will encourage π - π stacking thus easily allow electronic transfer through π orbital overlap.
2. The dominant limiting charge transfer factors are the core- core co-facial distance as it will exponentially increase electronic intermolecular delocalization at close distance and to large lateral slide in a realistic DLC column that will cause breaking of π - π overlap.
3. Stability of columnar phase in HAT6 have an inverse relation where maximum electronic transfer ability will cause the structure to become unstable and vice versa. This is due to atomic and electronic repulsion when they are closer. To overcome this problem, structural modification such as cross linking to tails section where there is less contribution to electronic transfer but will retain columnar structure through van der Waals interactions is suggested.
4. The naturally occurring twist in HAT6 column is intrinsically beneficial for tuning the BG. There are more electrons occupation allowed near Fermi level without

significant changes of BG, as supported by PDOS analysis and electronic population.

5. The twisting of the HAT6 in column resulted the molecule developing chiral characteristics, where it is found that the charge distribution in the molecule is asymmetric due to strong electronegativity of the O atom in the off-centre position. This naturally caused the electrons to localise and delocalise simultaneously at different parts of the molecules, which results in a symmetry breaking of charge distribution in the bulk DLC system.

From the key findings stated above, columnar conformation for the optimal charge transfer for HAT6 should be minimal core-core co-facial distance to retain the π - π overlap, a slight twist to encourage electronic occupation near Fermi level which can be achieved by natural core-core twist, and lateral slide is retained to below 3.0 Å. Such information will be useful for rational design of future DLC molecules for electronic applications.

CHAPTER 4: PROTIC IONIC LIQUID THERMODYNAMIC SIMULATION IN PERSPECTIVE OF THERMOELECTRIC APPLICATIONS

4.1. Introduction of Ionic Liquids

The ionic liquids (IL) are salts with melting points generally below 100 °C and structured in three dimensional networks of ions (anions and cations). This definition is very vague as it does not determine the materials involved but only based on its melting point and in form of ionic states. One of the common features of ILs are they have a very large melting and boiling point temperature difference, meaning they would stay in liquid state in a wide range of temperature compared to most molecular solvents making them a useful solvent. Since ILs are in ionic form, a room temperature IL particularly has very strong ion-ion interactions.

Historically, the use of *N*-butylpyridinium and 1-ethyl-3-methylimidazolium (EMIM)-containing ionic liquids can be traced to the work of J. S. Wilkes et al. (1982) as liquid electrolytes in electrochemical studies. The *N*-butylpyridinium and EMIM cations strongly influenced the choice of ILs for subsequent research (Hussey, 1983) and also the vast majority of work published on room-temperature ILs to date (Abate et al., 2012; Mousavi et al., 2016; Yaghini, Nordstierna, & Martinelli, 2014).

In addition to pyridinium and imidazolium systems, there are also ILs that contain quaternary ammonium, phosphonium, pyrrolidinium, and sulfonium cations combined with various anions as shown as examples in Figure 4.1. The applications of ILs in electrochemistry that used these classes of organic cations have been reported (Abdullah, Mohd Said, et al., 2015; Mousavi et al., 2016), and the synthesis is documented by Wasserscheid's group (Wasserscheid & Keim, 2000).

The wide liquid ranges exhibited by ILs, combined with low melting points, and the potential for tailoring size, shape and functionality offer opportunities for control in chemical reactivity is unobtainable with regular solvents. Many ILs particularly of those

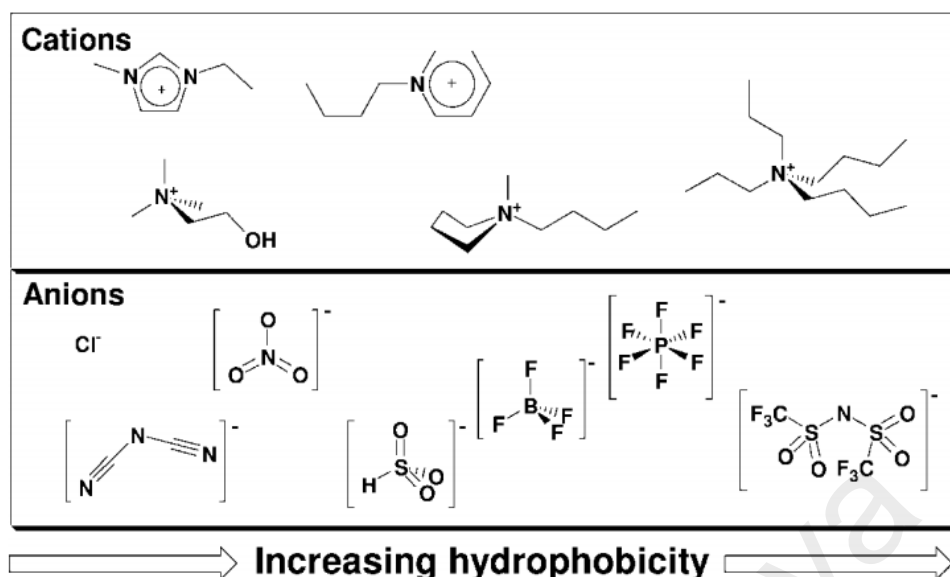


Figure 4.1. Examples of common cation and anion pairs used in the formation of ILs, and general progression of changes in IL properties with anion type.

quaternary ammonium, phosphonium, and related are being widely reinvestigated as the best IL choice for various applications, especially in synthetic chemistry (Abdallah et al., 2000; MacFarlane et al., 1999).

In addition, intrinsic property of ILs are ionic characteristic in liquid form which has open new field relating to electrochemical applications such as electrolytes (Belieres, Gervasio, & Angell, 2006), phase transfer reagents (Albanese et al., 1999), surfactants (Blackmore & Tiddy, 1988), and fungicides and biocides (Buseti et al., 2010) and many emerging examples of new IL materials are coming from the reinvestigation of chemical inventories in these fields.

4.2. Types of Ionic Liquids

There are three types of ILs of which is based on their composition difference, each type is suitable for specific applications as depicted in Figure 4.2. (1) Aprotic ionic liquids (AIL), which do not involve proton atom transfer in transition to ionic state, (2) protic ionic liquids (PIL); where ionic transfer includes the mobility of proton atom in reaction, and (3) zwitterionic molecules; where are dipolar molecules that have both positive and negative charge sites.

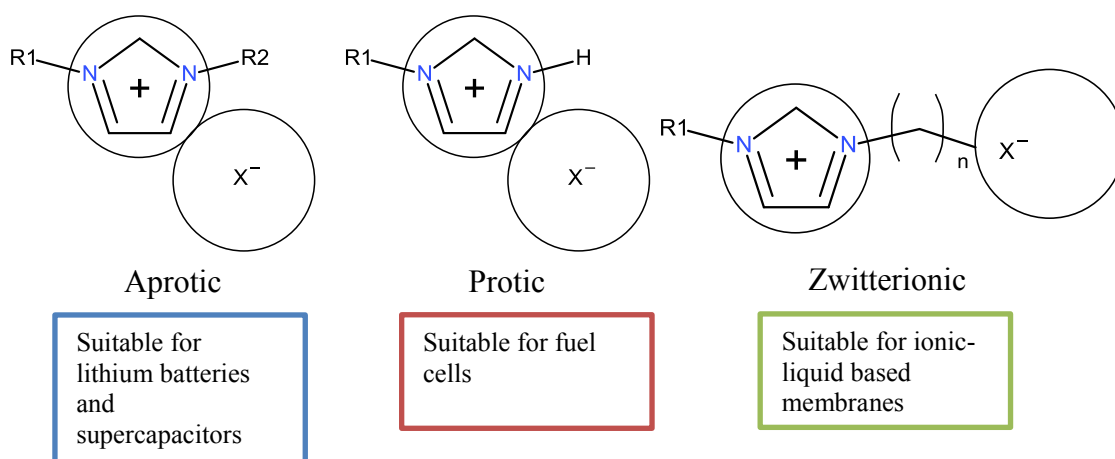


Figure 4.2. General types of IL and its applications.

4.2.1. Aprotic Ionic Liquids

AILs are suitable for lithium batteries as they do not involve proton in the reactions, as the Li ions are very reactive towards H ions. Li battery developed using AILs as electrolyte is shown to have higher safety features as it would not easily explode of exposure of H, and in addition having higher energy densities (Lewandowski & Świdarska-Mocek, 2009; Moreno et al., 2017). In addition, several other applications related to the use of AILs in battery are already explored not just as pure electrolyte, but also modification of electrolyte into gel polymer, doping and ionic binder that exploits the ILs characteristic as an ionic 3D network. There is also some prospect of supercooled ILs to promotes superfast diffusion (Eftekhari, Liu, & Chen, 2016).

4.2.2. Protic Ionic Liquids

The protic ionic liquids (PIL) are synthesised from a stoichiometric combination of a Brønsted acid to a Brønsted base reactions. The synthesis and molecular structure of PILs are discussed in detail by Tamar L. Greaves and Drummond (2008). The transferred H atom due to the acid + base neutralisation remains active in liquid phase, it can participate in the chemical reaction such as in electrochemical applications.

This has sparked researchers' interest, especially in the emerging areas of hydrogen transport and fuel cell technologies as well as in clean energy generation such as thermoelectric (Abraham, MacFarlane, & Pringle, 2013). Its main difference to the AILs

stated above is that in PILs, the free protons are available for ion transfer. The changes to ion type, substitution and composition give unique characteristics to PILs that can be explored and applied accordingly to address the applicational requirements.

PILs have drawn much attention lately as anhydrous proton conductors in hydrogen-oxygen fuel cells (Belieres et al., 2006; Xu & Angell, 2003). Xu and Angell (2003) demonstrated that the conductivities of some PILs can match those found for aqueous electrolyte solutions, which are generally assumed to provide superior electrolytic conductivity because of the unique dielectric and fluid properties of water. The high conductivities of PILs were attributed to the high fluidity and ionicity rather than the existence of the Grotthus mechanism (C. Zhao et al., 2008).

The concept of PILs may, therefore, be used with compatible polymers for the construction of solid-state proton conductors, (Noda & Watanabe, 2000) and furthermore, an acidic site and/or a basic site can be affixed to a polymer backbone. PILs derived from a simple combination of a wide variety of organic amines with bis(trifluoromethanesulfonyl) amide are found to be electroactive for H₂ oxidation and O₂ reduction at a Pt electrode under nonhumidifying conditions. The most promising is application in fuel cells where under non-humid condition the fuel cell may operate at temperature above 100 °C (Susan et al., 2003). This also provide a firm underpinning for further development. In addition, development of fundamental, molecular-based descriptions and models, will aid in tuning the PILs to desirable chemistry for potential application in multidisciplinary areas.

4.2.3. Zwitterion

Zwitterions are another type of IL in which both cation and anion are covalently bonded in a single molecule. It is also known as 'inner salts'. The fact that both positively charged cations and negatively charged anions are coexisting in a single molecule, the whole molecule itself has zero nett charge. Compared to other ILs, the zwitterions have

very little ionic migration, under the influence of a potential gradient. Due to this characteristic, liquid zwitterions at room temperature as well as polymer of zwitterions open a wide range of applications especially in electrochemistry as it can be used as solvent without diffusion under direct current condition (Ohno, 2006).

Thus, as illustrated above, ILs possess large potential of tunability through variation in structure and composition of both the anions and cations, which can be exploited in a large range of potential application.

4.3. Physicochemical Properties of Ionic Liquids

The usefulness of ILs has sparked the interest of researchers, where the application of ILs are highly tunable based on its molecular design which determine the physical, chemical and physicochemical properties. Properties of various ILs have been reported by J. Wilkes (2004) with emphasise on physical properties and, Hallett and Welton (2011) which have provided a review on chemical reactions involving ILs.

The ILs are generally more dense than water, and more viscous than typical solvents. The range of viscosities vary across < 10 to > 1000 mPa·s at room temperature, and most ILs follow an extended Arrhenius Vogel-Fulcher-Tammann (VFT) viscosity model which is temperature dependent (Ghatee et al., 2010). Thermal stability of ILs are usually very high with decomposition temperature up above 400°C (Chiappe & Pieraccini, 2005), along with low melting temperature ($< 100^{\circ}\text{C}$ for room temperature ILs), negligible vapor pressure at room temperature and wide liquidus range (glass transition temperature of ILs range from $-110 < T_g < -50^{\circ}\text{C}$ (Wishart, 2009)). Thus, they usually do not pose a problem when used as a solvent for a chemical reactions, and are thus favourable in wide range of applications as long as they do not directly react with the starting materials. From the refractive index of ILs, they are mostly considered to be moderately polar compared to conventional solvents. Substitution to a longer alkyl group increases the refractive index,

furthermore substitution with stronger polar groups such as hydroxyl will increase it significantly (T. L. Greaves et al., 2006).

The ionic conductivity of ILs is dependent on the mobility of its ions, where it is dependent to the number of charge carriers and viscosity, and is inherently dependent on the size of ionic molecules, molecular weight, and density. It is showed that ILs especially the ones with small molecules and viscous PILs such as ethylammonium nitrate and dimethylammonium difluorides exhibit relatively high ionic conductivity (> 150 mS/cm at room temperature) (Xu & Angell, 2003).

In addition, some AILs were found to have antielectrostatic properties, the antielectrostatic effect in ILs may be useful for electrolyte applications where the electrostatic effect may damages electronic function in device (Pernak, Czepukowicz, & Poźniak, 2001).

4.4. Application of Ionic Liquids

ILs have been documented to have a very wide range of applications to the extent that they are called the designer solvents in green chemistry. This is due to a vast range of combinations between the cation and anion molecules which affect the physicochemical properties of ILs itself which are able to replace conventional solvents that are more volatile, toxic and thermally unstable (Hallett & Welton, 2011). The majority of applications of ILs are in the field of electrochemistry especially relating to energy (MacFarlane et al., 2014; Wishart, 2009). In addition, many researches investigations are focused towards electrochemical applications of solar cells, fuel cells, and batteries (Tsuda & Hussey, 2007).

4.4.1. Ionic Liquids in Batteries

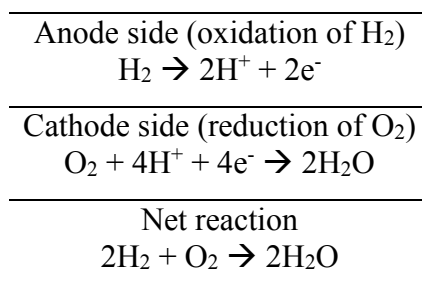
As mentioned above, one of the application examples is as the solvent in metal ion batteries, where there are used in commonly known Li based batteries (Byrne et al., 2005; Eftekhari et al., 2016; Moreno et al., 2017), to newer Na based (Ding et al., 2013; Hasa,

Passerini, & Hassoun, 2016; Mohd Noor et al., 2013) and Mg based batteries (Kakibe et al., 2010; NuLi, Yang, & Wu, 2005), and also in more advanced metal air battery designs (Endres & Zein El Abedin, 2006; J.-S. Lee et al., 2011; MacFarlane et al., 2014). The motivation using ILs as electrolyte in batteries is to overcome the limitation of conventional electrolytes (toxic, low thermal stability, volatile, electrode degradation rate, energy density, flammability) in which ILs have high conductivity, wide electrochemical window, low volatility, thermally stable at high temperatures, and less toxic.

In battery applications, the most effective strategy is to design the ILs' cation molecules to accept the metal (Li, Na, Mg) atoms, and they will function as transport carriers. Upon accepting the metal, the physicochemical properties of the ILs will change and the effort of the researches will mostly go to designing an IL to suit the operating condition in the batteries.

4.4.2. Ionic Liquids in Fuel Cells

Fuel cells are another application where ILs are extensively studied. A fuel cell is an electrical generator which uses H₂ (at anode) and O₂ (at cathode) as feed to produce electricity and produces an end product H₂O in as shown in Figure 4.3. A traditional fuel cell would require aqueous electrolyte to transport H⁺ or OH⁻ ions. This poses a problem where the aqueous electrolyte is volatile at high temperatures, reducing production. The PILs is suitable for this application as it involves proton transfer reaction in their mechanism as shown in the reaction below.



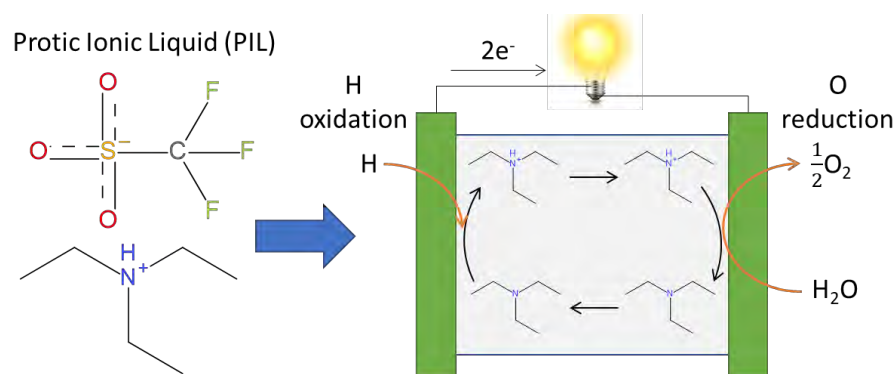


Figure 4.3. Simple schematic of fuel cells with PIL electrolyte. Insertion of H₂ gas turned into H⁺ at anode, then transferred to cathode by charge carrier PIL, in which react with O₂ gas at cathode producing electrical current and end product H₂O.

Function of PILs in a fuel cell is to transport proton from the anode side to the cathode side where it replaces conventional aqueous electrolyte which cannot operate at high temperature. PILs allow the electrolyte to be anhydrous eliminating high temperature limitation as PILs are stable in high temperatures and negligible vapor pressure is an added bonus (Belieres et al., 2006; Noda et al., 2003; Susan et al., 2003). The range of ammonium cation PILs for fuel cells were evaluated by S.-Y. Lee et al. (2010) providing potential of PILs at intermediate temperature.

Although examples stated above are mostly for intermediate and low temperature (< 100°C) applications, the use of PILs enable higher fuel cells operating temperature as the PILs have high thermal stability, thus may unlock additional potential of fuel cells of which can operate in higher temperature.

4.4.3. Ionic Liquids in Solar Cells

The ILs in solar cells applications are often used with dye-sensitised solar cells (DSSC). DSSC is a photo-electrochemical device which turns light energy into electricity like a conventional semiconductor solar cells, but due to organic based design and thin film construction, it is significantly cheaper to produce and yields better efficiency in low light conditions (O'Regan & Grätzel, 1991). In the DSSC, an organic dye which is absorbed onto a semiconductor such as TiO₂ captures a photon to an excited state, then injects an electron into the TiO₂ semiconductor. Then, the oxidised dye is reduced by

charge carrier (such as iodide) within the electrolyte creating oxidised carrier which acts as ‘hole’ in a semiconductor. Recombination of electron and oxidised carrier at counter electrode completes the circuit as shown in Figure 4.4.

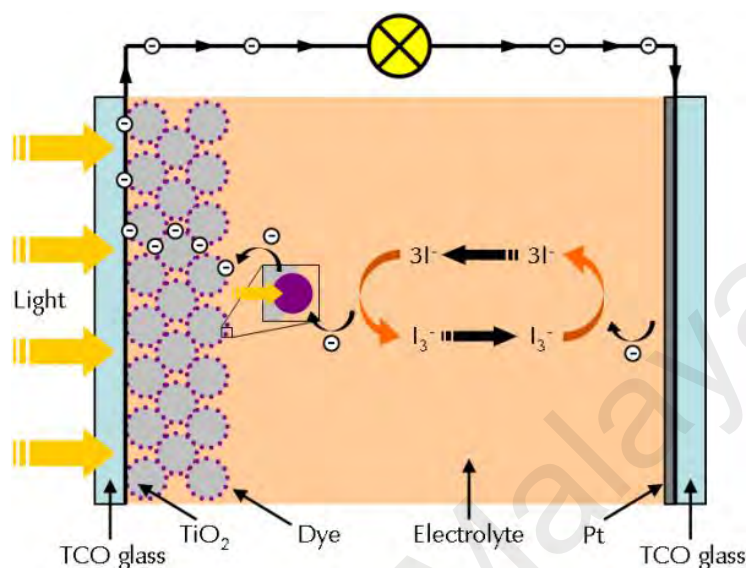


Figure 4.4. Simple schematic of DSSC. Dye absorb incoming light to an excited state, which then releases electron into semiconductor through reduction by charge carrier. The oxidised charge carrier recombined with electron at counter electrode to complete the circuit.

The motivation of using ILs in DSSC is the use of non-volatile electrolytes to develop longer lasting devices as repeated exposure to solar heating reduces the capability of DSSC as volatility of conventional electrolytes is a significant issue. Generally, ILs used in DSSC applications use low viscosity ILs to improve the diffusion rate of redox couples (Pringle & Armel, 2011). It should also be noted that ILs enhanced conductivity is due to small molecule size and low viscosity (Jarosik et al., 2006; Stoppa et al., 2010).

In addition, improvement of DSSCs can also be through changes of the redox couple, for example, the efficiency of DSSC using the ILs electrolyte is around 8% (Yu Bai et al., 2008; Y. Bai et al., 2011) with iodide-triiodide redox couple which is slightly lower than in conventional electrolyte highest at 12.3% (Yella et al., 2011) with a Co redox couple. Using modified ILs that accept Co redox couple as molecular spacer, it allow DSSC to reproduce similar efficiency (Yella et al., 2014). This highlights many ways of DSSC can be improved through ILs modifications.

4.4.4. Ionic Liquids in Thermoelectric Generator

The thermoelectric (TE) device is a device that directly convert thermal energy into usable electrical energy which enable repurposing thermal waste such as that from automobile engine heat into useful electric energy. In the TE, there is a sub category called thermoelectrochemical (TEC) cells. The TEC application concept is quite similar to DSSC where instead of photons, heat is the energy source to which causes oxidation of the redox couple at the hot electrode and then recombine again (reduction) at the cold electrode. This ionic transport and redox reaction is enable through the IL's ionic conductivity as shown in Figure 4.5 using the $[\text{Fe}(\text{CN})_6]^{3/4}$ redox couple as example (Abraham, MacFarlane, & Pringle, 2011).

The potential of TEC cells is dependent on temperature which is associated with the difference of reaction entropy of the redox couple. The electrical potential of TEC cells is defined as Seebeck coefficient, S_e which is generated through a temperature difference as in the first term in equation (4.1), that is associated with entropy difference, ΔS at the electrodes.

$$S_e = \frac{\delta E(T)}{\delta T} = \frac{\Delta S}{nF} \quad (4.1)$$

where n is the number of electron involved in redox reaction, and F is Faraday constant.

In the example mentioned above, the entropy difference, ΔS is correlated to the structural

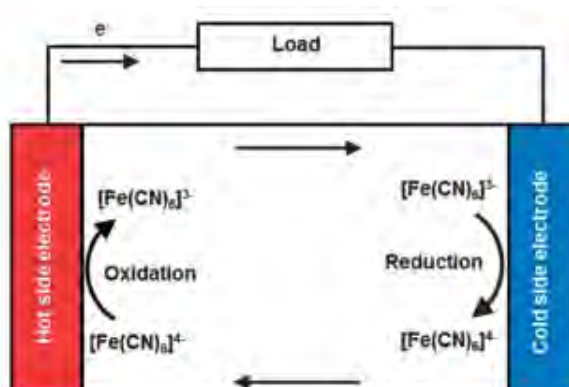


Figure 4.5. Simple schematic of TEC cells. Example $[\text{Fe}(\text{CN})_6]^{3/4}$ redox couple is oxidised at hot electrode injecting electron into electrode, then the $[\text{Fe}(\text{CN})_6]^{3-}$ is reduced at cold electrode through electron recombination.

changes of redox couple and surrounding solvent, however the ΔS can be associated toward the reaction entropy of both electrodes.

The motivation of using ILs in a TEC cell is to overcome the limitation of aqueous electrolyte for redox couple transport. The aqueous electrolyte used in conventional TEC cell design limits the TEC cells to operate $<100^\circ\text{C}$, thus limiting the range of applications. The substitution of conventional electrolytes with ILs will enable the TEC cells to have longer operation life time, due to its negligible vapour pressure and low volatility of ILs (MacFarlane et al., 2014). The strategy to improve the TEC cell using ILs is finding the ILs influences to the reaction entropy for different redox couple to obtain the possible highest entropy difference. Amongst the redox couples studied is $[\text{Fe}(\text{CN})_6]^{3-}/[\text{Fe}(\text{CN})_6]^{4-}$ shows the highest S_e at -1.49 mV/K, while $[\text{Fe}(\text{bpy})_3]^{3+}/[\text{Fe}(\text{bpy})_3]^{2+}$ and $[\text{Cr}(\text{bpy})_3]^{3+}/[\text{Cr}(\text{bpy})_3]^{2+}$ (bpy= 2,2' bipyridine) are both around 0.4 mV/K (Migita et al., 2009).

In addition, another useful property of ILs is its low thermal conductivity compared to water (e.g. [1-ethyl-3-methylimidazolium][BF₄] = 0.2 W/mK vs. water = 0.6 W/mK). In a TEC cells in order to maintain a constant electromotive force, a large and constant temperature gradient is essential, thus a low thermal conductivity ILs suppresses the loss of thermal energy throughout the cell.

In other developments, there is another type of TEC cell that does not use a redox couple in their design, and relies on using pure electrolytes instead. The potential is coming from the thermal drift of ions (Soret effect) which generates an internal electric field, where contact of the electrolyte with electrodes, a change in entropy is modified through changes of solvation layers, thus causing a Seebeck coefficient to arise. This design does not drive a current in the TEC circuit, and it thus operates as a pure capacitive effect at electrodes. ILs properties such as specific capacitance, good stability, and wide potential windows also make them suitable electrolytes for electrochemical capacitors

(Silvester Debbie & Compton Richard, 2006). Bonetti et al. (2015) has conducted a series of experiments using ILs as electrolyte utilising platinum foil and platinum + thin sheet of nanoporous carbon, where platinum + nanoporous carbon yields 4 times higher potential at 36.5 mF due to increased surface area.

As elaborated above, there is a wide range of applications utilising ILs as a strategy to improve the performance of device in the field of energy conversion and storage. The physicochemical properties of ILs such as high thermal stability, wide electrochemical windows, negligible vapour pressure and high ionic conductivity attracts researchers to study them for the above applications. However in recent developments, the study of ILs are more inclined towards PILs because special application made possible due to availability of proton activities in PILs (Angell, Byrne, & Belieres, 2007). Therefore, to further extend the application of ILs, this work is focused on the application of PIL as thermoelectric electrolyte where this work emphasises the molecular conformation changes especially regarding the H bonding in the PILs in the thermoelectric device as the source of Seebeck potential as discussed in section 4.8.2.

4.5. Thermodynamic study of Ionic Liquids

As elaborated in the section above, the thermoelectric device relies on the entropy difference in order to generate electric potential. From equation (4.1), a high entropy difference leads to a high Seebeck coefficient which is an important parameter towards high performance thermoelectric device. Thermodynamic calculations of free energy proton transfer shows that proton transfer generates a large entropy difference (J.-P. Belieres & C. A. Angell, 2007). Hence, it is important to have thermodynamic data from ILs in term of direct relation to entropy as well as in the chemical viewpoint such as to find activation sites, bond breaking sites, and dissociation energy.

There are many studies regarding the thermodynamics of ILs, where the thermodynamic analysis can be obtained through experiment and simulation. In many

applications, ILs are employed in a device as robust electrochemical electrolytes. In this case, the interaction of ILs and solvent become a prominent issue in addressing the practicability of the IL. For example, evaluation of [1-butyl-3-methylimidazolium][BF₄] IL-H₂O/D₂O interaction was done by Rebelo et al. (2004) in terms of an atmospheric phase diagram to explain the solution reorganisation effect and solution thermodynamics, which influence the bonding network of the solution. Thermodynamic and kinetic effect also may explain synthesis of Ag and Au nanostructures, where dissolution of Ag⁺ and Au³⁺ with room temperature [dimethylammonium][dimethylcarbamate] IL with presence of dimethylformamide reducing agent yields nanostructure particles, wires and clusters (Bhatt et al., 2007).

In computational studies, methods such as conductor-like screening model for realistic solvation (COSMO-RS) (a MM simulation) can be used to predict thermophysical data for liquid system (Diedenhofen & Klamt, 2010; Klamt, Eckert, & Arlt, 2010). As well as using pure molecular dynamic calculation in MM where they found a valid correlation for both imidazolium and non-imidazolium based ILs (Dommert et al., 2012). In addition, thermodynamic of ILs using MM method are compared to HF in other review by the same group (Wendler et al., 2012).

Thermodynamics of PILs especially in regard to proton redox or transfer has been studied by several groups (Bautista-Martinez et al., 2009; J. P. Belieres & C. A. Angell, 2007; Yoshizawa, Xu, & Angell, 2003). The proton transfer in PILs is considered to follow the Grotthuss mechanism (proton hopping mechanism), although the details are still in debate. In many PILs, proton donor such as protonated amines, require free proton acceptor sites for proton exchange as it is evident for the systems comprised of amines along with their protonated counterparts. With regard to simulation for H activity, effects of hydrogen bonding interactions on the redox potential and molecular vibrations of

plastoquinone as studied using density functional theory calculations (Ashizawa & Noguchi, 2014)

Hydrogen redox of PILs for electrolyte applications was studied by Bautista-Martinez et al. (2009). Their findings are that the H redox in PILs generate large potential gap where it is associated to the equivalence point in the titration curve which determines the lowest electrochemical potential needed to activate a proton when there are no lower energy sites available. They also calculated that the proton transfer in PIL has large entropy difference, up to 0.223 kJ/mol·K for ethylammonium nitrate. Thermodynamics of H activities are useful for instance in biochemistry, protein unfolding was studied in PIL medium where they find stability of protein against hydrolysis and aggregation (Byrne & Angell, 2008). There is also thermodynamic characterisation on the effect biocompatible ILs functional group on protein where solvent reorganisation energy play a role (Attri & Venkatesu, 2011).

In computational chemistry, thermodynamic are calculated through the vibration analysis of molecule. The theory of thermodynamic in computational chemistry are as elaborated in section below.

4.6. Thermodynamics of Protic Ionic Liquids

When considering the motion of molecule in a system, it is necessary to consider the molecular vibration. A molecule can vibrate in many ways, and each way is called a vibrational mode. For molecules with N number of atoms in them, linear molecules have $3N - 5$ degrees of vibrational modes (also called vibrational degrees of freedom), whereas nonlinear molecules have $3N - 6$ degrees of vibrational modes.

The modes in most organic molecules are symmetric and antisymmetric stretching, scissoring, rocking, wagging and twisting motion as shown in Figure 4.6.

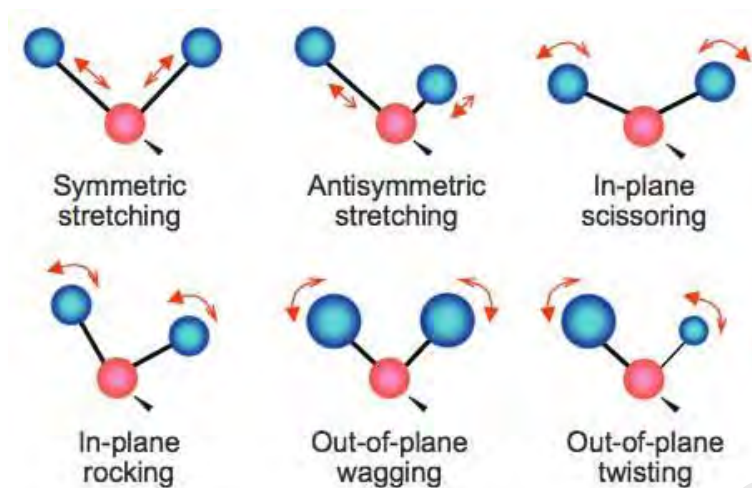


Figure 4.6. Types of molecular vibrations.

Calculating the molecular vibration thermodynamic properties gives us the partial contribution of each mode to thermodynamic changes.

4.6.1. Defining entropy from free energy

Important concepts and theories are summarized from (Zhou & Gilson, 2009) to further understand the calculations used. The free energy in a system is described by

$$F = -k_B T \ln Q, \quad (4.2)$$

where k_B is Boltzmann constant, and T is absolute temperature. Q is the partition function of a system to treat the system to be quantum mechanically which noted that Q is the total energy takes discrete values corresponding to specific microstates in the system. One of the system is harmonic oscillator when treated quantum mechanically. In this example, if considering energies of microstates j be $E_j, j = 1, 2, 3, \dots$ Then,

$$Q = \sum_j \exp(-\beta E_j), \quad (4.3)$$

where $\beta = (k_B T)^{-1}$. Under condition of constant volume, the Helmholtz free energy is the thermodynamic potential and is minimized at thermal equilibrium. The counterpart for constant pressure is Gibbs free energy, G . The relation is $G = F + PV$, where P is pressure and V is volume. The volume of the system is considered to be constant and work with free energy.

The present formulation relies on classical statistical thermodynamics, where it treats the energy as varying continuously which is excellent approximation for applications where the spacing of the relevant energy levels is small relative to thermal energy such as biomolecular applications.

Considering a system with energy of $E(x)$, the microstate of energy $E(x_j)$ is identified with a narrow range of x_j values, such as between x_j and $x_j + dx$, is simplifying the relationship between quantum and classical statistical mechanics. Then, applying equation (4.3), the partition function of the system is

$$Q = \sum_j \exp(-\beta E(x_j)). \quad (4.4)$$

Multiplying Q by a quantity of $\mathcal{N} dx$, and convert it into integral form, as below:

$$Q = \mathcal{N} \int dx \exp(-\beta E(x)). \quad (4.5)$$

The \mathcal{N} has reciprocal unit to those of x so that integral form of Q remains unitless, but the value of \mathcal{N} however has no significance for the problems of interest. When only x is a spatial coordinate, then the integral of the Boltzmann factor over x is known as a configurational integral.

Equation (4.5) can be viewed as the partition function for microstates located between x_j and $x + dx$. Then, the mean energy with respect to all of partition functions is

$$\langle E \rangle = \frac{\mathcal{N} \int dx E(x) \exp(-\beta E(x))}{Q} = \int dx E(x) \rho(x), \quad (4.6)$$

in which the equilibrium of probability density in x is defined as

$$\rho(x) = \frac{\mathcal{N} \exp(-\beta E(x))}{Q}. \quad (4.7)$$

The entropy is defined as below, at constant volume condition with respect to the temperature

$$S = - \left(\frac{\partial F}{\partial T} \right)_V. \quad (4.8)$$

Using equation (4.8), then entropy can be simplified to

$$\begin{aligned}
 S &= k_B \ln Q + \frac{kT}{Q} \left(\frac{\partial Q}{\partial T} \right)_V \\
 &= k_B \ln Q + \frac{\mathcal{N}}{TQ} \int dx E(x) \exp(-\beta E(x)) \\
 &= \frac{-F + \langle E \rangle}{T}.
 \end{aligned} \tag{4.9}$$

A useful expression by Gibbs/Shannon of equation (4.9) is

$$S = -k_B \int dx \rho(x) \ln \rho(x) + k_B \ln \mathcal{N} \tag{4.10}$$

4.6.2. Defining entropy component using harmonic oscillator

The thermodynamic of a molecular system vibration can be modelled through a simple harmonic oscillator. Harmonic oscillator is used to define the vibration of atoms through a simple model below as in Figure 4.7, where the atoms oscillates around centre mass of μ .

$$\mu = \frac{m_1 m_2}{m_1 + m_2} \tag{4.11}$$

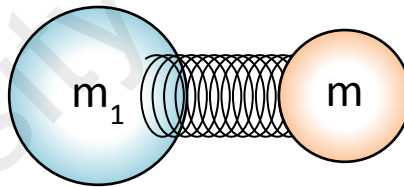


Figure 4.7. Diatomic simple harmonic oscillator model.

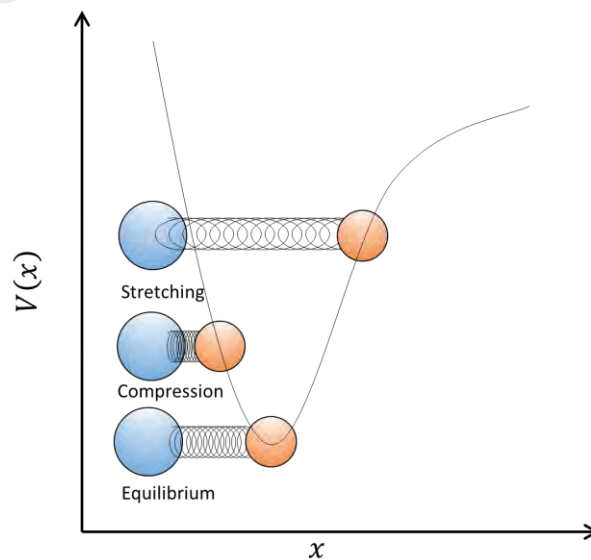


Figure 4.8. Depiction of diatomic potential energy of harmonic oscillator.

Potential energy of a ball-spring model in Figure 4.8 is

$$V(x) = \frac{1}{2}kx^2 \quad (4.12)$$

Inserting equation (4.11) and (4.12) into the Schrödinger equation (4.13), the Schrödinger equation in harmonic oscillator form is equation (4.14).

$$\frac{d^2\psi}{dx^2} + \frac{8\pi^2m}{h^2}(E - V)\psi = 0 \quad (4.13)$$

$$\frac{d^2\psi}{dx^2} + \frac{8\pi^2\mu}{h^2}\left(E - \frac{1}{2}kx^2\right)\psi = 0 \quad (4.14)$$

where h is Planck constant.

Equation (4.14) is solved using known solution as below,

$$\psi_n = AH_n \exp\left(-x^2/2\right) \quad (4.15)$$

$$E_n = \left(n + \frac{1}{2}\right)h\nu = \left(n + \frac{1}{2}\right)\hbar\omega \quad (4.16)$$

Equation (4.15) is solution for the harmonic oscillator wavefunction with A is amplitude of oscillation, and $H_n(z) \left(= (-1)^n \exp(z^2) \frac{d^n}{dz^n} (\exp(-z^2))\right)$ is called Hermite polynomials which give rise to eigenstates in the oscillator. Equation (4.16) is the solution for energy level where n is the number of level, in this equation the frequency ν can simply be substituted with angular momentum ω where $\nu = \frac{\omega}{2\pi}$.

The partition function with respect to diatomic harmonic oscillator can be defined by inserting into equation (4.4), and then simplify it into equation (4.17) using an exponential geometric series.

$$Q = \exp\left(-\frac{1}{2}\beta h\nu\right) \sum_{n=0}^{\infty} \exp(-n\beta h\nu).$$

$$Q = \exp\left(-\frac{\beta h\nu}{2}\right) \left(\frac{1}{1 - \exp(-\beta h\nu)}\right) \quad (4.17)$$

When considering many microstates involved, vibrational partition function is the sum of all microstates.

$$Q_{vib} = \sum_i \frac{1}{[1 - \exp(-h\nu_i/kT)]} \quad (4.18)$$

Using equation (4.6) and (4.7), the mean energy of harmonic oscillator is

$$\langle E \rangle = h\nu \left[\frac{1}{2} + \frac{\exp(-\beta h\nu)}{1 - \exp(-\beta h\nu)} \right]. \quad (4.19)$$

This is the mean energy for vibration component in molecular vibration which will be referred as E_{vib} .

The energy of vibration, E_{vib} , consider the vibrational energy for a molecule at the temperature T by simply expanding Boltzmann factor to;

$$E_{vib} = \sum_i \left\{ \frac{h\nu_i}{2} + \frac{h\nu_i \exp(-h\nu_i/kT)}{[1 - \exp(-h\nu_i/kT)]} \right\}. \quad (4.20)$$

where ν_i are the individual vibrational frequencies to define the energy in microstates.

Then, it is multiplied by Avogadro number, N_A , for a mole of molecules,

$$E_{vib} = N_A \sum_i \left\{ \frac{h\nu_i}{2} + \frac{h\nu_i \exp(-h\nu_i/kT)}{[1 - \exp(-h\nu_i/kT)]} \right\}. \quad (4.21)$$

The first term of equation (4.20) is the zero-point vibration energy. Hence, the second term is the additional vibrational contribution due to the temperature increase from 0 K to T K. To simplify the equations, it is separated into 2 equations as below:

$$E_{zero} = N_A \sum_i \frac{h\nu_i}{2}, \quad (4.22)$$

$$E_{vib}(0 \rightarrow T) = N_A \sum_i \left\{ \frac{h\nu_i \exp(-h\nu_i/kT)}{[1 - \exp(-h\nu_i/kT)]} \right\}. \quad (4.23)$$

Using equation (4.9), the entropy of molecular vibration is obtained as below,

$$S_{vib} = R \sum_i \frac{(h\nu_i/kT) \exp(-h\nu_i/kT)}{[1 - \exp(-h\nu_i/kT)]} - R \sum_i \ln \left[1 - \exp\left(-\frac{h\nu_i}{kT}\right) \right]. \quad (4.24)$$

The dynamic of a molecular system is then separated into 3 main parts, which are vibration, rotation, and translation. Vibration consist of the frequency of the periodic

motion, often known as vibration frequency. Rotational and translational motion denote the moment of inertia, and inertia of the molecule respectively.

Applying similar approach as elucidated above on vibrational motion, rotational and translational models are defined in Figure 4.9 and Figure 4.10 respectively.

The steps to obtaining the partition function for rotational and translational component are simplified. The partition function for rotational, Q_{rot} and translational, Q_{tra} component is summarised as below.

$$Q_{rot} = \frac{8\pi^2 I k_B T}{\sigma h^2} \quad (4.25)$$

(linear molecule)

$$Q_{rot} = \left(\frac{\sqrt{\pi}}{\sigma}\right) \left[\frac{8\pi^2 I k_B T}{h^2}\right]^{\frac{3}{2}} \sqrt{\prod_{j=1}^3 I_j} \quad (4.26)$$

(non-linear molecule)

$$Q_{tra} = \left(\frac{\sqrt{2\pi w k_B T / N_A}}{h}\right)^3 \quad (4.27)$$

where σ is symmetry number, I is moment of inertia, I_j is moments of inertia about j axes, and w is the molecular weight.

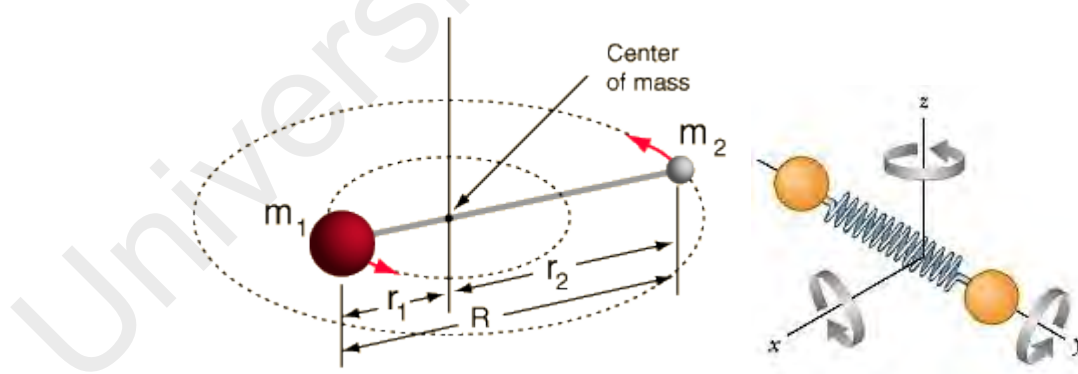


Figure 4.9. Diatomic rigid rotator model.

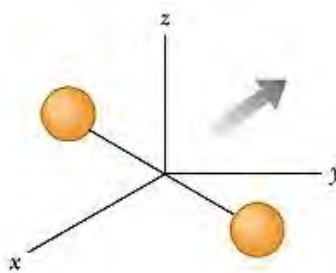


Figure 4.10. Diatomic translation model of the centre of mass.

The rotation and translation are simply the kinetic energy from rotational and translational motion. Using the concept of ideal gas to treat many atom molecule, and equipartition theorem as basis, energy of rotational, E_{rot} , and energy of translational, E_{tra} , in 3 dimensional degree of freedom system are

$$E_{rot} = \frac{1}{2} \sum_{j=1}^3 \langle I_j \omega_j^2 \rangle, \quad (4.28)$$

$$E_{tra} = \frac{1}{2m} \sum_{j=1}^3 \langle p_j^2 \rangle. \quad (4.29)$$

Note that p in equation (4.29) is momentum.

In an ideal gas system, the equipartition theorem defines the average internal energy for each moment and inertia to be $\frac{3}{2}kT$ per particle, therefore:

$$E_{rot} = \frac{3}{2}kT, \quad (4.30)$$

$$E_{tra} = \frac{3}{2}kT. \quad (4.31)$$

Also by multiplying it by N_A average energy per mole is defined and using relationship of ideal gas constant $R (= N_A k)$, equations above is expressed as:

$$E_{rot} = \frac{3}{2}RT \quad (4.32)$$

$$E_{tra} = \frac{3}{2}RT \quad (4.33)$$

However, note that for linear molecules we only have to consider only 2 degrees of freedom in rotational motion, therefore a separate equation for a linear molecule is defined where:

$$E_{rot} = RT. \quad (4.34)$$

Inserting equations above into equation (4.9), vibrational, S_{vib} , rotational, S_{rot} , and translational, S_{tra} , entropy equations are obtained expressed as follows, the sum of S_{vib} , S_{rot} , and S_{tra} , is the entropy of a molecular system, S ,

$$S_{rot} = R \ln \left(\frac{8\pi^2 I k T}{\sigma h^2} \right) + R \quad (4.35)$$

(for linear molecule)

$$S_{rot} = \frac{R}{2} \ln \left(\frac{\pi}{\sqrt{\sigma}} \prod_{j=1}^3 \frac{8\pi^2 I_j k T}{h^2} \right) + \frac{3}{2} R \quad (4.36)$$

(for non-linear molecule)

σ is symmetry number. I is moment of inertia. I_j is moments of inertia about j axes,

$$\begin{aligned} S_{tra} &= R \left\{ \frac{5}{2} + \frac{3}{2} \ln \left(\frac{2\pi k}{h^2} \right) + \ln k + \frac{3}{2} \ln \left(\frac{w}{N_A} \right) + \frac{5}{2} \ln T - \ln p \right\} \\ &= \frac{5}{2} R \ln T + \frac{3}{2} R \ln w - R \ln p - 2.31482 \end{aligned} \quad (4.37)$$

w is the molecular weight, and p is partial pressure.

4.7. Relationship between thermodynamics and thermoelectricity

The thermoelectric effect is an effect that a material creates an electromotive force (emf) under a temperature gradient, simple thermoelectric device is shown in Figure 4.11.

Generated emf is used to drive potential, V within the material.

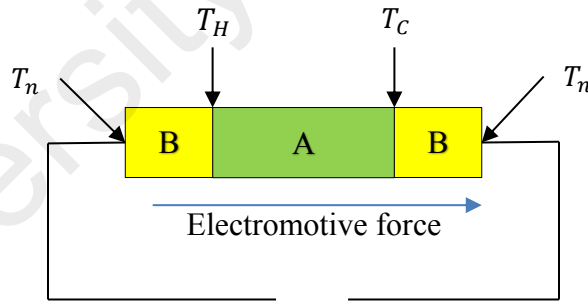


Figure 4.11. Schematic of simple thermoelectric device depicting an electromotive force (emf) generated by a temperature gradient where $\Delta T = T_H - T_C$, where $T_H > T_C$, T_n is ambient temperature. Material A is thermoelectric material, while B is a conductor material (wire). When direction of emf is generated as above, A is a p-type thermoelectric material, and if it is in opposite direction then A is an n-type.

An important physical property in a thermoelectric device is Seebeck coefficient, S_e which define the emf generated under a temperature gradient. Electromotive potential, V and S_e relation are defined as follows:

$$V = S_e(T_H - T_C) \quad (4.38)$$

$$S_e = \frac{V}{\Delta T} \quad (4.39)$$

The S_e is positive for potential direction from T_H to T_C and the material is considered as p-type, and negative for opposite direction potential and the material is called n-type.

4.7.1. Onsager-Callen Model

4.7.1.1. Irreversible Thermodynamics

A thermodynamic system is assembled under subsystem statistics, in which a thermodynamic system is not a static but a configuration of a fluctuating parameters. However, in a thermoelectric system, the thermal and electrical processes are coupled. These processes have been derived by Onsager (1931a, 1931b) and Callen (1948) on the framework of the thermodynamics of dissipative system by linking between out of equilibrium coupled processes. Fluctuating parameter of thermodynamics such as electrochemical potential, μ_e and temperature, T need to be defined under non-equilibrium thermodynamics or irreversible thermodynamics which require the parameters to be well defined in a quasi static environment. In a 'static' environment, from the first (4.40) and reversible second law of thermodynamics (4.41),

$$\delta Q = dU + W - \mu dn \quad (4.40)$$

$$dS = \frac{dQ}{T} \quad (4.41)$$

where δQ is heat absorbed, dU is internal system energy change, W is work against external forces, μ is chemical potential and dn is change of number of particles. Equations above is extended into finite time response thermodynamics in the flux form

$$\mathbf{J}_E = \mathbf{J}_Q + \mu_e \mathbf{J}_N \quad (4.42)$$

$$\mathbf{J}_S = \frac{\mathbf{J}_Q}{T} \quad (4.43)$$

where \mathbf{J}_E is energy flux, \mathbf{J}_Q is heat flux, μ_e is electrochemical potential, \mathbf{J}_N is particles flux, and \mathbf{J}_S is the entropy flux respectively.

Each of these fluxes are conjugated to its thermodynamic potential gradients, acting as generalised force.

$$\mathbf{F}_N = \nabla \left(-\frac{\mu_e}{T} \right) \quad (4.44)$$

$$\mathbf{F}_E = \nabla \left(\frac{1}{T} \right) \quad (4.45)$$

From fluxes and forces defined above, the linear coupling of transport of energy and particles is given by a set of coupled equations as below.

$$\begin{bmatrix} \mathbf{J}_N \\ \mathbf{J}_E \end{bmatrix} = \begin{bmatrix} L_{NN} & L_{NE} \\ L_{EN} & L_{EE} \end{bmatrix} \begin{bmatrix} \nabla \left(-\frac{\mu_e}{T} \right) \\ \nabla \left(\frac{1}{T} \right) \end{bmatrix} \quad (4.46)$$

$$\text{where } L_{NE} = L_{EN}$$

The Onsager description as described above is equivalent to the assumption of a minimal entropy production of a system out of equilibrium conditions. The linear response and fluctuations inside a dissipative system are related.

Using heat flux, \mathbf{J}_Q to substitute energy flux \mathbf{J}_E to simplify equation (4.46).

$$\begin{bmatrix} \mathbf{J}_N \\ \mathbf{J}_Q \end{bmatrix} = \begin{bmatrix} L_{11} & L_{12} \\ L_{21} & L_{22} \end{bmatrix} \begin{bmatrix} -\frac{1}{T} \nabla(\mu_e) \\ \nabla \left(\frac{1}{T} \right) \end{bmatrix} \quad (4.47)$$

$$\text{where } L_{12} = L_{21}$$

and the kinetic coefficients become as follows:

$$L_{11} = L_{NN} \quad (4.48)$$

$$L_{12} = L_{NE} - \mu_e L_{NN} \quad (4.49)$$

$$L_{22} = L_{EE} - \mu_e(L_{EN} + L_{NE}) + \mu_e L_{NN} \quad (4.50)$$

Explicit explanation on how to derive linear couplings parameters is given by Onsager and Callen (Goupil et al., 2011), therefore the kinetic coefficients and transport parameters are defined as below:

$$L_{11} = \frac{T}{e^2} \sigma_T \quad (4.51)$$

$$L_{12} = \frac{T^2}{e^2} \sigma_T S_J \quad (4.52)$$

$$L_{22} = \frac{T^3}{e^2} \sigma_T S_J^2 + T^2 \kappa_J \quad (4.53)$$

where T is absolute temperature, e is particle charge, σ_T is isothermal electrical conductivity, S_J is entropy per carrier, and κ_J is thermal conductivity of pure conductive contribution. In addition, the thermal conductivities under zero electrochemical gradient or particle transport is;

$$\kappa_E = T S_E^2 \sigma_T + \kappa_J. \quad (4.54)$$

Seebeck coefficient, S_e as defined in equation (4.1) can be expressed as the ratio between two forces, electrochemical gradient and temperature gradient, as in (4.55), while relationship between S_e and entropy per carrier, S_J is expressed as in (4.56) below:

$$S_e \equiv -\frac{1}{e} \frac{\nabla(\mu_e)}{\nabla(T)} \quad (4.55)$$

$$S_J = e S_e. \quad (4.56)$$

4.8. Study on thermodynamic-thermoelectric correlation of PILs

From this section, the study of thermoelectric properties of amine based PILs are discussed.

The physicochemical properties of ILs such as high thermal stability, wide electrochemical windows, negligible vapour pressure and high ionic conductivity attracts researchers to study them for application as electrochemical solvent. These properties of ILs are mainly utilised in electrochemical applications of solar cells, fuel cells, and batteries as discussed in previous sections. The intrinsic electrical conductivity of ILs usually means that the addition of supporting electrolyte may be avoided.

In many PILs, a proton donor such as a protonated amine, require free proton acceptor sites for proton exchange. Thermodynamic studies of the proton transfer reaction in PILs has been studied by many researchers (Bautista-Martinez et al., 2009; J. P. Belieres & C. A. Angell, 2007; Yoshizawa et al., 2003). The proton transfer in PIL has large entropy

difference, up to 0.223 kJ/mol.K for ethylammonium nitrate (Bautista-Martinez et al., 2009), which may translate to high Seebeck potential value.

For a thermoelectrochemical system, from equation (4.1), the Seebeck coefficient, S_e of the cells has direct relation with total entropy difference, $S_e = \frac{\Delta S}{nF}$, (ΔS is entropy difference, n is charge carrier number, F is Faraday constant). As mentioned in previous sections, the entropy difference is large due to H activities in PILs, which is favourable in thermoelectric applications. Using this properties of PIL, this work investigates the effect of molecular conformation of selected PILs.

In this work, the feasibility of a PIL as the base material in a TEC will be evaluated. Given that for a specific molecular geometry of the PIL, the entropy of the PIL when subjected to a temperature gradient can be calculated using the quantum thermodynamic approach, by evaluating the vibrational energy of the molecule. The relationship between entropy and Seebeck coefficient can then be calculated using equation (4.1) above to assess its bulk thermoelectric capability. For this work, PILs were specifically identified as the target electrochemical material as the proton vibration is expected to provide a large entropy difference.

4.8.1. Methodology

Thermodynamic calculations are based on the first principle calculations to provide precise calculation of proton vibration contributions to entropy. The entropy of a molecular system, in this case, PILs, is calculated through the vibrational analysis of the molecule. The entropy of a molecular system, S , is the sum of vibrational, S_{vib} , rotational, S_{rot} , and translational, S_{tra} , entropy equations, which the equations are expressed as follows which reinstating equation (4.24), (4.36) and (4.37):

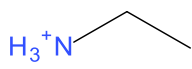
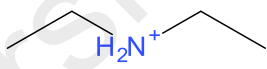
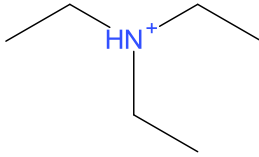
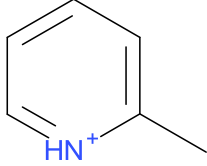
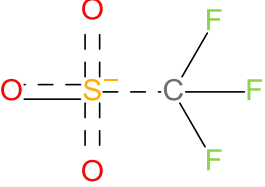
$$S_{vib} = R \sum_i \frac{(hv_i/kT) \exp(-hv_i/kT)}{[1 - \exp(-hv_i/kT)]} - R \sum_i \ln \left[1 - \exp \left(-\frac{hv_i}{kT} \right) \right]. \quad (4.24)$$

$$S_{rot} = \frac{R}{2} \ln \left(\frac{\pi}{\sqrt{\sigma}} \prod_{j=1}^3 \frac{8\pi^2 I_j kT}{h^2} \right) + \frac{3}{2} R \quad (4.36)$$

$$S_{tra} = R \left\{ \frac{5}{2} + \frac{3}{2} \ln \left(\frac{2\pi k}{h^2} \right) + \ln k + \frac{3}{2} \ln \left(\frac{w}{N_A} \right) + \frac{5}{2} \ln T - \ln p \right\} \quad (4.37)$$

The four PILs for this work, are the combination of cations and anions as listed in Table 4.1. They were selected based on molecular simplicity to study the contribution of their respective structure to the vibrational modes. In this work, ethylammonium (Ea), diethylammonium (Diea), triethylammonium (Triea) and 2-methylpyridinium (2mp) were chosen as the cation. In all cases, the triflate (Tf) was used as the anion. Ea, Diea and Triea contain one, two and three ethyl chains respectively, and 2mp has a benzene ring. The PIL system is considered to be in the liquid and ionic state throughout the modelling process. The PILs were labelled as **1**, **2**, **3**, and **4** for combination of Ea+Tf, Diea+Tf, Triea+Tf, and 2mp+Tf respectively.

Table 4.1. Molecular structure of PIL cation and anion in study.

Cation			
			
Ethylammonium (Ea)	Diethylammonium (Diea)	Triethylammonium (Triea)	2- methylpyridinium (2mp)
1	2	3	4
Anion			
			
Trifluoromethanesulfonate (Tf)			

4.8.1.1. Simulation flow

Application of the respective molecular geometry for the PIL cases to the thermodynamic cycle are carried out according to the steps outlined in Figure 4.12. All simulation works were carried out using Biovia Materials Studio modules.

Step 1: Identification of the PIL stable states through annealing. The model is initiated by defining the PIL molecular structure (for both cation and anion) in the ionic state, where there is an H atom attached to amine N atom. The PIL system is then subjected to an annealing process to identify the most stable conformational geometry of the PIL molecules, by identifying the conformations with the probability of lowest energy. This was carried out using molecular dynamic simulation through annealing in the Forcite module of Biovia Materials Studio. Forcite is a collection of molecular mechanics tools to investigate molecular system potential energy surface using classical forcefield. In this molecular mechanics study, the forcefield COMPASS II parameterisation is employed. One of the Forcite tool, the annealing method is a useful tool to explore the conformational space for low energy structures by periodically increasing and decreasing the temperature of classical dynamic trajectory to avoid trapping the structure in a conformation that represents a local energy minimum. In this case, the temperature range was 300 K-500 K, and the annealing cycle was repeated ten times. The thermal annealing forces the PIL molecular structure to form a different conformation after it is subjected to higher temperature (500 K) then relaxed to cooler temperature (300 K). For each cycle, the Hamiltonian (potential energy + kinetic energy) is recorded. From this annealing process, two of the lowest Hamiltonian energy structures (labelled as State I and II respectively) which reflected to low conformation energy that has higher conformation probability in normal conditions, were selected for the subsequent geometry optimisation and thermodynamic calculations. This procedure is repeated for all combinations of PILs to identify their respective two stable states.

Step 2: Geometry optimisation. The two lowest energy states of the PIL, namely States I and II were geometry optimised using first principle density functional theory (DFT) calculations with Perdew–Burke–Ernzerhof (PBE) exchange–correlation functional (Perdew et al., 1996). The molecules are optimised before any further analysis was done with energy convergence is below 10^{-5} Ha. The Kohn–Sham equation was expanded in a double numeric quality basis set (DNP) with polarization functions. **Step 3: Calculation of thermodynamic properties.** The thermodynamic properties of the conformational States I and II of the respective PILs were calculated using Hessian evaluation provided in the DFT calculation. The Hessian matrix is obtained through harmonic approximation, vibrational frequencies, and associated normal modes in the second energy-derivatives. This information (eigenvalues and eigenvectors) for each of the two conformations is then used in the equation (4.24), (4.36), and (4.37) to calculate entropy. This entropy will be used to calculate S_e .

Step 4: Identification of main vibration modes using Molecular Dynamics (MD). To complement the entropy calculation, molecular dynamics (MD) simulation was carried out to identify the main vibration modes which contribute to the entropy of conformation States I and II of the respective PIL combinations. All of the MD also employs first principle GGA-PBE DFT calculations as described in geometrical optimisation in step 2 to simulate the atomic vibrations. These vibrations were captured over 1001 structure snapshot at 1 fs increments, over 1 ps. In this exercise, the Nosé-Hoover algorithm was used to control temperature as thermostat using the NVT ensemble (Shuichi, 1991). In particular, the N-H bond length and frequency was analysed as it is the site of the proton, and hence any thermodynamic properties due to this bond would be of particular interest. The dominant modes were also analysed in term of its infrared (IR) spectra to distinguish between the 2 states.

Step 5: Temperature dependent evaluation of N-H bond length. In another work flow pathway, MD simulation is carried out after the annealing process to study the effect of temperature at 298K and 398K on the N-H bond length at the cation in the PIL. This will be used to correlate our understanding of the N-H bond length with the entropy calculations for the PILs.

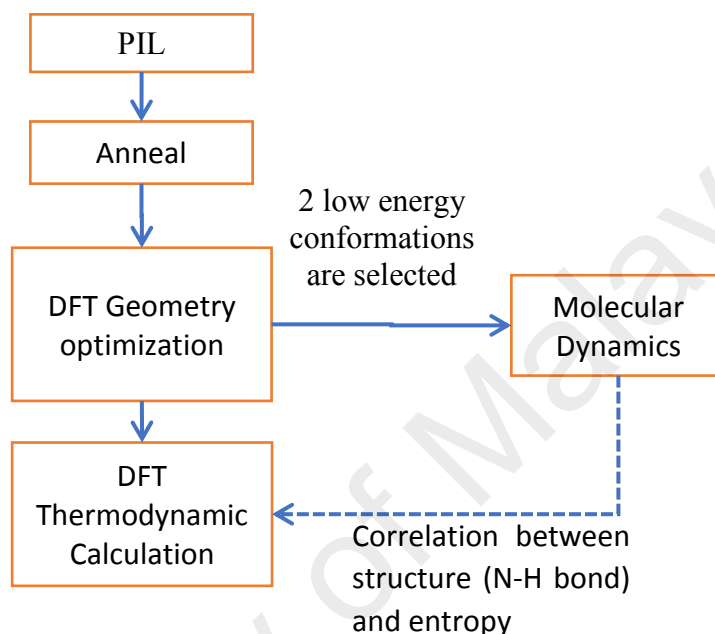


Figure 4.12. Work flowchart of amine based PIL in thermodynamic study for TE.

4.8.1.2. Simulation settings

Annealing process to PILs was done using classical mechanical modelling to avoid molecular structure falling into a local minimum. In this procedure, the first-principle forcefield COMPASS II (Condensed-phase Optimised Molecular Potentials for Atomistic Simulation Studies) parameterisation is employed for molecular annealing. Annealing of the PILs molecules was conducted from 300 K to 500 K that is repeated 10 times to find 2 stable molecular conformations. NVE ensemble was used for thermostat that is useful for constant volume or constant energy dynamics. The settings for annealing parameters in MS 2016 are depicted in Figure 4.13.

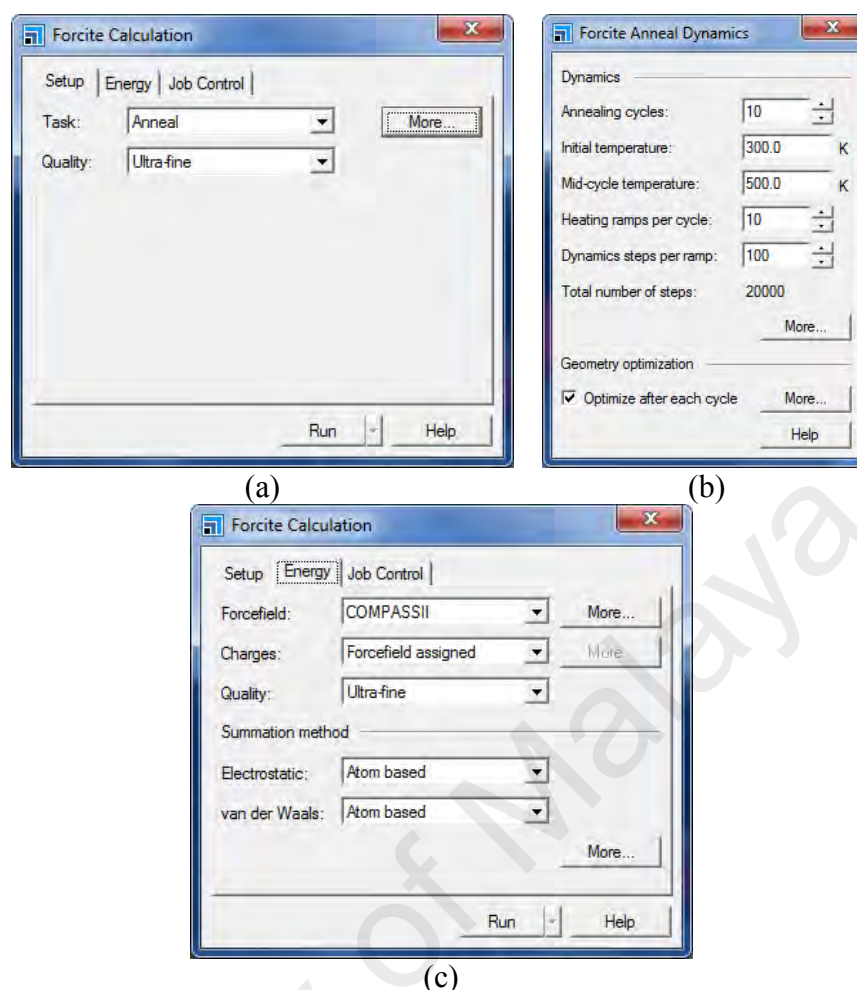


Figure 4.13. (a) PILs annealing setting. (b) Dynamics parameters used for annealing process. (c) Forcefield settings for annealing.

Amine based PILs were investigated using the first principle density functional theory (DFT) calculations with Perdew–Burke–Ernzerhof (PBE) exchange–correlation functional (Perdew et al., 1996). The molecular geometrical structures are optimized before any further analysis was done with energy convergence is below 10^{-5} Ha. The Kohn–Sham equation was expanded in a double numeric quality basis set (DNP) with polarization functions. The cationic and anionic structures were also optimized with same functional and basis set for computing the values of Ionization Potential and Electron Affinity. The settings for geometrical optimisation parameters in MS 2016 are depicted in Figure 4.14.

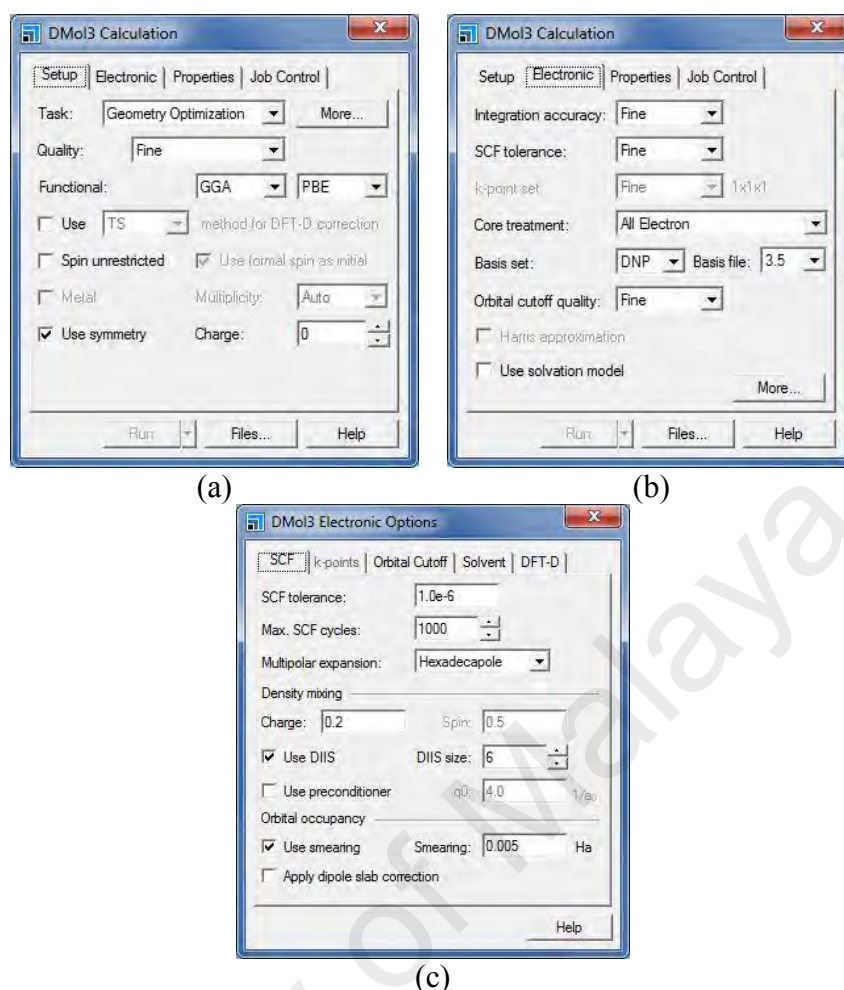


Figure 4.14. PIL GO settings. (a) Selection of GO task. (b) Core electron treatment and basis set settings. (c) SCF options settings.

4.8.2. Results and discussion

4.8.2.1. Conformation effect to IR spectra

Identification of State I and II, the most stable state which extracted from annealing. The dominant vibration for these states are analysed by the IR spectra. In this simulation, the IR spectra is an indication of the dominant vibration modes for States I and II of the PILs.

For example, the IR spectra for **1** as shown in Figure 4.15 (a), shows two high intensity peaks at 2481 cm^{-1} and 2238 cm^{-1} for state I and II respectively. The peaks are due to the proton vibration in the PIL system, i.e. at the N-H bond. Thus, a higher intensity of these peaks shows the dominant vibrations in the system as the intensity is related to concentration and IR absorbance. This is largely responsible for contributing to the large

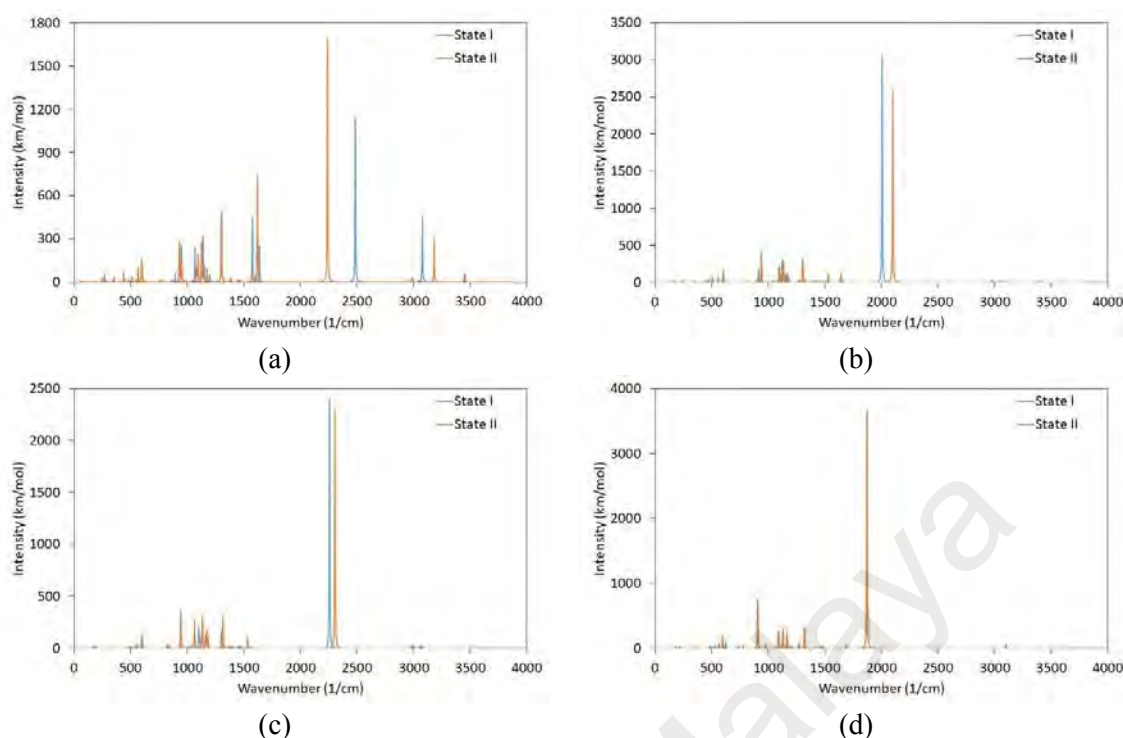


Figure 4.15. IR spectra of for PIL (a) **1**, (b) **2**, (c) **3**, and (d) **4**. Peaks of highest intensity are due to vibration of N-H atom in anion (Tf).

entropy difference in the PIL system. As shown in equation (4.1) that S_e is related to entropy, it is this mechanism where is expected to bring the potentially large thermoelectric behaviour of PILs. This can be compared to a first principle calculations of a benzene junction setup, where the vibration modes affects the ZT value (Hsu, Chiang, & Chen, 2012). Similar observations were noticed for the other PILs as shown in Figure 4.15 (b) to (d). For **2**, high intensity peaks are 2006 cm^{-1} and 1099 cm^{-1} for state I and II respectively, and **3** is 2255 cm^{-1} and 2303 cm^{-1} . While in **4**, the peaks are closer to each other at 1814 cm^{-1} and 1874 cm^{-1} for state I and II respectively. In **1**, **2**, and **3**, the difference of the two peaks are significant due to a large difference of N-H bond vibration mode type because the ethyl group in cation Ea, Diea and Triea are not rigid which can form many type of conformations. However, in **4**, the pyridine ring is more rigid thus the difference of the two peaks is negligible.

The total formation energy difference for States I and II for each PIL system is summarised in Table 4.2. The order of the formation energy difference is as follows; **2** > **3** > **1** > **4**. This formation energy difference is a function of the contribution atomic

energy, binding energy, kinetic and electrostatic energy. For example, the **2** system has a higher atomic number than **4**, however **4** has higher formation energy due to its partial double bond in the pyridine ring. In this study, ΔE from I to II is exothermic in all cases. This can be related to the entropy curve depicted in Figure 4.18 insets, the state I has more entropy than II. Considering the difference of energy contributions obtained from the calculations as showed in Table 4.2, a disordered PIL system i.e. state I has higher kinetic energy and lower electrostatic potential energy than state II. In general, the transition from State I to II has positive total energy difference which mean total energy for State I is always larger than State II which may explain the larger entropy on state I than II. On another ab-initio calculation by Chandran et al., PIL was reported to have high cohesive energy density and strong ionic packing compared to other type of ILs (Chandran, Prakash, & Senapati, 2010; T. L. Greaves & Drummond, 2015), which generally mean that they possess a significantly large potential energy. In addition, any loss in potential energy will result in a corresponding increase in kinetic energy due to energy conservation, as demonstrated by the magnitude of $\Delta E_{kinetic}$ and ΔE_{es} listed in Table 4.2.

Table 4.2. Energy contribution of PILs in comparison from State I to II in term of kinetic energy difference, $\Delta E_{kinetic}$, electrostatic energy difference, ΔE_{es} , and difference of total formation energy, ΔE_{total} . Energy unit (kJ/mol).

PIL	$\Delta E_{kinetic}$	ΔE_{es}	ΔE_{total}
1	-230.933	231.049	0.123
2	167.280	-161.130	6.382
3	-370.945	374.010	3.360
4	-66.064	65.369	0.013

4.8.2.2. Entropy difference of 2 conformations

After annealing process and geometrical optimization, the vibrational analysis as described above was carried out to deduce the entropy curve for the respective PILs for conformation States I and II when subjected to a temperature range from 100 K to 1000 K.

The difference between entropies of conformation States I and II can be visualised by separating into vibrational, rotational, and translational component as listed in Table 4.3. In the table, the PIL entropy is separated into its component vibrational, rotational, and translational entropy which is then compared to their respective conformation. Generally, it is observed that the difference of entropy between conformations are largely due to vibrational and rotational entropy, whilst translational entropy does not provide changes in the entropy for in any of the PIL cases. This is because the vibrational and rotational entropy are due to atomic movement bound by the atomic bonds (as described by equations (4.24) and (4.36), whilst the translational vibrations are governed by the physical condition as well as their molecular weight as defined in equation (4.37), which do not change throughout the temperature range.

Thus, absolute entropy difference, $|\Delta S|$ can be described as a function of its molecular geometry and can be ranked as follows:

1. ΔS_{vib} , $1 < 4 < 2 < 3$. This is related to the rigidity of the molecule and number of ethyl group that is associated to number of vibrational mode i.e. degree of freedom. For example, **4**, whilst containing a larger number of covalent bonds compare to **2**, is more

Table 4.3. Comparison of 2 conformation separated by entropy contribution, vibrational entropy, S_{vib} , rotational entropy, S_{rot} , and translational entropy, S_{tra} . (J/mol.K) at 298 K.

Entropy contribution	State I	State II	Absolute Difference, $ \Delta S $	
1	S_{vib}	175.53	175.41	0.12
	S_{rot}	129.72	130.31	0.59
	S_{tra}	174.44	174.44	0
2	S_{vib}	238.18	233.76	4.42
	S_{rot}	134.39	134.60	0.21
	S_{tra}	176.11	176.11	0
3	S_{vib}	295.73	283.70	12.03
	S_{rot}	137.20	137.04	0.16
	S_{tra}	177.59	177.59	0
4	S_{vib}	221.30	218.12	3.18
	S_{rot}	136.82	136.74	0.08
	S_{tra}	177.18	177.18	0

rigid through its possession of a pyridine ring. Hence, the entropy difference of **4** is lower than **2**.

2. $\Delta S_{rot}, 4 < 3 < 2 < 1$. In this particular PIL system, it is associated to rotation ability of anion counterpart due to number of protons attached to N atom in amine where it increases moment. For example, in the system **1** there are 3 positions of negative dipole moment at each O atoms in anion and there are also 3 positions of positive dipole moment at H atoms in cation causes the anion rotates easier since there is large moment of force produced by interaction of positive and negative dipoles. On the other hand, **2** has 2 positions, while **3** and **4** each has 1 position of positive dipole at cation molecule which makes moment reduced. A simple schematic of proton rotation is shown in Figure 4.16.

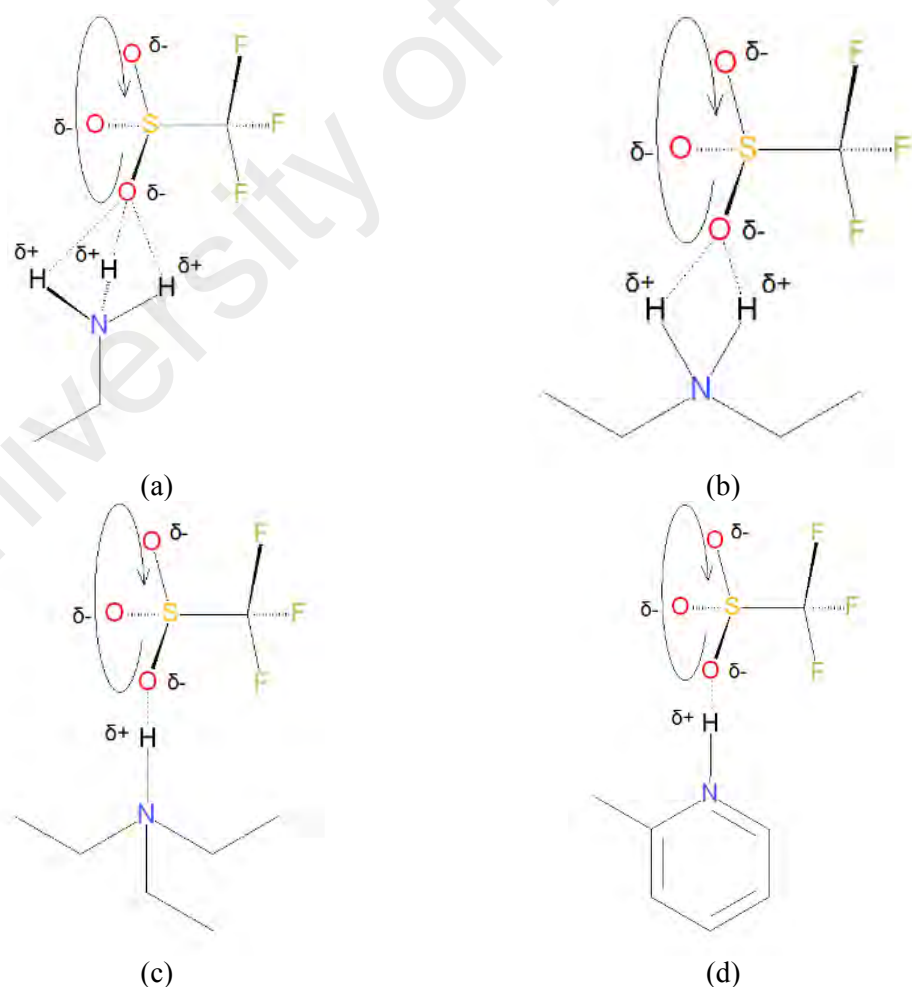


Figure 4.16. Schematic to show correlation S_{vib} to number of proton attachment to N atom. Larger number of proton increases ΔS_{rot} in entropy where the anion is more likely to rotate.

3. In all cases, S_{tra} is unchanged between the 2 conformations. There are no changes in physical condition across the temperature is considered. This is because in translational entropy, physical condition such as molecular weight and partial pressure.

From the above, we can arrive at a number of useful prescriptions for molecular design of PILs in TEC systems. In order to have a high ΔS molecular system (and correspondingly high S_e), the molecular system should have a long ligand to increase vibrational modes and eventually the S_{vib} , and high number of proton attached to increase S_{rot} . However, in entropy terms, the contribution of proton rotation quickly diminishes as the ΔS_{rot} is only small fraction of overall ΔS , which somehow make it less important to have large number proton attachments.

4.8.2.3. Temperature effect on N-H bond length

Given that the IR spectra indicate the highest vibration contribution come from the proton site, i.e. the N-H bond, where the bond length is analysed as a function of temperature. The atomic vibration at higher temperature is more energetic which makes the bond length distribution broader, and the bond length tends to be longer.

This is depicted in Figure 4.17, where the distribution of N-H bond is plotted. At colder temperatures (300 K), the peak is narrower indicating low amplitude vibration in all cases. On the other hand, vibration at 400 K has broad peak which indicate large amplitude is associated. It is due to more energetic atoms to produce vibrations at higher velocities. It is also useful to note that the peak is slightly biased to a longer bond length at higher temperature conformations. When the peak becomes broader, it changes the dynamics of the vibration which give rise to higher entropy state as the conformation becomes more disordered.

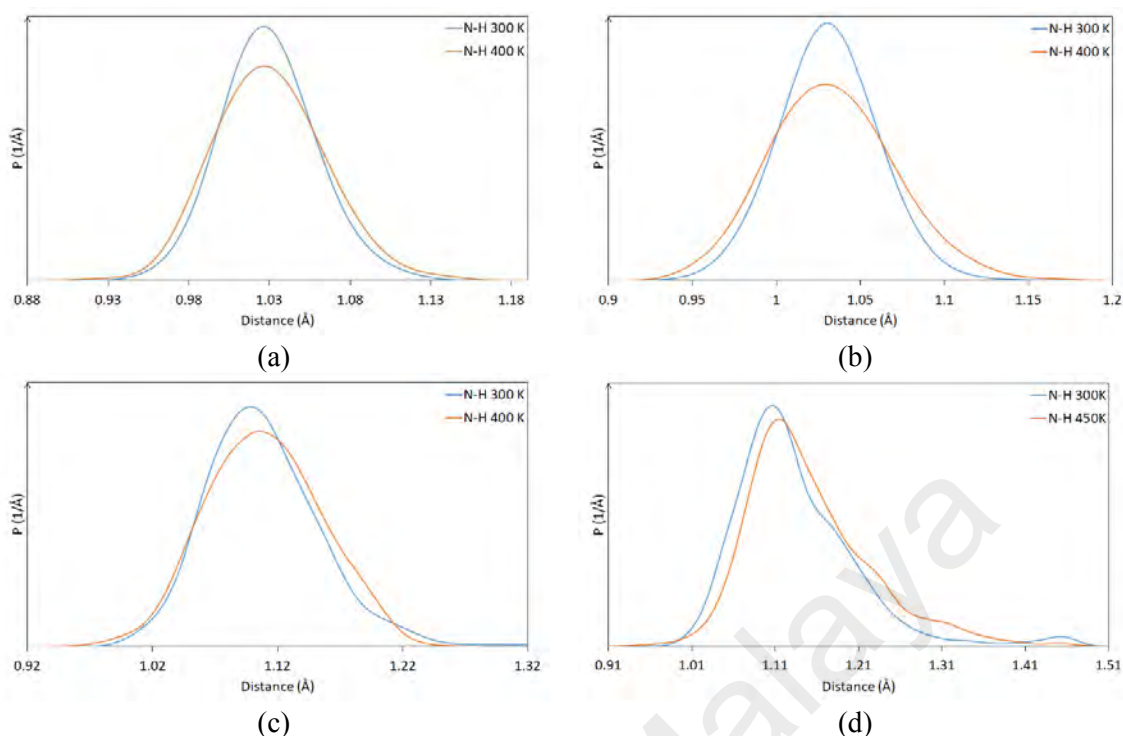


Figure 4.17. Comparison of bond length distribution of N-H of protonated (a) Ea (b) Diea (c) Triea (d) 2mp at $T = 300$ K and 400 K.

4.8.2.4. Thermodynamic cycle under a temperature gradient

The thermodynamic parameters of PILs was calculated by the vibration analysis and the sum of equation (2), (3), and (4), and was used deduce the entropy for the PIL when subjected to a temperature gradient. Two entropy curves were obtained from conformation States I and II as shown in Figure 4.18 insets.

Line I: Entropy curve for State I across temperature from 100 K to 1000 K.

Line II: Entropy curve for State II for the same temperature range.

A hypothetical thermodynamic cycle of PIL using entropy curves described in Figure 4.18 is constructed. The ionic state at minimum temperature will be the starting point for the thermodynamic cycle which will be described below, i.e. point 1 on Line I. When the PIL system is subjected to a temperature difference, $\Delta T (T_H - T_C)$ in a TEC system, the pathway taken is from point 1 to 2, representing the path of the PIL from the minimum temperature (T_C) to the maximum temperature (T_H). This process is adiabatic heat in (endothermic). The thermal energy will increase the entropy as the vibration becomes

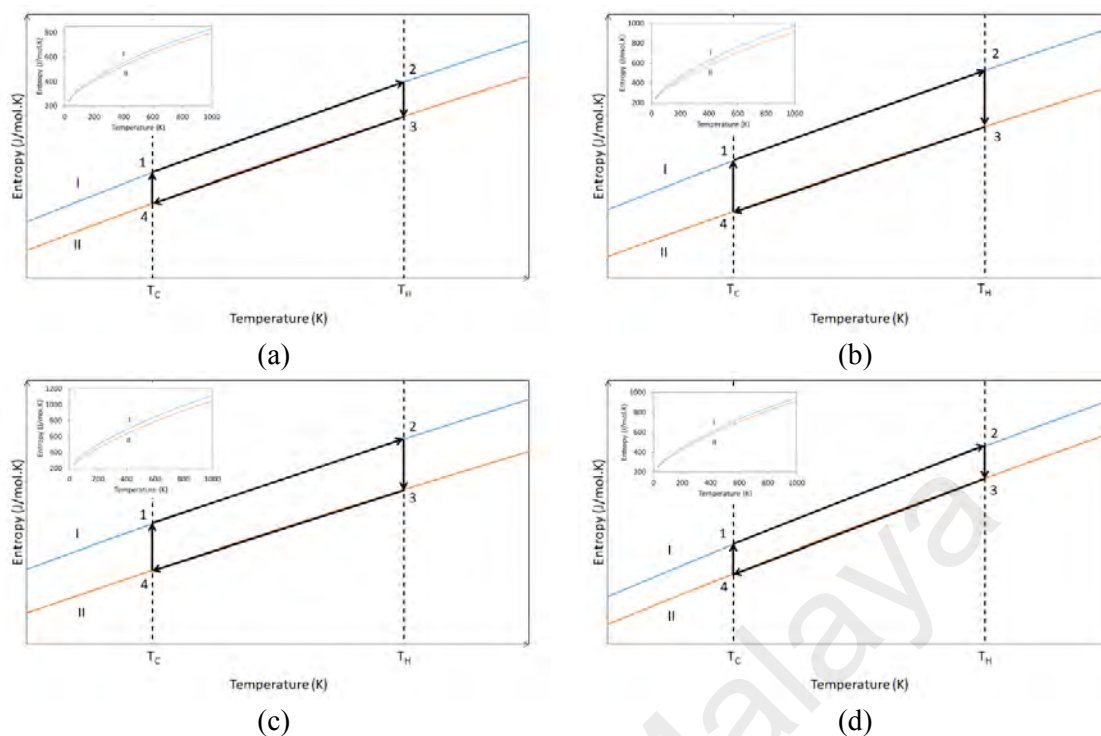


Figure 4.18. The hypothetical thermodynamic cycle of (a) 1, (b) 2, (c) 3 and (d) 4 depicted on entropy curve in arbitrary temperature range. (Inset) Calculated entropy in the function of temperature for respective PILs. Two curves are contributed by 2 stable states in different conformation.

more energetic, for example this is shown by having a longer N-H bond at higher temperature.

Once the PIL reaches the maximum temperature, it achieved the maximum energy and maximum entropy at point 2, then it changes its conformation into more stable form on conformation State II to point 3. The transition from 2 to 3 is an isothermal exothermic process, since conformation State II has lower energy than State I.

Therefore, upon reduction of temperature (from a hotter region to a cooler region), a reverse transition begins from this point and move towards the minimum defined temperature. From point 3, reduction of the temperature is traced by the curve to point 4, until it reaches a minimum value through an adiabatic exothermic process.

It then reverts to its initial state at point 1. This cycle will repeat as long as the external temperature gradient exists, where it is related to the temperature gradient in TEC system.

The calculated entropies are depicted in Figure 4.18 inset. Despite the geometrical similarities of the conformations, each conformation has different entropy which due to

different vibrational mode, especially at H atom attachment to N atom in amine which has been described above in the IR spectra section.

This temperature difference is essential in driving a thermoelectrochemical generator as it drives the entropy difference and thus driving the electromotive power in a TEC cell.

From the entropy difference, from equation (4.1) the Seebeck coefficient is obtained, considering the reference temperature represents the hot and cold terminals of the TEC cell ($T_{ref} = \frac{T_H + T_C}{2}$). The S_e of every PIL system in study is compared in Figure 4.19. Since the entropy difference and Seebeck coefficient has a direct relation, **3** has the highest Seebeck coefficient at 0.510 mV/K at temperature 300 K.

From the quantum thermodynamic cycle derived in this model, useful information on the macro-scale operation of the TEC cell can be deduced. For example, the quantum thermodynamic cycle can determine the mechanism of the heat cycle process and how much of the heat is transformed into usable energy. Thus, this discussion will be extended to estimate the cycle efficiency of a thermoelectric generator containing PILs. The theoretical efficiency, η , of the PIL system can be described as follows (Goupil et al., 2011);

$$\eta \equiv \frac{W_{out}}{Q_{in}} = \frac{\oint T dS}{\int_{T_H} T dS} \quad (4.57)$$

where W_{out} is work that can be extracted from system, Q_{in} is heat input to the system, T are absolute temperature of heat input, and S is entropy for the system. Using the equation

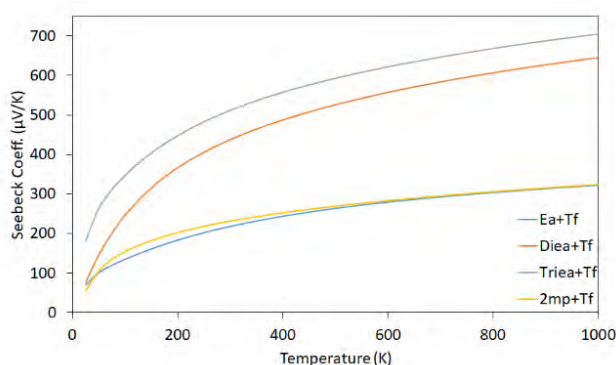


Figure 4.19. Calculated Seebeck coefficient across temperature of all PIL studied.

above and considering the T_C is the lowest possible temperature e.g. room temperature, $T = 298$ K, a maximum theoretical efficiency can be calculated. The work output and maximum theoretical efficiency are depicted in Figure 4.20.

From Figure 4.20, the maximum ratio of work to efficiency can be determined through the intersection of these curves. The maximum work output, W_{out} , can be extracted from the optimum temperature difference, ΔT_{opt} , and corresponding Seebeck coefficient, S_e , is summarised in Table 4.4 below.

Table 4.4. Summary of maximum work output, W_{out} , optimum temperature difference, ΔT_{opt} , and Seebeck coefficient, S_e , for each PIL.

PIL	Maximum W_{out} (kJ/mol)	ΔT_{opt} (K)	S_e (mV/K)
1	5.309	226	0.267
2	13.194	276	0.550
3	13.586	251	0.607
4	4.876	201	0.269

From Table 4.4, in ascending order the maximum W_{out} at their respective optimum temperature difference, ΔT_{opt} , is $4 < 1 < 2 < 3$, and order for the S_e is $1 < 4 < 2 < 3$. From this information, the **3** system has the most potential for PIL thermoelectric generator

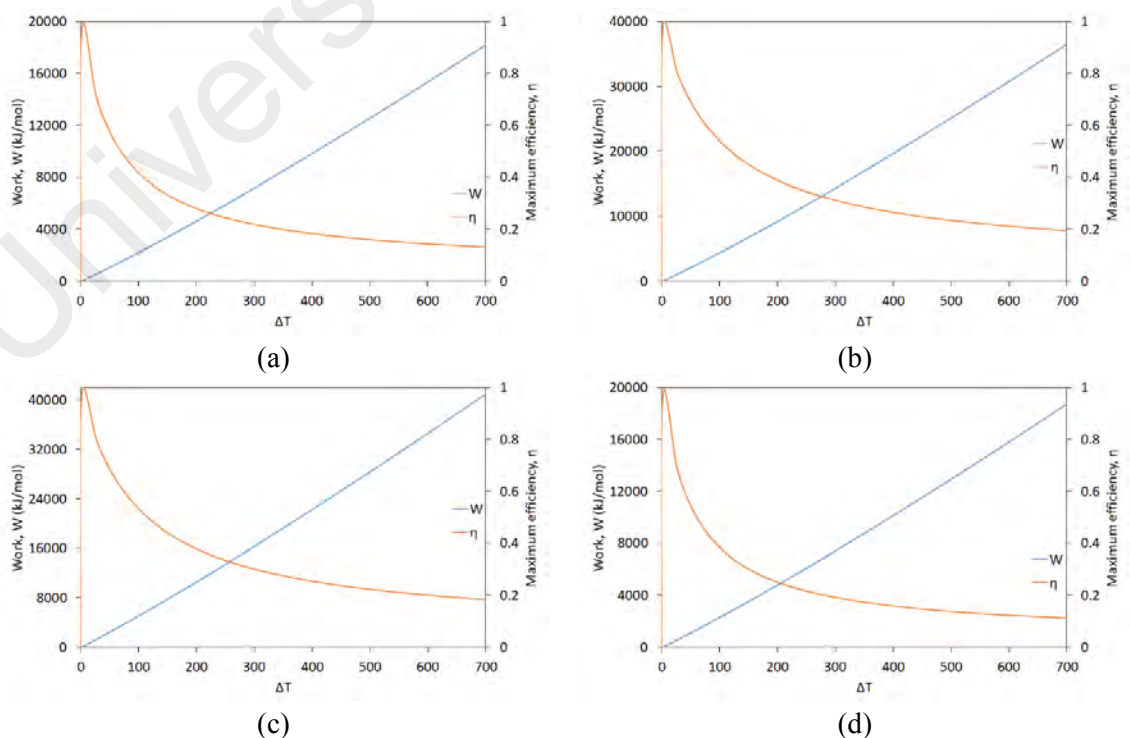


Figure 4.20. Work output and theoretical maximum efficiency at ΔT ($= T_H - T_C$) when $T_C = 298$ K for (a) 1, (b) 2, (c) 3, and (d) 4.

material as it has the highest S_e and maximum W_{out} among PILs studied. In term of maximum output, **1** and **4** are one order below than **2** and **3**, which is probably due to vibration energy are absorbed through vibration by extra H atom attached to N atom in **1**, while in **4** the energy is absorbed through pyridine ring vibration which reduces the degree of freedom proton thus reduces the kinetic energy.

Calculated values from this work are compared to literature values as shown in Table 4.5. These values are compared against molecularly near similar PILs experimental values which show they are not much different, and can be considered reliable.

Table 4.5. Comparison of Seebeck coefficient, S_e (mV/K) of pure PILs (unless stated) between this work calculated value and literatures.

PIL	S_e (mV/K)	Reference
Ethylammonium triflate (1)	0.267	This work
Diethylammonium triflate (2)	0.550	This work
Triethylammonium triflate (3)	0.607	This work
2-methylpyridinium triflate (4)	0.269	This work
1-butyl-3-methylimidazolium tetrafluoroborate	0.851	(Keppner et al., 2015)
1-hexyl-3-methylimidazolium iodide	-0.145	(Keppner et al., 2015)
Triethylsulfonium bis(trifluoromethylsulfonyl)imid	0.540	(Sosnowska et al., 2016)
1-Butyl-4-methylpyridinium tetrafluoroborate	0.465	(Sosnowska et al., 2016)
1-Ethyl-3-methylimidazolium triflate	0.361	(Sosnowska et al., 2016)
tris(2-ethylhexyl)ammonium triflate (with I/I ³ redox couple)	0.42	(Siddique et al., 2016)
1-ethyl-3-methylimidazolium tetrafluoroborate (with I/I ³ redox couple)	0.26	(Abraham et al., 2011)

4.9. Summary

This work studies the thermoelectric potential of amine based PIL systems. It was evaluated through vibration analysis of the molecular system using first principles calculation of molecular conformation and entropy. This approach is a useful strategy for molecular design, as it provides a direct pathway to assess the contribution of molecular conformation of PILs atomic vibration to the bulk thermoelectric parameters. From the work conducted, it is concluded that;

1. In a PIL system, the proton attached to N atom has a dominant vibration where the vibration mode from this bond absorbs more energy than other vibrations.

2. Under higher temperature the N-H bond vibrates more energetically and the bond length tends to be longer.
3. In these PILs systems, ΔS_{rot} are produced through the number of proton attachment to N atom. More proton are associated with more moment force that gives rise to S_{rot} . However, the ΔS_{rot} are substantially smaller than ΔS_{vib} , which make the rotational component less important. But it can possibly be augmented with a molecular system that has a large dipole moment.
4. Through a hypothetical thermodynamic cycle, the mechanism and its thermodynamic process is deduced. From the analysis, the maximum W_{out} , optimum S_e and optimum temperature gradient is calculated. The **3** system has the highest W_{out} and S_e , where its molecular system has more degree of freedom to produce more ΔS_{vib} in different conformation.

From the key findings stated above, to design a good thermoelectric material from PIL system it must has a molecular system with a large degree of freedom, and large dipole moment. This information will be useful for future rational design of future thermoelectric materials for use in TEC cells.

**CHAPTER 5: CORRELATION OF FLUORESCENCE-CHALCONE
CONFORMATION AND RELATIONSHIP TO PROTON AND CHARGE
TRANSFER MECHANISM**

5.1. Introduction to excited state intramolecular proton transfer

Excited state intramolecular proton transfer (ESIPT) in fluorescent organic molecules have been of intense interest in recent years, given their interesting photophysical properties which can be utilised in optoelectronic applications, such as biomedical imaging, sensors and optical modulators (Karton-Lifshin et al., 2011; Krawczyk et al., 2016; Oushiki et al., 2010; S. Wang et al., 2015). The prerequisite molecular structure for successful luminescence typically utilise a large p-conjugated framework or a strong donor-acceptor (D-A) skeleton. Taking example of an organic molecule in study, 4-dimethylamino-2'-hydroxychalcone (DHC), one of a molecule that has both proton donor (O atom at hydroxyl) and acceptor sites (O atom at ketone group in the chalcone backbone). The mechanism of ESIPT can be described as the chalcone existing in enol form in steady state forms an intramolecular proton transfer towards ketone group forming keto form due to photoexcitation reaction as shown in Figure 5.1.

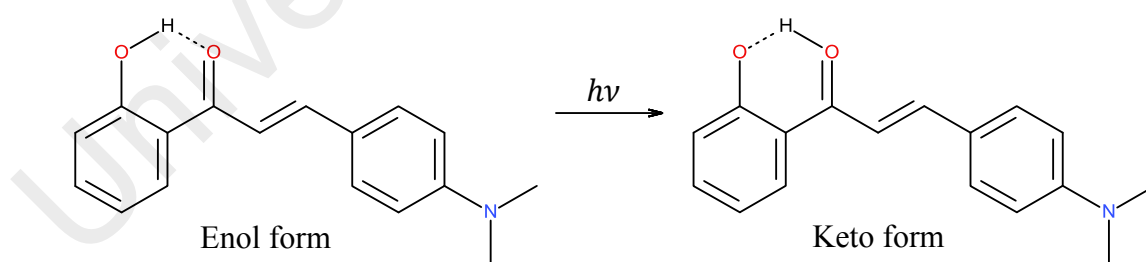


Figure 5.1. Depiction of a DHC undergoes ESIPT (from enol form to keto form) after a photoexcitation.

Upon successful ESIPT, relaxation of keto form DHC emits an intense near-infrared (NIR) fluorescence. More critically, rigid planar conformation of the chalcone backbone core both in the ground and excited states are critical for optimal fluorescence, as has been demonstrated by many molecules which possess steric hindrance have

correspondingly low quantum yield (Dommett & Crespo-Otero, 2017; Ghosh & Palit, 2015).

This can be attributed to the fact that twisting of the molecule during ESIPT provides a radiationless pathway which quenches fluorescence. Hence, extensive experimental and theoretical studies have been carried out for fluorescent organic molecules in solvents, where optimised quantum yield of fluorescence is achieved in high viscosity solvents, which are able to act as barriers to twisting of the organic molecule during the ESIPT process. In the crystalline state, however, fluorescence is limited by quenching which generally arises due to intermolecular aggregation of the molecules and their consequently adverse effect on their electronic configuration, either through attractive dipole-dipole interaction or effective intermolecular π stacking. Hence, molecular packing in the crystalline state is critical to fluorescence yield, where J-aggregation (slip-stacking/head-to-tail interaction) is favoured over H-aggregation (face-to-face interaction) for ESIPTs. J and H aggregation are shown in Figure 5.2.

ESIPT involves photo induced tautomerism between enol and keto states in a fully reversible four-level photocycle as shown in Figure 5.3, mediated by an intramolecular hydrogen bond. Emission can occur from either or both of the excited enol (E^*) or keto (K^*) states, dependent on external factors such as solvent polarity and viscosity. A signature product of the ESIPT is a characteristically large Stokes shifted fluorescence emission, in the range of $6000-12000\text{ cm}^{-1}$ without accompanying self-absorption.

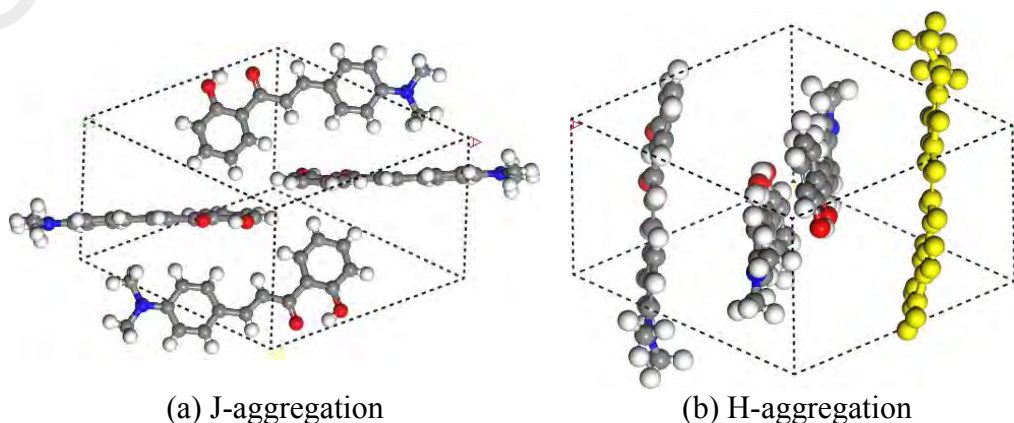


Figure 5.2. J and H aggregation crystalline packing of DHC.

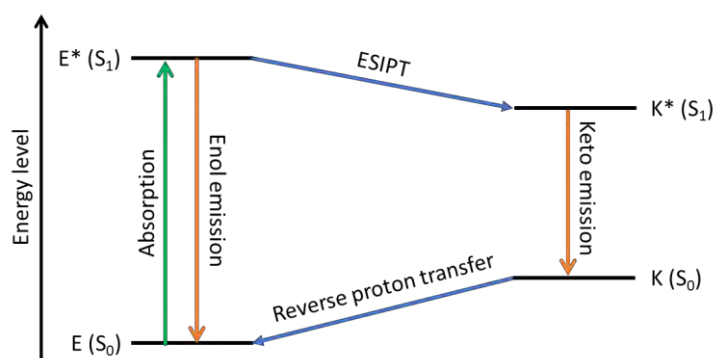


Figure 5.3. Reversible four-level photocycle.

Furthermore, population inversion of the resulting keto excited state can be easily achieved. (Kwon & Park, 2011).

The mechanism of ESIPT is extremely fast ($\sim 10^{-12}$ s), which requires ultrafast spectrometry techniques to provide a fundamental understanding of the mechanism for ESIPT. In particular, femtosecond time-resolved spectroscopy, has been particularly valuable in providing a fundamental understanding of ESIPT reaction dynamics (Douhal, Lahmani, & Zewail, 1996) and classification of photophysical properties of ESIPT molecules according to their intramolecular bonding structures (Tang et al., 2011). Prerequisite of ESIPT mechanism is D-A molecule structure where a chalcone derivative i.e. DHC among other is widely known to exhibit ESIPT (Dommett & Crespo-Otero, 2017).

5.2. Chalcones

Chalcones, belonging to the flavonoid family, are an important class of natural products with widespread distribution in fruits, vegetables, spices and tea (Ekbote et al., 2017; Orlikova et al., 2011; Varma, 1996). Chalcone is an aromatic ketone with two benzene rings. The (2*E*)-1,3-Diphenylprop-2-en-1-one (Figure 5.4) is the parent member of the chalcone series. It is known to be an important chemistry in biological compounds that often known collectively as chalcones or chalconoids. Some of these derivatives have

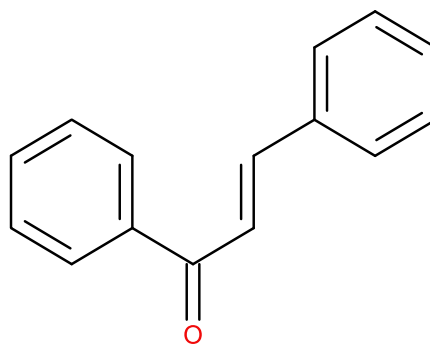


Figure 5.4. (2*E*)-1,3-Diphenylprop-2-en-1-one. Molecular structure of parent chalcone. With O atom at ketone group is often acting as acceptor site, while donor sites may come from aromatic structures or their addition groups such as -NH₃ and -OH.

been utilized as fluorescent probes in enzymatic reactions and in detecting fingerprints (Jin et al., 2015; Song et al., 2014).

They show antibacterial, antifungal, antitumor and anti-inflammatory properties. Examples from biological applications are therapeutic effect of chalcones to develop efficient medications (Katsori & Hadjipavlou-Litina, 2011; Ni, Meng, & Sikorski, 2004), and chalcones as promising lead antitumor-chemopreventive drugs by three different activities: antioxidants, cytotoxic and apoptosis inducers (Antonio et al., 2015; Chandrabose et al., 2015).

5.2.1. Applications of chalcone in opto-electronics

As mentioned briefly in sections above, chalcone derivatives are known to have wide range of applications. Despite that, this work will focus on the properties and applications in electronic fields. In electronics applications, chalcone derivatives has been researched for organic light-emitting diodes (OLED), organic field effect transistors (OFET), optics, communications, liquid crystals and frequency modulation candidates (Ramkumar et al., 2015; Ravindra et al., 2009; Tehfe et al., 2014).

In opto-electronic applications, a large p-conjugated framework or strong D-A skeleton is commonly adopted as the basic structural unit to construct NIR emitters. Chalcones that exhibit efficient luminescence in the NIR region have attracted much attention recently because of their potential applications in bioimaging, and night vision

devices (X. Cheng et al., 2015). In particular, the development of novel fluorescent molecules that emit in the physiologically relevant optical window 600-1000 nm is of increasing interest due to the large penetration of NIR radiation in most biological media, offering imaging at significant depths in living tissues which is extremely useful in bioimaging (Berezin et al., 2007; Weissleder, 2001). Chalcone nonlinear optical materials are expected to be dynamic for optical communication and opto-electronics because of their applications in high speed and high-density data processing (Prabhu et al., 2013). Second order nonlinear optical materials were used in optical switching, frequency conversion and electro-optical applications. It has been generally understood that the second-order molecular nonlinearity can be enhanced by large delocalized p-electron systems with strong donor and acceptor groups (Patil et al., 2007). The special intramolecular charge transfer (ICT) leads to delocalization of electrons within the chalcone molecule (Poornesh et al., 2009).

Photoinduced charge transfer or electron transfer processes play the fundamental role in conversion of light energy, e.g., photosynthesis in plants, artificial light harvesting systems, and in numerous existing or conceived molecular photonic applications (Balzani, 2008). Photoinduced ICT state may lead to quantitative charge separation by structural reorganization, which makes the ICT process irreversible, and this is highly desirable for solar energy conversion.

5.2.2. Photoexcitation mechanism in Chalcone

Chalcone molecule has an ESIPT-active fluorophores and D-A skeletons which are important components in the research area for constructing long-wavelength organic fluorescent molecules owing to their large Stokes shifted emission (Shimizu et al., 2012; K. Wang et al., 2014). Fluorescence originating from ESIPT is due to a large Stoke shift which avoid self-absorption or inner filter effect and it becomes a precise fluorophore analysis (J. Zhao et al., 2012). Meanwhile, the donor and acceptor substituted conjugated

organic molecular systems undergo extensive charge transfer upon photoexcitation to the electronically excited state. This D-A structure promotes electron pushing and pulling which helps the charge transfer upon excitation and thus causing fluorescence. The photoinduced ICT state may lead to quantitative charge separation by structural reorganization. In most cases, the fluorescent chalcones were obtained by attaching electron-pushing and electron-pulling functional group in the molecular backbone as well as an OH group in the phenyl ring in order to induce ESIPT (Gaber et al., 2008; Organero et al., 2000). Fluorescence coming from such molecules are more intense due to a double fluorescence mechanism.

Photoexcitation of chalcone undergoes structural changes in the charge transfer state, where the concept of relaxation of the excited state via twisting of single bond in the chalcone backbone has mainly evolved from the observations of dual fluorescence of 4-dimethylaminobenzonitrile (DMABN) and related molecules (Grabowski, Rotkiewicz, & Rettig, 2003). In this dual fluorescent mechanism, the higher energy emission occurs from the ICT state, while the twisted intramolecular charge transfer (TICT) state, in which the dimethylamino (D) group attains a dihedral angle of near perpendicular with respect to the molecular plane, is responsible for the fluorescence quenching and lower energy emission (Ghosh & Palit, 2015).. This twisted geometry allows maximum charge separation between D and A moieties due to the minimum orbital overlap that prevent electron pulling and pushing, leaving the only mechanism of fluorescence is through ICT in the remaining orbital overlap in the backbone.

5.3. 4-dimethylamino-2'-hydroxychalcone (DHC)

4-dimethylamino-2'-hydroxychalcone (DHC) (Figure 5.5) was chosen as the molecule for chalcone ESIPT-fluorescence study. DHC is a very interesting chalcone derivative where there are two photoexcitation fluorescent mechanism yields from ESIPT and ICT through the D-A backbone which give high intensity radiation.

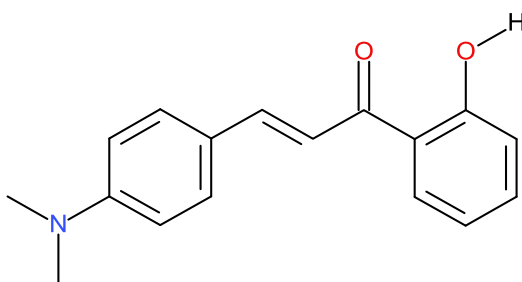


Figure 5.5. Molecule structure of chalcone in simulation, 4-dimethylamino-2'-hydroxychalcone (DHC). UIPAC name (E)-3-[4-(dimethylamino)phenyl]-1-(2-hydroxyphenyl)prop-2-en-1-one.

Regarding fluorescent characteristics of DHC, X. Cheng et al. (2015) have synthesised a series of highly efficient deep red to NIR emissive organic crystals based on the structurally simple 2'-hydroxychalcone derivatives, of which 4-dimethylamino-2'-hydroxychalcone (DHC) shows the highest fluorescence quantum yield $\phi_{em} = 0.32$ with $\lambda_{em}(max) = 650\text{--}710$ nm that is dependent on the crystal size. In solution, DHC was found to have no or weak green fluorescence that is solvent-dependent. The different spectroscopy in solution was attributed to active nonradiative channels that deplete the fluorescence intensity through intramolecular twisting and hydrogen bond disruption. A comprehensive theoretical investigation of the gas phase DHC and similar derivatives identified two major intramolecular rotation pathways in the enol and keto excited states (Dommett & Crespo-Otero, 2017). These twisting motions lead to a conical intersection that drives the molecule back to the ground state without fluorescence. In contrast, the source of the intense emission in the crystalline form was attributed to the π -conjugated framework, a strong electronic D-A skeleton (donor: $N(CH_3)_2$ -acceptor: $C=O$), and an ESIPT reaction (enol-keto tautomerisation). Fluorescence quenching due to molecular twisting and π - π stacking in the solid state was efficiently eliminated in the crystalline form of DHC due to molecular planarity and slip (edge-to-face) packing.

From absorption-fluorescence measurement reported during this study as reported by Zahid et al. (2017), the steady-state absorption and fluorescence (excitation at 450 nm) spectra of DHC in crystalline form and dissolved in methanol are shown in Figure 5.6. In

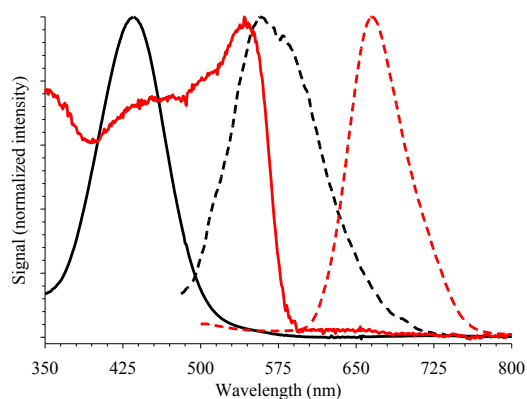


Figure 5.6. Steady-state absorption (solid lines) and fluorescence (dashed lines) spectra of DHC dissolved in methanol (black) and in crystalline form (red). $\lambda_{\text{ex}} = 450 \text{ nm}$.

methanol solution, the absorption peak at 425 nm and the fluorescence peak at 575 nm are assigned to the enol-tautomer. The absorption spectrum of the crystalline form shows a shoulder peak at $\sim 430 \text{ nm}$ for the enol tautomer and a major peak at $\sim 550 \text{ nm}$ which is assigned to the keto tautomer. Stabilization of the latter in the ground state is a consequence of the crystal packing that keeps the molecular structure of DHC rigid and planar. The red emission peak at $\sim 670 \text{ nm}$ is fluorescence from the keto tautomer (X. Cheng et al., 2015; Dommett & Crespo-Otero, 2017) that is characterized by a narrower band, compared to that in methanol, indicating more flexibility in solution in which internal motion is possible.

5.4. Study of correlation of fluorescence-conformation of Chalcone and its relationship to ESIPT and ICT effect

In this work, the use of computational molecular modelling will provide new insights to the ESIPT mechanism in chalcones. As discussed earlier, chalcones are a core structure found in many naturally occurring compounds and have been applied to wide extent in medicinal chemistry, such as detection and treatment of viral disorders, cardiovascular diseases and cancer. In fact, the D-A skeleton in chalcones enable electron withdrawal and release which leads to a drastic change in behaviour and this properties has been used in industry for various application (Ramkumar et al., 2013).

Given their biocompatibility and high quantum yield of fluorescence, it is a useful category of materials to exploit for biomedical sensing and imaging as well as non-toxic organic electronics. Normal spectroscopic techniques such as steady state absorption and fluorescence spectra, and time-resolved fluorescence spectroscopy, only provide indirect information of photo-physical and photo-chemical properties, and cannot determine the condition of the state whether the reaction occurs in the ground or excited state. In order to comprehend the detailed mechanism, computational chemistry of DFT and time-dependent density functional theory (TDDFT) have been used to clarify the different energetic and conformation structures that occur in the ESIPT and ICT states of DHC system. TDDFT is an extension of DFT calculation which is used to calculate excitation energies, frequency-dependent response properties, and photoabsorption spectra.

From previous literature, DHC has been reported to have a high yield fluorescence. It is hypothesised that it is due to combination of ESIPT and ICT fluorescence mechanism from proton transfer and electron transfer respectively. However, even though the fluorescence is occurring due to photoexcitation, it is not known fluorescence contribution from these two mechanisms quantitatively. In order to fully understand the ESIPT and ICT fluorescence mechanism of DHC in solution and crystalline, it is necessary to resolve the excited state in condition of solvent effect and crystalline state. The main objective of this study is to elucidate the mechanism of fluorescence by ESIPT and their relationship to DHC molecular conformation through DFT and TDDFT calculation by demonstrating that retaining a planar configuration during the excited state, and appropriate molecular packing are the key to high quantum yield of NIR fluorescence for chalcones.

5.4.1. Methodology

The correlation of ESIPT/ICT through chalcone conformation and fluorescence study was done using DFT and TDDFT to calculate the ground state and excited state

conformation respectively. The 4-dimethylamino-2'-hydroxychalcone (DHC) molecule input was obtained by using benzene as basic building blocks for the aromatic core and ketone, as shown in Figure 5.5. DHC molecule is simulated under two conditions which are in solution and crystalline state. In solution condition, there are 4 types of solution of different dielectric constant, ϵ_r , were studied, they are gas phase, water, methanol, and benzene, where the gas phase is the controlled environment. For crystalline condition, packing structure was obtained from single crystal XRD result, elaborated in supporting information by Zahid et al. (2017) paper.

DHC molecules in solution and crystalline is geometrically optimised in ground state and excited state using DFT and TDDFT respectively, to calculate the absorption and emission energy. Similar to other study, DFT calculations using GGA combined with exchange correlation functional PBE are utilised in geometrical optimisation. For TDDFT, the same functional GGA-PBE is used to optimised the DHC structure to its first excitation and calculate its formation energy. To evaluate the fluorescence, absorption and emission energy is calculated from DFT and TDDFT calculations.

The planarity of DHC is evaluated in ground and excited state, conformation stability is calculated as a function of bond torsion where the location of the torsion are the connecting bond between chalcone main molecule and hydroxylphenyl, p-(dimethylamino)phenyl, and dimethylamino which depicted in Figure 5.7 (a), (b) and (c) respectively.

Optimised DHC is the starting point for this simulation. Bond torsion parameters as described above are studied in solution and crystalline environments in both ground and excited states. Solution simulated through continuum solvation model are methanol, benzene and water, gas phase environment is used as control. For all environments, DHC molecule is simulated in ground and excited states condition. In this exercise, the absorption and emission energy are calculated to analyse fluorescence in the function of

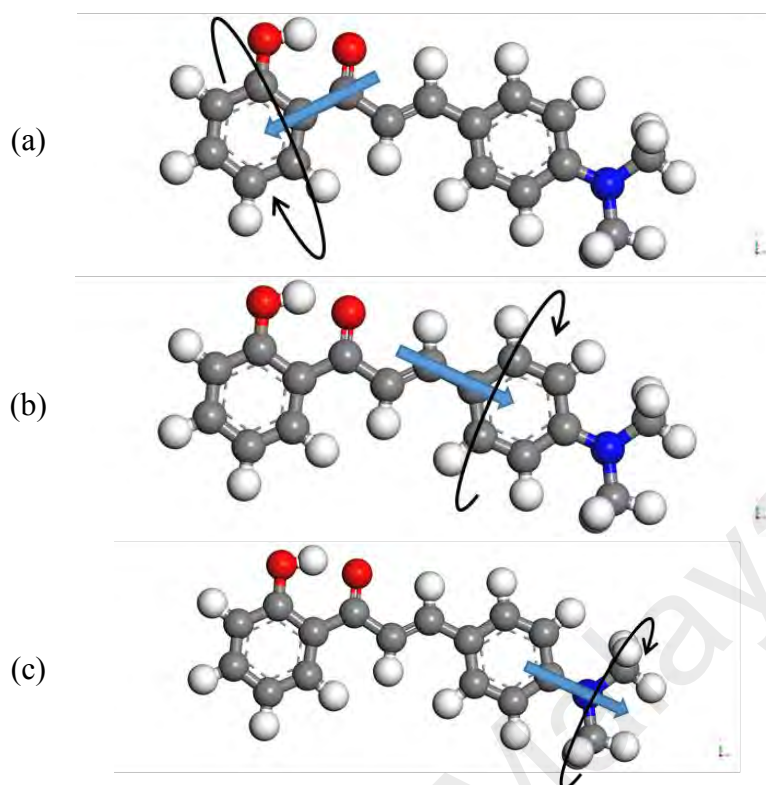


Figure 5.7. Torsion axis location of (a) hydroxyphenyl, (b) p-(dimethylamino)phenyl, and (c) dimethylamino group.

bond torsion. Meanwhile, the bond length is analysed to quantify the formation of enol and keto form of DHC. Overall flow for this exercise is shown in Figure 5.8.

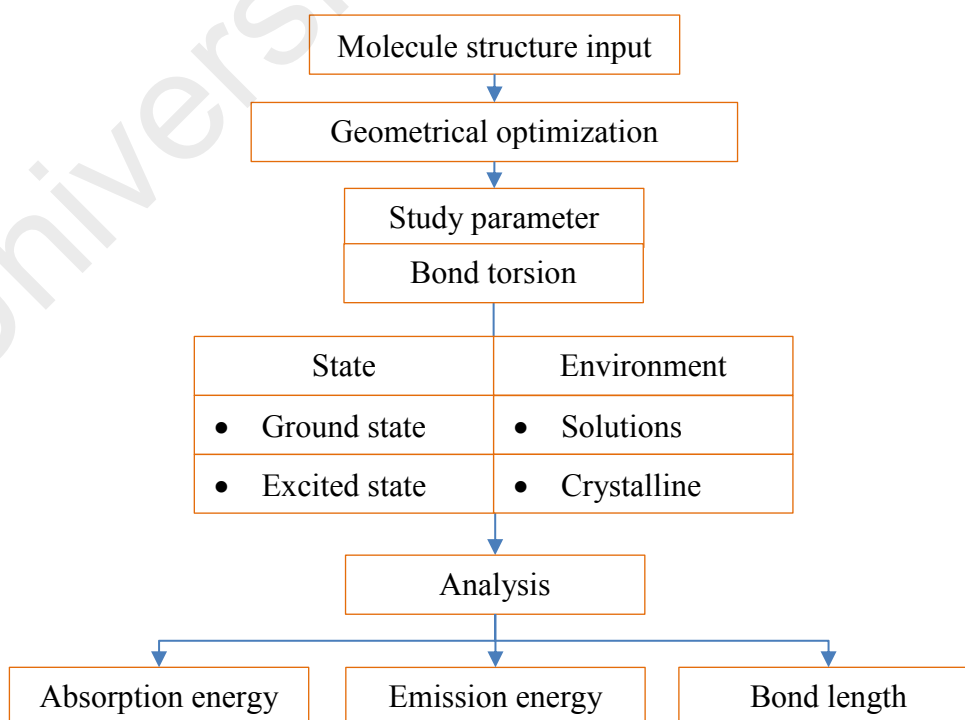


Figure 5.8. Simulation flow of DHC ESIPT study.

5.4.1.1. Simulation settings

The formation energy calculations for the DHC molecule in the ground and excited states were carried out using the first principle density functional theory (DFT) method provided by Materials Studio 2016 (MS 2016), DMol³ package. The initial molecular structure of the DHC molecule was defined by a ketone group connected to two benzene rings and was allowed full geometrical optimization without constraint. DFT calculations were performed using the general gradient approximation (GGA) with Perdew-Burke-Ernzerhof (PBE) exchange correlation functional (B. Delley, 1990, 2000; Perdew et al., 1996) with energy convergence below 10^{-5} Ha. The Kohn-Sham equation was expanded in a double numeric quality basis set with polarization functions (DNP) (B Delley, 2006) with polarization functions which should provide accurate approximation to d orbitals. The excited state geometrical optimization was accomplished by TDDFT method, employing adiabatic local density approximation (ALDA) kernels. For calculations in solvent conditions, a continuum solvation model of conductor-like screening model (COSMO) was employed to simulate solvent conditions where the dielectric constants, ϵ_r used in water, methanol and benzene were 78.54, 32.63, and 2.284, respectively. Torsional simulation of DHC was done to three bond locations that are hydroxyl-chalcone bond, p-(dimethylamino)phenyl-chalcone bond, and dimethylamino-chalcone bond, where entire DHC molecule except corresponding bond is constrained. The excited state calculations of the torsional rotation of the hydroxyphenyl ring in DHC are similar to those reported in gas phase using perturbation and coupled-cluster calculations by Dommett and Crespo-Otero (2017). Accordingly, it is assumed that including polarizable continuum models should yield reliable excited state torsional angles for DHC at the same level of theory. The settings of these calculation parameters in MS 2016 are depicted in Figure 5.9.

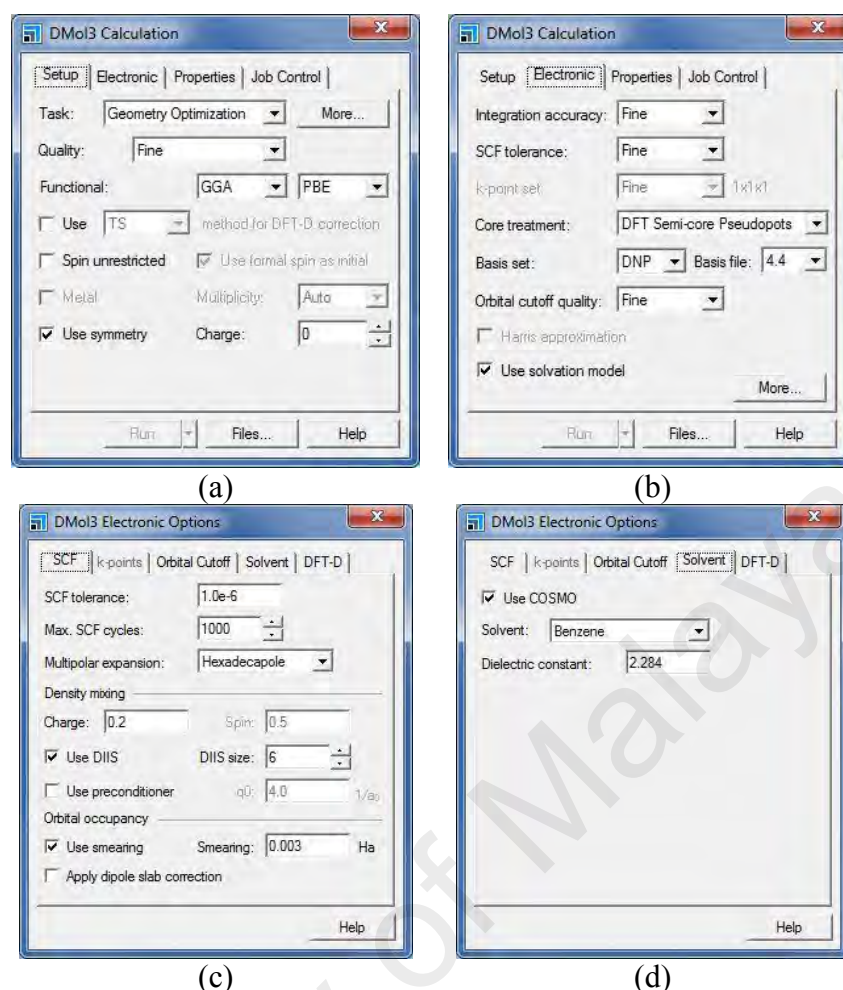


Figure 5.9. (a)Chalcone GO calculation setting. (b)Core electron treatment and basis set settings. (c) SCF options settings. (d)Solvent effect settings.

5.4.2. Results and discussion

5.4.2.1. Solvent effect on structural stability in the ground and excited states

The role of solvent is significant in the charge transfer and energy conversion process. Chemical process between solvent molecule and DHC that occurs in the condensed phase and the surrounding environment can have major effect on the absorption and emission spectra of DHC fluorophore. The polarisation and electrostatic potential of the environment helps to stabilise ground and excited states and also participate in charge and proton transfer.

To study the solvent effect to DHC bond torsion, simulation was done in several solvents as described above, i.e. methanol, benzene and water, also gas phase as controlled environment. In real condition, the chalcone family is insoluble in water,

however DHC molecule is simulated against water condition to study the solvent effect of under influence of strong dielectric solvent.

The formation energy as a function of chalcone-hydroxyphenyl group bond torsion in ground and excited state are depicted in Figure 5.10 (a) and (b) respectively. In the ground state the global minimum of torsion, τ is near to 0° which shows DHC which has a planar hydroxyphenyl bond with respect to the DHC chalcone plane. In addition, a local minimum is seen around 145° which is probably due to combination of hyperconjugation effect that caused stabilisation of OH group and O atom of ketone group (Carvalho et al., 2017) and the attraction forces of OH and O ketone. In all solutions studied, the trends obtained are similar where it is most stable at near 0° and the energy barrier in gas phase is calculated to be higher than other solvents by tenths of a kJ/mol.

In the excited state, it is found that the DHC global minimum is broad from around 30° to 40° for benzene and water condition, and from around 50° to 60° for gas phase and

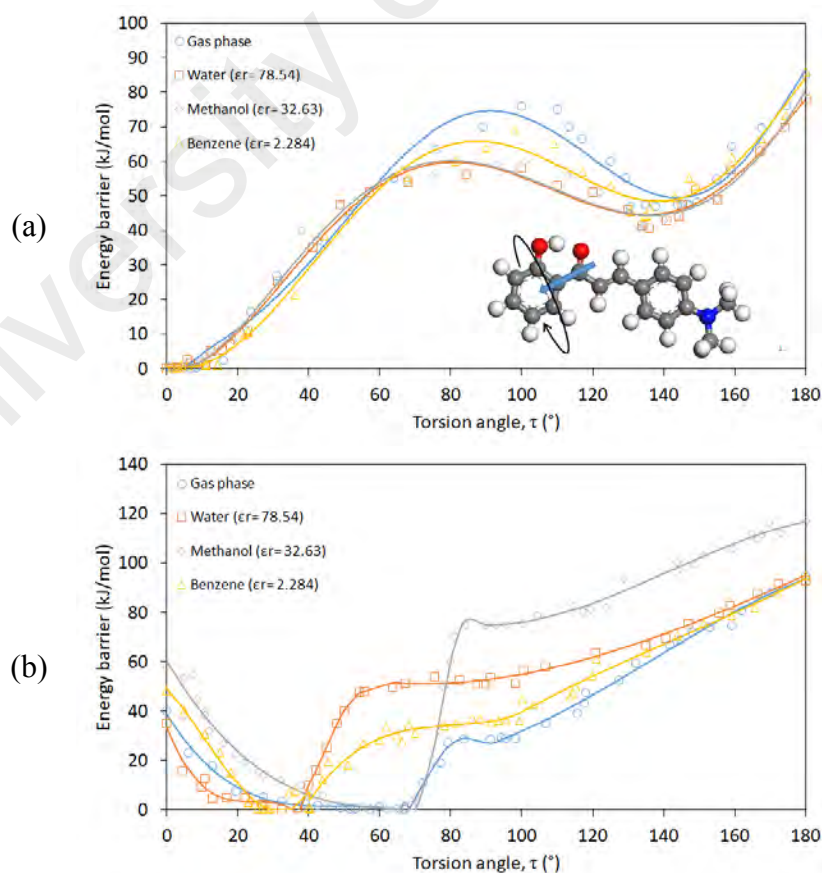


Figure 5.10. PES in the function of torsion of DHC in (a) ground state and (b) excited state. (inset) Torsion axis location of hydroxyphenyl group.

methanol. In all environment, the planarity of DHC is lost in the excited state. The conformation energy barrier from planar ground state to twisted excited state is calculated to be around 38 to 60 kJ/mol which is around 3 to 5 times of ethane staggered/eclipsed conformation difference (12 kJ/mol). However, in all condition, there is a steep energy barrier for torsion larger than the stable conformation and there is insignificant stable region around 90° in gas phase and methanol environment. The large energy barrier is probably due to changes of orbital which creates antibonding.

For p-(dimethylamino)phenyl bond torsion, DHC retains stability in planar conformation where it is stable near to $\tau \approx 0^\circ$ of as shown in Figure 5.11 (a). The maximum energy barrier obtained in all solvent condition is calculated to be around 68°, and then followed by a small local minimum around 85° to 90°. This local minimum is probably caused by the hyperconjugation of π bond of phenyl and σ bond of C-H in the chalcone backbone.

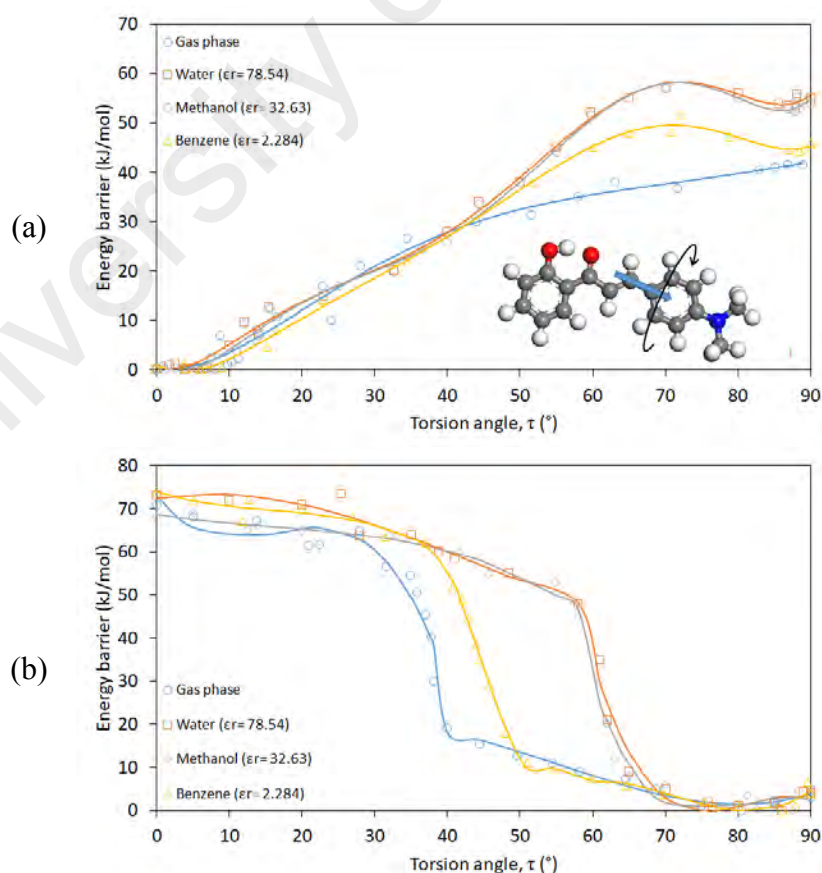


Figure 5.11. PES in the function of torsion of DHC in (a) ground state and (b) excited state. (inset) Torsion axis location of p-(dimethylamino)phenyl group.

The stability in excited state of p-(dimethylamino)phenyl bond torsion is the reverse to its ground state, where the most stable τ is 75° and extended to 90° as shown in Figure 5.11 (b). Energy barrier from planar to near perpendicular is calculated to be around 70 kJ/mol and steep transition is observed to be around 40° to 50° in gas phase and benzene, and around 65° for methanol and water. The reason of steep energy barrier is probably due to overlapping of antibonding orbital of C-phenyl and π orbital of phenyl, which reduces the stability of chalcone-p-(dimethylamino)phenyl bond.

A near linear energy barrier is observed for dimethylamino bond torsion in the ground state as depicted in Figure 5.12 (a). Similar to hydroxylphenyl and p-(dimethylamino)phenyl torsion, the most stable conformation is to retain the planarity of the DHC molecule. Lower stability for perpendicular torsion is caused by antibonding of N-C σ bond and phenyl π bond.

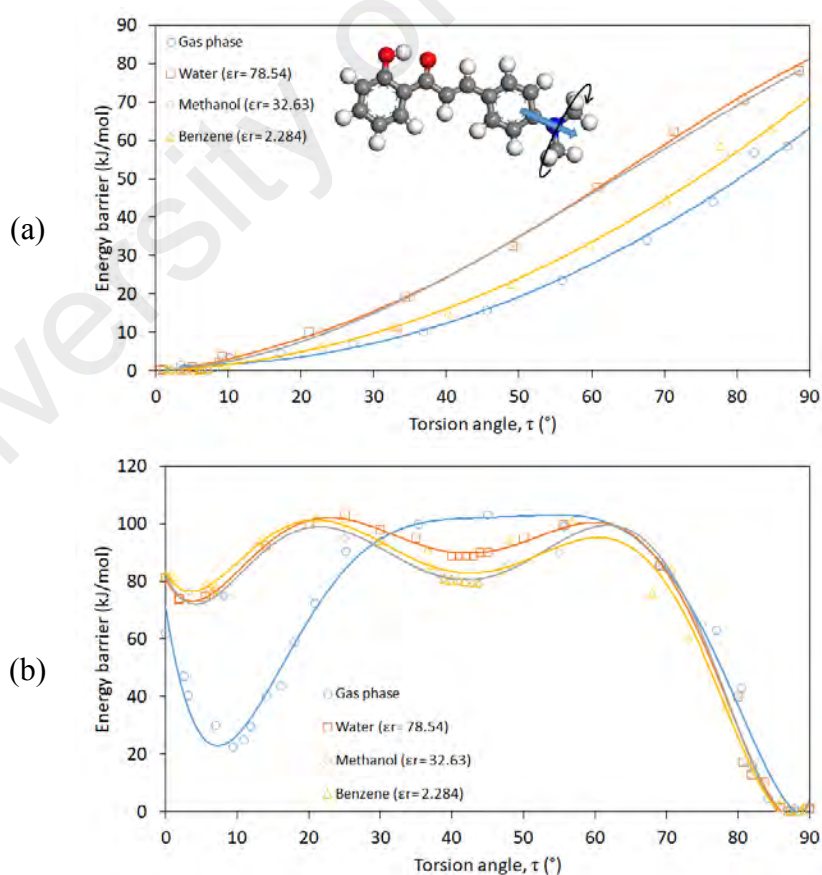


Figure 5.12. PES in the function of torsion of DHC in (a) ground state and (b) excited state. (inset) Torsion axis location of dimethylamino group.

For excited state, torsion stability in gas phase environment is found at two τ angles where there is local minimum at 8° and global minimum at 90° . In the other hand, all solvent conditions show two small minima at around 5° and 43° , and a global minimum at 90° . Local minimum in gas phase has lower energy barrier than in solvent. This and other small local minimum in solvent is may be caused by the solvent effect to the dimethylamino group which the pair electron of N atom is very sensitive to external effect such as strong dielectric solvents (Witanowski et al., 1993). However, in this result, no relationship is found leading to influence of solvent dielectric level such that methanol and benzene environment did not show significant difference.

In p-(dimethylamino)phenyl and dimethylamino torsion conditions suggests near perpendicular torsion will give stability to the DHC conformation in excited state. A perpendicular torsion requires about 60 and 80 kJ/mol for p-(dimethylamino)phenyl and dimethylamino bond respectively, meanwhile hydroxylphenyl bond only requires about 30 kJ/mol to complete a 40° to be in excited state. Compared to p-(dimethylamino)phenyl and dimethylamino bond torsion, the hydroxylphenyl torsion has the least excitation conformation energy barrier which may explain the conformation of DHC in excited state that has been reported by several literatures (Ghosh & Palit, 2015; S. Wang et al., 2015).

From here, it is simulated that in solution condition the excited state will introduce bond torsion which inhibit electronic transfer from DHC molecule D-A skeleton that quench fluorescence. Therefore, for an effective fluorescence the molecule has to be rigid to allow electron transfer. In the next section, DHC molecule is simulated in crystalline condition to see the stability of packing and to prohibit bond torsion.

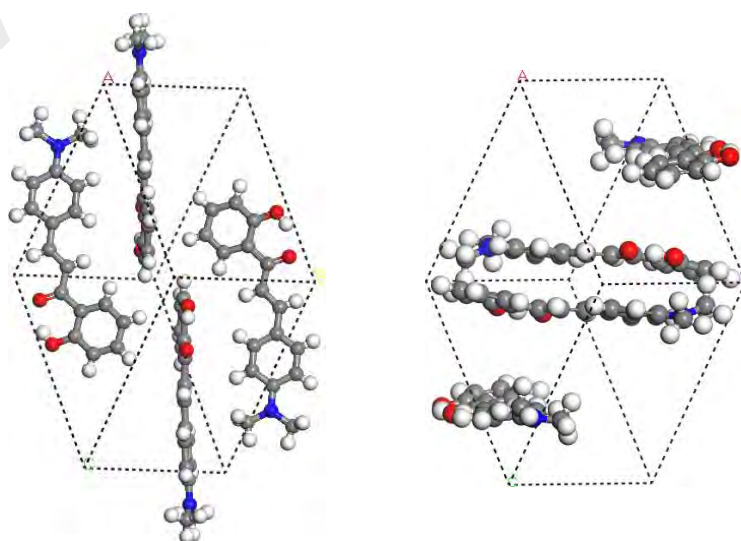
5.4.2.2. Crystalline conformation in ground and excited state

The DHC crystal conformation in the crystalline phase was conducted in 2 packing conformations (1) edge-face packing (J-aggregate) and (2) face-face packing (H-aggregate). Edge-face packing is defined when the edge of the DHC is the nearest point

to the face of adjacent molecule, while face-face packing is when the DHC planar plane is parallel to each other as shown in Figure 5.13. These two packing conformations were constructed using crystallographic data obtained from XRD analysis (Zahid et al., 2017), where it is a monoclinic crystal system of space group P-21/c. The unit cell dimensions for a, b and c length are 12.1032 Å, 10.2752 Å and 12.4890 Å respectively, and the angle for α , β and γ are 90°, 115.833° and 90° respectively.

Based on the XRD data, structure and packing optimisation is done via DFT and TDDFT for ground state and excited state respectively. DHC molecules in edge-face crystal setup retain their planarity in both ground and excited state, is expected to produce the intense fluorescence in crystal as reported (Zahid et al., 2017).

A relative formation energy of these states is listed in Table 5.1, with respect to geometrically optimised edge-face packing formation energy. ΔE_{form} of edge-face ground state to excited state is 523.473 kJ/mol, while to face-face ground state $\Delta E_{form} = 51073.6$ kJ/mol which is about 100 times more than latter. This shows that the face-face packing DHC is not stable compared to the edge-face ground state conformation. As for face-face excited state, the formation energy the geometry optimisation calculation did not able to reach a desirable convergence range of $<10^{-5}$ eV (9.648×10^{-4} kJ/mol), hinting



(a) Edge-face packing (J-aggregate) (b) Face-face packing

Figure 5.13. DHC packing conformation in crystal phase of (a) edge-face packing and (b) face-face packing.

the structure very unstable or may not exist at all. In all conditions, optimised DHC molecular geometry retains its planarity which support torsion suppression on crystalline condition. This is favourable for producing fluorescence that is induced through electron transfer in DHC D-A sites.

Table 5.1. Relative formation energy, E_{form} of DHC crystal edge-face and face-face packing with respect to ground state edge-face packing.

Crystalline packing	Relative formation energy, ΔE_{form} (kJ/mol)	
	Ground state	Excited state
Edge-face	0	523.473
Face-face	51073.6	n/a

n/a: not available.

5.4.2.3. Analysis of bond length-proton transfer

Photoexcitation of DHC also cause the ESIPT to occur as discussed above. ESIPT can be evaluated through changes of bond length in ground and excited state. Table 5.2 shows the bond length comparison between optimised conformation in ground and excited state of O_{enol} -H and O_{keto} -H, corresponding atom designation and position are shown in Figure 5.14.

In the ground state, optimisation of DHC conformation prefers shorter O_{enol} -H bond length in all solvent condition and including crystalline phase as DHC retains its planarity where all torsion angles are small ($<10^\circ$).

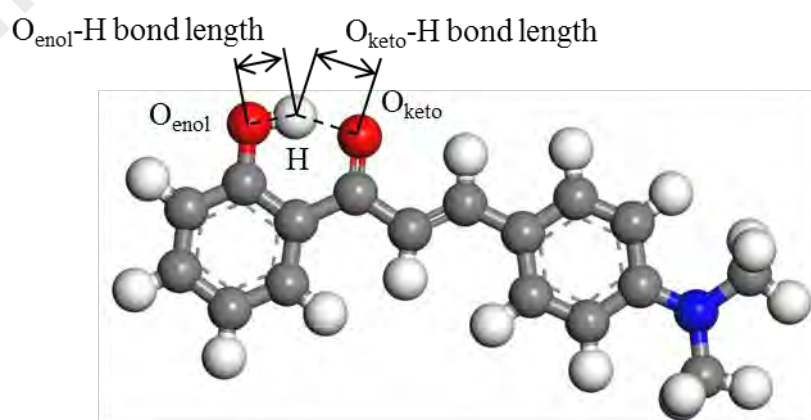


Figure 5.14. Position of O_{enol} , O_{keto} and involved H atoms and corresponding O_{enol} -H and O_{keto} -H bond lengths.

Table 5.2. Bond lengths and corresponding torsion angles of O_{enol}-H and O_{keto}-H in ground and excited state for solvent condition and crystalline phase. Torsion of hydroxylphenyl, p-(dimethylamino)phenyl and dimethylamino are labelled **1**, **2**, and **3** respectively. Shorter bond lengths values are bolded.

Torsion	Solvent (dielectric constant)	Ground state			Excited state		
		Torsion angle, τ	Bond length, Å		Torsion angle, τ	Bond length, Å	
			O _{enol} -H	O _{keto} -H		O _{enol} -H	O _{keto} -H
1	Gas phase	2.1°	1.034	1.505	57°	1.280	1.193
	Methanol ($\epsilon_r = 32.63$)	2.4°	1.044	1.474	65°	3.178	0.978
	Benzene ($\epsilon_r = 2.284$)	2.6°	1.037	1.497	28°	1.407	1.094
	Water ($\epsilon_r = 78.54$)	2.3°	1.045	1.473	32°	1.621	1.029
2	Gas phase	3.9°	1.020	1.567	89°	1.094	1.358
	Methanol	3.6°	1.042	1.479	88°	1.086	1.378
	Benzene	6.1°	1.036	1.500	89°	1.062	1.429
	Water	3.8°	1.043	1.477	87°	1.086	1.375
3	Gas phase	6.4°	1.033	1.511	9.7°	1.233	1.210
					89°	1.058	1.440
	Methanol	4.1°	1.035	1.505	8.0°	1.042	1.490
					44°	1.051	1.459
					88°	1.067	1.416
					89°	1.064	1.426
	Benzene	2.6°	1.040	1.486	6.5°	1.036	1.505
					43°	1.041	1.486
Water	5.3°	1.045	1.474	2.0°	1.043	1.489	
				42°	1.051	1.451	
				87°	1.068	1.413	
				87°	1.068	1.413	
Crystal	Edge-face	n/a	1.050	1.451	n/a	1.308	1.147

n/a: not applicable.

In the excited state, conformation optimisation of DHC structure changes the bond strength which indicate ESIPT in hydroxylphenyl torsion condition and crystalline phase, where the O_{keto}-H bond length were found to be smaller than O_{enol}-H. ESIPT of DHC in crystalline state has been confirmed in several reports (Dommett & Crespo-Otero, 2017; Zahid et al., 2017). However, ESIPT in solvent condition due to torsion at hydroxylphenyl-chalcone bond is yet to be reported, despite the emission due to hydroxylphenyl torsion dwells in far IR region which quenches fluorescence in NIR as discussed in previous section. In most mechanisms reported, ESIPT in solvent condition is inhibited due to hydrogen bonding to solvent, this finding may alter the explanation for

ESIPT mechanism. It can be hypothesised that; emission energy is quenched by hydroxylphenyl torsion and not due to ESIPT inhibition.

As for p-(dimethylamino)phenyl and dimethylamino torsion, ESIPT was inhibited where bond length of $O_{\text{enol}}\text{-H}$ remained shorter than $O_{\text{keto}}\text{-H}$ even in excited state indicating of no proton transfer, except for dimethylamino torsion in gas phase at small angle. The conformation for dimethylamino small torsion angle is actually similar to that crystalline phase condition where DHC molecule retains its planarity thus ESIPT occurrence also follows. ESIPT inhibition due to these torsions is caused by the torsion using energy absorbed for torsion rather than energy use for ESIPT process. The energy is used for destabilising corresponding bond thus allowing torsion and proton transfer cannot occur as there is not enough energy. From this, ESIPT inhibition is probably unrelated to solvent making hydrogen bonding to OH but due to torsion at p-(dimethylamino)phenyl and dimethylamino.

5.4.2.4. Absorption and emission energy analysis

From the excited state simulation, the absorption energy and emission energy are calculated for every excited stable conformation of each torsion. This is to identify the absorption and emission energy in the function of bond torsion and compared against experimental results. Absorption and emission energy along with corresponding torsion angle, τ are listed in Table 5.3. In the table, absorption and emission energy are converted into wavelength expression to compare the absorption and emission wavelength.

In solvent condition, the molecule conformation in gas phase is used as control condition where absorption energy, E_{ab} are 248.07 and 192.10 kJ/mol for hydroxylphenyl and p-(dimethylamino)phenyl bond torsion respectively, and 248.00 and 131.26 kJ/mol for dimethylamino bond torsion at 9° and 89° . Torsion of hydroxylphenyl and p-

Table 5.3. Absorption energy, E_{ab} and emission energy, E_{em} of hydroxylphenyl (1), p-(dimethylamino)phenyl (2) and dimethylamino (3) stable bond torsion in excited state.

Torsion	Solvent (dielectric constant)	Torsion angle, τ	Absorption		Emission		
			E_{ab} (kJ/mol)	λ_{ab} (nm)	E_{em} (kJ/mol)	λ_{em} (nm)	
1	Gas phase	57°	248.07	482	59.37	2015	
	Methanol ($\epsilon_r = 32.63$)	65°	234.53	510	40.64	2944	
	Benzene ($\epsilon_r = 2.284$)	28°	191.73	624	117.02	1022	
	Water ($\epsilon_r = 78.54$)	32°	235.35	508	109.34	1094	
2	Gas phase	89°	192.10	623	88.09	1358	
	Methanol	88°	155.72	768	98.19	1218	
	Benzene	89°	142.75	838	128.93	928	
	Water	87°	154.74	773	96.85	1235	
3	Gas phase	9.7°	248.00	482	161.52	741	
		89°	131.26	911	83.12	1439	
	Methanol	8.0°	232.68	514	205.38	582	
		44°	219.78	544	188.87	633	
		88°	207.35	577	59.53	2010	
		6.5°	244.62	489	216.74	552	
	Benzene	43°	233.08	513	202.03	592	
		89°	221.20	541	73.15	1635	
		Water	2.0°	231.85	516	205.51	582
			42°	184.06	650	125.81	951
87°	206.48		579	58.71	2038		
Crystalline							
Edge-face	n/a	238.78	501	185.18	646		

n/a: not applicable.

(dimethylamino)phenyl bond can be correlated to solvent dielectric constant where under influence of low dielectric solvent benzene ($\epsilon_r = 2.284$), the torsion of hydroxylphenyl and p-(dimethylamino)phenyl in excited state absorption energy, E_{ab} is the smallest compared than in higher dielectric solvent (i.e. methanol ($\epsilon_r = 32.63$) and water ($\epsilon_r = 78.54$)). On the other hand, E_{ab} of dimethylamino torsion is highest for benzene. From this, presence of benzene destabilises hydroxylphenyl and p-(dimethylamino)phenyl bond while strengthens dimethylamino bond by interaction to the phenyls of DHC. Meanwhile, methanol and water interact with OH and N(CH₃)₂ groups to create hydrogen bonds. This will cause the stabilisation of those bonds through solvents of higher polarity that reduces the electron donating effect by the OH group in

hydroxyphenyl and N(CH₃)₂ group of dimethylaminophenyl. This effect is demonstrated by the fact that in dimethylamino the torsion absorption energy of DHC in methanol and water are less than those in the benzene solvent.

When E_{ab} is expressed in term of wavelength, λ_{ab} , through equation $E = hc / \lambda$ (h : Planck's constant, c : speed of light, λ : wavelength), it can be correlated to Figure 5.6 where the wavelength of absorption and emission are plotted. From the simulation, absorption wavelength, λ_{ab} is overestimated over tenth of nm to around 500 nm while experimentally, the absorption of DHC solution in methanol peaked at 425 nm. This is probably due to the method approximation of GGA-PBE functional which is not the best choice of functional for long range interaction such as hydrogen bonding. Examples of better functional for H bond are hybrid functional B3LYP and DFT meta-GGA TPSS.

For emissions, all E_{em} at global minimum are calculated to be around <128 kJ/mol, which makes λ_{em} in the far-IR region, which may explain the fluorescence quenching in solution condition. In addition, λ_{em} of dimethylamino for small angle torsion calculated to be around 552-582 nm which is overestimation of small intensity 575 nm emission peak obtained from spectroscopy of DHC in methanol. The small intensity is due to a small probability of occurrence of that torsion.

A similar approach for crystalline phase for edge-face packing shows that λ_{ab} and λ_{em} are 501 nm and 646 nm, correlated to 550 nm and 670 nm of experimental method respectively. In the crystal phase, simulation give off an underestimation of wavelength, against experimental wavelength.

Fluorescence of DHC relies on both electron transfer between donor and acceptor sites, and formation of keto tautomer through ESIPT which enable the reversible four level photocycle. This is apparent where the highest fluorescence is calculated in crystalline condition where it allow ESIPT forming keto tautomer and good electron transfer through D-A sites by planar structure.

In other conditions, there is no intense fluorescence calculated that is caused by neither allowing electron transfer nor ESIPT mechanism. The stability of DHC molecule in excited state as listed in Table 5.2 shows that keto tautomer formation only occurred in the hydroxyphenyl torsion and crystalline condition. Meanwhile, the emission wavelength of DHC excited state as listed in Table 5.3, hydroxyphenyl and p-(dimethylamino)phenyl torsion DHC emission is quenched into invisible wavelength, leaving several emissions of dimethylamino torsion. These emissions of dimethylamino torsion can be correlated to weak green emission observed in solution.

5.5. Summary

This work studies mechanism of ESIPT of DHC of the chalcone family using DFT and TDDFT computational chemistry method for ground and excited states respectively. This approach is very useful to investigate the ground and excited states conformation and their relating properties and characteristics which is helpful to determine mechanism of certain process such as fluorescence. From energy-torsion PES in various solvent, crystalline packing conformation, analysis on absorption and emission energy, and ESIPT mechanism analysis on DHC as discussed above, the conclusions are as follows:

1. DHC prefers to retain its planarity in ground state condition regardless of solvent. The molecule is stable in excited state when p-(dimethylamino)phenyl and dimethylamino bond torsion, τ is near to 90° . However, for hydroxyphenyl torsion it is stable when $\tau \approx 40^\circ - 60^\circ$.
2. In crystalline phase, DHC prefers the edge-face packing which more stable than face-face packing. Edge-face packing prohibits π - π orbital overlap and promotes ESIPT which induce NIR fluorescence.
3. Intense fluorescence is found in crystalline phase DHC. The fluorescence is induced by ease of electron transfer in DHC D-A sites in planar molecule structure

and keto tautomer formation by ESIPT mechanism that allow four level photocycle.

4. The ESIPT in solvent condition is found to be inhibited when torsion occurs at p-(dimethylamino)phenyl and dimethylamino. However, ESIPT is allowed for hydroxyphenyl torsion where it forms keto tautomer in excited state.
5. In most solvent condition, NIR fluorescence of DHC is quenched by emission wavelength is shifted to far IR-microwave region compared to crystalline phase.
6. However, the local minima introduced in dimethylamino bond torsion due to solvent effect helps to explain weak emission of DHC in solvent that these minima enable emission at around 552 nm to 582 nm from coming from relaxation of those torsion.

From these key findings stated above, fluorescence of DHC is promoted due to its ability to retain planar molecule and facilitates ESIPT mechanism such as in crystalline phase. This information surely helps in order to design a useful material for fluorescence of chalcone based.

CHAPTER 6: CONCLUSION

There are 3 major categories of materials that was studied in this work. The summary of conclusion is described as below.

6.1. Structural effect of DLC

In the first work, 2,3,6,7,10,11-hexahydroxytriphenylene (HAT6) has been investigated in its 3 parameters of columnar conformation; core-core facial separation (D), angular twist (θ), and lateral slide (L) toward effect of formation energy, band gap (BG), and density of state (DOS).

This work has successfully elucidated the relationship between electronic structure and columnar structure. First, stacking distance of HAT6 is the main factor of electronic transfer through the column where π - π overlap at closer distance lower BG thus allowing electronic transfer, while large distance increase intermolecular delocalisation and breaks the π - π overlap. Second, the electronic transfer ability is an inverse relation to columnar stability, due to atomic repulsion. This can be overcome by structural modification at tails to allow stacking at close distance. Third, twist in HAT6 column resulted the molecule to develop chiral characteristics due to strong electronegativity of O atom and creates localised and delocalised region across the molecule. This also effect the column to be naturally in twisted conformation.

Through the work illustrated above, an important understanding of the correlation between the structural parameters of the DLC on the electronic structure can be derived as a function of molecular structure. The electronic structure can be designed through refinement of the columnar phase packing. This is particularly important for the investigations of DLCs as potential candidates for OTEs, and is projected to be useful for other scenarios such as the orbital interaction between the DLC and electrode material to study charge injection from electrodes.

6.2. Thermodynamic study of PIL

The second work explain thermodynamic of four types of amine based PILs (ethylammonium triflate, diethylammonium triflate, triethylammonium triflate, 2-pyridinium triflate) were studied in 2 stable states where the entropy difference from the two states was calculated in terms of thermoelectric Seebeck potential in the second work.

Quantum thermodynamic analysis approach is a useful strategy for molecular design, as it provides a direct pathway to assess the contribution of molecular conformation of PILs atomic vibration to the bulk thermoelectric parameters. In conclusion, the PIL thermoelectric potential can be simulated through vibrational analysis of the molecule. In PIL system, N-H bond has the dominant vibration than others. The bond length also longer under high temperature where it vibrates energetically. Large dipole moment may increase rotational entropy that can be additional to larger vibrational entropy that will increase Seebeck coefficient.

A hypothetical thermodynamic cycle constructed from entropy difference of 2 PILs conformations predict the vibrational Seebeck potential. The mechanism and its thermodynamic process is also deduced from the cycle. The thermodynamic potential, such as work output, and Seebeck coefficient are compared to each other.

From work done above, the PIL is a promising system for energy generation applications. Thermodynamic reaction mechanism of proton transfer in PIL provide a useful insight on how the system itself work and how can it be gained.

6.3. Excitation-structure effect in Chalcone

In the third work, fluorescence mechanism of 2'-hydroxychalcone ((E)-3-[4-(dimethylamino)phenyl]-1-(2-hydroxyphenyl)prop-2-en-1-one) (DHC) was studied using DFT quantum modelling. DHC is a molecule that consist of donor (D) and acceptor (A) substituted conjugated organic molecular systems, undergo extensive charge transfer upon photoexcitation to the electronically excited state. The fluorescence of DHC is

caused by electronic transfer between D-A and excited state intermolecular proton transfer (ESIPT). This work studies mechanism of ESIPT of DHC of the chalcone family using DFT and TDDFT computational chemistry method for ground and excited states respectively. This approach is very useful to investigate the ground and excited states conformation and their relating properties and characteristics which is helpful to determine mechanism of certain process such as fluorescence.

From this work it is found that the intense fluorescence is found in crystalline phase. It is induced by ease of electron transfer in DHC D-A sites in planar molecule structure and keto tautomer formation by ESIPT mechanism that allow four level photocycle. Where in crystalline phase, DHC prefers the edge-face packing which more stable than face-face packing. Edge-face packing prohibits π - π orbital overlap and promotes ESIPT which induce NIR fluorescence.

In most solvent condition, NIR fluorescence of DHC is quenched by emission wavelength is shifted to far IR-microwave region compared to crystalline phase. Despite the fact that DHC prefers to retain its planarity in ground state condition regardless of solvent. The molecule is stable in excited state when p-(dimethylamino)phenyl and dimethylamino bond torsion, τ is near to 90° . However, for hydroxyphenyl torsion it is stable when $\tau \approx 40^\circ - 60^\circ$.

In addition, the local minima introduced in dimethylamino bond torsion due to solvent effect induces weak green emission of DHC in solvent that these minima enable emission at around 552 nm to 582 nm from coming from relaxation of those torsion.

The ESIPT in solvent condition is found to be inhibited when torsion occurs at p-(dimethylamino)phenyl and dimethylamino. ESIPT only occurred for hydroxyphenyl torsion where it forms keto tautomer in excited state.

Through the three segments work elaborated above, demonstration of molecular design of organic electronic materials using DFT modelling to provide an understanding

of the correlation between structure and electronic property has been illustrated. This will provide a useful basis for optimised molecular design for targeted applications, through enhancement of electronic properties through rationally considered molecular structure.

University of Malaya

REFERENCES

- Abate, A., Petrozza, A., Roiati, V., Guarnera, S., Snaith, H., Matteucci, F., . . . Resnati, G. (2012). A polyfluoroalkyl imidazolium ionic liquid as iodide ion source in dye sensitized solar cells. *Organic Electronics*, 13(11), 2474-2478.
- Abdallah, D. J., Robertson, A., Hsu, H.-F., & Weiss, R. G. (2000). Smectic Liquid-Crystalline Phases of Quaternary Group VA (Especially Phosphonium) Salts with Three Equivalent Long n-Alkyl Chains. How Do Layered Assemblies Form in Liquid-Crystalline and Crystalline Phases? *Journal of the American Chemical Society*, 122(13), 3053-3062.
- Abdullah, N., Arifin, Z., Tiekink, E. R. T., Sharmin, N., Syamimi, N., Tajidi, A., & Hussin, S. A. M. (2016). Covalent and ionic Cu(II) complexes with cyclam and substituted benzoato ligands: structural, thermal, redox and mesomorphic properties. *Journal of Coordination Chemistry*, 69(5), 862-878.
- Abdullah, N., Azil, A., Marlina, A., & M. Noor, N. L. (2015). Magnetic, Photophysical and Thermal Properties of Complexes of Iron(II) with Structurally Different Schiff Bases. *Asian Journal of Chemistry*, 27(7), 2359-2364.
- Abdullah, N., Halid, Y. Y., Ti, T. J., & Azil, A. (2016). Crystal structures and mesomorphic properties of Schiff base homologs and derivatives, and magnetic properties of their dimeric and dinuclear copper(II) complexes. *Molecular Crystals and Liquid Crystals*, 624(1), 132-143.
- Abdullah, N., Hashim, R., Ozair, L. N., Al-Hakem, Y., Samsudin, H., Marlina, A., . . . Nordin, A. R. (2015). Structural, mesomorphic, photoluminescence and thermoelectric studies of mononuclear and polymeric complexes of copper(ii) with 2-hexyldecanoato and 4,4'-bipyridine ligands. *J. Mater. Chem. C*, 3(42), 11036-11045.
- Abdullah, N., M. Noor, N. L., Nordin, A. R., Halcrow, M. A., MacFarlane, D. R., Lazar, M. A., . . . Heinrich, B. (2015). Spin-crossover, mesomorphic and thermoelectrical properties of cobalt(ii) complexes with alkylated N3-Schiff bases. *J. Mater. Chem. C*, 3(11), 2491-2499.
- Abdullah, N., Mohd Said, S., Marlina, A., Roslan, M. F., Azil, A., & Nordin, A. R. (2015). Photophysical and electrochemical studies of multinuclear complexes of iron(II) with acetate and extended conjugated N-donor ligands. *ScientificWorldJournal*, 2015, 860537.
- Abraham, T. J., MacFarlane, D. R., & Pringle, J. M. (2011). Seebeck coefficients in ionic liquids--prospects for thermo-electrochemical cells. *Chem Commun (Camb)*, 47(22), 6260-6262.

- Abraham, T. J., MacFarlane, D. R., & Pringle, J. M. (2013). High Seebeck coefficient redox ionic liquid electrolytes for thermal energy harvesting. *Energy & Environmental Science*, 6(9), 2639-2645.
- Adam, D., Schuhmacher, P., Simmerer, J., Häussling, L., Siemensmeyer, K., Etzbacher, K., . . . Haarer, D. (1994). Fast photoconduction in the highly ordered columnar phase of a discotic liquid crystal. *Nature*, 371(6493), 141-143.
- Alameddine, B., Aebischer, O. F., Amrein, W., Donnio, B., Deschenaux, R., Guillon, D., . . . Jenny, T. A. (2005). Mesomorphic hexabenzocoronenes bearing perfluorinated chains. *Chemistry of Materials*, 17(19), 4798-4807.
- Albanese, D., Landini, D., Maia, A., & Penso, M. (1999). Phase transfer catalysis: some recent applications in organic synthesis. *Journal of Molecular Catalysis A: Chemical*, 150(1-2), 113-131.
- Angell, C. A., Byrne, N., & Belieres, J. P. (2007). Parallel developments in aprotic and protic ionic liquids: physical chemistry and applications. *Acc Chem Res*, 40(11), 1228-1236.
- Antonio, J. L.-G., Nuria, A., Dolores, M.-M., Inmaculada, N., & Carmen, M.-C. (2015). Chalcones as Promising Lead Compounds on Cancer Therapy. *Current Medicinal Chemistry*, 22(30), 3407-3425.
- Arikainen, E. O., Boden, N., Bushby, R. J., Clements, J., Movaghar, B., & Wood, A. (1995). Effects of side-chain length on the charge transport properties of discotic liquid crystals and their implications for the transport mechanism. *Journal of Materials Chemistry*, 5(12), 2161.
- Asahina, S., & Sorai, M. (2003). Thermodynamic properties of discotic mesogens: heat capacities and phase transitions of benzene-hexa-n-alkanoates. *Journal of Chemical Thermodynamics*, 35(4), 649-666.
- Ashizawa, R., & Noguchi, T. (2014). Effects of hydrogen bonding interactions on the redox potential and molecular vibrations of plastoquinone as studied using density functional theory calculations. *Phys Chem Chem Phys*, 16(24), 11864-11876.
- Attri, P., & Venkatesu, P. (2011). Thermodynamic characterization of the biocompatible ionic liquid effects on protein model compounds and their functional groups. *Physical Chemistry Chemical Physics*, 13(14), 6566-6575.
- Bag, S., Maingi, V., Maiti, P. K., Yelk, J., Glaser, M. A., Walba, D. M., & Clark, N. A. (2015). Molecular structure of the discotic liquid crystalline phase of hexa-peri-hexabenzocoronene/oligothiophene hybrid and their charge transport properties. *The Journal of Chemical Physics*, 143(14), 144505.

- Bai, Y., Cao, Y., Zhang, J., Wang, M., Li, R., Wang, P., . . . Grätzel, M. (2008). High-performance dye-sensitized solar cells based on solvent-free electrolytes produced from eutectic melts. *Nature Materials*, 7, 626.
- Bai, Y., Zhang, J., Wang, Y., Zhang, M., & Wang, P. (2011). Lithium-modulated conduction band edge shifts and charge-transfer dynamics in dye-sensitized solar cells based on a dicyanamide ionic liquid. *Langmuir*, 27(8), 4749-4755.
- Balzani, V. (2008). *Electron Transfer in Chemistry*: Wiley-VCH Verlag GmbH.
- Barlow, S., Zhang, Q., Kaafarani, B. R., Risko, C., Amy, F., Chan, C. K., . . . Marder, S. R. (2007). Synthesis, ionisation potentials and electron affinities of hexaazatrinaphthylene derivatives. *Chemistry*, 13(12), 3537-3547.
- Bässler, H. (1993). Charge Transport in Disordered Organic Photoconductors a Monte Carlo Simulation Study. *physica status solidi (b)*, 175(1), 15-56.
- Bautista-Martinez, J. A., Tang, L., Belieres, J. P., Zeller, R., Angell, C. A., & Friesen, C. (2009). Hydrogen Redox in Protic Ionic Liquids and a Direct Measurement of Proton Thermodynamics. *Journal of Physical Chemistry C*, 113(28), 12586-12593.
- Becke, A. D. (1988). A multicenter numerical integration scheme for polyatomic molecules. *The Journal of Chemical Physics*, 88(4), 2547-2553.
- Becke, A. D. (1993). Density- functional thermochemistry. III. The role of exact exchange. *The Journal of Chemical Physics*, 98(7), 5648-5652.
- Belieres, J.-P., & Angell, C. A. (2007). Protic Ionic Liquids: Preparation, Characterization, and Proton Free Energy Level Representation. *J Phys Chem B*, 111(18), 4926-4937.
- Belieres, J.-P., Gervasio, D., & Angell, C. A. (2006). Binary inorganic salt mixtures as high conductivity liquid electrolytes for >100 °C fuel cells. *Chem. Commun.*(46), 4799-4801.
- Belieres, J. P., & Angell, C. A. (2007). Protic ionic liquids: preparation, characterization, and proton free energy level representation. *J Phys Chem B*, 111(18), 4926-4937.
- Benning, S., Kitzerow, H.-S., Bock, H., & Achard, M.-F. (2000). Fluorescent columnar liquid crystalline 3, 4, 9, 10-tetra-(n-alkoxycarbonyl)-perylene. *Liquid Crystals*, 27(7), 901-906.
- Berezin, M. Y., Lee, H., Akers, W., & Achilefu, S. (2007). Near infrared dyes as lifetime solvatochromic probes for micropolarity measurements of biological systems. *Biophys J*, 93(8), 2892-2899.
- Bhatt, A. I., Mechler, A., Martin, L. L., & Bond, A. M. (2007). Synthesis of Ag and Au nanostructures in an ionic liquid: thermodynamic and kinetic effects

- underlying nanoparticle, cluster and nanowire formation. *Journal of Materials Chemistry*, 17(21), 2241-2250.
- Blackmore, E. S., & Tiddy, G. J. T. (1988). Phase behaviour and lyotropic liquid crystals in cationic surfactant-water systems. *Journal of the Chemical Society, Faraday Transactions 2: Molecular and Chemical Physics*, 84(8), 1115-1127.
- Boden, N., Bushby, R., & Clements, J. (1994). Electron transport along molecular stacks in discotic liquid crystals. *Journal of Materials Science: Materials in Electronics*, 5(2), 83-88.
- Boden, N., Bushby, R. J., Clements, J., Donovan, K., Movaghar, B., & Kreouzis, T. (1998). Charge dynamics and recombination kinetics in columnar discotic liquid crystals. *Physical Review B*, 58(6), 3063-3074.
- Boden, N., Bushby, R. J., Clements, J., & Movaghar, B. (1999). Device applications of charge transport in discotic liquid crystals. *Journal of Materials Chemistry*, 9(9), 2081-2086.
- Boden, N., Bushby, R. J., Clements, J., Movaghar, B., Donovan, K. J., & Kreouzis, T. (1995). Mechanism of charge transport in discotic liquid crystals. *Phys Rev B Condens Matter*, 52(18), 13274-13280.
- Boden, N., J. Bushby, R., Clements, J., & Movaghar, B. (1999). Device applications of charge transport in discotic liquid crystals. *Journal of Materials Chemistry*, 9(9), 2081-2086.
- Bonetti, M., Nakamae, S., Huang, B. T., Salez, T. J., Wiertel-Gasquet, C., & Roger, M. (2015). Thermoelectric energy recovery at ionic-liquid/electrode interface. *J Chem Phys*, 142(24), 244708.
- Born, M., & Oppenheimer, R. (1927). Zur Quantentheorie der Molekeln. *Annalen der Physik*, 389(20), 457-484.
- Brunsveld, L., Folmer, B. J. B., Meijer, E. W., & Sijbesma, R. P. (2001). Supramolecular Polymers. *Chemical Reviews*, 101(12), 4071-4098.
- Bubnova, O., & Crispin, X. (2012). Towards polymer-based organic thermoelectric generators. *Energy & Environmental Science*, 5(11), 9345.
- Buseti, A., Crawford, D. E., Earle, M. J., Gilea, M. A., Gilmore, B. F., Gorman, S. P., . . . Seddon, K. R. (2010). Antimicrobial and antibiofilm activities of 1-alkylquinolinium bromide ionic liquids. *Green Chemistry*, 12(3), 420-425.
- Byrne, N., & Angell, C. A. (2008). Protein unfolding, and the "tuning in" of reversible intermediate states, in protic ionic liquid media. *J Mol Biol*, 378(3), 707-714.

- Byrne, N., Howlett, P. C., MacFarlane, D. R., & Forsyth, M. (2005). The Zwitterion Effect in Ionic Liquids: Towards Practical Rechargeable Lithium-Metal Batteries. *Advanced Materials*, 17(20), 2497-2501.
- Callen, H. B. (1948). The Application of Onsager's Reciprocal Relations to Thermoelectric, Thermomagnetic, and Galvanomagnetic Effects. *Physical Review*, 73(11), 1349-1358.
- Cammidge, A. N., Obi, G., Turner, R. J., Coles, S. J., & Tizzard, G. J. (2015). The synthesis of unsymmetrically substituted triphenylenes through controlled construction of the core and subsequent aromatic substitution reactions – a perspective and update. *Liquid Crystals*, 1-7.
- Caprion, D., Bellier-Castella, L., & Ryckaert, J. P. (2003). Influence of shape and energy anisotropies on the phase diagram of discotic molecules. *Phys Rev E Stat Nonlin Soft Matter Phys*, 67(4 Pt 1), 041703.
- Care, C. M., & Cleaver, D. J. (2005). Computer simulation of liquid crystals. *Reports on Progress in Physics*, 68(11), 2665.
- Carvalho, P. S., Jr., Custodio, J. M., Vaz, W. F., Cirilo, C. C., Cidade, A. F., Aquino, G. L., . . . Napolitano, H. B. (2017). Conformation analysis of a novel fluorinated chalcone. *J Mol Model*, 23(3), 97.
- Chakrabarti, D., & Bagchi, B. (2006). Energy landscape view of phase transitions and slow dynamics in thermotropic liquid crystals. *Proceedings of the National Academy of Sciences*, 103(19), 7217-7221.
- Chakrabarti, D., & Wales, D. J. (2008). Energy landscape of a model discotic liquid crystal. *Phys Rev E Stat Nonlin Soft Matter Phys*, 77(5 Pt 1), 051709.
- Chandrabose, K., Narayana, S. H. N. M., Sakthivel, R., Uma, V., Elangovan, M., Devarajan, K., & Piyush, T. (2015). Advances in Chalcones with Anticancer Activities. *Recent Patents on Anti-Cancer Drug Discovery*, 10(1), 97-115.
- Chandran, A., Prakash, K., & Senapati, S. (2010). Structure and dynamics of acetate anion-based ionic liquids from molecular dynamics study. *Chemical Physics*, 374(1-3), 46-54.
- Chandrasekhar, S., & Balagurusamy, V. (2002). *Discotic liquid crystals as quasi-one-dimensional electrical conductors*. Paper presented at the Proceedings of the Royal Society of London A: Mathematical, Physical and Engineering Sciences.
- Chaudhry, A. R., Irfan, A., Muhammad, S., Al-Sehemi, A. G., Ahmed, R., & Jingping, Z. (2017). Computational study of structural, optoelectronic and nonlinear optical properties of dynamic solid-state chalcone derivatives. *J Mol Graph Model*, 75, 355-364.

- Cheng, X., Wang, K., Huang, S., Zhang, H., Zhang, H., & Wang, Y. (2015). Organic Crystals with Near-Infrared Amplified Spontaneous Emissions Based on 2'-Hydroxychalcone Derivatives: Subtle Structure Modification but Great Property Change. *Angew Chem Int Ed Engl*, 54(29), 8369-8373.
- Cheng, Y. C., Silbey, R. J., da Silva Filho, D. A., Calbert, J. P., Cornil, J., & Brédas, J. L. (2003). Three-dimensional band structure and bandlike mobility in oligoacene single crystals: A theoretical investigation. *The Journal of Chemical Physics*, 118(8), 3764-3774.
- Chiang, C. K., Fincher, C. R., Park, Y. W., Heeger, A. J., Shirakawa, H., Louis, E. J., . . . MacDiarmid, A. G. (1977). Electrical Conductivity in Doped Polyacetylene. *Physical Review Letters*, 39(17), 1098-1101.
- Chiappe, C., & Pieraccini, D. (2005). Ionic liquids: solvent properties and organic reactivity. *Journal of Physical Organic Chemistry*, 18(4), 275-297.
- Cinacchi, G., Colle, R., & Tani, A. (2004). Atomistic molecular dynamics simulation of hexakis(pentyloxy)triphenylene: Structure and translational dynamics of its columnar state. *Journal of Physical Chemistry B*, 108(23), 7969-7977.
- Cinacchi, G., Colle, R., & Tani, A. (2004). Atomistic Molecular Dynamics Simulation of Hexakis(pentyloxy)triphenylene: Structure and Translational Dynamics of Its Columnar State. *The Journal of Physical Chemistry B*, 108(23), 7969-7977.
- Cornil, J., Lemaure, V., Calbert, J. P., & Brédas, J. L. (2002). Charge transport in discotic liquid crystals: a molecular scale description. *Adv Mater*, 14(10), 726-729.
- Coropceanu, V., Cornil, J., da Silva Filho, D. A., Olivier, Y., Silbey, R., & Brédas, J.-L. (2007). Charge transport in organic semiconductors. *Chemical Reviews*, 107(4), 926-952.
- Craats, A. M. v. d., Warman, J. M., Fechtenkötter, A., Brand, J. D., Harbison, M. A., & Müllen, K. (1999). Record Charge Carrier Mobility in a Room-Temperature Discotic Liquid-Crystalline Derivative of Hexabenzocoronene. *Advanced Materials*, 11(17), 1469-1472.
- Crispin, X., Cornil, J., Friedlein, R., Okudaira, K. K., Lemaure, V., Crispin, A., . . . Salaneck, W. R. (2004). Electronic Delocalization in Discotic Liquid Crystals: A Joint Experimental and Theoretical Study. *Journal of the American Chemical Society*, 126(38), 11889-11899.
- Delley, B. (1990). An All-Electron Numerical-Method for Solving the Local Density Functional for Polyatomic-Molecules. *Journal of Chemical Physics*, 92(1), 508-517.

- Delley, B. (2000). From molecules to solids with the DMol3 approach. *The Journal of Chemical Physics*, 113(18), 7756.
- Delley, B. (2002). Hardness conserving semilocal pseudopotentials. *Physical Review B*, 66(15).
- Delley, B. (2006). Ground-state enthalpies: evaluation of electronic structure approaches with emphasis on the density functional method. *The Journal of Physical Chemistry A*, 110(50), 13632-13639.
- Diedenhofen, M., & Klamt, A. (2010). COSMO-RS as a tool for property prediction of IL mixtures—A review. *Fluid Phase Equilibria*, 294(1-2), 31-38.
- Dimitrakopoulos, C. D., & Mascaro, D. J. (2001). Organic thin-film transistors: A review of recent advances. *IBM Journal of Research and Development*, 45(1), 11-27.
- Ding, C., Nohira, T., Kuroda, K., Hagiwara, R., Fukunaga, A., Sakai, S., . . . Inazawa, S. (2013). NaFSA–C1C3pyrFSA ionic liquids for sodium secondary battery operating over a wide temperature range. *Journal of Power Sources*, 238, 296-300.
- Dommert, F., Wendler, K., Berger, R., Delle Site, L., & Holm, C. (2012). Force Fields for Studying the Structure and Dynamics of Ionic Liquids: A Critical Review of Recent Developments. *ChemPhysChem*, 13(7), 1625-1637.
- Dommett, M., & Crespo-Otero, R. (2017). Excited state proton transfer in 2'-hydroxychalcone derivatives. *Phys Chem Chem Phys*, 19(3), 2409-2416.
- Douhal, A., Lahmani, F., & Zewail, A. H. (1996). Proton-transfer reaction dynamics. *Chemical Physics*, 207(2), 477-498.
- Eftekhari, A., Liu, Y., & Chen, P. (2016). Different roles of ionic liquids in lithium batteries. *Journal of Power Sources*, 334, 221-239.
- Eichhorn, S. H., Paraskos, A. J., Kishikawa, K., & Swager, T. M. (2002). The interplay of bent-shape, lateral dipole and chirality in thiophene based di-, tri-, and tetracatenar liquid crystals. *J Am Chem Soc*, 124(43), 12742-12751.
- Eichhorn, S. H., Paraskos, A. J., Kishikawa, K., & Swager, T. M. (2002). The interplay of bent-shape, lateral dipole and chirality in thiophene based di-, tri-, and tetracatenar liquid crystals. *J Am Chem Soc*, 124(43), 12742-12751.
- Ekbote, A., Patil, P. S., Maidur, S. R., Chia, T. S., & Quah, C. K. (2017). Structural, third-order optical nonlinearities and figures of merit of (E)-1-(3-substituted phenyl)-3-(4-fluorophenyl) prop-2-en-1-one under CW regime: New chalcone derivatives for optical limiting applications. *Dyes and Pigments*, 139(Supplement C), 720-729.

- Endres, F., & Zein El Abedin, S. (2006). Air and water stable ionic liquids in physical chemistry. *Phys Chem Chem Phys*, 8(18), 2101-2116.
- Espinoza-Hicks, J. C., Camacho-Dávila, A. A., Flores-Holguín, N. R., Nevárez-Moorillón, G. V., Glossman-Mitnik, D., & Rodríguez-Valdez, L. M. (2013). Experimental and quantum chemical studies of a novel synthetic prenylated chalcone. *Chemistry Central Journal*, 7(1), 17.
- Fechtenkötter, A., Saalwächter, K., Harbison, M. A., Müllen, K., & Spiess, H. W. (1999). Highly Ordered Columnar Structures from Hexa-peri-hexabenzocoronenes—Synthesis, X-ray Diffraction, and Solid-State Heteronuclear Multiple-Quantum NMR Investigations. *Angewandte Chemie International Edition*, 38(20), 3039-3042.
- Fontes, E., Heiney, P. A., & de Jeu, W. H. (1988). Liquid-crystalline and helical order in a discotic mesophase. *Phys Rev Lett*, 61(10), 1202-1205.
- Foster, E. J., Jones, R. B., Lavigueur, C., & Williams, V. E. (2006). Structural factors controlling the self-assembly of columnar liquid crystals. *J Am Chem Soc*, 128(26), 8569-8574.
- Fuechsle, M., Miwa, J. A., Mahapatra, S., Ryu, H., Lee, S., Warschkow, O., . . . Simmons, M. Y. (2012). A single-atom transistor. *Nat Nanotechnol*, 7(4), 242-246.
- Gaber, M., Fayed, T. A., El-Daly, S. A., & El-Sayed, Y. S. (2008). Spectral properties and inclusion of a hetero-chalcone analogue in organized media of micellar solutions and beta-cyclodextrin. *Photochemical & Photobiological Sciences*, 7(2), 257-262.
- Gearba, R. I., Anokhin, D. V., Bondar, A. I., Bras, W., Jahr, M., Lehmann, M., & Ivanov, D. A. (2007). Homeotropic alignment of columnar liquid crystals in open films by means of surface nanopatterning. *Adv Mater*, 19(6), 815-820.
- Ghatee, M. H., Zare, M., Moosavi, F., & Zolghadr, A. R. (2010). Temperature-Dependent Density and Viscosity of the Ionic Liquids 1-Alkyl-3-methylimidazolium Iodides: Experiment and Molecular Dynamics Simulation. *Journal of Chemical & Engineering Data*, 55(9), 3084-3088.
- Ghosh, R., & Palit, D. K. (2015). Effect of Donor-Acceptor Coupling on TICT Dynamics in the Excited States of Two Dimethylamine Substituted Chalcones. *J Phys Chem A*, 119(45), 11128-11137.
- Goupil, C., Seifert, W., Zabrocki, K., Muller, E., & Snyder, G. J. (2011). Thermodynamics of Thermoelectric Phenomena and Applications. *Entropy*, 13(8), 1481-1517.
- Grabowski, Z. R., Rotkiewicz, K., & Rettig, W. (2003). Structural Changes Accompanying Intramolecular Electron Transfer: Focus on Twisted

- Intramolecular Charge-Transfer States and Structures. *Chemical Reviews*, *103*(10), 3899-4032.
- Greaves, T. L., & Drummond, C. J. (2008). Protic Ionic Liquids: Properties and Applications. *Chemical Reviews*, *108*(1), 206-237.
- Greaves, T. L., & Drummond, C. J. (2015). Protic Ionic Liquids: Evolving Structure-Property Relationships and Expanding Applications. *Chem Rev*, *115*(20), 11379-11448.
- Greaves, T. L., Weerawardena, A., Fong, C., Krodkiewska, I., & Drummond, C. J. (2006). Protic ionic liquids: solvents with tunable phase behavior and physicochemical properties. *J Phys Chem B*, *110*(45), 22479-22487.
- Grimme, S., Hujo, W., & Kirchner, B. (2012). Performance of dispersion-corrected density functional theory for the interactions in ionic liquids. *Phys Chem Chem Phys*, *14*(14), 4875-4883.
- Hachmann, J., Olivares-Amaya, R., Atahan-Evrenk, S., Amador-Bedolla, C., Sánchez-Carrera, R. S., Gold-Parker, A., . . . Aspuru-Guzik, A. n. (2011). The Harvard Clean Energy Project: Large-Scale Computational Screening and Design of Organic Photovoltaics on the World Community Grid. *The Journal of Physical Chemistry Letters*, *2*(17), 2241-2251.
- Hagele, C., Wuckert, E., Laschat, S., & Giesselmann, F. (2009). Anomalous odd-even effects in columnar and smectic phases of discotic tetraphenylenes. *ChemPhysChem*, *10*(8), 1291-1298.
- Hallett, J. P., & Welton, T. (2011). Room-temperature ionic liquids: solvents for synthesis and catalysis. 2. *Chem Rev*, *111*(5), 3508-3576.
- Hammer, B., Hansen, L. B., & Nørskov, J. K. (1999). Improved adsorption energetics within density-functional theory using revised Perdew-Burke-Ernzerhof functionals. *Physical Review B*, *59*(11), 7413-7421.
- Hartree, D. R. (1928). The Wave Mechanics of an Atom with a Non-Coulomb Central Field. Part I. Theory and Methods. *Mathematical Proceedings of the Cambridge Philosophical Society*, *24*(1), 89-110.
- Hasa, I., Passerini, S., & Hassoun, J. (2016). Characteristics of an ionic liquid electrolyte for sodium-ion batteries. *Journal of Power Sources*, *303*, 203-207.
- Hatsusaka, K., Ohta, K., Yamamoto, I., & Shirai, H. (2001). Discotic liquid crystals of transition metal complexes, Part 30: spontaneous uniform homeotropic alignment of octakis(dialkoxyphenoxy)phthalocyaninatocopper() complexes. *Journal of Materials Chemistry*, *11*(2), 423-433.
- Haverkate, L. A., Zbiri, M., Johnson, M. R., Carter, E., Kotlewski, A., Picken, S., . . . Kearley, G. J. (2014). Electronic and vibronic properties of a discotic

- liquid-crystal and its charge transfer complex. *J Chem Phys*, 140(1), 014903.
- Haverkate, L. A., Zbiri, M., Johnson, M. R., Deme, B., de Groot, H. J., Lefeber, F., . . . Kearley, G. J. (2012). On the morphology of a discotic liquid crystalline charge transfer complex. *J Phys Chem B*, 116(43), 13098-13105.
- Haverkate, L. A., Zbiri, M., Johnson, M. R., Deme, B., Mulder, F. M., & Kearley, G. J. (2011). Conformation, defects, and dynamics of a discotic liquid crystal and their influence on charge transport. *J Phys Chem B*, 115(47), 13809-13816.
- Haverkate, L. A., Zbiri, M., Johnson, M. R., Deme, B., Mulder, F. M., & Kearley, G. J. (2012). Correction to "Conformation, Defects, and Dynamics of a Discotic Liquid Crystal and Their Influence on Charge Transport". *The Journal of Physical Chemistry B*, 116(12), 3908-3908.
- Hirshfeld, F. L. (1977). Bonded-atom fragments for describing molecular charge densities. *Theoretica chimica acta*, 44(2), 129-138.
- Hohenberg, P., & Kohn, W. (1964). Inhomogeneous Electron Gas. *Physical Review*, 136(3B), B864-B871.
- Hsu, B. C., Chiang, C. W., & Chen, Y. C. (2012). Effect of electron-vibration interactions on the thermoelectric efficiency of molecular junctions. *Nanotechnology*, 23(27), 275401.
- Hussey, C. L. (1983). Room temperature molten salt systems. *Advances in Molten Salt Chemistry*, 5, 185-230.
- Imrie, C. T., & Henderson, P. A. (2007). Liquid crystal dimers and higher oligomers: between monomers and polymers. *Chem Soc Rev*, 36(12), 2096-2124.
- Jarosik, A., Krajewski, S. R., Lewandowski, A., & Radzimski, P. (2006). Conductivity of ionic liquids in mixtures. *Journal of Molecular Liquids*, 123(1), 43-50.
- Jensen, F. (2007). *Introduction to computational chemistry*: Wiley.
- Jin, X., Dong, L., Di, X., Huang, H., Liu, J., Sun, X., . . . Zhu, H. (2015). NIR luminescence for the detection of latent fingerprints based on ESIPT and AIE processes. *RSC Adv.*, 5(106), 87306-87310.
- Kaafarani, B. R. (2011). Discotic Liquid Crystals for Opto-Electronic Applications†‡. *Chemistry of Materials*, 23(3), 378-396.
- Kakibe, T., Yoshimoto, N., Egashira, M., & Morita, M. (2010). Optimization of cation structure of imidazolium-based ionic liquids as ionic solvents for rechargeable magnesium batteries. *Electrochemistry Communications*, 12(11), 1630-1633.

- Karton-Lifshin, N., Segal, E., Omer, L., Portnoy, M., Satchi-Fainaro, R., & Shabat, D. (2011). A unique paradigm for a Turn-ON near-infrared cyanine-based probe: noninvasive intravital optical imaging of hydrogen peroxide. *J Am Chem Soc*, *133*(28), 10960-10965.
- Kastler, M., Pisula, W., Wasserfallen, D., Pakula, T., & Mullen, K. (2005). Influence of alkyl substituents on the solution- and surface-organization of hexa-peri-hexabenzocoronenes. *J Am Chem Soc*, *127*(12), 4286-4296.
- Katsori, A.-M., & Hadjipavlou-Litina, D. (2011). Recent progress in therapeutic applications of chalcones. *Expert Opinion on Therapeutic Patents*, *21*(10), 1575-1596.
- Kayal, H., Ahmida, M. M., Dufour, S., Taing, H., & Eichhorn, S. H. (2013). Cross-linking of discotic tetraazaporphyrin dyes in 2 and 3 dimensions by “click” chemistry. *Journal of Materials Chemistry C*, *1*(42), 7064-7072.
- Keppner, H., Uhl, S., Laux, E., Jeandupeux, L., Tschanz, J., & Journot, T. (2015). Ionic Liquid-based Thermoelectric Generator: Links between Liquid Data and Generator Characteristics. *Materials Today: Proceedings*, *2*(2), 680-689.
- Klamt, A., Eckert, F., & Arlt, W. (2010). COSMO-RS: An Alternative to Simulation for Calculating Thermodynamic Properties of Liquid Mixtures. *Annual Review of Chemical and Biomolecular Engineering*, *1*(1), 101-122.
- Krawczyk, P., Pietrzak, M., Janek, T., Jędrzejewska, B., & Cysewski, P. (2016). Spectroscopic and nonlinear optical properties of new chalcone fluorescent probes for bioimaging applications: a theoretical and experimental study. *Journal of Molecular Modeling*, *22*(6), 125.
- Kumar, S. (2004). Recent developments in the chemistry of triphenylene-based discotic liquid crystals. *Liquid Crystals*, *31*(8), 1037-1059.
- Kumar, S. (2006). Self-organization of disc-like molecules: chemical aspects. *Chem Soc Rev*, *35*(1), 83-109.
- Kumar, S. (2013). Nanoparticles in the supramolecular order of discotic liquid crystals. *Liquid Crystals*, *41*(3), 353-367.
- Kumar, S. (2014). Discotic liquid crystal-nanoparticle hybrid systems. *NPG Asia Materials*, *6*(1), e82.
- Kumar, S., Wachtel, E. J., & Keinan, E. (1993). Hexaalkoxytricycloquinazolines: new discotic liquid crystals. *The Journal of Organic Chemistry*, *58*(15), 3821-3827.
- Kwon, J. E., & Park, S. Y. (2011). Advanced organic optoelectronic materials: harnessing excited-state intramolecular proton transfer (ESIPT) process. *Adv Mater*, *23*(32), 3615-3642.

- Laschat, S., Baro, A., Steinke, N., Giesselmann, F., Hagele, C., Scalia, G., . . . Tosoni, M. (2007). Discotic liquid crystals: from tailor-made synthesis to plastic electronics. *Angew Chem Int Ed Engl*, 46(26), 4832-4887.
- Lee, C., Yang, W., & Parr, R. G. (1988). Development of the Colle-Salvetti correlation-energy formula into a functional of the electron density. *Physical Review B*, 37(2), 785-789.
- Lee, J.-S., Tai Kim, S., Cao, R., Choi, N.-S., Liu, M., Lee, K. T., & Cho, J. (2011). Metal-Air Batteries with High Energy Density: Li-Air versus Zn-Air. *Advanced Energy Materials*, 1(1), 34-50.
- Lee, S.-Y., Ogawa, A., Kanno, M., Nakamoto, H., Yasuda, T., & Watanabe, M. (2010). Nonhumidified Intermediate Temperature Fuel Cells Using Protic Ionic Liquids. *Journal of the American Chemical Society*, 132(28), 9764-9773.
- Lemaur, V., da Silva Filho, D. A., Coropceanu, V., Lehmann, M., Geerts, Y., Piris, J., . . . Cornil, J. (2004). Charge transport properties in discotic liquid crystals: a quantum-chemical insight into structure-property relationships. *J Am Chem Soc*, 126(10), 3271-3279.
- Lemaur, V., da Silva Filho, D. A., Coropceanu, V., Lehmann, M., Geerts, Y., Piris, J., . . . Cornil, J. (2004). Charge Transport Properties in Discotic Liquid Crystals: A Quantum-Chemical Insight into Structure–Property Relationships. *J Am Chem Soc*, 126(10), 3271-3279.
- Lever, L. J., Kelsall, R. W., & Bushby, R. J. (2005). Band transport model for discotic liquid crystals. *Physical Review B*, 72(3), 035130.
- Lewandowski, A., & Świdarska-Mocek, A. (2009). Ionic liquids as electrolytes for Li-ion batteries—An overview of electrochemical studies. *Journal of Power Sources*, 194(2), 601-609.
- Lewars, E. G. (2016). *Computational chemistry: introduction to the theory and applications of molecular and quantum mechanics*: Springer.
- Liu, X. Y., Usui, T., & Hanna, J. (2014). Self-directed orientation of molecular columns based on n-type hexaazatrinaphthylenes (HATNAs) for electron transport. *Chemistry*, 20(44), 14207-14212.
- MacFarlane, D. R., Meakin, P., Sun, J., Amini, N., & Forsyth, M. (1999). Pyrrolidinium Imides: A New Family of Molten Salts and Conductive Plastic Crystal Phases. *The Journal of Physical Chemistry B*, 103(20), 4164-4170.
- MacFarlane, D. R., Tachikawa, N., Forsyth, M., Pringle, J. M., Howlett, P. C., Elliott, G. D., . . . Angell, C. A. (2014). Energy applications of ionic liquids. *Energy & Environmental Science*, 7(1), 232-250.

- Malthete, J., Jacques, J., Tinh, N. H., & Destrade, C. (1982). Macroscopic Evidence of Molecular Chirality in Columnar Mesophases. *Nature*, 298(5869), 46-48.
- McKenzie, I., Cammidge, A. N., Dilger, H., Gopee, H., Scheuermann, R., Stoykov, A., & Jayasooriya, U. A. (2010). Muon spin spectroscopy of the discotic liquid crystal HAT6. *Phys Chem Chem Phys*, 12(33), 9900-9908.
- McNeill, R., Siudak, R., Wardlaw, J., & Weiss, D. (1963). Electronic Conduction in Polymers. I. The Chemical Structure of Polypyrrole. *Australian Journal of Chemistry*, 16(6), 1056-1075.
- Migita, T., Tachikawa, N., Katayama, Y., & Miura, T. (2009). Thermoelectromotive Force of Some Redox Couples in an Amide-type Room-temperature Ionic Liquid. *Electrochemistry*, 77(8), 639-641.
- Milgrom, L. R., Yahioğlu, G., Bruce, D. W., Morrone, S., Henari, F. Z., & Blau, W. J. (1997). Mesogenic Zinc(u) complexes of 5,10,15,20-tetraarylethynyl-substituted porphyrins. *Advanced Materials*, 9(4), 313-316.
- Miyajima, D., Araoka, F., Takezoe, H., Kim, J., Kato, K., Takata, M., & Aida, T. (2012). Ferroelectric columnar liquid crystal featuring confined polar groups within core-shell architecture. *Science*, 336(6078), 209-213.
- Mohd Noor, S. A., Howlett, P. C., MacFarlane, D. R., & Forsyth, M. (2013). Properties of sodium-based ionic liquid electrolytes for sodium secondary battery applications. *Electrochimica Acta*, 114, 766-771.
- Mohr, B., Wegner, G., & Ohta, K. (1995). Synthesis of triphenylene-based porphyrazinato metal(II) complexes which display discotic columnar mesomorphism. *Journal of the Chemical Society, Chemical Communications*(10), 995-996.
- Moreno, M., Simonetti, E., Appetecchi, G. B., Carewska, M., Montanino, M., Kim, G.-T., . . . Passerini, S. (2017). Ionic Liquid Electrolytes for Safer Lithium Batteries: I. Investigation around Optimal Formulation. *Journal of The Electrochemical Society*, 164(1), A6026-A6031.
- Mousavi, M. P., Wilson, B. E., Kashefolgheta, S., Anderson, E. L., He, S., Buhlmann, P., & Stein, A. (2016). Ionic Liquids as Electrolytes for Electrochemical Double-Layer Capacitors: Structures that Optimize Specific Energy. *ACS Appl Mater Interfaces*, 8(5), 3396-3406.
- Mulder, F. M., Stride, J., Picken, S. J., Kouwer, P. H. J., de Haas, M. P., Siebbeles, L. D. A., & Kearley, G. J. (2003). Dynamics of a Triphenylene Discotic Molecule, HAT6, in the Columnar and Isotropic Liquid Phases. *Journal of the American Chemical Society*, 125(13), 3860-3866.

- Muller, S., & Mullen, K. (2007). Expanding benzene to giant graphenes: towards molecular devices. *Philos Trans A Math Phys Eng Sci*, 365(1855), 1453-1472.
- Nekovee, M., Foulkes, W. M. C., & Needs, R. J. (2003). Quantum Monte Carlo investigations of density functional theory of the strongly inhomogeneous electron gas. *Physical Review B*, 68(23), 235108.
- Ni, L., Meng, C. Q., & Sikorski, J. A. (2004). Recent advances in therapeutic chalcones. *Expert Opinion on Therapeutic Patents*, 14(12), 1669-1691.
- Noda, A., Susan, M. A. B. H., Kudo, K., Mitsushima, S., Hayamizu, K., & Watanabe, M. (2003). Brønsted Acid–Base Ionic Liquids as Proton-Conducting Nonaqueous Electrolytes. *The Journal of Physical Chemistry B*, 107(17), 4024-4033.
- Noda, A., & Watanabe, M. (2000). Highly conductive polymer electrolytes prepared by in situ polymerization of vinyl monomers in room temperature molten salts. *Electrochimica Acta*, 45(8–9), 1265-1270.
- Norton, J. E., & Brédas, J.-L. (2008). Theoretical characterization of titanyl phthalocyanine as a p-type organic semiconductor: Short intermolecular π - π interactions yield large electronic couplings and hole transport bandwidths. *The Journal of Chemical Physics*, 128(3), 034701.
- NuLi, Y., Yang, J., & Wu, R. (2005). Reversible deposition and dissolution of magnesium from BMIMBF₄ ionic liquid. *Electrochemistry Communications*, 7(11), 1105-1110.
- O'Regan, B., & Grätzel, M. (1991). A low-cost, high-efficiency solar cell based on dye-sensitized colloidal TiO₂ films. *Nature*, 353, 737.
- Ochse, A., Kettner, A., Kopitzke, J., Wendorff, J. H., & Bäessler, H. (1999). Transient photoconduction in discotic liquid crystals. *Physical Chemistry Chemical Physics*, 1(8), 1757-1760.
- Ohno, H. (2006). Functional Design of Ionic Liquids. *Bulletin of the Chemical Society of Japan*, 79(11), 1665-1680.
- Olivier, Y., Muccioli, L., Lemaire, V., Geerts, Y. H., Zannoni, C., & Cornil, J. (2009). Theoretical Characterization of the Structural and Hole Transport Dynamics in Liquid-Crystalline Phthalocyanine Stacks. *The Journal of Physical Chemistry B*, 113(43), 14102-14111.
- Ono, I., & Kondo, S. (1992). A Computational Approach to the Structure and Motion of Hexakis (pentyloxy) triphenylene (THE5) in Discotic Mesophase. *Bulletin of the Chemical Society of Japan*, 65(4), 1057-1061.
- Onsager, L. (1931a). Reciprocal Relations in Irreversible Processes. I. *Physical Review*, 37(4), 405-426.

- Onsager, L. (1931b). Reciprocal Relations in Irreversible Processes. II. *Physical Review*, 38(12), 2265-2279.
- Organero, J. A., Moreno, M., Santos, L., Lluch, J. M., & Douhal, A. (2000). Photoinduced Proton Transfer and Rotational Motion of 1-Hydroxy-2-acetonaphthone in the S1 State: A Theoretical Insight into Its Photophysics. *The Journal of Physical Chemistry A*, 104(36), 8424-8431.
- Orlikova, B., Tasdemir, D., Golais, F., Dicato, M., & Diederich, M. (2011). Dietary chalcones with chemopreventive and chemotherapeutic potential. *Genes & Nutrition*, 6(2), 125-147.
- Oushiki, D., Kojima, H., Terai, T., Arita, M., Hanaoka, K., Urano, Y., & Nagano, T. (2010). Development and Application of a Near-Infrared Fluorescence Probe for Oxidative Stress Based on Differential Reactivity of Linked Cyanine Dyes. *Journal of the American Chemical Society*, 132(8), 2795-2801.
- Palenberg, M. A., Silbey, R. J., Malagoli, M., & Brédas, J. L. (2000). Almost temperature independent charge carrier mobilities in liquid crystals. *The Journal of Chemical Physics*, 112(3), 1541.
- Park, J. H., Kim, K. H., Park, Y. W., Lagerwall, J. P., & Scalia, G. (2015). Ultralong Ordered Nanowires from the Concerted Self-Assembly of Discotic Liquid Crystal and Solvent Molecules. *Langmuir*, 31(34), 9432-9440.
- Patil, P. S., Dharmaprakash, S. M., Ramakrishna, K., Fun, H.-K., Sai Santosh Kumar, R., & Narayana Rao, D. (2007). Second harmonic generation and crystal growth of new chalcone derivatives. *Journal of Crystal Growth*, 303(2), 520-524.
- Perdew, J. P., Burke, K., & Ernzerhof, M. (1996). Generalized gradient approximation made simple. *Physical Review Letters*, 77(18), 3865-3868.
- Perdew, J. P., Ruzsinszky, A., Csonka, G. I., Constantin, L. A., & Sun, J. (2009). Workhorse semilocal density functional for condensed matter physics and quantum chemistry. *Phys Rev Lett*, 103(2), 026403.
- Perdew, J. P., Ruzsinszky, A., Csonka, G. I., Vydrov, O. A., Scuseria, G. E., Constantin, L. A., . . . Burke, K. (2008). Restoring the Density-Gradient Expansion for Exchange in Solids and Surfaces. *Physical Review Letters*, 100(13), 136406.
- Perdew, J. P., & Wang, Y. (1992). Accurate and simple analytic representation of the electron-gas correlation energy. *Physical Review B*, 45(23), 13244-13249.

- Pernak, J., Czepukowicz, A., & Poźniak, R. (2001). New Ionic Liquids and Their Antielectrostatic Properties. *Industrial & Engineering Chemistry Research*, 40(11), 2379-2383.
- Pi, S., Lin, P., & Xia, Q. (2016). Fabrication of sub-10 nm metal nanowire arrays with sub-1 nm critical dimension control. *Nanotechnology*, 27(46), 464004.
- Pisula, W., Menon, A., Stepputat, M., Lieberwirth, I., Kolb, U., Tracz, A., . . . Müllen, K. (2005). A Zone-Casting Technique for Device Fabrication of Field-Effect Transistors Based on Discotic Hexa-peri-hexabenzocoronene. *Advanced Materials*, 17(6), 684-689.
- Poornesh, P., Shettigar, S., Umesh, G., Manjunatha, K. B., Kamath, K. P., Sarojini, B. K., & Narayana, B. (2009). Nonlinear optical studies on 1,3-disubstituent chalcones doped polymer films. *Optical Materials*, 31(6), 854-859.
- Prabhu, A. N., Jayarama, A., Bhat, K. S., & Upadhyaya, V. (2013). Growth, characterization and structural investigation of a novel nonlinear optical crystal. *Journal of Molecular Structure*, 1031, 79-84.
- Pringle, J. M., & Armel, V. (2011). The influence of ionic liquid and plastic crystal electrolytes on the photovoltaic characteristics of dye-sensitised solar cells. *International Reviews in Physical Chemistry*, 30(4), 371-407.
- Ramkumar, V., Anandhi, S., Kannan, P., & Gopalakrishnan, R. (2013). Synthesis, single crystal growth, characterization and comparison of two new enone shifted chalcones and their NLO behaviour. *CrystEngComm*, 15(13), 2438-2449.
- Ramkumar, V., Anandhi, S., Kannan, P., & Gopalakrishnan, R. (2015). Substitution effect on chalcone based materials for corrosion and photocrosslinking applications. *RSC Adv.*, 5(1), 586-596.
- Ravindra, H. J., Harrison, W. T. A., Kumar, M. R. S., & Dharmaprakash, S. M. (2009). Synthesis, crystal growth, characterization and structure-NLO property relationship in 1,3-bis(4-methoxyphenyl)prop-2-en-1-one single crystal. *Journal of Crystal Growth*, 311(2), 310-315.
- Rebelo, L. P. N., Najdanovic-Visak, V., Visak, Z. P., Nunes da Ponte, M., Szydłowski, J., Cerdeiriña, C. A., . . . de Sousa, H. C. (2004). A detailed thermodynamic analysis of [C4mim][BF4] + water as a case study to model ionic liquid aqueous solutions. *Green Chem.*, 6(8), 369-381.
- Reichert, T., Saragi, T. P. I., & Salbeck, J. (2012). Magnetoresistive field-effect transistors based on organic donor-acceptor blends. *RSC Advances*, 2(19), 7388-7390.
- Saha, S., Roy, R. K., & Ayers, P. W. (2009). Are the Hirshfeld and Mulliken population analysis schemes consistent with chemical intuition? *International Journal of Quantum Chemistry*, 109(9), 1790-1806.

- Said, S. M., Mahmood, M. S., Daud, M. N., Mohd Sabri, M. F., & Sairi, N. A. (2016). Structure-electronics relations of discotic liquid crystals from a molecular modelling perspective. *Liquid Crystals*, 1-22.
- Said, S. M., Nordin, A. R., Abdullah, N., & Balamurugan, S. (2015). *Thermoelectricity in liquid crystals*. Paper presented at the SPIE Organic Photonics+ Electronics.
- Schmidtke, J. P., Friend, R. H., Kastler, M., & Müllen, K. (2006). Control of morphology in efficient photovoltaic diodes from discotic liquid crystals. *The Journal of Chemical Physics*, 124(17), 174704.
- Segura, J. L., Juarez, R., Ramos, M., & Seoane, C. (2015). Hexaazatriphenylene (HAT) derivatives: from synthesis to molecular design, self-organization and device applications. *Chem Soc Rev*, 44(19), 6850-6885.
- Seguy, I., Jolinat, P., Destruel, P., Farenc, J., Mamy, R., Bock, H., . . . Nguyen, T. P. (2001). Red organic light emitting device made from triphenylene hexaester and perylene tetraester. *Journal of Applied Physics*, 89(10), 5442-5448.
- Senthilkumar, K., Grozema, F. C., Bickelhaupt, F. M., & Siebbeles, L. D. A. (2003). Charge transport in columnar stacked triphenylenes: Effects of conformational fluctuations on charge transfer integrals and site energies. *Journal of Chemical Physics*, 119(18), 9809-9817.
- Sergeyev, S., Pisula, W., & Geerts, Y. H. (2007). Discotic liquid crystals: a new generation of organic semiconductors. *Chem Soc Rev*, 36(12), 1902-1929.
- Shimizu, M., Kaki, R., Takeda, Y., Hiyama, T., Nagai, N., Yamagishi, H., & Furutani, H. (2012). 1,4-Bis(diarylamino)-2,5-bis(4-cyanophenylethenyl)benzenes: fluorophores exhibiting efficient red and near-infrared emissions in solid state. *Angew Chem Int Ed Engl*, 51(17), 4095-4099.
- Shkir, M., Muhammad, S., AlFaify, S., Irfan, A., Patil, P. S., Arora, M., . . . Jingping, Z. (2015). An investigation on the key features of a D- π -A type novel chalcone derivative for opto-electronic applications. *RSC Adv.*, 5(106), 87320-87332.
- Shuichi, N. (1991). Constant Temperature Molecular Dynamics Methods. *Progress of Theoretical Physics Supplement*, 103, 1-46.
- Siddique, T. A., Balamurugan, S., Said, S. M., Sairi, N. A., & Normazlan, W. M. D. W. (2016). Synthesis and characterization of protic ionic liquids as thermoelectrochemical materials. *RSC Advances*, 6(22), 18266-18278.
- Silvester Debbie, S., & Compton Richard, G. (2006). Electrochemistry in Room Temperature Ionic Liquids: A Review and Some Possible Applications *Zeitschrift für Physikalische Chemie* (Vol. 220, pp. 1247).

- Song, Z., Kwok, R. T., Zhao, E., He, Z., Hong, Y., Lam, J. W., . . . Tang, B. Z. (2014). A ratiometric fluorescent probe based on ESIPT and AIE processes for alkaline phosphatase activity assay and visualization in living cells. *ACS Appl Mater Interfaces*, 6(19), 17245-17254.
- Sosnowska, A., Barycki, M., Gajewicz, A., Bobrowski, M., Freza, S., Skurski, P., . . . Puzyn, T. (2016). Towards the Application of Structure–Property Relationship Modeling in Materials Science: Predicting the Seebeck Coefficient for Ionic Liquid/Redox Couple Systems. *ChemPhysChem*, 17(11), 1591-1600.
- Staroverov, V. N., Scuseria, G. E., Tao, J., & Perdew, J. P. (2003). Comparative assessment of a new nonempirical density functional: Molecules and hydrogen-bonded complexes. *The Journal of Chemical Physics*, 119(23), 12129-12137.
- Stephens, P. J., Devlin, F. J., Chabalowski, C. F., & Frisch, M. J. (1994). Ab Initio Calculation of Vibrational Absorption and Circular Dichroism Spectra Using Density Functional Force Fields. *The Journal of Physical Chemistry*, 98(45), 11623-11627.
- Stokbro, K., Taylor, J., & Brandbyge, M. (2003). Do Aviram–Ratner Diodes Rectify? *J Am Chem Soc*, 125(13), 3674-3675.
- Stoppa, A., Zech, O., Kunz, W., & Buchner, R. (2010). The Conductivity of Imidazolium-Based Ionic Liquids from (–35 to 195) °C. A. Variation of Cation’s Alkyl Chain†. *Journal of Chemical & Engineering Data*, 55(5), 1768-1773.
- Sun, S.-S., & Dalton, L. R. (2016). *Introduction to Organic Electronic and Optoelectronic Materials and Devices: Second Edition*: CRC Press/Taylor & Francis Group: Boca Raton, Florida, USA.
- Susan, M. A. B. H., Noda, A., Mitsushima, S., & Watanabe, M. (2003). Brønsted acid–base ionic liquids and their use as new materials for anhydrous proton conductors. *Chemical Communications*(8), 938.
- Takezoe, H., & Araoka, F. (2013). Polar columnar liquid crystals. *Liquid Crystals*, 41(3), 393-401.
- Tang, K. C., Chang, M. J., Lin, T. Y., Pan, H. A., Fang, T. C., Chen, K. Y., . . . Chou, P. T. (2011). Fine tuning the energetics of excited-state intramolecular proton transfer (ESIPT): white light generation in a single ESIPT system. *J Am Chem Soc*, 133(44), 17738-17745.
- Tao, J., Perdew, J. P., Staroverov, V. N., & Scuseria, G. E. (2003). Climbing the density functional ladder: nonempirical meta-generalized gradient approximation designed for molecules and solids. *Phys Rev Lett*, 91(14), 146401.

- Tehfe, M. A., Dumur, F., Xiao, P., Delgove, M., Graff, B., Fouassier, J. P., . . . Lalevee, J. (2014). Chalcone derivatives as highly versatile photoinitiators for radical, cationic, thiol-ene and IPN polymerization reactions upon exposure to visible light. *Polymer Chemistry*, 5(2), 382-390.
- Tong, Y., Tang, Q., Lemke, H. T., Moth-Poulsen, K., Westerlund, F., Hammershoj, P., . . . Bjornholm, T. (2010). Solution-based fabrication of single-crystalline arrays of organic nanowires. *Langmuir*, 26(2), 1130-1136.
- Toulouse, J., Colonna, F., & Savin, A. (2005). Short-range exchange and correlation energy density functionals: beyond the local-density approximation. *J Chem Phys*, 122(1), 14110.
- Troisi, A., & Orlandi, G. (2006). Dynamics of the intermolecular transfer integral in crystalline organic semiconductors. *The Journal of Physical Chemistry A*, 110(11), 4065-4070.
- Tsuda, T., & Hussey, C. L. (2007). Electrochemical applications of room-temperature ionic liquids. *Interface-Electrochemical Society*, 16(1), 42-49.
- Tsuji, Y., & Yoshizawa, K. (2012). Current Rectification through π - π Stacking in Multilayered Donor-Acceptor Cyclophanes. *The Journal of Physical Chemistry C*, 116(50), 26625-26635.
- Varma, R. S. (1996). Dietary bioflavonoids, chalcones, and related alkenones in prevention and treatment of cancer. *Nutrition*, 12(9), 643-645.
- Vaughan, G., Heiney, P., McCauley Jr, J., & Smith III, A. B. (1992). Conductivity and structure of a liquid-crystalline organic conductor. *Physical Review B*, 46(5), 2787.
- Vaughan, G. B., Heiney, P. A., McCauley, J. P., Jr., & Smith, A. B., 3rd. (1992). Conductivity and structure of a liquid-crystalline organic conductor. *Phys Rev B Condens Matter*, 46(5), 2787-2791.
- Wang, K., Zhang, H., Chen, S., Yang, G., Zhang, J., Tian, W., . . . Wang, Y. (2014). Organic polymorphs: one-compound-based crystals with molecular-conformation- and packing-dependent luminescent properties. *Adv Mater*, 26(35), 6168-6173.
- Wang, S., Yan, X., Cheng, Z., Zhang, H., Liu, Y., & Wang, Y. (2015). Highly Efficient Near-Infrared Delayed Fluorescence Organic Light Emitting Diodes Using a Phenanthrene-Based Charge-Transfer Compound. *Angew Chem Int Ed Engl*, 54(44), 13068-13072.
- Warman, J. M., & Van De Craats, A. M. (2003). Charge Mobility in Discotic Materials Studied by Pr-Trmc. *Molecular Crystals and Liquid Crystals*, 396(1), 41-72.

- Wasserscheid, P., & Keim, W. (2000). Ionic Liquids—New “Solutions” for Transition Metal Catalysis. *Angewandte Chemie International Edition*, 39(21), 3772-3789.
- Wegewijs, B. R., Siebbeles, L. D. A., Boden, N., Bushby, R. J., Movaghar, B., Lozman, O. R., . . . Mason, L. A. (2002). Charge-carrier mobilities in binary mixtures of discotic triphenylene derivatives as a function of temperature. *Physical Review B*, 65(24).
- Weissleder, R. (2001). A clearer vision for in vivo imaging. *Nature Biotechnology*, 19, 316.
- Wendler, K., Dommert, F., Zhao, Y. Y., Berger, R., Holm, C., & Delle Site, L. (2012). Ionic liquids studied across different scales: a computational perspective. *Faraday Discuss*, 154, 111-132; discussion 189-220, 465-171.
- Wilkes, J. (2004). Properties of ionic liquid solvents for catalysis. *Journal of Molecular Catalysis A: Chemical*, 214(1), 11-17.
- Wilkes, J. S., Levisky, J. A., Wilson, R. A., & Hussey, C. L. (1982). Dialkylimidazolium chloroaluminate melts: a new class of room-temperature ionic liquids for electrochemistry, spectroscopy and synthesis. *Inorganic Chemistry*, 21(3), 1263-1264.
- Wishart, J. F. (2009). Energy applications of ionic liquids. *Energy & Environmental Science*, 2(9), 956.
- Witanowski, M., Sicinska, W., Grabowski, Z., & Webb, G. A. (1993). Pyrrole and N-Methylpyrrole as Models for Solvent Polarity and Solute-to-Solvent Hydrogen-Bonding Effects on Nitrogen NMR Shielding. *Journal of Magnetic Resonance, Series A*, 104(3), 310-314.
- Wohrle, T., Wurzbach, I., Kirres, J., Kostidou, A., Kapernaum, N., Litterscheidt, J., . . . Laschat, S. (2016). Discotic Liquid Crystals. *Chem Rev*, 116(3), 1139-1241.
- Xu, W., & Angell, C. A. (2003). Solvent-free electrolytes with aqueous solution-like conductivities. *Science*, 302(5644), 422-425.
- Yaghini, N., Nordstierna, L., & Martinelli, A. (2014). Effect of water on the transport properties of protic and aprotic imidazolium ionic liquids - an analysis of self-diffusivity, conductivity, and proton exchange mechanism. *Phys Chem Chem Phys*, 16(20), 9266-9275.
- Yella, A., Lee, H.-W., Tsao, H. N., Yi, C., Chandiran, A. K., Nazeeruddin, M. K., . . . Grätzel, M. (2011). Porphyrin-Sensitized Solar Cells with Cobalt (II/III)-Based Redox Electrolyte Exceed 12 Percent Efficiency. *Science*, 334(6056), 629-634.
- Yella, A., Mai, C.-L., Zakeeruddin, S. M., Chang, S.-N., Hsieh, C.-H., Yeh, C.-Y., & Grätzel, M. (2014). Molecular Engineering of Push–Pull Porphyrin Dyes

for Highly Efficient Dye-Sensitized Solar Cells: The Role of Benzene Spacers. *Angewandte Chemie*, 126(11), 3017-3021.

- Yoshizawa, M., Xu, W., & Angell, C. A. (2003). Ionic liquids by proton transfer: vapor pressure, conductivity, and the relevance of ΔpK_a from aqueous solutions. *J Am Chem Soc*, 125(50), 15411-15419.
- Zahid, N. I., Mahmood, M. S., Subramanian, B., Mohd Said, S., & Abou-Zied, O. K. (2017). New Insight into the Origin of the Red/Near-Infrared Intense Fluorescence of a Crystalline 2-Hydroxychalcone Derivative: A Comprehensive Picture from the Excited-State Femtosecond Dynamics. *J Phys Chem Lett*, 8(22), 5603-5608.
- Zahn, S., & Kirchner, B. (2008). Validation of Dispersion-Corrected Density Functional Theory Approaches for Ionic Liquid Systems. *The Journal of Physical Chemistry A*, 112(36), 8430-8435.
- Zbiri, M., Johnson, M. R., Haverkate, L., Mulder, F. M., & Kearley, G. J. (2010). Molecular Modelling of Ground- and Excited-States Vibrations in Organic Conducting Devices: Hexakis(n-hexyloxy)triphenylene (HAT6) as Case Study. *Australian Journal of Chemistry*, 63(3), 388.
- Zbiri, M., Johnson, M. R., Kearley, G. J., & Mulder, F. M. (2009). Density functional calculations of potential energy surface and charge transfer integrals in molecular triphenylene derivative HAT6. *Theoretical Chemistry Accounts*, 125(3-6), 445-451.
- Zerner, M. C., Loew, G. H., Kirchner, R. F., & Mueller-Westerhoff, U. T. (1980). An intermediate neglect of differential overlap technique for spectroscopy of transition-metal complexes. Ferrocene. *Journal of the American Chemical Society*, 102(2), 589-599.
- Zhao, C., Burrell, G., Torriero, A. A., Separovic, F., Dunlop, N. F., MacFarlane, D. R., & Bond, A. M. (2008). Electrochemistry of room temperature protic ionic liquids. *J Phys Chem B*, 112(23), 6923-6936.
- Zhao, J., Ji, S., Chen, Y., Guo, H., & Yang, P. (2012). Excited state intramolecular proton transfer (ESIPT): from principal photophysics to the development of new chromophores and applications in fluorescent molecular probes and luminescent materials. *Phys Chem Chem Phys*, 14(25), 8803-8817.
- Zhao, X. M., Zhong, G. H., Zhang, J., Huang, Q. W., Goncharov, A. F., Lin, H. Q., & Chen, X. J. (2016). Combined experimental and computational study of high-pressure behavior of triphenylene. *Sci Rep*, 6, 25600.
- Zhou, H.-X., & Gilson, M. K. (2009). Theory of Free Energy and Entropy in Noncovalent Binding. *Chemical Reviews*, 109(9), 4092-4107.

LIST OF PUBLICATION AND PAPERS PRESENTED

Publications

1. Said, S. M., Mahmood, M. S., Daud, M. N., Mohd Sabri, M. F., & Sairi, N. A. (2016). Structure-electronics relations of discotic liquid crystals from a molecular modelling perspective. *Liquid Crystals*, 1-22. doi:10.1080/02678292.2016.1209792.
2. Mahmood, M. S., Said, S. M., Chatterjee, A., Mohd Sabri, M. F., Mainal, A., Daud, M. N., Sairi, N. A. (2018). DFT Studies of Structural–Electronic Correlation for The HAT6 Discotic Liquid Crystal Columnar Stacking. *Materials Research Express*.
3. Zahid, N. I., Mahmood, M. S., Subramanian, B., Mohd Said, S., & Abou-Zied, O. K. (2017). New Insight into the Origin of the Red/Near-Infrared Intense Fluorescence of a Crystalline 2-Hydroxychalcone Derivative: A Comprehensive Picture from the Excited-State Femtosecond Dynamics. *J Phys Chem Lett*, 8(22), 5603-5608. doi:10.1021/acs.jpcllett.7b02601.

Paper presented

1. Mahmood, M. S., Said, S. M., Daud, M. N., & Sairi, N. A. (2016, November 10). *Quantum Thermodynamics Transitional States in Protic Ionic Liquid*. Paper presented at the 1st International Research Conference on Engineering, Science and Humanities (IRCESH 2016), UKM, Bangi, Malaysia.